

**NICKEL BASED CATALYSTS FOR HYDROGEN
PRODUCTION FROM THE
PYROLYSIS/GASIFICATION OF REFUSE DERIVED
FUEL (RDF)**

By

Paula Helena Blanco Sanchez

Submitted in accordance with the requirements for the degree of
Doctor of Philosophy

The University of Leeds
School of Process, Environmental and Materials Engineering
Energy Research Institute

June 2014

The candidate confirms that the work submitted is her own, except where work which has formed part of jointly-authored publications has been included. The contribution of the candidate and the other authors to this work has been explicitly indicated below. The candidate confirms that appropriate credit has been given within the thesis where reference has been made to the work of others.

This copy has been supplied on the understanding that it is copyright material and that no quotation from the thesis may be published without proper acknowledgement.

Journal Papers

Investigation of different bed type and process conditions in CHAPTER 4 was based on the following published paper:

1. Blanco, P. H., Wu, C., Onwudili, J. A., and Williams, P. T. (2012) Characterization of Tar from the Pyrolysis/Gasification of Refuse Derived Fuel: Influence of Process Parameters and Catalysis, *Energy & Fuels* 26, 2107-2115.

Investigation of diverse nickel-based catalysts during the pyrolysis-gasification of RDF in CHAPTER 5 was based on the following published papers:

2. Blanco, P. H., Wu, C., Onwudili, J. A., and Williams, P. T. (2013) Characterization and evaluation of Ni/SiO₂ catalysts for hydrogen production and tar reduction from catalytic steam pyrolysis-reforming of refuse derived fuel, *Applied Catalysis B: Environmental* 134–135, 238-250.
3. Blanco, P., Wu, C., Onwudili, J., Dupont, V., and Williams, P. (2013) Catalytic Pyrolysis/Gasification of Refuse Derived Fuel for Hydrogen Production and Tar Reduction: Influence of Nickel to Citric Acid Ratio Using Ni/SiO₂ Catalysts, *Waste and Biomass Valorization Journal*, 1-12.

4. Blanco, P. H., Wu, C., and Williams, P. T. (2014) Influence of Ni/SiO₂ catalyst preparation methods on hydrogen production from the pyrolysis/reforming of refuse derived fuel, *International Journal of Hydrogen Energy*, 39, 5723-5732.

Conference Papers

1. Williams, P. T., Efika, C. E., Blanco, P. H., Myers, L., Wu, C., and Onwudili, J. A. (2011) Hydrogen and syngas production from pyrolysis-gasification of RDF and wood pellets in a continuous screw kiln reactor, In *19th European Biomass Conference and Exhibition*, Berlin, Germany.
2. Blanco, P. H., Wu, C., Onwudili, J. A., Dupont, V., and Williams, P. T. (2012) High hydrogen/low tar syngas from pyrolysis/gasification of Municipal Solid Waste, In *4th International Conference on Engineering for Waste and Biomass Valorisation*, Porto, Portugal.
3. Blanco, P. H., Efika, C. E., Wu, C., Onwudili, J. A., and Williams, P. T. (2013) Hydrogen generation from the pyrolysis-catalytic gasification of solid wastes and biomass using different nickel based catalysts, In *21st European Biomass Conference and Exhibition*, Copenhagen, Denmark.
4. Blanco, P. H., Wu, C., Williams, P. T. (2014) Hydrogen-rich syngas from pyrolysis-catalytic steam reforming of solid waste, In *7th Annual World Congress of Industrial Biotechnology*, Dalian, China.

The candidate Paula Helena Blanco Sanchez performed the experimental and analytical work, wrote the initial drafts of the papers along with supporting material including Tables and Figures, and carried out the calculation and summarisation of the results and developed the discussion part.

The co-authors, Prof. P. T. Williams, C. Wu, and J. Onwudili, supervised and supported the entire research work, proof read the drafts and made suggestions and corrections to the draft papers.

The right of Paula Helena Blanco Sanchez to be identified as Author of this work has been asserted by her in accordance with the Copyright, Designs and Patents Act 1988.

© 2014 The University of Leeds and Paula Helena Blanco Sanchez

Acknowledgements

Foremost, I would like to express my profound gratitude to the National Council of Science and Technology in Mexico (Conacyt), for the scholarship to undertake this PhD. I want to thank the support from the White Rose Collaboration Fund and the WUN research mobility programme, for the financing to carry out a one-month research stay at the laboratory for Catalysis Engineering, School of Chemical and Biomolecular Engineering, University of Sydney, in Australia. I would like to thank the support from the Leeds for Life Foundation, for the support to present my research work in two international conferences, in Portugal and Copenhagen. Also I would like to acknowledge the Transnational Access granted from the Biofuels Research Infrastructure for Sharing Knowledge programme (BRISK), in joint with the KTH Royal Institute of Technology, to carry out experiments in a pilot plant at the Energy Research Centre of the Netherlands (ECN).

My deepest and sincere gratitude to my supervisor Professor Paul T. Williams, for his kind help, excellent guidance, caring, encouragement, support and patience since the beginning of this research. Thanks also for sharing your knowledge, for always being available, and for helping me with my queries and concerns all the time. Thanks for reading this thesis and for your aid with the development of this research work. I feel very fortunate to have had an admirable supervisor.

I want to especially thank to Dr. Chunfei Wu, Dr. Jude Onwudilli and Dr. Surjit Singh for their feedback, perseverance, for their academic advices and for sharing your knowledge with me; but most importantly for their friendship and support during the last three years. Thanks to Mr. Ed Woodhouse for his technical support in design and modification of the reactor. I also want to thank to my colleagues in my research group: Chidi, Anas, Ramzi, Eyup, Jonathan,

Amal, Chika, and Juniza, for your help and friendship. It has been an enrichment experience to work with all of you.

Above all, I would like to thank to my beloved family: my mom who shows me that every day is a battle, to my dad for helping me to develop my character and for believe in me, thanks to both of you for your unconditional love and support, thanks for showing me there is no worst enemy than oneself. This work is also part of your tireless effort. I would have to write another Thesis to thank my brother for cheering me up, for his patience and love; you have always been and will be my role model. To my brother Francisco, who is no longer with us, but will live always in my heart. To my grand mom, cousins, uncles, aunts, nephews and nieces, for always have me in your thoughts. Thanks for making me feel close to you, when being so far.

I am fortunate to have met several awesome people in the last few years, and I am sure some of them will be in my life for long time. All of you contributed to really enjoy my time in Leeds: Sac, Azael, Javier, Alexis, Boyangcita, Dianis, Oli, Yanis, Fer, Nabil, Ray, Raul, Richard, Claire and Dorian, thanks for sharing a cup of coffee, for the discussions, for the team work, for sharing your food, for the laughs, for listening my complaints...for your friendship. Ryan thanks for bringing more shine and joy to my life, for your patience and for encouraging me to give my best. I am most grateful to my friends I left back in Mexico when I decided to undertake this professional and personal adventure. I want to thank all of you for believe in me and for making me feel so lucky and beloved.

Abstract

Hydrogen can be used as fuel for power generation; however current hydrogen production processes are not sustainable as they involve considerable CO₂ emissions, and are mostly based on production from fossil fuels. Municipal solid waste (MSW) in the form of refuse derived fuel (RDF) can be subjected to thermal processes such as pyrolysis and/or gasification to produce a hydrogen rich syngas. Nevertheless some operational problems associated with tar formation arise, which significantly reduces the overall process yield.

In this work a two-stage reaction system was used for hydrogen production and tar reduction, during the pyrolysis/gasification of RDF, using different types of catalysts. Firstly RDF was pyrolyzed at 600°C, the pyrolysis gases were then passed through a second gasification stage where the catalytic steam reforming process took place at 800°C, in order to generate hydrogen and promote tar cracking reactions. Different analytical techniques were used in this work to characterise RDF, product gases, tars/oils, and fresh/reacted catalysts.

Initially two different Ni/Al₂O₃ catalysts were prepared, and their catalytic activity towards hydrogen production and tar reduction were assessed during the pyrolysis/gasification of RDF. The results were compared with those obtained using a bed of sand. Using a 10 wt.% Ni/Al₂O₃ catalyst, about 45 vol.% of hydrogen in the syngas was obtained together with other gases: CO₂, CO, CH₄, C₂-C₄. Also the condensed tar fraction was analysed and was found to contain polyaromatic hydrocarbon (PAH) constituents included naphthalene, fluorene and phenanthrene as the major components. Additionally, diverse Ni/SiO₂ catalysts were prepared using different synthesis methods, including sol-gel, impregnation and homogenous precipitation. Among the catalysts tested for tar reduction, a 20wt.% Ni/SiO₂ catalyst presented the highest activity resulting in a tar concentration of 0.15mg_{tar} g⁻¹_{RDF}; PAH and oxygenated tar compounds were also identified within the analysed samples. For the catalysts tested in relation to hydrogen production, using a 10wt.% Ni/SiO₂ catalyst prepared by homogeneous precipitation-sol-gel based method, resulted in a H₂ concentration of 59 vol.%. Finally different Fe/SiO₂ and Ni/SiO₂ catalysts were prepared using nano-porous silica as the oxide support. Better catalyst activity in relation to H₂ production was observed for the Ni/SiO₂ catalysts. However the maximum H₂ concentration obtained was around 44 vol.%. It was found that using calcination temperatures higher than 700°C, both the surface area and the catalytic activity for hydrogen production was diminished for this series of catalysts.

Table of Contents

Acknowledgements.....	iv
Abstract	vi
Table of Contents	vii
List of Tables.....	xiii
List of Figures.....	xvi
Abbreviations.....	xxi
CHAPTER 1 INTRODUCTION.....	- 1 -
1.1 Municipal Solid Waste (MSW) generation.....	- 1 -
1.1.1 Refuse Derived Fuel (RDF) production and composition	- 3 -
1.1.2 Current MSW disposal methods and alternative treatments	- 3 -
1.1.2.1 Pyrolysis and Gasification of solid wastes	- 4 -
1.2 Syngas production and potential uses	- 5 -
1.3 Hydrogen production, applications and future	- 6 -
1.4 Tar: definition, composition and problems associated	- 7 -
1.4.1 Tar removal methods	- 7 -
1.4.1.1 Catalytic steam reforming.....	- 8 -
1.5 Description and Objectives of this Research	- 8 -
CHAPTER 2 LITERATURE REVIEW.....	- 14 -
2.1 Municipal Solid Waste (MSW).....	- 14 -
2.1.1 MSW generation and composition.....	- 14 -
2.1.2 Refuse Derived Fuel (RDF) definition and composition.....	- 19 -
2.1.2.1 MSW disposal and treatment methods.....	- 24 -
2.1.2.2 Alternative thermal treatment for MSW and RDF.....	- 26 -
2.1.2.3 Pyrolysis.....	- 28 -
2.1.2.4 Gasification	- 33 -
2.1.2.4.1 Types of gasifier	- 35 -
2.2 Pyrolysis-gasification for hydrogen production	- 37 -
2.2.1 Syngas and Hydrogen; potential applications	- 39 -
2.3 Tar: definition and composition	- 44 -

2.3.1	Syngas tar requirements.....	- 51 -
2.3.2	Alternatives for tar removal and tar reduction.....	- 52 -
2.4	Pyrolysis-catalytic steam reforming process	- 53 -
2.4.1	Tar cracking reactions in the catalytic process.....	- 54 -
2.4.2	Tar model compounds	- 55 -
2.4.3	Tar sampling methods	- 57 -
2.4.4	Types of catalysts used for catalytic steam reforming	- 60 -
2.4.5	Nickel-based catalysts during the pyrolysis-gasification process.....	- 61 -
2.4.5.1	Addition of metal promoters to nickel-based catalysts.....	- 64 -
2.4.6	Summary of nickel-based catalysts.....	- 65 -
CHAPTER 3 EXPERIMENTAL METHODOLOGY		- 78 -
3.1	Introduction	- 78 -
3.2	Materials.....	- 78 -
3.2.1	Refuse derived fuel (RDF)	- 78 -
3.2.1.1	Elemental Analysis of RDF	- 78 -
3.2.1.2	Thermogravimetric Analysis of RDF.....	- 79 -
3.2.2	Researched catalysts	- 81 -
3.2.2.1	Ni/Al ₂ O ₃ impregnated catalysts.....	- 81 -
3.2.2.2	Ni/SiO ₂ catalysts by different preparation methods and metal loadings	- 81 -
3.2.2.3	Ni/SiO ₂ catalysts prepared using different nickel to citric acid (Ni:CA) ratios	- 82 -
3.2.2.4	Ni/SiO ₂ catalysts prepared by homogeneous precipitation methods.....	- 83 -
3.2.2.5	Fe-Ni/SiO ₂ catalysts using a nano-support	- 84 -
3.3	Two-stage fixed bed pyrolysis/gasification reaction system.....	- 85 -
3.3.1	Reactor Set-up.....	- 85 -
3.3.2	Experiment Reproducibility and Selection of Process Conditions	- 86 -
3.3.2.1	Experimental Procedure.....	- 90 -
3.4	Characterisation of materials and products	- 91 -
3.4.1	Analysis of produced gases (GC).....	- 91 -
3.4.1.1	Permanent Gas Chromatography (GC) Analysis.....	- 92 -
3.4.1.2	Hydrocarbons Gas Chromatography (GC) Analysis.....	- 92 -

3.4.1.3	Calibration of Gas Chromatograph instruments	- 92 -
3.4.1.4	Calculation of gas concentration	- 94 -
3.4.1.5	Reproducibility of gas analysis	- 95 -
3.4.2	Characterization of catalysts (fresh/reacted)	- 98 -
3.4.2.1	Determination of surface area by Brunauer-Emmett-Teller (BET) method.....	- 98 -
3.4.2.2	Determination of micropore volume by Dubinin-Radushkevich (DR) method.....	- 100 -
3.4.2.3	Barrett, Joyner & Halenda (BJH) method for total pore volume and pore diameter determination	- 101 -
3.4.2.4	Pore size distribution by Density Functional Theory (DFT)	- 102 -
3.4.2.5	X-ray Diffraction (XRD)	- 102 -
3.4.2.6	Temperature programmed oxidation (TGA-TPO).....	- 104 -
3.4.2.7	Scanning Electron Microscopy (SEM) and Transmission Electron Microscopy (TEM).....	- 105 -
3.4.2.8	Infrared Spectrometry (FTIR).....	- 108 -
3.4.3	Analysis of liquid fraction (tar/oil/H ₂ O)	- 109 -
3.4.3.1	Sample preparation: centrifugation for DCM evaporation.....	- 110 -
3.4.3.2	Karl-Fischer Titration	- 110 -
3.4.3.3	Gas Chromatography/Mass Spectrometry (GC-MS).....	- 112 -
3.4.3.4	Size Exclusion Chromatography (SEC) and FTIR.....	- 117 -
CHAPTER 4 EFFECTS OF OPERATIONAL PARAMETERS ON GAS AND LIQUID YIELDS AND COMPOSITION.....		- 122 -
4.1	Effects of bed type and gasification temperature, on gas and liquid products during pyrolysis-gasification of RDF	- 122 -
4.1.1	Ni/Al ₂ O ₃ catalysts	- 122 -
4.1.2	Gas composition and Mass Balance	- 123 -
4.1.3	Tar Analysis.....	- 126 -
4.1.3.1	GC-MS analysis of the collected tar.....	- 126 -
4.1.3.2	Size Exclusion Chromatography (SEC)	- 132 -
4.1.3.3	FTIR Analysis	- 134 -
4.1.4	Summary	- 137 -

CHAPTER 5 PREPARATION, CHARACTERIZATION AND EVALUATION OF NICKEL BASED CATALYSTS.....	- 141 -
5.1 Ni/SiO ₂ catalysts: Influence of metal loading, metal promoters and preparation method on catalyst characteristics	- 142 -
5.1.1 Characterization of fresh Ni/SiO ₂ catalysts	- 142 -
5.1.2 Test of the catalytic activity of Ni/SiO ₂ catalysts.....	- 148 -
5.1.2.1 Performance of Ni/SiO ₂ catalysts towards hydrogen production.....	- 152 -
5.1.3 GC-MS analysis of the condensed tar fraction	- 152 -
5.1.4 Analysis of reacted Ni/SiO ₂ catalysts	- 163 -
5.1.4.1 Thermogravimetric analysis (TGA).....	- 163 -
5.1.4.2 Scanning electron microscopy (SEM).....	- 166 -
5.1.5 Summary of Ni/SiO ₂ characteristics and performance.....	- 168 -
5.2 Effects of nickel to citric acid ratio (Ni:CA)	- 174 -
5.2.1 Catalysts preparation and characterization	- 174 -
5.2.2 Study of the catalytic activity	- 177 -
5.2.3 Analysis of the tar fraction	- 179 -
5.2.4 Analysis of reacted catalysts.....	- 183 -
5.2.5 Summary	- 185 -
5.3 Ni/SiO ₂ catalysts prepared by homogeneous precipitation (HPG) and homogeneous precipitation with phase separation (B-HPG) methods	- 189 -
5.3.1 Characteristics of Ni/SiO ₂ catalysts prepared by HPG and B-HPG methods.....	- 191 -
5.3.2 Analysis of catalytic activity of Ni/SiO ₂ catalysts prepared by HPG and B-HPG methods.....	- 199 -
5.3.3 Analysis of reacted catalysts.....	- 202 -
5.3.4 Summary of HPG and B-HPG catalysts	- 207 -
CHAPTER 6 COMPARISON BETWEEN NICKEL AND IRON BASED CATALYSTS	- 210 -
6.1 Fe/SiO ₂ and Ni/SiO ₂ catalysts.....	- 210 -
6.2 Characterization of fresh Fe/SiO ₂ and Ni/SiO ₂ catalysts	- 211 -
6.3 Hydrogen production using Fe/SiO ₂ and Ni/SiO ₂ in the pyrolysis- gasification process	- 220 -
6.4 Analysis of reacted Fe/SiO ₂ and Ni/SiO ₂ catalysts.....	- 223 -
6.5 Summary.....	- 225 -

CHAPTER 7 GASIFICATION AND COMBUSTION OF RDF: PILOT SCALE	
FLUIDISED BED.....	- 228 -
7.1 Introduction	- 228 -
7.2 Fluidised bed system	- 228 -
7.2.1 WOB reaction system considerations.....	- 231 -
7.3 Physical properties of the fuel and bed material	- 231 -
7.3.1 Refuse derived fuel (RDF) characteristics	- 231 -
7.3.2 Olivine as bed material	- 232 -
7.4 Sampling and analysis of gaseous and solid samples.....	- 232 -
7.4.1 Gas chromatography for on-line and off-line analyses	- 233 -
7.4.1.1 Solid phase adsorption (SPA) tar sampling method.....	- 234 -
7.4.2 Definition of operational variables and control system	- 234 -
7.4.3 Gasification and combustion processes	- 236 -
7.5 Results from the analysis of gaseous and solid fractions	- 236 -
7.5.1 Gas composition	- 238 -
7.5.2 Tar analysis	- 240 -
7.5.3 Ash characterisation using SEM-EDX.....	- 241 -
7.6 Challenges of scaling up and additional results required.....	- 243 -
7.7 Summary.....	- 244 -
CHAPTER 8 CONCLUSIONS AND SUGGESTIONS FOR FUTURE WORK.....	- 247 -
8.1 General conclusions.....	- 247 -
8.1.1 Analysis of process conditions on gas and tar compositions.....	- 247 -
8.1.2 Characterisation and assessment of Ni/SiO ₂ catalysts prepared by two methods and promoted with Mg, Ce and Al.....	- 248 -
8.1.3 Effects of varying the Ni:CA ratio over catalysts properties and performance towards hydrogen production and tar reduction	- 248 -
8.1.4 Ni/SiO ₂ catalysts prepared by homogeneous precipitation based methods; effects over catalysts properties and catalytic activity.....	- 249 -
8.1.5 Comparison and assessment of Fe/SiO ₂ and Ni/SiO ₂ catalysts prepared using a nano-porous silica support.....	- 249 -
8.1.6 Performance of olivine as bed material in a pilot scale fluidised bed gasifier, analysis of gas and tar composition.....	- 250 -
8.1.7 General remarks.....	- 250 -

8.2	Future work.....	- 251 -
8.2.1	Analysis of catalysts characteristics and activity	- 251 -
8.2.2	Lifecycle tests of catalysts	- 251 -
8.2.3	Modifications in process conditions.....	- 252 -
8.2.4	Efficiency of catalysts for tar reduction	- 252 -
8.2.5	Applications of nickel-based catalysts for hydrogen production using RDF as feedstock.....	- 252 -

List of Tables

Table 2.1-1. MSW fractions and description.....	- 17 -
Table 2.1-2. Typical properties of MSW.....	- 18 -
Table 2.1-3. Refuse derived fuel (RDF) classification.....	- 21 -
Table 2.1-4. Elemental analysis of RDF from diverse sources.....	- 22 -
Table 2.1-5. Properties of the MSW and RDF Samples.....	- 22 -
Table 2.1-6. Evolution of pyrolysis reactions according to the temperature.....	- 30 -
Table 2.1-7. Characteristics of products from the pyrolysis of organic material.....	- 30 -
Table 2.1-8. Product yields from the pyrolysis of RDF and plastics mixtures.....	- 31 -
Table 2.1-9. Basic homogeneous and heterogeneous reactions during gasification of solid waste.....	- 34 -
Table 2.1-10. Strengths and weaknesses of gasifiers according to their design.....	- 37 -
Table 2.2-1. Main characteristics of pyrolysis and gasification processes.....	- 38 -
Table 2.3-1. Classification of tar compounds.....	- 48 -
Table 2.3-2. Examples of PAH compounds and associated carcinogenicities.....	- 50 -
Table 2.3-3. Syngas requirements for Internal Combustion engines (ICEs) and Gas Turbines (GTs).....	- 52 -
Table 2.4-1. Catalytic steam reforming reactions.....	- 54 -
Table 2.4-2. Tar decomposition reactions.....	- 54 -
Table 3.3-1. Solid decomposition yield at different reaction times.....	- 87 -
Table 3.3-2. Validation of the two-stage pyrolysis/gasification reaction system.....	- 88 -
Table 3.3-3. Influence of the gas collection time in general Mass Balance.....	- 89 -
Table 3.3-4. Blank experiments for water yield calculation.....	- 89 -
Table 3.4-1. Concentration of permanent gases and hydrocarbons from standard values.....	- 96 -
Table 3.4-2. BET Surface area of some nickel and iron-based catalysts.....	- 99 -
Table 3.4-3. Compounds used for the standard solution (PAH and oxygenated compounds) for GC-MS calibration.....	- 115 -
Table 4.1-1. Results of pyrolysis-gasification of RDF in terms of product yield and gas composition using different bed materials.....	- 123 -

Table 4.1-2. Identified compounds in tars from the gasification of RDF at 600, 700 and 800°C.....	- 129 -
Table 4.1-3. Influence of the bed type over the tar composition during gasification at 800°C ^a	- 130 -
Table 4.1-4. Bond stretching and IR absorption.....	- 136 -
Table 5.1-1. Description and properties of the prepared Ni/SiO ₂ catalysts.....	- 143 -
Table 5.1-2. Surface area and porous properties of fresh Ni/SiO ₂ catalysts.....	- 145 -
Table 5.1-3. Gas yield and composition using diverse Ni/SiO ₂ catalysts.....	- 149 -
Table 5.1-4. Identified compounds from GC-MS analysis of tar samples (µg _{compound} /g _{RDF}).....	- 154 -
Table 5.1-5. Classification of tar compounds found in analysed tar samples.....	- 159 -
Table 5.2-1. Surface area and porous properties Ni/SiO ₂ catalysts.....	- 175 -
Table 5.2-2. Gas composition, product yields and mass balance.....	- 177 -
Table 5.2-3. Reaction taking place during gasification.....	- 178 -
Table 5.2-4. Identification of tar compounds using GC-MS analysis (µg _{compound} /g _{RDF}).....	- 180 -
Table 5.3-1. Surface area and porous properties of HPG and B-HPG catalysts.....	- 192 -
Table 5.3-2. Gas composition, mass balance and gas yield from the pyrolysis-gasification products.....	- 199 -
Table 6.2-1. Surface area and porous properties of Ni/SiO ₂ and Fe/SiO ₂ catalysts.....	- 211 -
Table 6.3-1. Gas composition, gas and solid yields and mass balance from the experiments carried out using Ni/SiO ₂ and Fe/SiO ₂ catalysts.....	- 221 -
Table 7.4-1. Column types and gases measured.....	- 233 -
Table 7.4-2. Initial RDF gasification conditions.....	- 234 -
Table 7.4-3. Operational conditions for RDF-char combustion.....	- 235 -
Table 7.4-4. Selected conditions for each experiment.....	- 235 -
Table 7.5-1. Gas composition for experiments carried out in the WOB system.....	- 237 -

List of Figures

Figure 1.1-1. MSW composition by Region, 2012	- 1 -
Figure 1.1-2. Global MSW Composition	- 2 -
Figure 1.1-3. Municipal waste generation (kg/capita, 2005 and 2010)	- 3 -
Figure 2.1-1. Projection MSW generation according to the income level.....	- 14 -
Figure 2.1-2. Materials flow and solid waste generation.....	- 15 -
Figure 2.1-3. MSW composition in developed countries	- 16 -
Figure 2.1-4. RDF manufacturing process	- 19 -
Figure 2.1-5. Refuse Sorting Processes.....	- 20 -
Figure 2.1-6. Thermogravimetric analysis of RDF.....	- 24 -
Figure 2.1-7. MSW disposal methods used for some OECD countries.....	- 25 -
Figure 2.1-8. Diagram showing different conversion options for MSW.....	- 26 -
Figure 2.1-9. Net output of various thermal processes	- 27 -
Figure 2.1-10. Pyrolysis process of a fuel particle.....	- 29 -
Figure 2.1-11. Pyrolysis steps related with the process temperature.....	- 29 -
Figure 2.1-12. Influence of the gasification temperature over product characteristics, using different raw materials	- 35 -
Figure 2.1-13. Configuration of gasification reactor systems	- 36 -
Figure 2.2-1. Pyrolysis and Gasification primary and secondary products.....	- 38 -
Figure 2.2-2. Pyrolysis and gasification main products and combination of both processes	- 39 -
Figure 2.2-3. Potentials uses of syngas from carbon based feedstocks.....	- 40 -
Figure 2.2-4. Typical energy recovery flow diagrams.....	- 41 -
Figure 2.2-5. World total energy consumption, 1990-2040	- 43 -
Figure 2.3-1. Pathway of tar formation during increased gasification temperature.....	- 45 -
Figure 2.3-2. Proposed pathway for thermal conversion of tar aromatic compounds.....	- 46 -
Figure 2.3-3. Diels-Alder and subsequent dehydrogenation reaction for the formation of benzene (a) and naphthalene (b)	- 47 -

Figure 2.3-4. Phenol cracking reactions pathways for cyclopentadiene formation...	- 47 -
Figure 2.3-5. Schematic of tar formation from lignin air-steam gasification	- 51 -
Figure 2.4-1. Kinetic model for cracking of a tar component.....	- 55 -
Figure 2.4-2. Naphthalene decomposition mechanism	- 56 -
Figure 2.4-3. Steam gasification of phenol over nickel based catalysts	- 57 -
Figure 2.4-4. Diagram of tar sampling and analysis.....	- 58 -
Figure 2.4-5. General diagram SPA tar sampling method in the produced gas.....	- 59 -
Figure 2.4-6. Timeline of the most common nickel based catalysts synthesized since 1928	- 61 -
Figure 3.2-1. Appearance of RDF: (a) original pellets, and (b) shredded samples	- 79 -
Figure 3.2-2. TGA and DTG thermograms of RDF samples	- 80 -
Figure 3.2-3. Comparative of homogeneous precipitation-based preparation methods.....	- 84 -
Figure 3.3-1. Schematic diagram of the two-stage fixed-bed catalytic reactor	- 86 -
Figure 3.3-2. Assembled and main parts of the pyrolysis/gasification reactor.....	- 91 -
Figure 3.4-1. GC general layout and gas chromatograph equipment.....	- 92 -
Figure 3.4-2. GC response peaks for a standard gas mixture of permanent gases (H ₂ , O ₂ , N ₂ , CO)	- 93 -
Figure 3.4-3. GC response peaks: standard gas mixture of hydrocarbons (C ₁ -C ₄).....	- 94 -
Figure 3.4-4. BET surface area and pore size analyser: Quantachrome NOVA 2200e.....	- 99 -
Figure 3.4-5. Graphical used for micropore and mesopore volumes determination	- 101 -
Figure 3.4-6. X-ray Bruker D-8 for diffraction analysis	- 103 -
Figure 3.4-7. XRD patterns of Ni-based fresh catalyst, using <i>DIFFRACplus</i> software.	- 104 -
Figure 3.4-8. Thermogravimetric analysis (TPO) of 40wt.% Ni/SiO ₂ reacted catalyst.....	- 105 -
Figure 3.4-9. Main components of an electron column (a) and energy filter diagram (b)	- 106 -
Figure 3.4-10. SEM-EDXS results of 10wt.% Ni/SiO ₂ fresh catalyst	- 107 -
Figure 3.4-11. Micrograph images of fresh 10wt.% Ni/SiO ₂ catalyst, obtained by TEM analysis	- 108 -

Figure 3.4-12. Basic FTIR spectrometer components.....	108 -
Figure 3.4-13. FTIR spectrum of tar/oil from pyrolysis-gasification of RDF using no catalyst bed or steam.....	109 -
Figure 3.4-14. Karl-Fischer Metrohm Titration equipment for moisture determination in liquid samples.....	111 -
Figure 3.4-15. Sequential steps for water and tar determination in condensed fraction	112 -
Figure 3.4-16. General diagram of a typical GC-MS system	113 -
Figure 3.4-17. Methodology followed for the preparation of the PAH and oxygenated standard solution.....	114 -
Figure 3.4-18. Calibration curves at different concentration for some oxygenated and PAH compounds in the GC-MS equipment.....	116 -
Figure 3.4-19. Size exclusion chromatogram of tar/oil samples	118 -
Figure 4.1-1. Chromatograms of tar samples showing the effect of gasification temperature (a, b); and bed type (c, d, e, f).	127 -
Figure 4.1-2. Diels-Alder cyclo-addition reaction for a single ring structure formation.....	131 -
Figure 4.1-3. Size exclusion chromatograms (SEC) of tar samples.....	133 -
Figure 4.1-4. Possible assignment of MW reported by SEC	134 -
Figure 4.1-5. Sample preparation, FTIR analysis and interpretation.....	134 -
Figure 4.1-6. Types of CH ₂ vibrations.....	135 -
Figure 4.1-7. Fourier transform infrared spectra (FTIR) of tar from pyrolysis- gasification of RDF at frequency of 4000-650cm ⁻¹	136 -
Figure 5.1-1. BET Adsorption-desorption isotherms from fresh Ni/SiO ₂ catalysts .-	144 -
Figure 5.1-2. Trends in concentrations for major tar compounds identified in the analysed samples.....	156 -
Figure 5.1-3. Concentration of tar classes using different catalysts	159 -
Figure 5.1-4. DTG-TPO and TGA-TPO analysis from reacted Ni/SiO ₂ catalysts.....	164 -
Figure 5.1-5. Scanning electron images (SEM) of reacted Ni/SiO ₂ catalysts.....	167 -
Figure 5.2-1. BET adsorption-desorption isotherms of Ni/SiO ₂ catalysts	176 -
Figure 5.2-2. Classification of tar compounds	181 -
Figure 5.2-3. Pyrolysis of phenol (a); formation mechanism of naphthalene and (methyl)indene (b)	182 -

Figure 5.2-4. DTG-TPO (a) and TGA-TPO (b) of reacted Ni/SiO ₂ catalysts	184 -
Figure 5.2-5. SEM images of reacted Ni/SiO ₂ catalysts.....	185 -
Figure 5.3-1. Homogeneous precipitation method (HPG), for Ni/SiO ₂ catalyst preparation	190 -
Figure 5.3-2. Phase separation followed by aging of the gel to promote wider pore distribution in the catalyst	190 -
Figure 5.3-3. N ₂ adsorption-desorption isotherms of fresh HPG (a), and B-HPG (b) Ni/SiO ₂ catalysts.....	193 -
Figure 5.3-4. DFT pore size distribution for HPG (a) and B-HPG (b) Ni/SiO ₂ catalysts.....	194 -
Figure 5.3-5. Analysis of Ni/ SiO ₂ samples: (a) XRD analysis; and (b) IR spectra	196 -
Figure 5.3-6. Analysis of fresh Ni/SiO ₂ catalysts; SEM images: (a) HPG700; (b) B-HPG700; TEM images: (c) HPG700; (d) B-HPG700.....	197 -
Figure 5.3-7. SEM images of fresh HPG700 (a), HPG900 (b), B-HPG700 (c), and B-HPG900 (d) catalysts	198 -
Figure 5.3-8. Variation in the gas composition for HPG and B-HPG catalysts.	200 -
Figure 5.3-9. Temperature programme reduction (TPR) of fresh catalysts.....	202 -
Figure 5.3-10. Elementary reactions taking place allowing growth of coke layer	203 -
Figure 5.3-11. DTG-TPO thermograms from reacted Ni/SiO ₂ catalysts: B-HPG (a), and HPG (b).....	204 -
Figure 5.3-12. Morphologies of reacted Ni/SiO ₂ catalysts; SEM: (a)HPG700; (b)HPG900; (c)B-HPG900. TEM: (d)HPG700; (e, f)B-HPG700	205 -
Figure 5.3-13. SEM-EDX from fresh and reacted B-HPG700 Ni/SiO ₂ catalyst.....	206 -
Figure 6.2-1. N ₂ adsorption-desorption isotherms of fresh Fe/SiO ₂ and Ni/SiO ₂ catalysts.....	212 -
Figure 6.2-2. Pore size distribution of selected Ni/SiO ₂ and Fe/SiO ₂ catalysts.....	214 -
Figure 6.2-3. XRD patterns of (a) Ni/SiO ₂ catalysts, and (b) Fe/SiO ₂ catalysts.....	216 -
Figure 6.2-4. Fe/SiO ₂ morphological changes occurring to crystalline haematite particles (α -Fe ₂ O ₃) during activation and reaction conditions	218 -
Figure 6.2-5. TEM and SEM images of fresh Ni/SiO ₂ and Fe/SiO ₂ catalysts.....	219 -
Figure 6.4-1. SEM images of reacted 7.5Ni/SiO ₂ catalyst.....	224 -
Figure 7.2-1. Interaction between bubbles of gas and particles in a fluidised bed gasifier	229 -

Figure 7.2-2. Flow diagram of the WOB fluidised bed gasification system.....	230 -
Figure 7.2-3. Appearance of the control system for the WOB gasifier.....	230 -
Figure 7.3-1. RDF pellets to be fed into the WOB reactor: (a) 4x1.5cm; (b) 4x3mm.....	232 -
Figure 7.4-1. (a) Mobile GC online and micro GC; (b) GC four channel micro GC in flight case.....	234 -
Figure 7.5-1. Gas composition of the produced syngas at different temperatures...-	239 -
Figure 7.5-2. Effect of steam/fuel ratio on the gas composition at 800 °C.....-	239 -
Figure 7.5-3. Variation of some compounds with the gasification temperature	240 -
Figure 7.5-4. Identified compounds: SPA tar sample from Experiment 4.....-	241 -
Figure 7.5-5. SEM images from selected ash samples collected from the cyclone....-	242 -
Figure 7.5-6. Variation in ash compositions of selected experiments	243 -

Abbreviations

MSW	Municipal Solid Waste
RDF	Refuse Derived Fuel
OECD	Organisation for Economic Co-operation and Development
WtE	Waste to Energy
ISWM	Integrated Solid Waste Management
ASTM	American Society for Testing and Materials
EPA	U. S. Environmental Protection Agency
EIA	Energy Information Administration
IGT	Institute of Gas Technology, Chicago, USA
ECN	Energy Research Centre of the Netherlands
ER	Equivalence Ratio
TGA	Thermogravimetric analysis
DTG	Differential Thermogravimetry
TPO	Temperature Programmed Oxidation
GC	Gas Chromatograph or Gas Chromatography
MS	Mass Spectrometer or Mass Spectrometry
GC-MS	Gas Chromatograph coupled to a Mass Spectrometer
FID	Flame Ionisation Detector
TCD	Thermal Conductivity Detector
BET	Brunauer-Emmet-Teller method for surface area and porous determination
DR	Dubinin-Radushkevich method for micropore volume determination
BJH	Barrett, Joyner & Halenda method for total pore volume and pore diameter determination
DFT	Density Functional Theory for pore size distribution determination

XRD	X-Ray Diffraction
SEM	Scanning Electron Microscopy
TEM	Transmission Electron Microscopy
CRT	Cathode Ray Tube
EDXS	Energy Dispersive X-Ray Spectrometer
FTIR	Fourier Transform Infrared Spectrometry
DCM	Dichloromethane
PAH	Polycyclic Aromatic Hydrocarbons
HPLC	High-performance liquid chromatography
EtOH	Ethanol
KFT	Karl-Fisher Titration
SEC	Size Exclusion Chromatography
SPA	Solid Phase Adsorption method for tar collection and analysis
THF	Tetrahydrofuran
<i>R</i>	Constant value from the Ideal Gases Law= $8.31441 \text{ J K}^{-1} \text{ mol}^{-1}$
PEO	Polyethylene oxide
TEOS	Tetraethyl orthosilicate $\text{Si}(\text{OC}_2\text{H}_5)_4$
IMP	Impregnation catalyst preparation method
SG	Sol-gel catalyst preparation method
HPG	Homogeneous Precipitation based on sol-gel method for catalyst preparation
B-HPG	Combination of Homogeneous Precipitation and Phase Separation methods for catalyst preparation
Ni:CA	Nickel to Citric Acid ratio
R_STDV	Relative Standard Deviation, given in percentage (%)
Syngas	Mixture of permanent and hydrocarbon gases in different concentrations. Mainly composed by H_2 and CO
Tar	Mixture of aromatic and oxygenated compounds in gaseous or liquid form

CHAPTER 1. INTRODUCTION

1.1 Municipal Solid Waste (MSW) generation

The production and generation rate of solid wastes around the world has become a major concern, due to the different associated economic, environmental and social problems. All those wastes generated in household or commercial activities, and managed by authorities and municipalities are known as municipal solid waste (MSW) [1-4]. The composition of solid wastes is diverse and depends on factors such as the generation point, population income level, and the season of the year. The typical composition of MSW includes paper/cardboard, plastics, glass, metal, textiles, and food/garden waste [3, 5]. The World Bank made a comparison between the variability of the waste composition in different regions of the world as shown in Figure 1.1-1 [6].

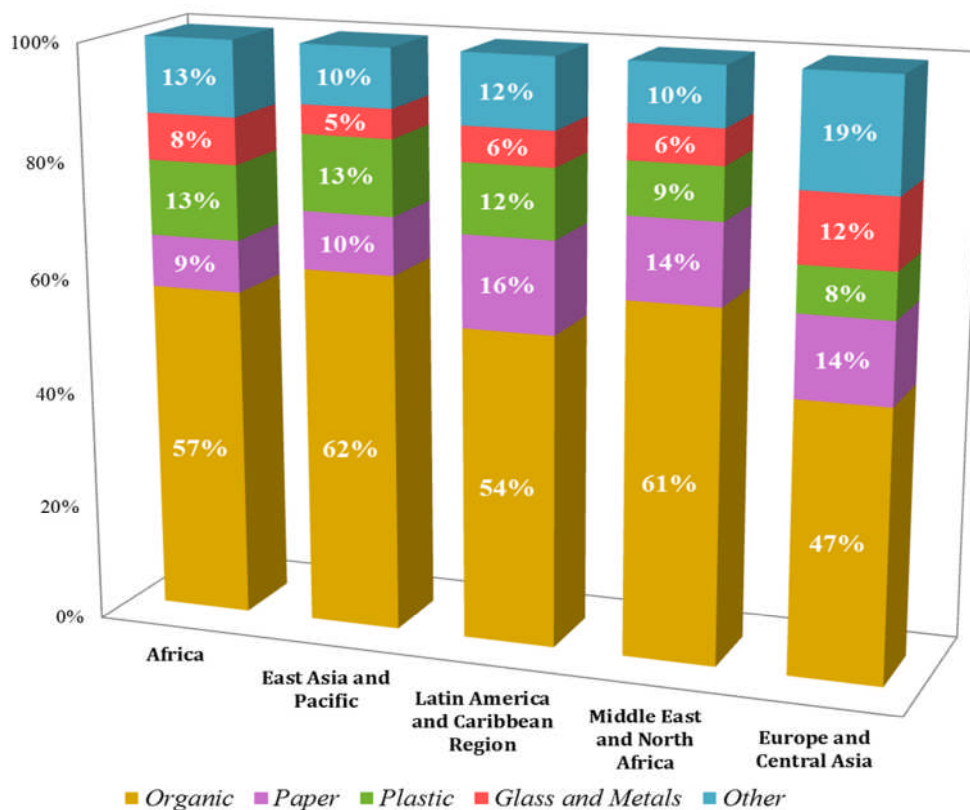


Figure 1.1-1. MSW composition by Region, 2012

In Figure 1.1-2 is presented the MSW worldwide composition in 2009, based on data reported by the World Bank (2012) [6]. It is observed that the majority of the MSW are composed of organic matter, followed by other components including textiles, leather, rubber, multi-laminates, e-waste, appliances, ash and other inert materials.

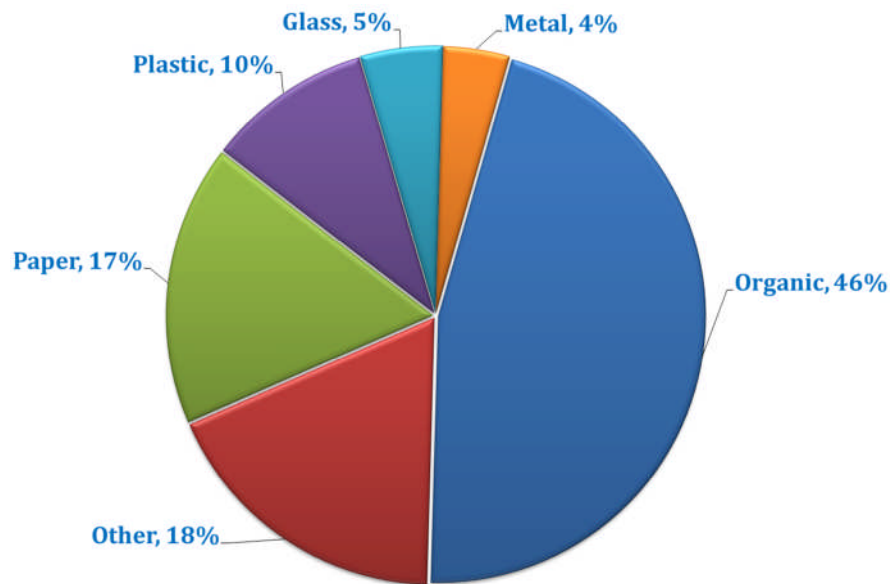


Figure 1.1-2. Global MSW Composition

The growth in the world population and the development of social economy, together with changes in lifestyles have prompted an increase in the daily amount of MSW generated worldwide [7]. The precise data concerning the global generation of MSW is difficult to obtain due to the data availability and homogeneity which is also related to the different definitions of MSW in countries. However according to World Bank predictions [6], by 2025 about 2.2 billion tonnes per year of solid waste will be generated by the world's cities, this estimate is based on economic and demographic growth rates. Figure 1.1-3 presents data on generation intensities of municipal waste (kg/capita/year) for the years 2005 and 2010, for a range of OECD (Organisation for Economic Co-operation and Development) countries; data from Brazil, China, and the Russian Federation were also included for comparison [8].

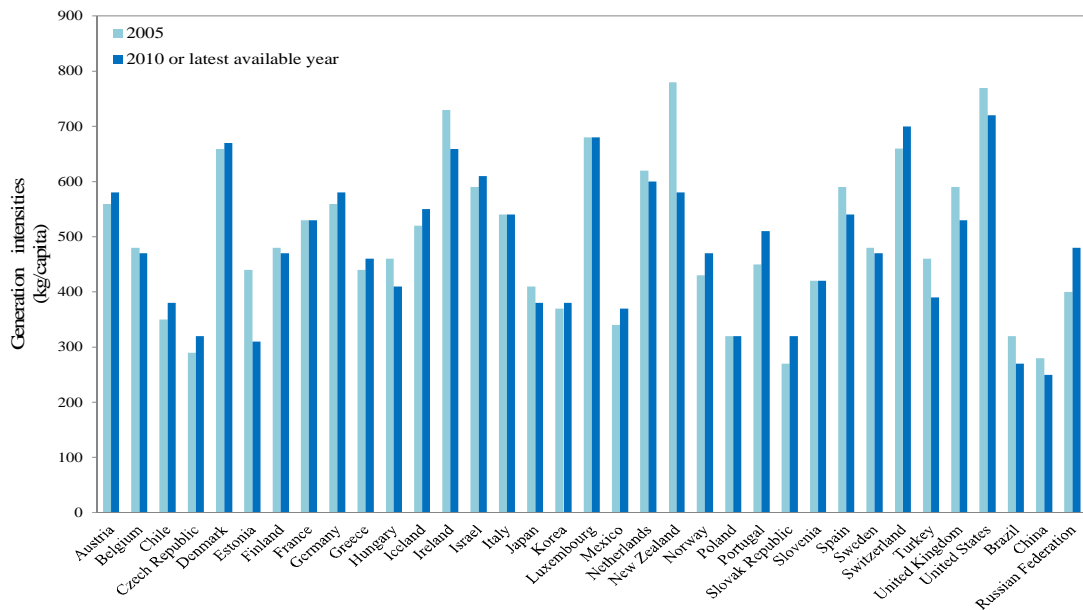


Figure 1.1-3. Municipal waste generation (kg/capita, 2005 and 2010)

1.1.1 Refuse Derived Fuel (RDF) production and composition

MSW might be subjected to a pre-sorting process aimed to classify, sort and separate the non-combustible fractions such as glass, metals and heavyweight inert materials. After this the remaining fraction is subjected to further processing including drying, crushing, and pelletizing [9, 10]. As a result a high calorific value derived fuel is obtained, containing mainly paper, cardboard and plastics. This fraction is generally referred to as refuse derived fuel (RDF) [10]. According to the Waste Incineration Directive (BMLFUW, Austria 2010) [11], the term refuse derived fuel refers to “wastes used entirely or used up to some extent for the purpose of energy generation and satisfies certain quality criteria laid down in the aforementioned Directive”. Main advantages of obtaining RDF include an easier storage, treating and manipulation than the original MSW stream. Additionally the calorific value of the solid waste stream is increased, typical calorific values of RDF pellets range between 11 to 25 MJ kg⁻¹ with common particle sizes between 5mm < 300mm, depending on its subsequent use [5, 9].

1.1.2 Current MSW disposal methods and alternative treatments

As mentioned above, the global MSW generation is growing at an alarming rate, therefore governments and authorities have sought integrated management

options to treat and confine wastes, in order to minimise as much as possible the potential impact on human health and environment. The most common disposal methods used worldwide are landfills, composting, incineration, discharge to water, and land treatment. However most of these options are no longer acceptable due to the environmental and social problems associated [12]. For example when using landfills greenhouse gases are generated, also there is the possibility of water supply pollution associated with leachate generation, and the growing lack of land areas available for landfills [1, 12-14]. Incineration disadvantages include the large gas flue emissions and the hazardous potential of fly ash produced [15]. Modern waste management is moving from using traditional landfills, to recycling and energy recovery systems, aimed to combine technology and sustainability. For example waste to energy facilities (WtE) such as pyrolysis and gasification have emerged to address these issues [15]. The main advantages of using WtE facilities for solid waste treatment and disposal include: the reduction of mass (70-80%) and volume (80-90%) of the solid waste, the reduction of use of land areas, destruction of organic contaminants, utilization of recyclables, reduction in the emission of greenhouse gases, and reduction in the environmental impact. In general WtE facilities can convert solid materials into valuable energy forms such as heat and electricity through different thermochemical routes including pyrolysis, gasification, or combination of both [16-19].

1.1.2.1 Pyrolysis and Gasification of solid wastes

Pyrolysis and gasification are thermal processes aimed to obtain products such as char, oil/tar and pyrolysis gases with medium to high calorific value through the thermal conversion of solid waste [20]. Pyrolysis is a thermal degradation process in which large molecules of carbonaceous materials are broken down into smaller hydrocarbon molecules, through a combination of thermal cracking and condensation reactions. This process takes place in temperatures between 300-800°C and is carried out in the absence of an oxidising agent such as oxygen or air [5, 20, 21]. Sometimes the pyrolysis process is aimed to increase the yield of hydrocarbon liquids to be later used as liquid fuels [14].

On the other hand, gasification processes take place with an external agent or gasification medium, which can be oxygen, air, steam or mixtures of these. In general, the conversion of solid wastes into gases and chemicals through gasification is an exothermic process. Gasification is normally carried out at temperatures ranging between 800-1100 °C when air is used as an oxidising agent, and can be further increased up to 1500 °C when using oxygen [20, 21]. The products from the gasification process are similar to those obtained from the pyrolysis, including gas, liquid and a solid fraction. However the tar and char from the pyrolysis process are further converted into CO, CO₂, CH₄ and H₂ gases, due to the use of gasification agent and higher temperatures [20].

For both pyrolysis and gasification processes, products yields and composition are highly dependent on the fuel type, reactor configuration, gas-solid residence time, reaction temperature, pressure, gasifying agent (if used), and catalyst of the gasification process [22].

Sometimes pyrolysis and gasification processes are combined with the aim to increase the calorific value of the final gas, also known as syngas. The main outputs from the pyrolysis process might then be upgraded by partial oxidation (gasification) at higher temperatures. As a result, the syngas containing H₂, CO, CO₂, CH₄, C₂-C₄, and some fractions of tar is obtained together with solid and liquid fractions. Tar concentration varies depending on the raw material used, process conditions, etc. Unfortunately, the presence of tars significantly reduces both the quality of the syngas and the overall yield of the process [23].

1.2 Syngas production and potential uses

The syngas from the pyrolysis/gasification of solid wastes is composed of the permanent gases and light hydrocarbons. Syngas can be obtained from different hydrocarbon based feedstocks such as natural gas, naphtha, coal, biomass and other solid wastes [24]. Currently there are different technological routes used for syngas generation, being steam methane reforming (SMR) the predominant technology so far [25]. Depending on its final composition synthesis gas or

syngas can have many potential applications such as Fischer-Tropsch or methanol production, also can be upgraded to hydrogen and further converted into transportation fuel, liquid products, and can be also used in fuel cell applications [24, 26]. When the syngas is obtained through the gasification of carbon based feedstock such as waste, the gasification can be integrated to combined-cycle (IGCC) systems for example using Internal Combustion Engines (ICE), and gas or steam turbines for electric power generation [1, 27]. When a high hydrogen concentration is desired in the syngas composition, certain reactions such as water gas shift can be promoted depending on the syngas production process. In general a syngas with a H_2/CO ratio higher than 1.7, is suitable to be used in the chemical industry and for the synthesis of diverse products such as methanol and naphtha [26, 28].

1.3 Hydrogen production, applications and future

Hydrogen is the most abundant element in the Universe, unfortunately it cannot be found in its natural form as it is highly reactive so normally is found mixed with other compounds as oxygen and carbon, for example as water or hydrocarbons [29, 30]. Hydrogen can be produced by different methods such as water electrolysis, and steam-reforming of methanol or ethanol [31]. However, most of the current hydrogen production processes are based on the processing of natural gas and other light hydrocarbons, which in turn comes from non-renewable sources as fossil fuels therefore are not sustainable [32, 33]. In addition some pollutants including carbon dioxide are released during this process which contributes to the greenhouse gases emissions [34].

Hydrogen has a flexibility to be used in diverse applications, for example in semiconductor processing, petroleum refining, ammonia production, metals treatment, as coolant in electrical generators, among others. Hydrogen as an energy carrier represents an alternative to fossil fuel use without the problems of CO_2 emissions [30, 34]. For example hydrogen can be used as fuel and also as energy store, which is particularly relevant for the transport sector representing a zero emission alternative replacing the current dependence on fossil fuels [30].

The hydrogen global demand is expected to increase up to 4.1% annually through 2016 [35]; for this reason the pursuit of renewable sources for hydrogen production has increased through the years. The term “hydrogen economy” has been recently used and refers to all the factors that require a change and adaptation to systems for hydrogen production, utilisation and inclusion into the global economy [30, 34]. Bearing in mind this scenario, the role of hydrogen as an alternative fuel for power generation, is increasing in importance as part of a sustainable energy economy [36]. Therefore a future energy framework based on hydrogen should ensure its production from an abundant, clean and secure renewable source to fit with the required environmental benefits [37].

1.4 Tar: definition, composition and problems associated

Tar formation during the pyrolysis and/or gasification of solid waste, has been one of the major challenges to overcome, as significantly reduces the quality of the produced syngas. Tar is complex mixture of polyaromatic and oxygenated compounds formed during the thermal degradation of solid waste, through a series of complex chemical reactions under thermal or partial-oxidation conditions [38-41]. A high tar concentration in the produced syngas might create diverse operational problems such as attrition and clogging in pipelines and equipment which reduce both the quality of the syngas, and the overall gasification yield [42]. Thus the reduction of tar formation during the gasification process is a priority when the gasification process is proposed as an alternative treatment for solid wastes.

1.4.1 Tar removal methods

Different physical and chemical methods have been studied in order to minimise tar formation considering criteria such as efficiency, economic feasibility and influence over gas formation [40, 43, 44]. Physical methods (or secondary methods) take place outside the gasifier and are cleaning techniques based on the use of gas filtering, scrubbers, cyclones and electrostatic precipitators. Whereas, chemical methods (primary methods) comprise:

catalytic steam reforming (bed of catalyst), thermal cracking and plasma reactors [39, 45, 46].

1.4.1.1 Catalytic steam reforming

Catalytic steam reforming processes have been recognized as the most efficient methods to promote tar cracking reactions and reduce gas yield in the syngas [15]. Therefore have been widely assessed as the use of catalyst help to increase both the hydrogen content and the calorific value in the syngas [47]. During the catalytic steam reforming, a bed of a specific catalyst is used and the gases are passed through it. The reactants are adsorbed onto the catalyst's surface to rearrange and combine into products that are later desorbed from the surface allowing tar cracking reactions to take place [24]. So far there are a variety of catalysts reported in the literature to reduce tar concentration in gasifier streams with nickel-based catalysts the most popular [48-54]. Among the main advantages of using nickel based catalysts are their high activity for tar elimination at process temperatures around 900°C, and the increase in the H₂ and CO yields in the syngas [55].

1.5 Description and Objectives of this Research

Considering the relevance of hydrogen as a fuel for power generation, and the large availability of municipal solid waste (MSW); both factors might be correlated by means of thermal treatments such as pyrolysis and gasification for the conversion of solid wastes into hydrogen. By combining the pyrolysis and gasification methods, a high hydrogen rich syngas can be obtained. In addition, the reduction in tar formation can be promoted by the use of different nickel-based catalysts during the gasification stage.

In this research, diverse nickel based catalysts were tested in a two stage the pyrolysis/gasification reaction system, using refuse derived fuel (RDF) as raw material. A series of experiments were carried out with the following objectives:

- To find the most suitable process conditions such as pyrolysis and gasification temperatures, for the thermal degradation of refuse derived fuel (RDF).
- To analyse the influence of catalyst type, catalyst ratio, metal loading, etc., of different catalysts to be used during the catalytic steam reforming of RDF, for hydrogen production and tar reduction.
- To characterise quantitatively the condensed tar fraction and to qualitatively identify the major tar compounds.
- To analyse the used catalysts from the gasification stage to identify the carbon deposition.
- To propose a tar formation and degradation mechanism through the pyrolysis/gasification of RDF.

References

1. Tchobanoglous, G., Theisen, H., Vigil, S. A., *Integrated Solid Waste Management: Engineering principles and management issues*. Civil Engineering Series, ed. M.H.I. Editions. 1993, New York.
2. Williams, P.T., *Waste Treatment and Disposal*. 2nd ed, ed. J.W.S. Ltd. 2005, Chichester, UK.
3. McDougall, F.R., P.R. White, M. Franke, and P. Hindle, *Integrated solid waste management: a life cycle inventory*. 2nd ed. 2007, GB: Wiley-Blackwell.
4. Christensen, T.H., *Solid Waste Technology and Management*. Solid Waste Technology & Management. Vol. 1. 2010, Malaysia: John Wiley & Sons, Ltd. i-xiv.
5. Buah, W.K., A.M. Cunliffe, and P.T. Williams, *Characterization of Products from the Pyrolysis of Municipal Solid Waste*. Process Safety and Environmental Protection, 2007. 85(5): p. 450-457.
6. Hoornweg, D. and P. Bhada-Tata (2012) *What a waste : a global review of solid waste management*. Urban development series 1.
7. Karak, T., R.M. Bhagat, and P. Bhattacharyya, *Municipal Solid Waste Generation, Composition, and Management: The World Scenario*. Critical Reviews in Environmental Science and Technology, 2011. 42(15): p. 1509-1630.
8. OECD, *OECD Factbook 2013*: OECD Publishing.
9. Lorber, K.E., R. Sarc, and A. Aldrian, *Design and quality assurance for solid recovered fuel*. Waste Management & Research, 2012. 30(4): p. 370-380.
10. Hernandez-Atonal, F.D., C. Ryu, V.N. Sharifi, and J. Swithenbank, *Combustion of refuse-derived fuel in a fluidised bed*. Chemical Engineering Science, 2007. 62(1-2): p. 627-635.
11. Bundesministerium für Land und Forstwirtschaft Umwelt und Wasserwirtschaft, B., *Verordnung über die Verbrennung von Abfällen. Abfallverbrennungsverordnung (AVV) ("Waste Incineration Directive")*, BMLFUW, Editor. 2010: Vienna, Austria.
12. A. L. Juhasz, G. Magesan, and R. Naidu, *Waste Management*. 2004: Science Publishers,U.S. 355.
13. Reddy, P.J., *Municipal Solid Waste Management: Processing - Energy Recovery - Global Examples*. 2011: CRC Press.
14. Williams, P.T. and S. Besler, *The Pyrolysis of Municipal Solid-Waste*. Journal of the Institute of Energy, 1992. 65(465): p. 192-200.
15. Li, J., J. Liu, S. Liao, X. Zhou, and R. Yan, *Syn-Gas Production from Catalytic Steam Gasification of Municipal Solid Wastes in a Combined Fixed Bed Reactor*, in *International Conference on Intelligent System Design and Engineering Application (ISDEA)*. 2010: Changsha. p. 530-534.
16. Arena, U., *Process and technological aspects of municipal solid waste gasification. A review*. Waste Management, 2012. 32(4): p. 625-639.
17. Schiefelbein G, F., J. Sealock L, and S. Ergun, *Thermochemical Conversion of Biomass to Fuels and Feedstocks: An Overview of R&D Activities Funded*

- by the Department of Energy, in *Thermal Conversion of Solid Wastes and Biomass*. 1980, American Chemical Society. p. 13-26.
18. Landreth, R.E. and P.A. Rebers, *Municipal solid wastes: problems and solutions*. 1997, Boca Raton: CRC Press.
 19. Stehlik, P., *Some Aspects Contributing to Improved Process and Equipment Design in the Field of Waste-To-Energy and Environmental Protection*, in *New and Renewable Technologies for Sustainable Development*, N. Afgan and M. Graça Carvalho, Editors. 2002, Springer US. p. 443-458.
 20. Astrup, T. and B. Bilitewski, *Pyrolysis and gasification*, in *Solid Waste Technology and Management*, T.H. Christensen, Editor. 2010, John Wiley & Sons, Ltd: Malaysia. p. 502-512.
 21. Basu, P., *Biomass Gasification and Pyrolysis: Practical Design and Theory*. 2010, Oxford: Elsevier.
 22. Dalai, A.K., N. Batta, I. Eswaramoorthi, and G.J. Schoenau, *Gasification of refuse derived fuel in a fixed bed reactor for syngas production*. *Waste Management*, 2009. 29(1): p. 252-258.
 23. Bridgwater, A.V., *The technical and economic feasibility of biomass gasification for power generation*. *Fuel*, 1995. 74(5): p. 631-653.
 24. Spath, P.L. and D.C. Dayton, *Preliminary Screening -- Technical and Economic Assessment of Synthesis Gas to Fuels and Chemicals with Emphasis on the Potential for Biomass-Derived Syngas*, in *Other Information: PBD: 1 Dec 2003*. 2003. p. Medium: ED; Size: 160 pages.
 25. Wilhelm, D.J., D.R. Simbeck, A.D. Karp, and R.L. Dickenson, *Syngas production for gas-to-liquids applications: technologies, issues and outlook*. *Fuel Processing Technology*, 2001. 71(1-3): p. 139-148.
 26. Choudhary, T.V. and V.R. Choudhary, *Energy-efficient syngas production through, catalytic oxy-methane reforming reactions*. *Angewandte Chemie-International Edition*, 2008. 47(10): p. 1828-1847.
 27. Busby, R., L., *Hydrogen and Fuel Cells: A Comprehensive Guide*. 1st ed, ed. S. Hill. 2005, Oklahoma, USA: PennWell.
 28. De Filippis, P., C. Borgianni, M. Paolucci, and F. Pochetti, *Prediction of syngas quality for two-stage gasification of selected waste feedstocks*. *Waste Management*, 2004. 24(6): p. 633-639.
 29. Hoffmann, P.D., B. , *Tomorrow's Energy:Hydrogen, Fuel Cells, and the Prospects for a Cleaner Planet*. 2012: MIT Press.
 30. Cruden, A.J., *4.01 - Preface and Context to Hydrogen and Fuel Cells*, in *Comprehensive Renewable Energy*, S. Editor-in-Chief: Ali, Editor. 2012, Elsevier: Oxford. p. 1-27.
 31. Akande, A.J., *Production of Hydrogen by Reforming of Crude Ethanol*, in *Chemical Engineering*. 2005, University of Saskatchewan: Saskatoon.
 32. Balat, M., *Potential importance of hydrogen as a future solution to environmental and transportation problems*. *International Journal of Hydrogen Energy*, 2008. 33(15): p. 4013-4029.
 33. Burke, K., *Current Perspective on Hydrogen and Fuel Cells*, in *Comprehensive Renewable Energy*, S. Ali, Editor. 2012, Elsevier: Oxford. p. 29-63.
 34. Momirlan, M. and T.N. Veziroglu, *Current status of hydrogen energy*. *Renewable and Sustainable Energy Reviews*, 2002. 6(1-2): p. 141-179.

35. Freedonia Group, T., *World Hydrogen - Industry study with forecast for 2013 and 2018*. 2010. p. 345.
36. García Cortés, C., Tzimas, E., Peteves, S. D., *Technologies for Coal based Hydrogen and Electricity Co-production Power Plants with CO₂ Capture*, in *JRC Scientific and Technical Reports*, E.C.J.R.C.I.f. Energy., Editor. 2009: Luxembourg.
37. Lubitz, W. and W. Tumas, *Hydrogen: An Overview*. Chemical Reviews, 2007. 107(10): p. 3900-3903.
38. Reichenbach de Sousa, L.C., *Gasification of Wood, Urban Wastewood (Altholz) and other Wastes in a Fluidised Bed Reactor*, in *Technical Sciences*. 2001, Swiss Federal Institute of Technology Zürich: Zürich. p. 286.
39. Devi, L., K.J. Ptasinski, and F.J.J.G. Janssen, *A review of the primary measures for tar elimination in biomass gasification processes*. Biomass and Bioenergy, 2003. 24(2): p. 125-140.
40. Milne, T.A., Evans, R. J., *Biomass Gasifier "Tars": Their Nature, Formation and Conversion*. 1998, National Renewable Energy Laboratory.
41. Dabai, F., Paterson, N., Millan, M., Fennell, P., Kandiyoti, R., *Tar formation and destruction in a fixed-bed reactor simulating downdraft gasification: equipment development and characterization of tar-cracking products*. Energy and Fuels, 2010. 24(8): p. 4560-4570.
42. Bergman, P.C.A., van Paasen, S. V. B., Boerrigter, H. , *The novel "OLGA" technology for complete tar removal from biomass producer gas*, in *Pyrolysis and Gasification of Biomass and Waste, Expert Meeting*. 2002: Strasbourg, France.
43. van der Hoeven, T.A., *Partial product gas combustion for tar reduction*. 2007, Eindhoven University: Eindhoven. p. 164.
44. Kirkels, A.F. and G.P.J. Verbong, *Biomass gasification: Still promising? A 30-year global overview*. Renewable and Sustainable Energy Reviews, 2011. 15(1): p. 471-481.
45. Kuhn, J.N., Z. Zhao, L.G. Felix, R.B. Slimane, C.W. Choi, and U.S. Ozkan, *Olivine catalysts for methane- and tar-steam reforming*. Applied Catalysis B: Environmental, 2008. 81(1-2): p. 14-26.
46. Basu, P., *Combustion and Gasification in Fluidized Beds*, ed. T.F. Group. 2005, Florida, USA: CRC Press. 473.
47. Luo, S., B. Xiao, X. Guo, Z. Hu, S. Liu, and M. He, *Hydrogen-rich gas from catalytic steam gasification of biomass in a fixed bed reactor: Influence of particle size on gasification performance*. International Journal of Hydrogen Energy, 2009. 34(3): p. 1260-1264.
48. Bona, S., P. Guillén, J.G. Alcalde, L. García, and R. Bilbao, *Toluene steam reforming using coprecipitated Ni/Al catalysts modified with lanthanum or cobalt*. Chemical Engineering Journal, 2008. 137(3): p. 587-597.
49. Miccio, F., B. Piriou, G. Ruoppolo, and R. Chirone, *Biomass gasification in a catalytic fluidized reactor with beds of different materials*. Chemical Engineering Journal, 2009. 154(1-3): p. 369-374.
50. Li, J., J. Liu, S. Liao, and R. Yan, *Hydrogen-rich gas production by air-steam gasification of rice husk using supported nano-NiO/[gamma]-Al₂O₃ catalyst*. International Journal of Hydrogen Energy, 2010. 35(14): p. 7399-7404.

51. Ma, L. and G.V. Baron, *Mixed zirconia-alumina supports for Ni/MgO based catalytic filters for biomass fuel gas cleaning*. Powder Technology, 2008. 180(1-2): p. 21-29.
52. Courson, C., E. Makaga, C. Petit, and A. Kiennemann, *Development of Ni catalysts for gas production from biomass gasification. Reactivity in steam- and dry-reforming*. Catalysis Today, 2000. 63(2-4): p. 427-437.
53. Kimura, T., T. Miyazawa, J. Nishikawa, S. Kado, K. Okumura, T. Miyao, S. Naito, K. Kunimori, and K. Tomishige, *Development of Ni catalysts for tar removal by steam gasification of biomass*. Applied Catalysis B: Environmental, 2006. 68(3-4): p. 160-170.
54. Caballero, M.A., Corella, J. Aznar, M. P. Gil, J., *Biomass gasification with air in fluidized bed. Hot gas cleanup with selected commercial and full-size nickel-based catalysts*. Industrial and Engineering Chemistry Research, 2000. 39(5): p. 1143-1154.
55. Abu El-Rub, Z., Bramer, E. A., Brem, G. , *Review of Catalysts for Tar Elimination in Biomass Gasification Processes*. Industrial and Engineering Chemistry Research, 2004. 43(22): p. 6911-6919.

CHAPTER 2. LITERATURE REVIEW

2.1 Municipal Solid Waste (MSW)

Various definitions of municipal solid waste (MSW) have been stated in the literature over the years, but in general the term encompasses all the by-products with a lack of value, generated during human activities in households and commerce [1-4]. The MSW fraction accounts for less than 10% of the total waste produced in the world, however there are major environmental, social, and economical issues associated with their management and final disposal [2]. In general MSW is collected by municipalities, excluding sewage networks, construction, and demolition waste [5].

2.1.1 MSW generation and composition

The production rates and the composition of MSW vary according to factors such as economic development, population growth and lifestyle, sociocultural habits, trends in urbanisation, climate, recycling potential etc., [3, 6]. A projection of the production of MSW based in income level for different countries from the year 2010 to 2025 is presented in Figure 2.1-1 [5].

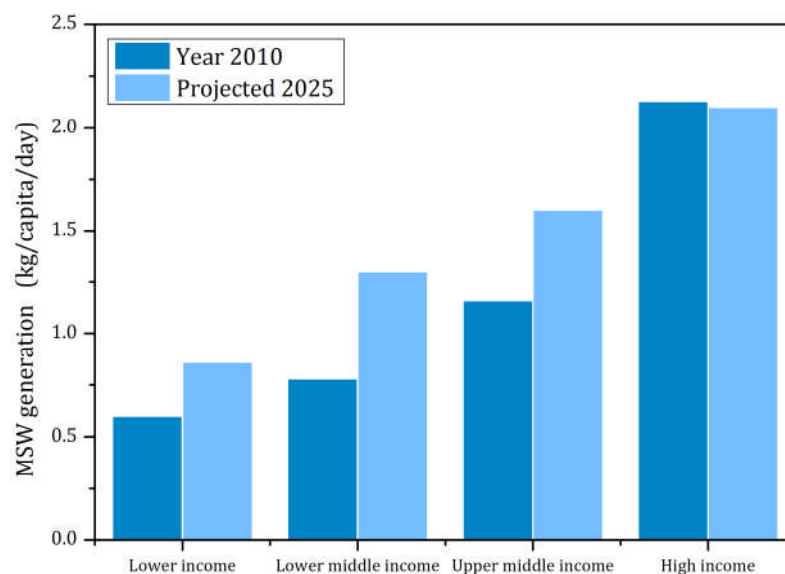


Figure 2.1-1. Projection MSW generation according to the income level

Figure 2.1-1, shows that countries with a high income level tend to produce more kg of waste per capita per day than countries with lower income. However the estimated production for the year 2025 for low income to upper middle income countries will increase significantly when compared with the increase in trend for high income countries. This trend is related to the size and affluence for each country as well as the consumption habits [5, 7].

A flow diagram of the solid waste generation during the conversion of raw materials into goods for consumption, is shown in Figure 2.1-2 [8]. From Figure 2.1-2 it can be observed that solid wastes are generated through the whole conversion process including some recovery and recycling intermediate steps.

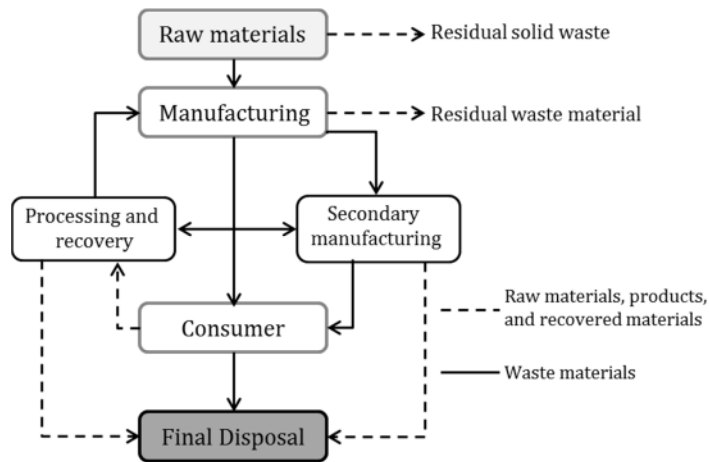


Figure 2.1-2. Materials flow and solid waste generation

Waste generation intensities are good markers for solid waste management implementation in countries. Currently, the world's cities generate around 1.3 billion tonnes of MSW per year, and it is estimated that by 2025 this amount will increase up to 2.2 billion tonnes per year, based on economic and urban population growth rates from the World Bank [6]. Due to the significant increase in the municipal solid waste (MSW) production it is necessary to find sustainable and environmentally friendly routes to treat and dispose MSW efficiently [9]. The most common activities carried out once MSW is generated include collection, handling, separation of certain fractions, storage, processing and disposal; these set of activities are part of the waste management process. When these activities also include the selection and application of technologies

to meet specific waste management goals, then the process can be defined as integrated solid waste management (ISWM) [8]. Additionally a hierarchy of the different elements that compose the ISWM has been set out, starting with source reduction, reuse of materials, recycling and recovering, waste transformation (including energy recovery), and finally the disposal (e.g. landfilling) [8, 10].

The composition of the MSW is a major parameter as it gives information about the materials contained and its potential to be segregated, for example, for recycling purposes. In general MSW is characterised by having organic and inorganic materials, but radical changes over the years such as modifications in the eating habits of the population and the way in which goods are packaged promotes variations in the composition of household wastes [7, 8, 11]. For example the generation source is a factor that influences the composition of MSW, thus the materials contained in MSW varies from country to country as observed in Figure 2.1-3 [7]. The composition considered 6 major groups: metal, glass, plastics, paper, organic, and other material fractions [7].

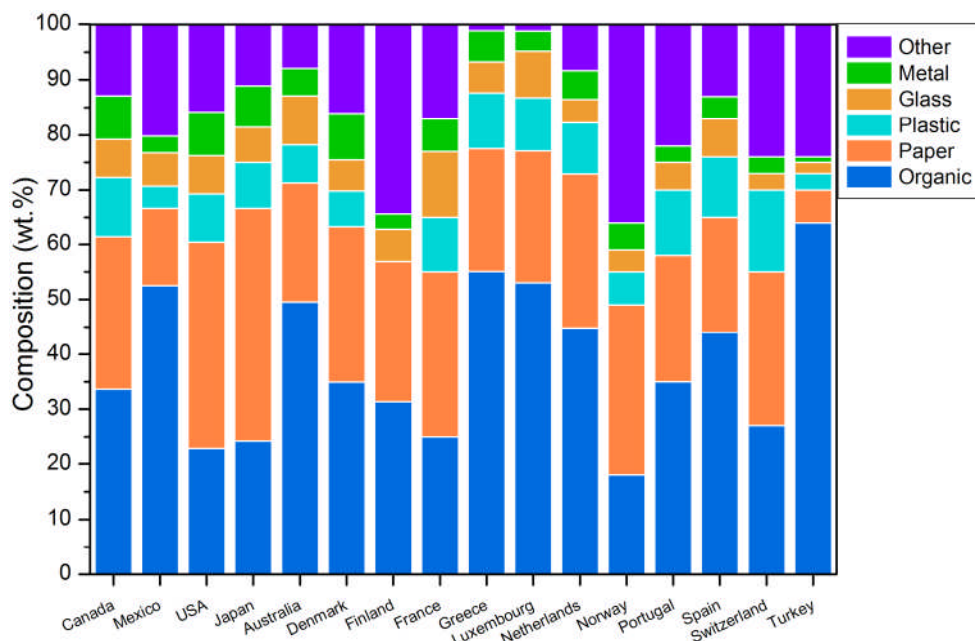


Figure 2.1-3. MSW composition in developed countries

Most of the countries presented in Figure 2.1-3 have a high income level; however variations in the waste stream are still unclear. For example the

organic fraction of wastes from Norway is very low with similar proportions of metal, glass and plastics, and considerably higher amounts of other materials [6]. In general of the total MSW stream, between 50 and 75 per cent comes from residential and community activities [8]. Wastes from household activities might include newspapers, clothing, disposable tableware, food packaging, cans and bottles, garden waste, food scraps, etc.; whereas the commercial waste stream might contain corrugated boxes, food scraps, office disposable tableware, paper napkins, etc., [4, 12]. The inorganic fraction consists of residues of paper, plastic, metals and other materials, a more detailed description of each fraction contained in the MSW stream is presented in Table 2.1-1 [6].

Table 2.1-1. MSW fractions and description

Fraction	Materials and sources
Organic	Food scraps, yard waste (leaves, grass, brush), wood, process residues
Paper	Paper scraps, cardboard, newspapers, magazines, bags, boxes, wrapping paper, telephone books, shredded paper, and paper beverage cups. When paper is contaminated is not considered within the organic fraction.
Plastic	Bottles, packaging, containers, bags, lids, cups
Glass	Bottles, broken glassware, light bulbs, coloured glass
Metal	Cans, foil, tins, non-hazardous aerosol cans, appliances (white goods), railings, bicycles
Other	Textiles, leather, rubber, multi-laminates, e-waste, appliances, ash, other inert materials

Some physical, chemical and biological characteristics are of interest when materials in a MSW stream require recycling and further treatment. The physical properties of MSW refers to specific weight, particle size and size distribution, etc.; chemical analysis gives specific information about chemical composition, energy content, etc.; and biological analysis is focused on the organic fraction to get mainly information about biodegradability [8, 10].

Chemical characterisation of solid wastes is essential when solid wastes are meant to be used as fuel. Four main analyses are carried out to obtain information about MSW composition including proximate analysis, ultimate analysis, fusing point of ash, and energy content. However the most common are the proximate analysis that determines moisture, combustible content, volatiles, and ash content; and the ultimate analysis that gives mass fraction values of

elements contained in the sample such as C, H, N, O and S [13]. The moisture content in the MSW is one of the most relevant parameters as it influences the weight of the waste, its processing, handling, and final treatment. High moisture content promotes a faster degradation of the biodegradable fraction of waste, and also makes the waste unsuitable for thermal conversion [7]. This parameter depends on the climatic conditions such as rainfall and harvest season, and is measured according to the loss of moisture when the solid waste is heated to 105 °C for 1 hour [8, 10, 14]. The potential contaminants that might be found in waste streams include heavy metals, soluble salts, organic matter, etc. [15]. An example of the typical properties of MSW is presented in Table 2.1-2 [3, 8].

Table 2.1-2. Typical properties of MSW

Composition	Wt.%	Elemental Analysis	
		Element	Wt.%
Paper/cardboard	33.0	Carbon	21.5
Plastics	7.0	Hydrogen	3.0
Glass	10.0	Oxygen	16.9
Metals	8.0	Nitrogen	0.5
Food/garden	20.0	Sulphur	0.2
Textiles	4.0	Chlorine	0.4
Others	18.0		
Proximate Analysis		Element	(ppm)
Property	Wt.%		
Combustibles	42.1	Lead	100-2000
Moisture	31.0	Cadmium	1-150
Ash	26.9	Arsenic	2-5
		Zinc	400-1400
		Copper	200-700
		Chromium	40-200
		Mercury	1-50

All the MSW characteristics are relevant when selecting management and disposal methods. New technological alternatives based on energy efficient and environmentally friendly approaches for the disposal of MSW have been used around the world [11]. These alternatives are aimed at enhancing resource recovery from MSW, such as the production of a value added material including refuse derived fuel (RDF) obtained from the processing of the MSW stream.

2.1.2 Refuse Derived Fuel (RDF) definition and composition

Refuse derived fuel (RDF) is a fraction obtained from the main MSW stream via a pre-sorting process including manual and mechanical operations, aimed to remove non-combustible materials such as glass and metals. Once the non-combustible materials are segregated, the remaining fraction has better physical and combustion characteristics. The major benefits of obtaining RDF are the higher calorific value and homogeneous particle size and composition [1, 8, 16, 17]. The calorific value of the raw MSW has a typical calorific value around 9 MJ kg^{-1} , whereas the calorific value of RDF pellets is around 18 MJ kg^{-1} [18]. The more the solid waste is pre-treated; the better is its quality and heating value, as the volume and size of plastics and paper is reduced resulting in a material that can be combusted more evenly [10, 11].

RDF pellets are also produced in order to facilitate the handling and storage of MSW. RDF can be stored for long periods, and then can be used as fuel for heat or electricity generation. The unitary operations or sequential steps used to produce RDF pellets include segregation or separation, drying, crushing, shredding, screening, air classification, magnetic separation, screening, solidifying, and pelletizing [19]. An example of the combination of some of these unitary operations is shown in Figure 2.1-4 [7, 20, 21].

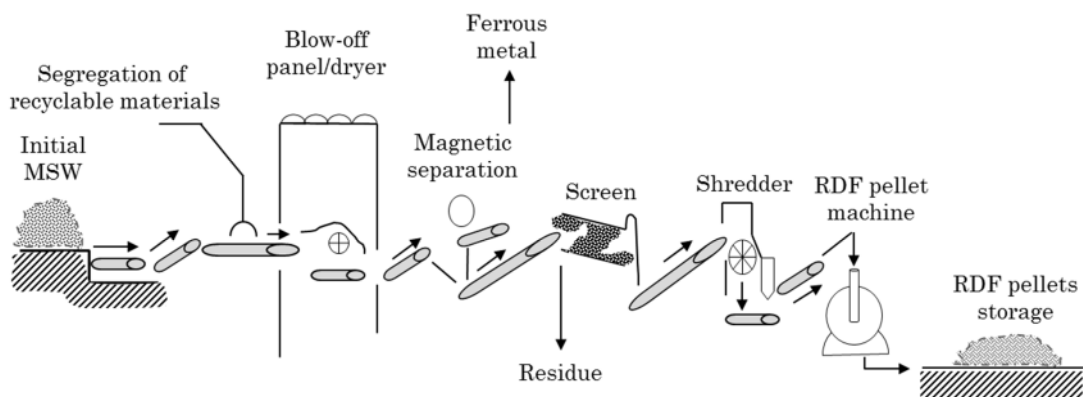


Figure 2.1-4. RDF manufacturing process

The most common materials that are segregated from the MSW, due to their potential to be recycled include fibre (cardboard, paper, newspaper, office

paper), metals (ferrous and aluminium), mixed glass, and plastics (polyethylene terephthalate-PET and high density polyethylene-HDPE) [3, 22]. Once the solid waste is passed through these steps, a RDF fraction with a similar energy potential to coal is obtained [23]. For example Lin et al [24], reported the production of RDF from MSW through a mechanical separation consisting of bag ripping, magnetic sorting, shedding and a rotary trommel screening. Additional inert materials contained in the MSW stream such as glass and ceramics were also segregated, to obtain final RDF pellets with particle size between 25-100mm. Different pathways are followed to obtain RDF depending on the specific requirements and further use. A general diagram showing major separation processes from the original MSW to obtain RDF is shown in Figure 2.1-5 [17].

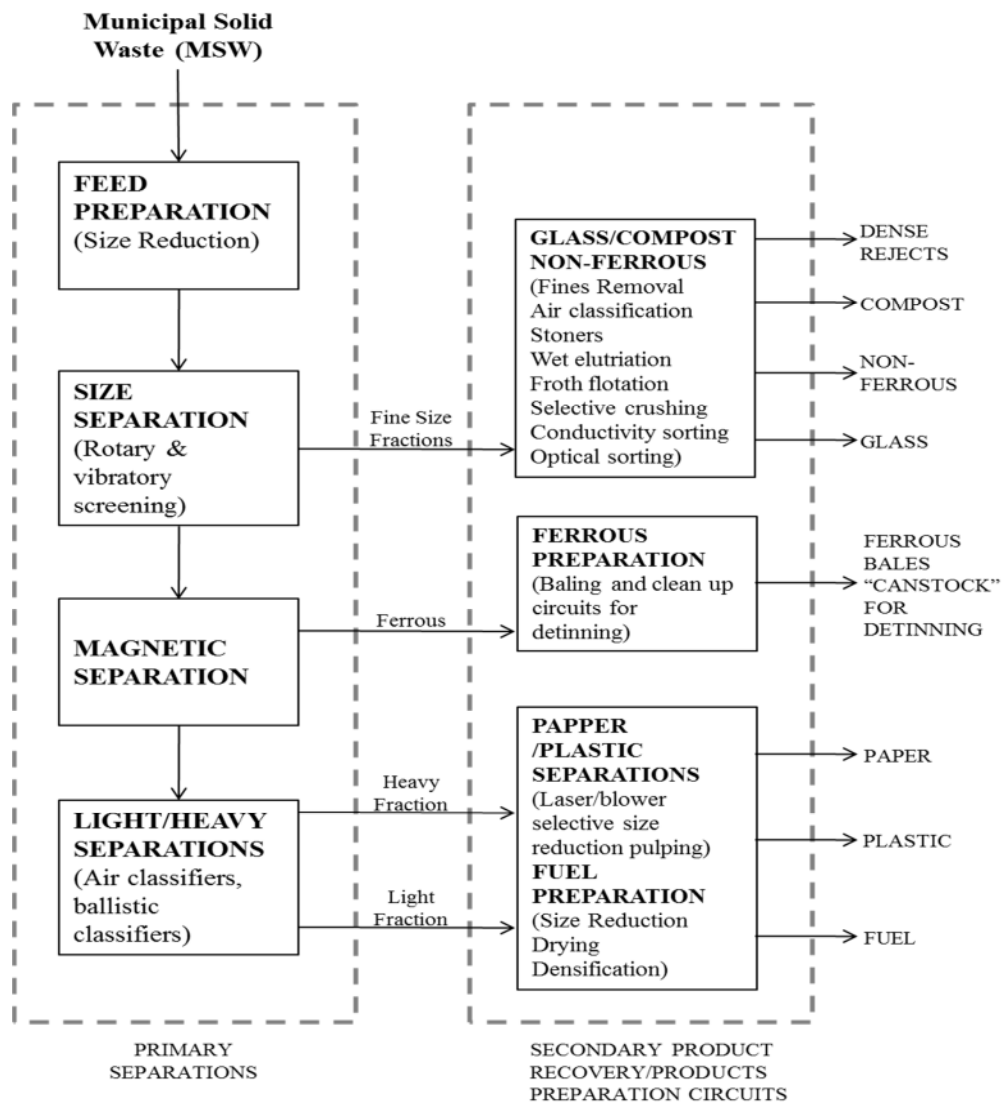


Figure 2.1-5. Refuse Sorting Processes

Seven different classes of RDF have been suggested by the American Society for Testing and Materials (ASTM) and U. S. Environmental Protection Agency (EPA) considering its general composition. The description of each RDF type is summarized in Table 2.1-3 [8, 10].

Table 2.1-3. Refuse derived fuel (RDF) classification

Type	Composition-use
RDF1	Used as fuel as-discarded
RDF2	Wastes treated to get big particle size, might contain ferrous materials
RDF3	Wastes are shredded and processed to remove metal, glass and other inorganic materials (passed through a 50mm square mesh screen)
RDF4	Combustible fraction obtained in powder form (passed through a 2mm mesh screen)
RDF5	Densified RDF in the form of pellets, slugs, cubettes, or briquettes
RDF6	Combustible waste processed into liquid fuel
RDF7	Combustible waste processed into gaseous fuel

Dalai et al [11], carried out characterisation of two different RDF samples differing slightly in composition, the thermal analysis indicated the presence of plastics and cellulose materials in both samples. The composition of any carbonaceous based fuel is very complex as they include some inorganic and organic fractions. The organic fraction is mostly composed of C, H, O, and N; arranged in hydrocarbon chains together with other elements such as metals, glass, and polymers from plastic residues [13]. Proximate and ultimate analyses carried out to characterise MSW samples, are also used to characterise RDF samples. When RDF samples from different sources are subjected to elemental analysis (proximate and ultimate analyses), slight variations in certain parameters might be found, as the solid waste composition is diverse. Therefore a solid knowledge of the main constituents is useful for further applications of the RDF. Examples of the elemental analyses carried out on RDF samples from different sources, are presented in Table 2.1-4.

Table 2.1-4. Elemental analysis of RDF from diverse sources

	RDF ¹ (wt%)	RDF ² (wt%)	RDF ³ (wt%)
Proximate Analysis			
Moisture Content	4.0	4.0	11.8
Ash Content	17.0	12.3	13.4
Volatile Matter	64.0	77.8	71.0
Fixed Carbon	15.0	9.9	3.8
Ultimate Analysis			
C	40.0	45.9	56.8
H	6.9	6.8	8.4
N	0.6	1.1	0.5
S	0.1	nd**	nd
O*	52.4	33.7 ^a	3.0 ^a

¹ Buah et al, 2007 [18]; ² Cozzani et al, 1995 [25];

³ Dou et al, 2007 [26]; *O- obtained by difference; **nd- no detected

^a value as appear in the cited reference

More specific analysis of solid waste samples can be carried out, for example a comparison of the properties of MSW and two RDF samples differing in particle size have been reported by Chang and collaborators [27]. The results are presented in Table 2.1-5.

Table 2.1-5. Properties of the MSW and RDF Samples

	MSW	RDF	
		25-100 mm	> 100 mm
Bulk density (kg/m ³)	289.90	334.80	179.10
Paper (%)	28.62	8.08	5.70
Plastics (%)	26.33	29.15	57.81
Garden trimmings (%)	4.05	4.60	4.21
Textiles (%)	9.03	7.43	18.23
Food Waste (%)	14.04	0.00	0.00
Leather/rubber (%)	0.58	1.13	1.48
Metal (%)	6.99	1.09	0.03
Glass (%)	7.26	0.00	0.00
Ceramics and China	0.47	0.00	0.00
< 5 mm	1.59	16.15	8.89
> 5 mm	1.04	32.36	3.65
<i>Heat Value</i>			
HHV (kcal/kg)	2277.80	2554.50	3715.90
LHV (kcal/kg)	1816.30	2095.70	3296.00
<i>Chemical Composition on wet basis (%)</i>			
C	20.11	24.45	29.24
H	2.92	3.21	3.30
N	0.55	1.09	1.04
Cl	0.18	0.16	0.23
S	0.80	0.10	0.05
O	12.58	11.69	15.90
<i>Proximate Analysis on wet basis (%)</i>			
Moisture (%)	50.65	47.55	40.28
Ash (%)	12.21	11.75	9.96
Combustibles	37.15	40.70	49.76

From Table 2.1-5, a variation between the percentage of materials found in the MSW and RDF samples can be seen. Also there is an influence of different particle size on the properties of RDF samples, for example higher heating values were reported for RDF pellets with a particle size greater than 100mm, this parameter is relevant when RDF is meant to be used as fuel [10, 27].

Thermogravimetric analysis (TGA) is used to study the thermal degradation behaviour and combustion characteristics of solid samples, since different decomposition stages can be identified. A solid sample is combusted under specific conditions and changes in the sample weight are recorded and related with the increase of the temperature. Sørum et al [28], analysed the thermal degradation of cellulosic and plastics fractions contained in MSW, and observed a major weight loss occurring within the region of 250 °C to 400 °C. Additional studies focused on the analysis of the thermal degradation of polystyrene, polypropylene, low-density polyethylene and high-density polyethylene, and identified the degradation between the range 350-500 °C. The thermal decomposition of the main paper compounds has been also reported in the literature [29]. For example the thermal analysis of hemicellulose was reported to start around 250 °C with the major weight loss between 250-350 °C; whereas the main weight loss for cellulose occurs between 325 and 400 °C. The study of the degradation of these components is relevant as most of them can be found in RDF samples.

In general it has been reported that RDF decomposition starts around 230 °C, a first weight loss occurs within the region between 240-380 °C, which might be related with the decomposition of cellulosic material; a second weight loss takes place at around 410 and 500 °C, which may be mainly influenced by the presence of plastics in the RDF samples [11, 18]. An example of the thermal degradation analysis of RDF is presented in Figure 2.1-6.

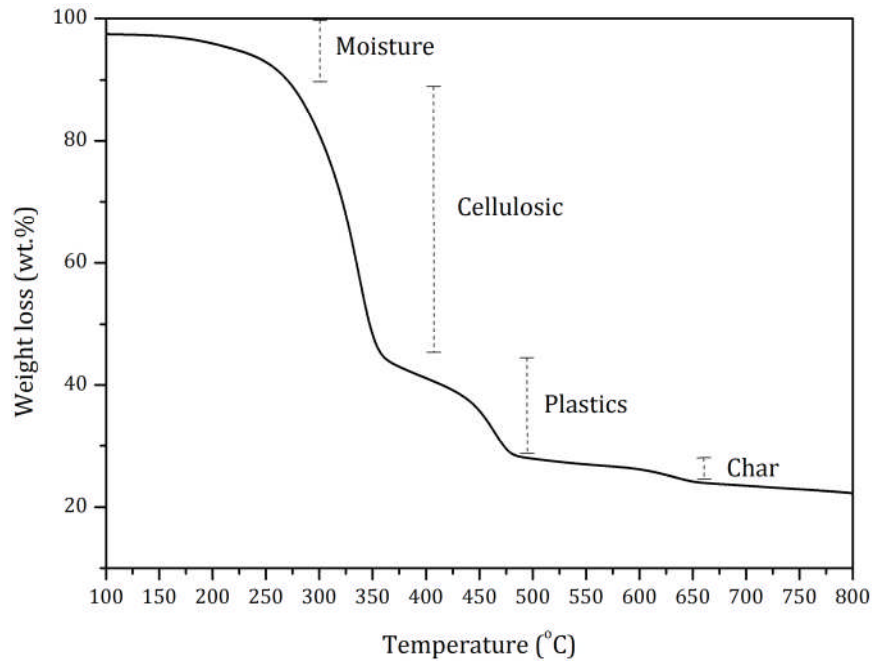


Figure 2.1-6. Thermogravimetric analysis of RDF

From Figure 2.1-6 the first weight loss is associated with the loss of moisture or water due to evaporation, the remaining fraction at the end of the analysis is considered as ash or carbon, and is represented as a straight line as there are no more weight variations.

The main characteristics that make RDF an attractive renewable source are its abundance, the localized source since the collection of MSW is already arranged, and the cost is more stable as in many cases is even subsidized by municipalities as part of waste management policies [30].

2.1.2.1 MSW disposal and treatment methods

MSW treatment practices adopted around the world include incineration, recycling, compost, landfill, dump, and others [6]. The use of landfill sites has been the most common MSW disposal option worldwide and just a small percentage of the wastes are subjected to a recycling process. Other treatment options such as composting or anaerobic digestion are used in smaller percentages [18]. Figure 2.1-7 shows the distribution of the MSW treatment methods used during 2012 by some OECD countries (Organisation for Economic Co-operation and Development) [6].

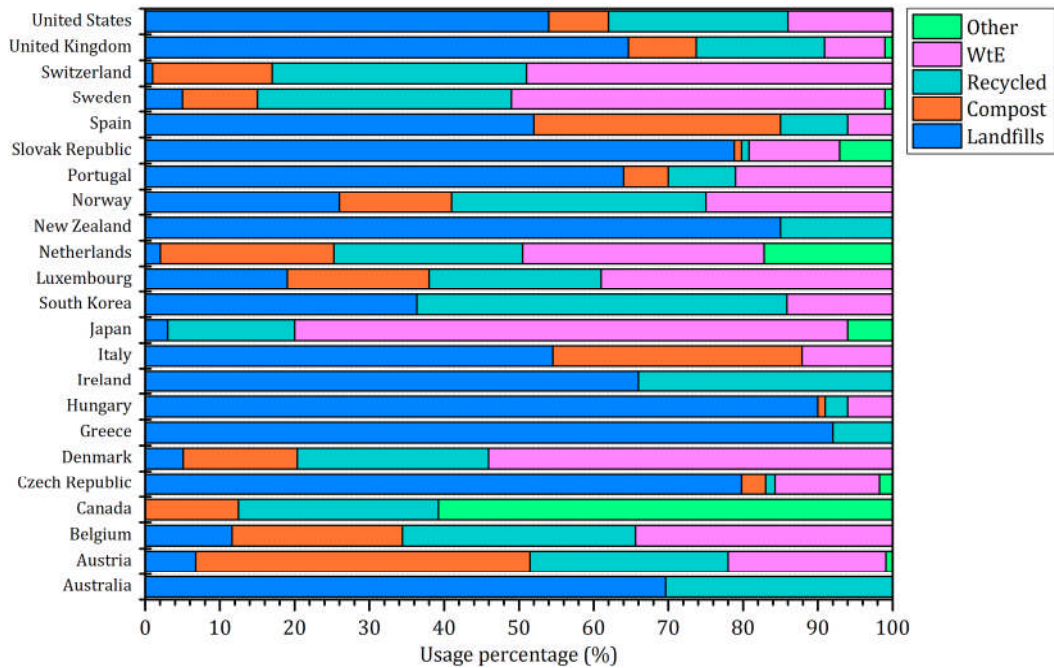


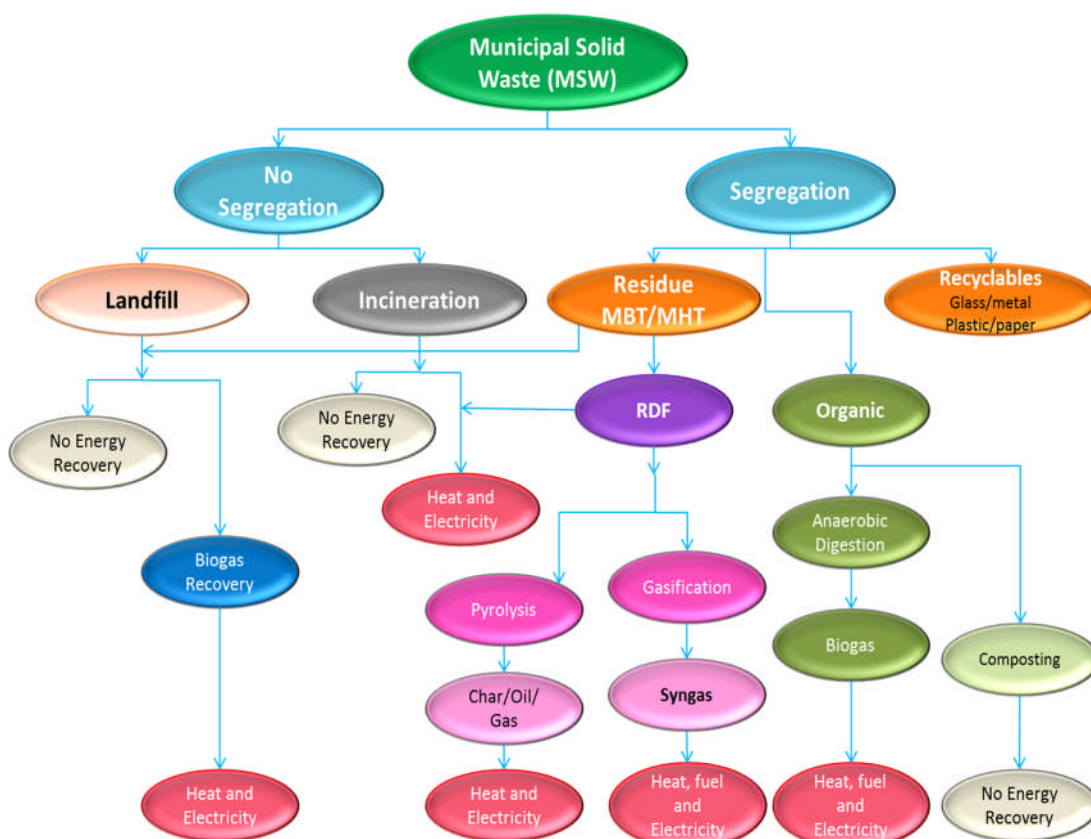
Figure 2.1-7. MSW disposal methods used for some OECD countries

From Figure 2.1-7, it is observed that some countries like Japan have promoted the use of waste-to-energy facilities (WtE) as major waste disposal method using about 70% this alternative in combination with about 17% of recycling. It is also observed that other countries such as Switzerland and Sweden have used a combination of recycling and waste-to-energy options.

These changes are based on the fact that landfills contribute to greenhouse gases emissions and also to the pollution of surface and groundwater due to the leachate generation [15]. During the waste degradation process diverse contaminants such as methane, carbon dioxide, and hydrogen sulphide are generated, which contributes to atmospheric pollution [2]. These environmental and health associated problems together with the lack of land areas and society opposition, have prompted the assessment of alternative waste disposal methods to be integrated into the waste management regulations. Also different regulation measures and guidelines have been developed with the aim to reduce the waste associated problems [8, 15, 26].

2.1.2.2 Alternative thermal treatment for MSW and RDF

A wide range of processes including physical, chemical and biological transformations have been assessed in order to reduce the volume of wastes, to segregate as much recyclable materials as possible, to facilitate the handling, to dispose of them in an environmental friendly way, to recover energy, etc. A diagram showing the potential pathways for collected MSW is shown in Figure 2.1-8 [1, 8].



* MBT Mechanical Biological Treatment; MHT Mechanical Heat Treatment

Figure 2.1-8. Diagram showing different conversion options for MSW

Most of the methods shown in Figure 2.1-8 seek the production of heat, fuel and/or electricity by different means. Technologies can be classified as thermal, biochemical, and chemical processes, focused on the energy recovery [7]. Diverse thermal treatments can be used either as a way to valorise the waste for energy recovery or as pre-treatment of waste prior to disposal, and are also referred as thermo-chemical processes. The main aims of using thermo-chemical technologies are the volume reduction, the stabilisation of the waste,

recovery of energy from waste and the sterilisation of waste [1, 31]; therefore are a viable and environmental friendly way to process wastes.

There are several types of thermal process technologies namely plasma arc gasification, conventional gasification, pyrolysis and/or gasification. The thermal efficiency of each process is different, a comparison between the net energy production from each technology is shown in Figure 2.1-9 [12].

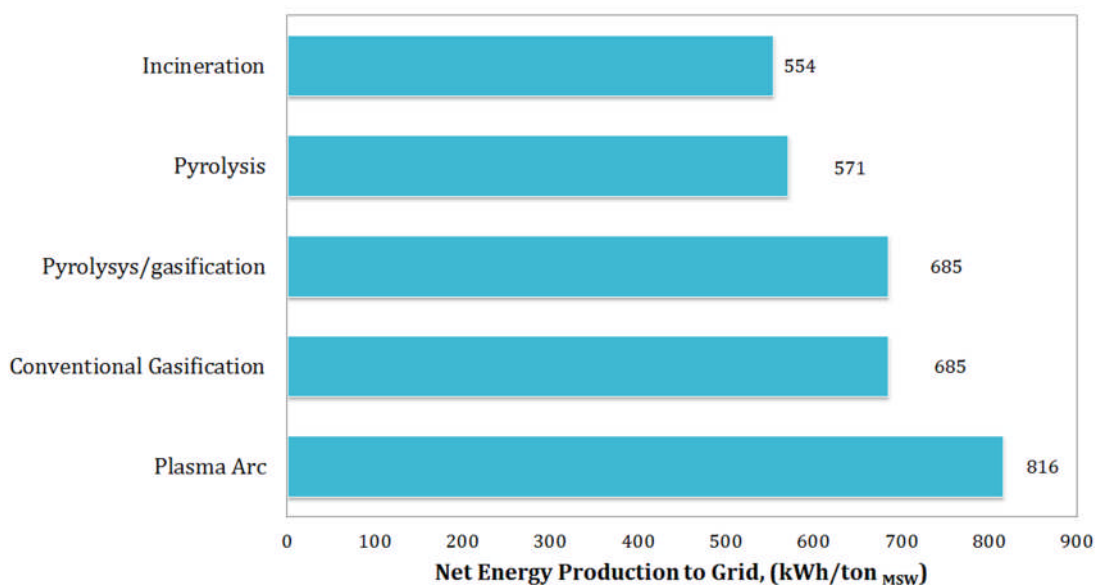


Figure 2.1-9. Net output of various thermal processes

Renewable energy sources are seen as an alternative to partly covers the energy requirements of the future, as they have broad availability. One example is the use of municipal solid waste (MSW), in the form of refuse derived fuel (RDF) as raw material in processes such as pyrolysis and gasification [32].

The design and selection of the thermochemical process it is highly influenced by the physicochemical properties of the MSW [7], as the diverse decomposition reactions taking place depend on the raw material characteristics, as well as the process conditions [13]. Thermal treatments are an essential part of an integrated waste management system because of the benefits that the use of this technology brings [33]. When MSW or RDF are subjected to thermal treatments, the energy recovery through heat or power generation is feasible, which is desired within the waste management hierarchy [32]. Furthermore the

original mass and volume are reduced around 70-80%, and 80-90% respectively; therefore the land area required for landfill for the same quantity of MSW is also diminished. Due to the elevated temperatures of the process (500-1000°C), some relevant organic contaminants such as hydrocarbons and halogenated materials are eliminated. Nowadays most of the thermal processing facilities are well equipped with pollution control systems and also represent a nearly complete recycling alternative and a source of clean and renewable energy if implemented in a proper manner [22, 34]. However there is still a concern regarding the disposal alternatives for the 10% remaining waste fraction [10], and also a concern about the possible diverse toxic effects of the emissions. For example a fraction known as tar might contain diverse components such as tri- and tetra-methylphenanthrenes, chrysene, methylchrysenes, and benzapyrenes, which are of known carcinogenic and/or mutagenic activity [35-37].

Among the thermal processes options presented in Figure 2.1-8, pyrolysis and gasification have been broadly studied for energy recovery, using diverse types of carbon based feedstocks. A description of both thermal processes is addressed in the following sections.

2.1.2.3 Pyrolysis

The pyrolysis process is the thermal conversion or degradation of a solid waste or organic material in the total absence of oxidising agents such as oxygen, steam or carbon dioxide. The overall pyrolysis process is endothermic, thus requires an external heating source to reach process temperatures between 300 to 800 °C. At these temperatures the chemical bonds forming the organic material break down; and as a result gaseous, liquid and solid fractions are released [8, 13, 38-40]. The major weight loss occurs during the evolution of volatile matter, followed by the decomposition of char as observed in [26, 41].

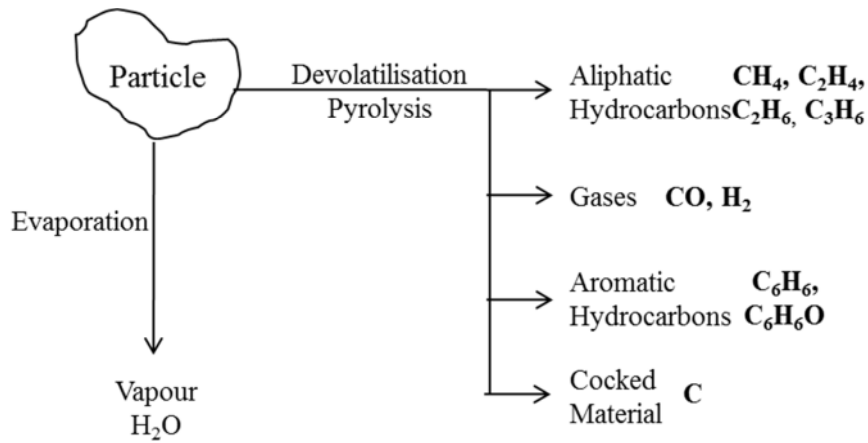


Figure 2.1-10. Pyrolysis process of a fuel particle

Initially the solid waste undergoes a drying process aimed to release all the moisture contained in the solid waste between 100-120 °C. After that the pyrolysis (or devolatilization) process takes place and the long polymer chains contained in the fuel material break down into shorter molecule chains releasing mainly gases such as H₂, CH₄, CO, CO₂, H₂O, etc., together with other hydrocarbons; this occurs as a result of different complex reactions taking place at temperatures around 200-800 °C; also a carbonaceous or coked material remains as solid residue (Figure 2.1-10). These reactions are sometimes referred to as primary reactions; whereas secondary reactions further convert products and increase the concentrations of CO₂ and CH₄ in the produced gas. Secondary reactions might also take place during the gasification process as will be discussed in Section 2.1.2.4. A more general evolution of the pathway correlating the pyrolysis temperature and the products formed was proposed by De Souza-Santos et al [13], in Figure 2.1-11:

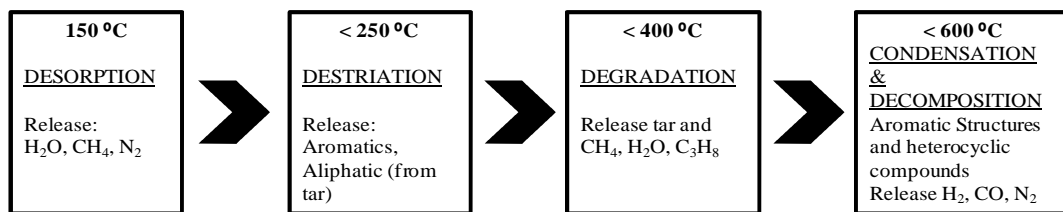
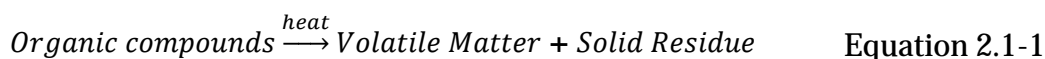


Figure 2.1-11. Pyrolysis steps related with the process temperature

The overall pyrolysis reaction can be expressed according to Equation 2.1-1 [42]:



The evolution of the chemical reactions that occur during the pyrolysis process are described in Table 2.1-6 [38, 43].

Table 2.1-6. Evolution of pyrolysis reactions according to the temperature

Temperature (°C)	Chemical Reaction
100-120	Thermal drying, dehydration
250	Deoxidation, desulfurization, molecular separation of water and carbon dioxide, starts cleaving hydrogen sulphide
340	Breakage of bonds of aliphatic compounds, splitting of methane and other aliphatic compounds
380	Carbonization phase (residues)
400	Breakage of carbon-oxygen and carbon-nitrogen bonds
400-600	Decomposition of bituminous compounds into low-temperature carbonization oils and tars
600	Cracking of bituminous compounds into heat resistant components formation of aromatic compounds (light hydrocarbons and derivatives)
>600	Olefin (ethylene) dimerization, dehydrogenation to butadiene, reaction of ethylene to cyclohexane, thermal aromatization to benzene and higher-volatility aromatic compounds

The specific characteristics of the pyrolysis products depend on diverse factors including the raw material composition, and operational conditions such as temperature, pressure, and heating rate [3]. The general characteristics of each fraction are addressed in Table 2.1-7 [8, 38].

Table 2.1-7. Characteristics of products from the pyrolysis of organic material

Fraction or product	Characteristics
Gaseous	Mainly composed by H ₂ , CH ₄ , CO, CO ₂ , plus other volatile constituents, and hydrocarbons. Pyrolysis gas yield is 20-50% weight of the input; with heating values are between 3-12 MJ/Nm ³ .
Liquid	Contain mainly tar, oil and water in different amounts. It is mainly composed by polyaromatic hydrocarbons (PAH), and oxygenated compounds. Liquid yields are around 30-50% in weight with heating values around 5-15MJ/kg.
Solid	Char-like material consisting almost entirely of carbon, plus some inert materials (metals, glass, etc.) present in the raw material. The heating value of the char might be between 10-35 MJ/kg.

Pyrolysis gases are mainly composed of carbon dioxide, carbon monoxide, hydrogen, methane and hydrocarbon gases. Both liquid and gaseous fractions

contain complex mixtures of hydrocarbons and other organic compounds, whose yield and composition is related to the fuel used and process conditions. For example a raw material or fuel with high amounts of oxygenated structures such as lignin or hemicellulose, might promote an increase in the concentration of carbon monoxide and carbon dioxide in the produced gas, also known as syngas [3]. Chars from pyrolysis are sometimes used as fuel, or are also upgraded to produce a high grade activated carbon [3]. Also Horne and Williams [44], reported the influence of the pyrolysis temperature over the products from the flash pyrolysis of biomass. They found that by increasing the pyrolysis temperature, the concentration of polyaromatic hydrocarbons (PAH) also increased in both liquid and gaseous fractions. In general the increase in the pyrolysis temperature promotes an increase in the H₂ and CH₄ concentrations in the produced syngas, and also it has been found that the final heating value of the syngas is influenced by both the raw material and the process temperature [11].

During the pyrolysis of municipal solid waste it has been reported that a yield of about 35% of char, with a high ash content (up to 37%) was obtained [3]. Lin et al [24], reported a yield of about 28wt.% of oils, 30wt.% of non-condensable hydrocarbons, and 42wt.% of solid fraction when RDF were subjected to pyrolysis at 500°C. Product yields for solid, liquid and gaseous fractions using RDF and a mixture of plastics are presented in Table 2.1-8 [24, 29, 45, 46].

Table 2.1-8. Product yields from the pyrolysis of RDF and plastics mixtures

Waste	Pyrolysis Process	Temperature (°C)	Heating rate	Char (wt.%)	Liquid (wt.%)	Gas (wt.%)
RDF ¹	Moderate (fixed-bed)	500	-	42.0	28.0	30.0
RDF ²		600	20°C/min	35.2	49.2	18.8
RDF ³	Moderate (batch)	700	-	30.0	49.0	22.0
Plastics ⁴		550	25°C/min	5.6	57.1	24.5

¹ Lin et al, 1999; ² Williams & Besler, 1996; ³ Rampling & Hickey, 1988; ⁴ Williams & Williams, 1997

From Table 2.1-8, it can be observed a difference in the products yields when temperature, heating rate or pyrolysis process were changed. Williams and

Williams [46], reported that for a mixture of plastics, the increase in the pyrolysis temperature increased the gas yield as the molecules break down promoting the formation of smaller molecules; whereas the yield of tar/oil tend to be reduced. In general the increase in the pyrolysis temperature, and/or longer residence times result in an increase in the gas fraction at the expense of the oil produced [24].

Some pyrolysis facilities are focused on the production of the oil fraction as it can be later used as a liquid fuel in further processes. However, sometimes not all of the oil characteristics match with the equipment or facilities requirements, thus the oil can require further upgrading to be used as chemical feedstock, in fuel applications, conventional electricity-generating systems such as diesel engines, or can also be used to produce refined fuels [3, 47].

Some of the polymeric materials contained in RDF are poor heat conductors and require a significant amount of energy to break down the macromolecules that comprise them, therefore the pyrolysis of RDF is a complicated process [24, 25]. For this reason a better understanding of the kinetics of RDF during the pyrolysis process is important. The thermogravimetric kinetics of the pyrolysis process have been investigated; specifically focused on the behaviour of municipal solid waste (MSW) [48]. Using thermogravimetric analysis (TGA) different decomposition reactions and the kinetic parameters of the MSW decomposition can be obtained. For example the thermal decomposition of refuse derived fuel (RDF) has been analysed by Cozzani et al [16]; they assumed that the thermal degradation of RDF can be considered as the sum of the thermal degradation of the main compounds including cellulose, lignin and hemicellulose from paper and wood-like materials, and polyethylene (PE) from plastics. The overall kinetics of thermal degradation or rate of conversion during the pyrolysis process can be addressed by a model of independent and parallel reactions. The single reaction model and rate of conversion can be expressed according to the Arrhenius equation (Equation 2.1-2) [24, 28]:

$$\frac{d\alpha}{dt} = A \exp(-E/RT)(1 - \alpha) \quad \text{Equation 2.1-2}$$

Where E and A are the activation energy and the frequency factor respectively; R is the universal gas constant ($8.314 \times 10^{-3} \text{ kJ kg mol}^{-1} \text{ K}^{-1}$), and α is the conversion or reacted fraction that can be described as follows [28]:

$$\alpha = \frac{1 - m}{1 - m_{char}} \quad \text{Equation 2.1-3}$$

Where m and m_{char} are the original sample mass and the char yield respectively. As the RDF is composed of more than one simple material (Section 2.1.2), the decomposition rate of each material is independent from each other, thus the overall conversion can be described as [28]:

$$-\frac{dm}{dt} = \sum_i c_i \frac{d\alpha_i}{dt}; i = 1, 2, 3, \dots, N \quad \text{Equation 2.1-4}$$

The individual decomposition of each material can be thus calculated according to the Equation 2.1-2; using experimental values from the thermogravimetric analysis [28]. By using these expressions, a quantitative prediction of the RDF pyrolysis behaviour can be obtained [24].

Variations in the pyrolysis process include conventional pyrolysis, flash-liquid, flash-gas, and carbonisation. For each type of pyrolysis, features such as the heating rate and temperature are varied according to the different products which are targeted to be obtained, namely: charcoal, gas, char, liquid, and or chemicals [3].

2.1.2.4 Gasification

The gasification process is strictly speaking a continuation of the pyrolysis process. It differs from the pyrolysis process as the thermal decomposition takes place at higher temperatures and under partial-oxidizing conditions i.e. in the presence of oxidising agents. The relation between the actual amount of

oxidising agent (air, oxygen, steam, or mixtures of these) and the amount of fuel used in order to achieve full combustion (under stoichiometric conditions) is known as the equivalence ratio or stoichiometric ratio [43, 49]. During the gasification, the carbonaceous based materials are converted into gas with a low amount of liquid and solid fraction, through a series of different reactions [11, 12]. In Table 2.1-9, are summarized the main chemical reactions occurring during the gasification process [33, 34]. The exothermic reactions include the reactions of oxygen with carbon, hydrogen and carbon monoxide, and the endothermic reactions include the reactions of carbon with carbon dioxide and steam.

Table 2.1-9. Basic homogeneous and heterogeneous reactions during gasification of solid waste

Chemical Reaction	Type of Reaction
<i>Oxidation reactions</i>	
$C + \frac{1}{2} O_2 \rightarrow CO$	Carbon partial oxidation
$CO + \frac{1}{2} O_2 \rightarrow CO_2$	Carbon monoxide oxidation
$C + O_2 \rightarrow CO_2$	Carbon oxidation
$H_2 + \frac{1}{2} O_2 \rightarrow H_2O$	Hydrogen oxidation
$C_n H_m + \frac{n}{2} O_2 \leftrightarrow n CO + \frac{m}{2} H_2$	$C_n H_m$ partial oxidation
<i>Gasification reactions involving steam</i>	
$C + H_2O \leftrightarrow CO + H_2$	Water-gas reaction
$CO + H_2O \leftrightarrow CO_2 + H_2$	Water-gas shift reaction
$CH_4 + H_2O \leftrightarrow CO + 3H_2$	Steam methane reforming
$C_n H_m + n H_2O \leftrightarrow n CO + (n + \frac{m}{2}) H_2$	Steam reforming
<i>Gasification reactions involving hydrogen</i>	
$C + 2H_2 \leftrightarrow CH_4$	Hydrogasification
$CO + 3H_2 \leftrightarrow CH_4 + H_2O$	Methanation
<i>Gasification reactions involving carbon dioxide</i>	
$C + CO_2 \leftrightarrow 2CO$	Boudouard reaction
$C_n H_m + n CO_2 \leftrightarrow 2n CO + \frac{m}{2} H_2$	Dry reforming
<i>Decomposition reactions of tars and hydrocarbons</i>	
$p C_x H_y \rightarrow q C_n H_m + r H_2$	Dehydrogenation
$C_n H_m \rightarrow n C + \frac{m}{2} H_2$	Carbonization
$C_x H_y$ represents tars, and heavy fragments from thermal cracking $C_n H_m$ represent hydrocarbons with smaller number of carbon atoms than $C_x H_y$	

In a similar way as in the pyrolysis process, there are some factors that influence the products distribution and composition from the gasification process, including raw material characteristics, process temperature, pressure, gasifying medium, catalyst and additives, equivalence ratio (ER), residence time, etc. The selection of these parameters is also related to the design of the gasification reactor [50]. For example the moisture content of the solid waste influences process temperatures, composition and amounts of products. When the moisture content is above 20wt.% and gasification temperatures around 600 °C, MSW cannot be easily degraded [13, 51]. Also an increase in the gasification temperature and/or in the heating rate might result in higher hydrogen concentrations in the produced gas [42].

The gasification temperature has significant influence on the gas heating value, tar content in the produced gas, etc. Figure 2.1-12., shows the effects of the gasification temperature over various parameters when different feedstocks are used during the gasification process [50].

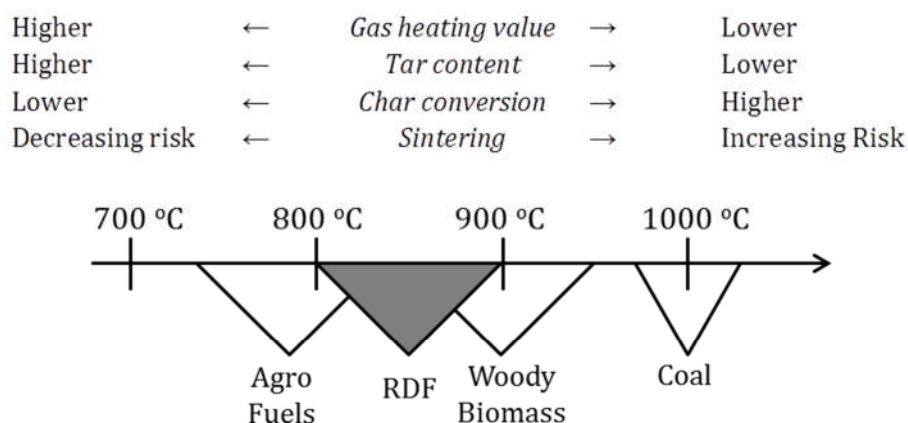


Figure 2.1-12. Influence of the gasification temperature over product characteristics, using different raw materials

2.1.2.4.1 Types of gasifier

The design of each gasifier is defined according to the products requirements, raw materials used, operational conditions, etc. Different gasifier designs include fixed bed, fluidized bed, and entrained flow; the general configuration of each reaction system is presented in Figure 2.1-13 [11, 52-54].

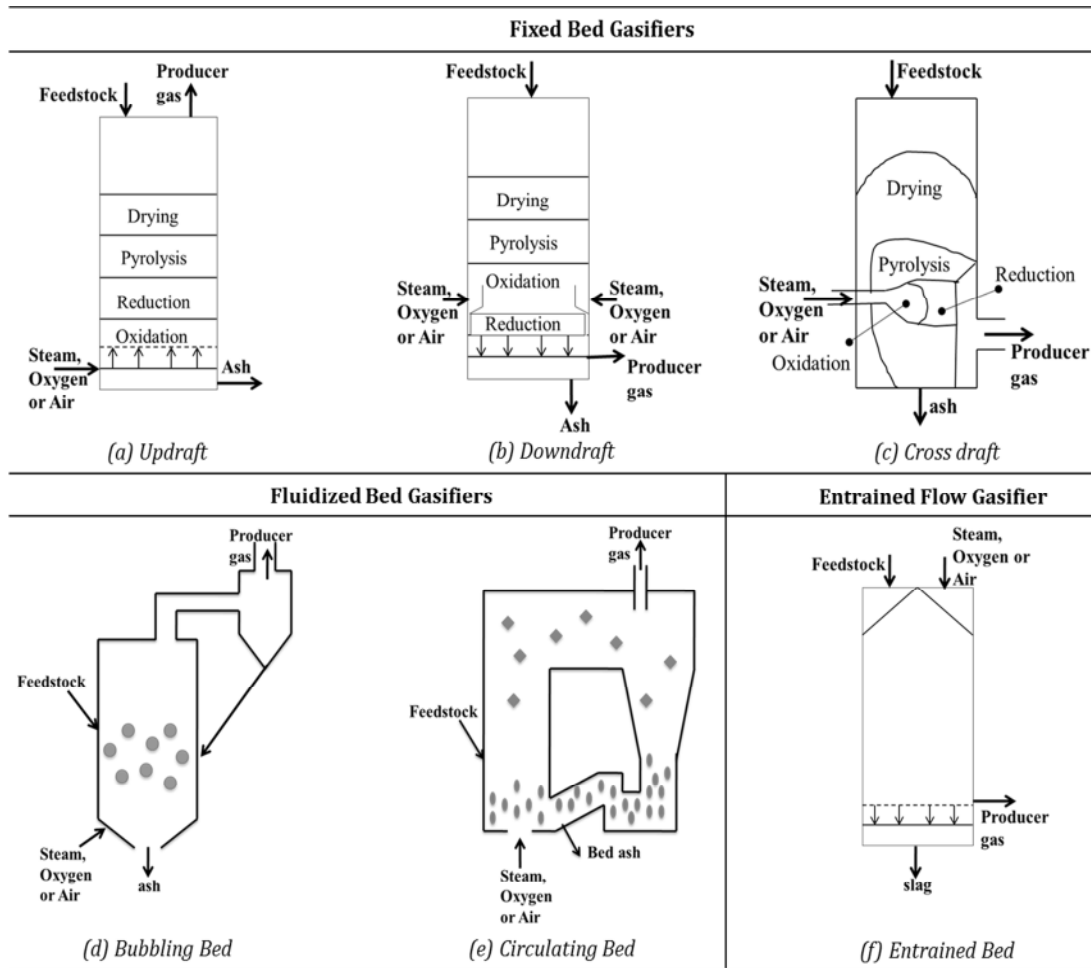


Figure 2.1-13. Configuration of gasification reactor systems

For each one of the reaction systems presented in Figure 2.1-13 there are diverse operational advantages and disadvantages, which are summarised in Table 2.1-10.

Table 2.1-10. Strengths and weaknesses of gasifiers according to their design

Gasifier Type		Strength		Weakness		Size
Entrained flow		Short residence time (seconds or tens of seconds) High temperatures achieved (good fuel conversion)		High temperatures required Entrainment of some molten slag in the raw syngas Relatively large oxidant requirements Large amount of sensible heat in the raw syngas		Large Scale
Fixed bed	Updraft	Low oxidant requirements Counter flow gives a high proportion of chemical energy, increasing the gas calorific value. High thermal efficiency.	Small pressure drop. Little tendency towards slag formation. Good turndown.	The temperature of the gas exiting is lower than the temperature needed for complete material conversion Production of liquid hydrocarbons, tars and oils Limited ability to handle fines	Great sensitivity to tar and moisture content of fuel. Long time required to start up. Poor reaction capability with heavy gas load. Limited turndown.	Small to medium scale
	Downdraft		Moderate dust Low tar formation			
Fluidized bed	Bubbling bed	Uniform and moderate temperature through the bed Moderate oxygen and steam requirements Availability to treat small particle size feed. Very good scale-up potential.	Good temperature distribution. Easily started and stopped.	Temperature control Difficult to achieve high feed conversions Poor fuel conversion to gas		Medium Scale
	Circulating bed					

Adapted from [54-57]

From all the different gasifier designs the most used are fluidized and fixed bed reactors. Fixed bed gasifiers with a downdraft configuration have been reported to attain high feedstock conversion, to produce a gas with higher quality and lower tar levels, when compared with other gasifiers under similar conditions using the same feedstock [55, 58].

2.2 Pyrolysis-gasification for hydrogen production

Pyrolysis and gasification processes are focused on the thermal degradation of solid wastes; however both differ in some operational and technical parameters. A summary including the main characteristics of pyrolysis and gasification processes is shown in Table 2.2-1 [33].

Table 2.2-1. Main characteristics of pyrolysis and gasification processes

Condition	Pyrolysis	Gasification
Aim of the thermochemical process	Thermally decompose solid material into gases and condensed fraction	Maximize the solid conversion into gas containing mainly CO, H ₂ and CH ₄
Oxidising medium	No oxidising agent used	Air, oxygen, steam or mixtures of these gases (lower amount than that required for stoichiometric combustion)
Operating temperatures	300-800°C	550-900°C (air) 800-1500°C (oxygen)
Pressure	Slightly over pressure	Atmospheric
Output gases	CO, H ₂ , CH ₄ and other hydrocarbons	CO, CO ₂ , H ₂ O, H ₂ , CH ₄
Contaminants in the output gas	H ₂ S, HCl, NH ₃ , HCN, tar, particulate	H ₂ S, HCl, COS, NH ₃ , HCN, tar, alkali, particulate
Gas cleaning requirement	Syngas cleaning required for further use; e.g. in chemical production processes or high efficiency energy conversion devices	

The different primary products, recovery potential and secondary products from pyrolysis and gasification processes are shown in Figure 2.2-1 [59].

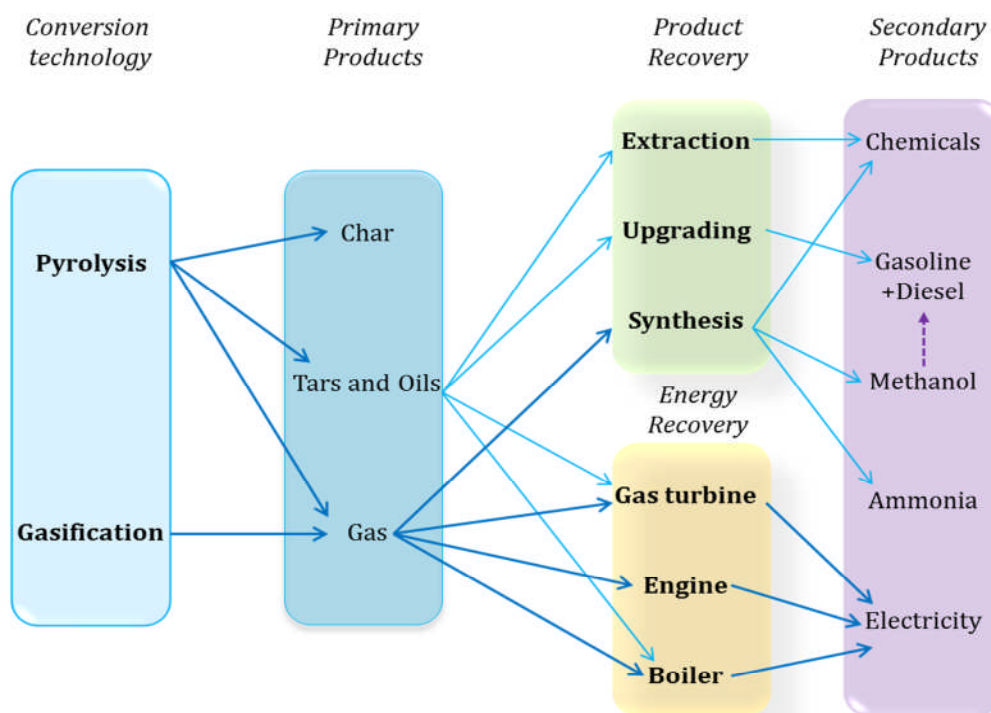


Figure 2.2-1. Pyrolysis and Gasification primary and secondary products

Pyrolysis and gasification processes can be combined offering several advantages rather than using each process separately. An example of the

combination of pyrolysis and gasification processes and products is presented in Figure 2.2-2 [38].

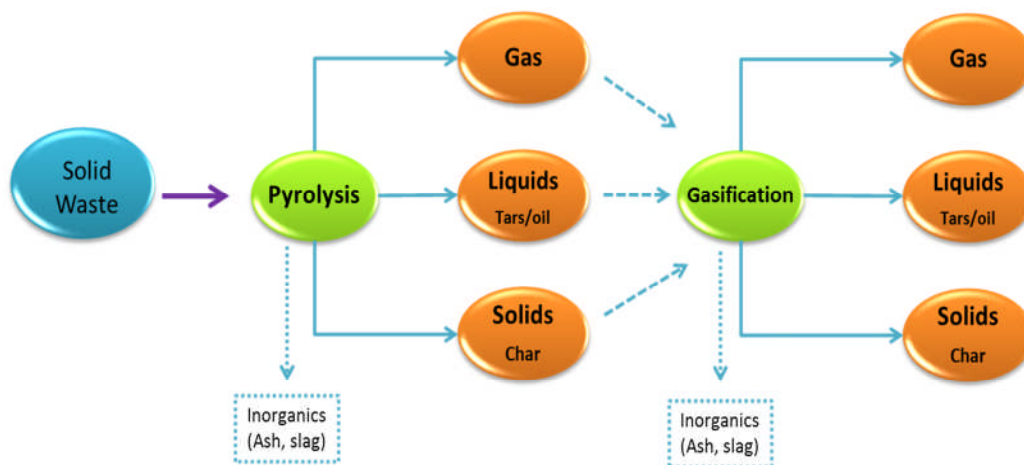


Figure 2.2-2. Pyrolysis and gasification main products and combination of both processes

In order to use the syngas as feedstock for methanol and naphtha production in the chemical industry, it should meet certain requirements such as a H_2/CO ratio higher than 1.7. To achieve this requirement during the gasification of wastes, it is necessary to add steam into the process [60]. When steam is added into the combined process, some chemical reactions are promoted (water gas-shift, steam methane reforming, steam reforming, etc.), resulting in the formation of CO and H_2 [12].

The recovery of energy from solid wastes processing can be addressed from two different perspectives namely electricity and/or heat production. However the type of energy recovery is highly dependent on the produced gas or syngas characteristics [38]. Therefore by combining pyrolysis and gasification processes seems a viable way to obtain a high-hydrogen rich syngas, with a high heating value and low tar content.

2.2.1 Syngas and Hydrogen; potential applications

A syngas with different H_2 to CO ratio can be obtained through different production processes using diverse carbon based feedstocks. A general diagram showing some of the most common syngas production routes and applications is shown in Figure 2.2-3 [61-63].

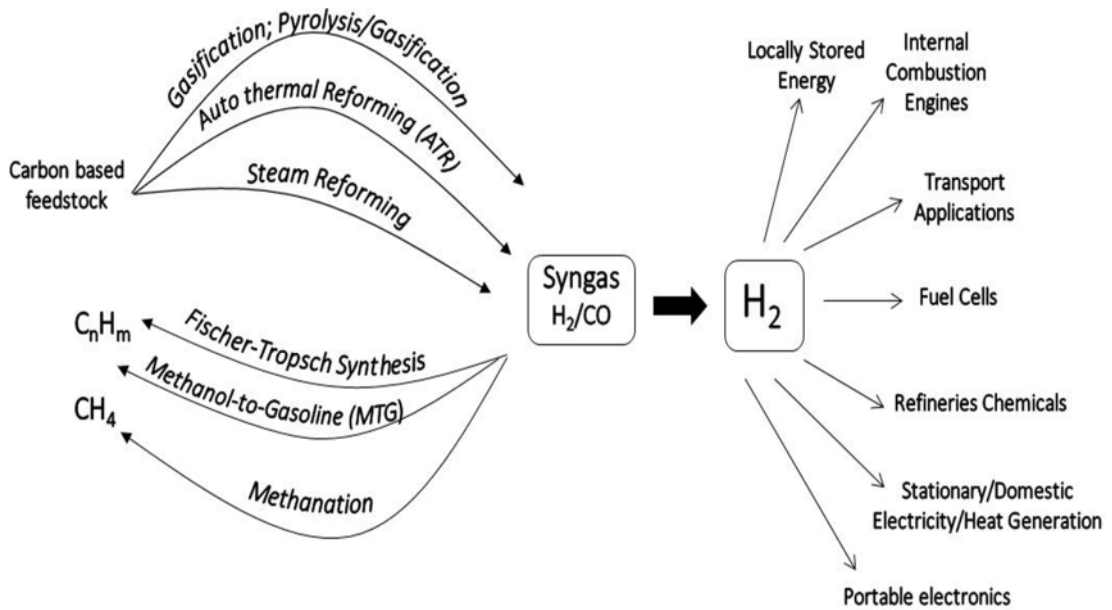


Figure 2.2-3. Potential uses of syngas from carbon based feedstocks

A partially cleaned syngas can be fed into combustion chambers to recover energy by a water-steam cycle. As shown in Figure 2.2-3, the syngas can be further upgraded e.g. to obtain hydrogen. A cleaned syngas can be used in small scale internal combustion for electricity production, furthermore when the gases are thoroughly cleaned can be directly used in combined cycles for electricity production including a gas turbine and a second cycle for steam production and further use of a steam turbine [12, 38]. Figure 2.2-4 shows diagrams of the most common systems used for energy recovery [8].

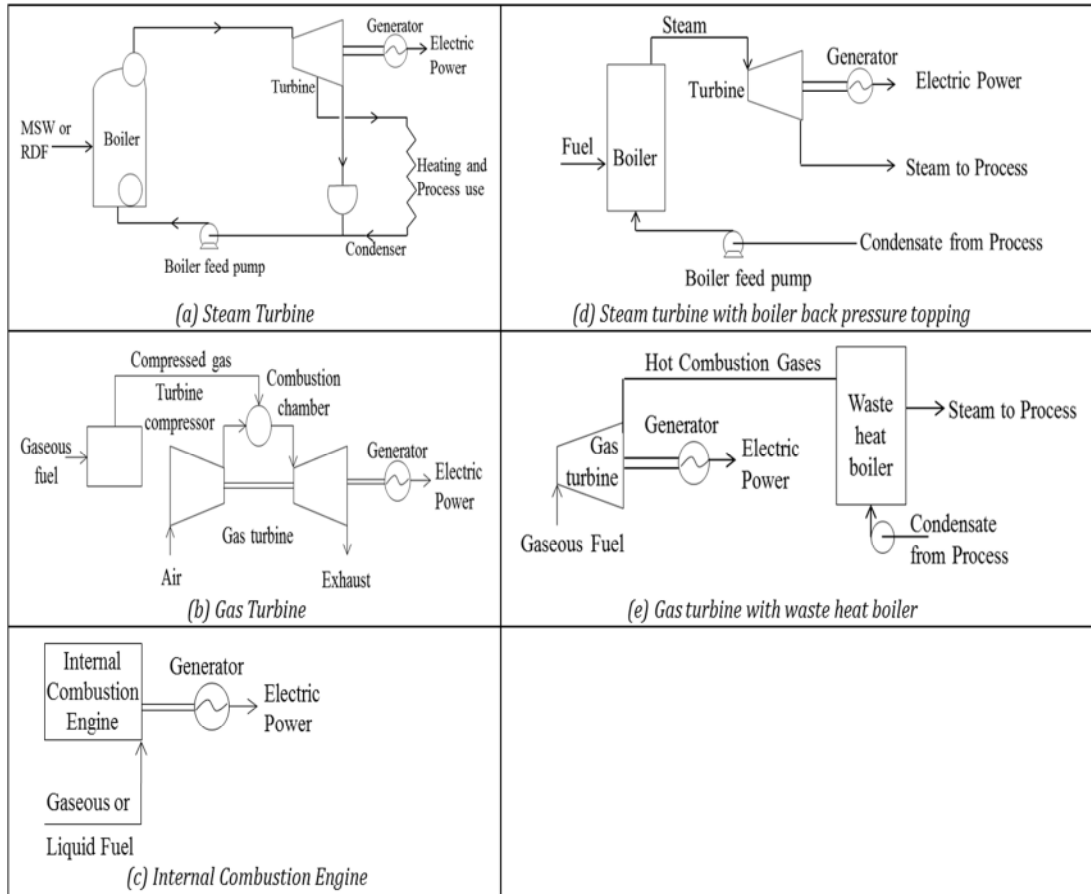


Figure 2.2-4. Typical energy recovery flow diagrams

Steam turbines (Figure 2.2-4a) are the most common energy recovery devices and are normally used for large systems (10-50MW). Gas turbines (Figure 2.2-4b) are compact and efficient systems that can be fed with gaseous or liquid fuels. Internal combustion engines are alternative equipment to gas turbines and are modifications of original systems designed for natural gas or propane (Figure 2.2-4c). Figure 2.2-4d and Figure 2.2-4e, are examples of systems used for cogeneration, these types of engines are widely used in the industry for electricity generation [8].

Hydrogen has a broader potential to be used for power generation both in the form of heat and/or electricity, when compared with the raw syngas. Hydrogen potential yield is defined as the sum of the hydrogen in the produced syngas and the theoretical hydrogen from the water-gas-shift reaction, as well as the complete reforming of hydrocarbons in the produced syngas according to (Equation 2.2-1) [64]:



Gaseous hydrogen can be burned as fuel or used in fuel cells for power generation [65]. When hydrogen is combusted with oxygen, energy is released in the form of heat, also water (steam) is released into the atmosphere, thus the hydrogen cycle is closed [66]. Hydrogen can be also used as feedstock in chemical processes, fuel cells or for methanol and/or ammonia generation [11]. Hydrogen is a fuel with high energy per unit mass, can be produced by renewable sources (solid waste, water, etc.), and is also a clean energy alternative therefore is also referred to as an energy carrier [67, 68]. For these reasons many researchers have focused on the further upgrade of syngas to hydrogen (Figure 2.2-3).

Currently about 95% of the total hydrogen produced comes from the use of carbonaceous raw material (mainly from a fossil source), and is widely used worldwide in the hydrocarbon processing industry. The hydrogen demand in the year 2000 was approximately 50 million tonnes and is expected to increase about 4 per cent per annum, thus by the year 2016 will be required about 300 million tonnes of hydrogen; therefore it is essential to develop alternative routes to produce hydrogen different from those based on fossil fuels [69, 70]. Currently there are a number of processes for hydrogen production namely electrochemical routes, thermochemical processes, photochemical and photocatalytic processes, or photoelectrochemical processes [71]. Among the thermochemical routes used for hydrogen production, the most common is the natural gas steam reforming process, which is used to supply about half of the world's hydrogen demand [71].

Of the total energy produced in the world, about 80% comes from fossil fuels sources, including natural gas, oil, and coal [66, 72]. The world energy demand tends to increase every year; for example according to the Energy Information Administration (EIA, 2013) IEO report, the energy consumption in 2010 was 2.67×10^{20} joules; it will increase to 6.65×10^{20} joules in 2020 and up to 8.65×10^{20}

joules by 2040 [73]. About 85% of the world energy demand from 2010 to 2040 will come from countries outside the Organization for Economic Cooperation and Development (non-OECD); according to the projections showed in Figure 2.2-5 [73].

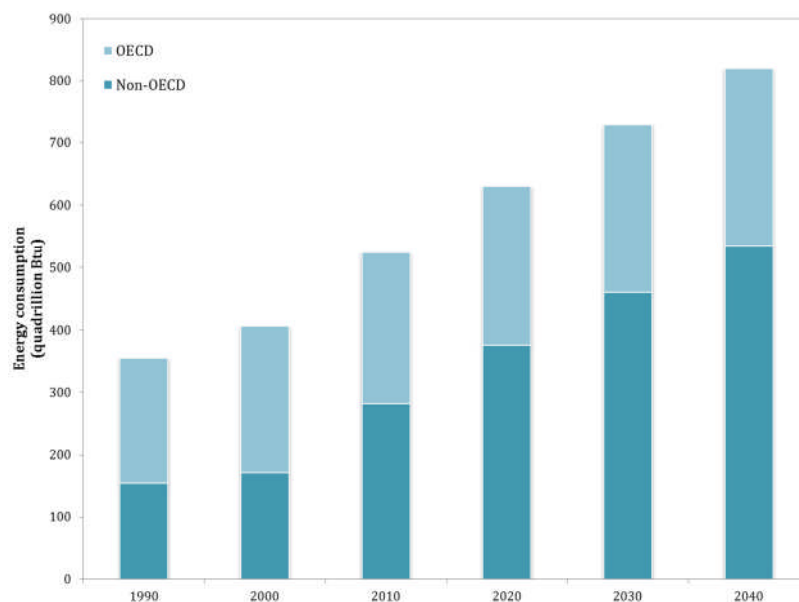


Figure 2.2-5. World total energy consumption, 1990-2040

In order to propose a clear scenario about the future use of hydrogen it is necessary to ensure its production, safe storage and conversion potential methods [66]. For this reason, different production routes are considered to ensure its supply in the future. In addition there are some challenges associated with the potential of hydrogen to be stored and transported. Different ultra-high capacity materials have been researched to ensure the highest potential hydrogen storage, as most of the time there is a significant loss (up to half the storage capacity by weight) in the systems integration [74]. All these parameters give an idea about the different challenges that hydrogen as an energy carrier must meet to be further considered as an alternative fuel.

High hydrogen content is desirable to simplify the hydrogen production route from syngas (Figure 2.2-3); unfortunately sometimes impurities such as tar and particulates are present in the syngas composition, reducing its quality and hindering its use for further applications.

2.3 Tar: definition and composition

The term tar encompasses different aromatic hydrocarbons contained in the product gas from single ring aromatic structure to 5-ring aromatic compounds together with other oxygen-containing hydrocarbons and polyaromatic hydrocarbons (PAH); hence tar is not a single compound [50, 75-77]. For example Pober and Bauer [78], analysed the oil fraction from the pyrolysis of MSW and found a large number of compounds with molecular weights ranging from 32 to 10,000 Da; therefore the tar boiling point also varies from about 55 to 300 °C. The variety of compounds that can be found in the tar fraction is influenced by diverse parameters such as process conditions and raw materials used.

In the literature, different definitions of tar have been stated, for example Milne et al [76], defined tars as highly aromatic compounds resulting from thermal processing of organic materials. Also in the literature it has been reported that tar includes all the aromatic compounds, excluding benzene and light hydrocarbons from C₁-C₆ [79, 80]. In a joint meeting among diverse experts in the field organised by the IGT (Institute of Gas Technology, Chicago, USA), in Brussels on March 1998; it was agreed to define tar as “hydrocarbons with molecular weight higher than benzene”; this definition was considered along this research work [81].

The first global approach to the study and characterisation of tars from thermal processing of solid waste was carried out by Elliot and collaborators in 1986 [82], using capillary gas chromatography coupled to mass spectrometry techniques. Elliot et al, correlated the formation of oxygenated tar at low temperature with the deoxygenated tars formed at higher temperatures. Tar evolution and composition has been studied during the gasification process according to the gasification temperature, residence time, gasification medium, and equivalence ratio (ER). However most of the studies have centred their attention on the effects of the temperature on tar composition. For example, Phuphuakrat et al [83], reported that an increase in the ER and high

temperature enhanced tar cracking reactions during the gasification of dry sewage sludge, using a fixed bed reaction system. In general the overall yield of PAHs has been found to increase as process temperature and gas residence times are also increased during the thermochemical processing of solid waste [84]. Williams and Besler [85], reported that the formation of PAH were influenced by both the process temperature and the residence time during the pyrolysis of diverse waste materials. They stated that the aliphatic tar fraction was reduced and the aromatic fraction increased when the pyrolysis temperature was increased.

When a solid fuel is exposed to elevated temperatures, thermal cracking takes place breaking the molecular bonds of the organic material and generating two phases. The first one is a gas phase formed by the smallest molecules and the larger molecules generate the primary tars. Primary tar reacts to generate secondary tars then, the formation of tertiary tars results from the increase of process temperature, and finally the condensed tertiary tars appear at higher temperatures around 800 °C and 900 °C. The pathway starts with the formation of small molecules until the formation of larger molecules and, depends to some extent on the process temperature. The formation pathway can be exemplified in Figure 2.3-1 [76, 86].

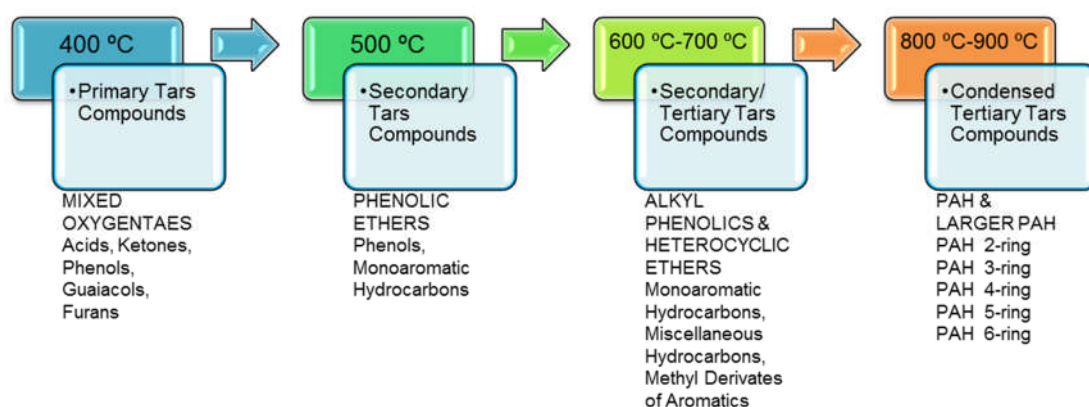


Figure 2.3-1. Pathway of tar formation during increased gasification temperature

According to van Paasen [87], primary tars are characterised by cellulose, hemicelluloses and lignin derived products, i.e. the main components of organic

fraction of solid waste. Secondary tars are characterised by phenolics and alkenes, and are products from the conversion of primary tars. The alkyl tertiary products include methyl derivatives of aromatics such as styrene and xylene; and finally, the condensed tertiary tars are polyaromatic hydrocarbons (PAH) without substituents.

The development of tar decomposition mechanisms is useful to understand the conversion of aromatic hydrocarbons, a pathway showing this mechanism in the presence of hydrogen and steam has been proposed by Jess et al [88], and is shown in Figure 2.3-2.

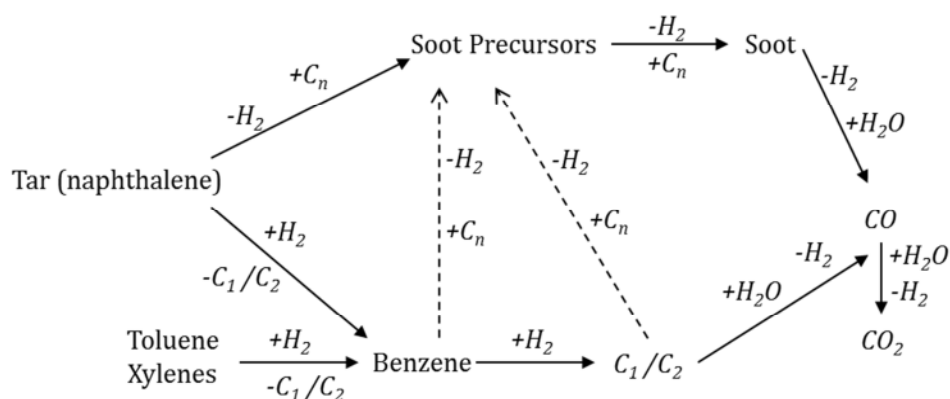


Figure 2.3-2. Proposed pathway for thermal conversion of tar aromatic compounds

In Figure 2.3-2, the main soot precursors are pyrene and fluoranthene, formed through polymerization and condensation reactions. Other cracking products such as indene, indane, dihydronaphthalene and toluene are formed through hydrogenation reactions, and are formed in a limited extent [88].

The formation of PAH's during the thermal decomposition of carbon based feedstock, is attributed to reactions of the Diels-Alder and deoxygenation type [85]. For example tertiary tars can be formed as a result of the (4+2)cycloaddition; according to Diels-Alder a conjugated diene and a dienophile (e.g., an alkene) react together resulting in the formation of substituted cyclohexanes [77, 89]. In Figure 2.3-3 is presented the Diels-Alder mechanism followed by the dehydrogenation reaction for the formation of benzene Figure 2.3-3(a), and PAH formation of naphthalene Figure 2.3-3(b) [90].

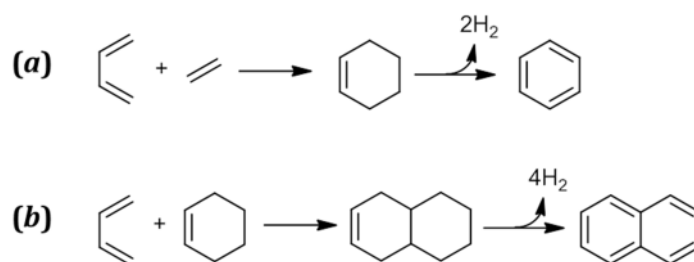


Figure 2.3-3. Diels-Alder and subsequent dehydrogenation reaction for the formation of benzene (a) and naphthalene (b)

Regarding the oxygen-containing compounds, two different thermal decomposition routes have been proposed for phenol [91]. The first one includes the isomerization of phenol, to 2,4-cyclohexadienone followed by endothermic decarbonylation to produce cyclopentadiene (C_5H_6) and CO (Figure 2.3-4a). The second thermal route is radical fragmentation to produce hydrogen atoms and phenoxy radicals (Figure 2.3-4b). Both pathways for the thermal decomposition of phenol are presented in Figure 2.3-4 [91].

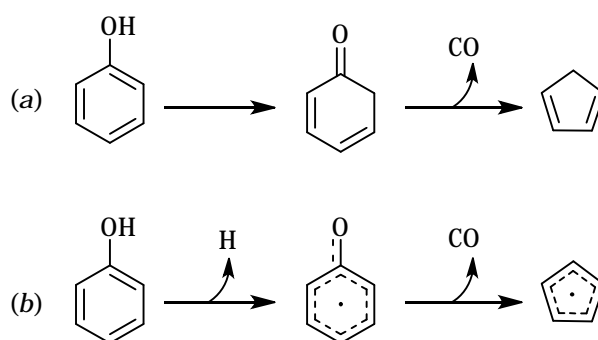


Figure 2.3-4. Phenol cracking reactions pathways for cyclopentadiene formation

Kinoshita et al [92], reported that during the gasification of sawdust at temperatures around 800 °C the formation of aromatic species such as naphthalene and phenanthrene was favoured; whereas the destruction of these compounds can be achieved at process temperatures above 850 °C. Additionally Yu et al [93], reported that an increase in the gasification temperature from 700 to 900 °C, promoted a reduction of about 40% in the tar yield. It was also observed that the total amount of oxygen containing compounds, and 1-2 ring aromatic compounds were reduced, however the amount of 3-4 ring aromatic compounds was increased.

Based on the molecular weight of the different compounds contained in tars, different authors have classified tar compounds into five groups [75, 94-96]. This classification is shown in Table 2.3-1.

Table 2.3-1. Classification of tar compounds

Group	Type	Examples
Class 1	Undetectable by GC method	Solid fragments
Class 2	Heterocyclic Aromatics (High solubility in water)	Phenol, pyridine, cresol, quinoline
Class 3	Aromatics (1 Ring)	Ethylbenzene, xylene, styrene
Class 4	Light polyaromatic hydrocarbons (PAH compounds with 2-3 rings)	Indene, biphenyl, naphthalene, acenaphthylene, fluorene, phenantrene, anthracene
Class 5	Heavy polyaromatic hydrocarbons (PAH compounds ≥ 4 rings)	Fluoranthene, pyrene, chrysene, benzofluoranthene, benzopyrene, perylene, coronene

Considering the previous tar classification, it has been reported that an increase in the process temperature has a positive effect on the decomposition of tar Class 1 and 2, whereas concentrations of tar Class 3 and 5 tend to increase as the temperature increases [94]. Also it has been reported by van Paasen and Kiel [87], that tar compounds such as alkyl-substituted PAH can shift to polyaromatic hydrocarbons by increasing the gasification temperature from 750 °C to 950 °C.

The temperature at which the tar condensation begins is referred as to tar dew point, and can be calculated for individual tar compounds using the Equation 2.3-1 [97].

$$22400 \frac{C}{M} \frac{T}{273} \frac{1}{p_{sv}(T)} = 1 \quad \text{Equation 2.3-1}$$

From Equation 2.3-1, C refer to as the compound concentration given in g/Nm³, M is the molecular weight, T is the absolute temperature, and $p_{sv}(T)$ is the saturated vapour pressure at the temperature T . The total tar dew point can be therefore calculated by taking the sum of the dew points of each individual tar compound, assuming that tar vapours behave as ideal gases. In order to prevent

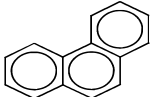
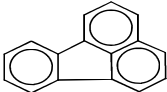
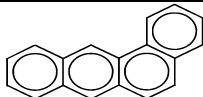
downstream tar associated problems, and to facilitate the tar dew point calculation the ECN in joint with Michell Instruments developed a device capable to measure the tar dew point [97].

The tar composition also has influence over the overall gas dew point. For example has been reported that tar having 4 or more aromatic rings can raise the gas dew point from 120 °C to temperatures above 200 °C [98]. It has been also reported that for gasification temperatures below 750 °C the generated tar contains low molecular weight compounds but more heterogeneous atoms. Whereas at higher temperatures larger molecules are generated, decreasing the reactivity of tar and increasing the tar dew point [99].

Some authors have reported a correlation between the raw materials properties and tar composition. For example Pinto et al [100], analysed the effect of different plastics waste in relation to the pyrolysis products yield. They reported that the presence of specific plastic materials has a large effect, for example an increase in the presence of polyethylene (PE) in the feedstock promoted an increase in the alkane content, whereas a higher amount of polystyrene (PS) led to a higher aromatic content in the final liquid product. Pyrolysis oils are known to contain polycyclic aromatic hydrocarbons (PAH) and oxygenated compounds. Also Desbène et al [101], worked in the characterisation of oils from biomass slow pyrolysis, they found that the main aromatic compounds include alkylated naphthalenes, biphenyls, fluorene, anthracene, pyrene and benzofluorene.

The characterization of the tar is important to get a better idea about the variety of compounds present as well as their concentration, also has been reported in the literature that some of the polyaromatic hydrocarbons (PAHs) found in tar samples might present some carcinogenic characteristics. An example of polyaromatic hydrocarbons and their carcinogenicity is shown in Table 2.3-2 [102].

Table 2.3-2. Examples of PAH compounds and associated carcinogenicities

Compound	Carcinogenicity
 Naphthalene	
 Acenaphthene	Non-carcinogen
 Anthracene	
 Phenanthrene	
 Fluoranthene	Weak carcinogen
 Pyrene	Non-carcinogen
 Benz[a]anthracene	Carcinogen

Depending on the main components of the raw material used for the pyrolysis and/or gasification process, the tar formation routes are different. According to Qin and collaborators [103], most of the aromatic compounds present in tar are derived from lignin, therefore a mechanism schematic was derived from the lignin air-steam gasification. The formation of different compounds with temperature increase is presented in Figure 2.3-5 [103].

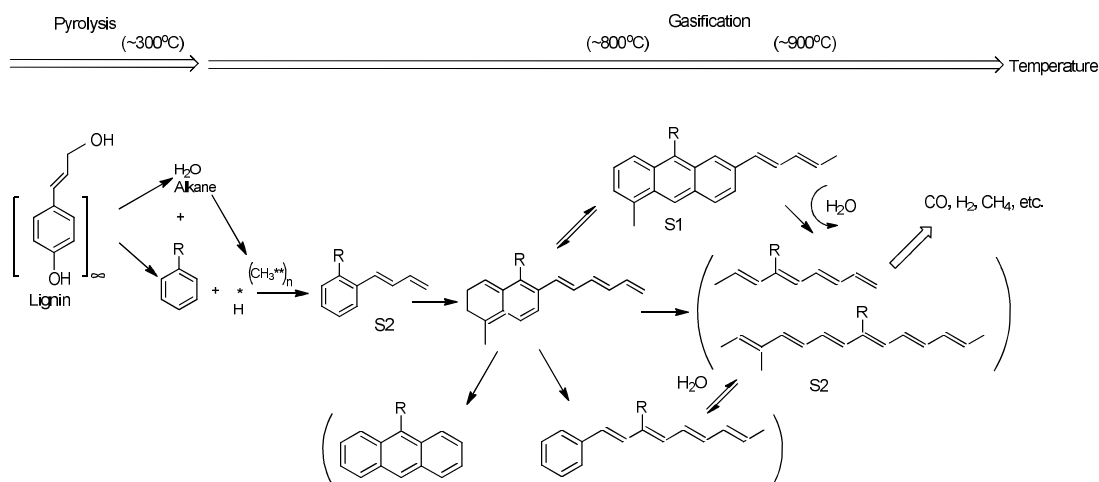


Figure 2.3-5. Schematic of tar formation from lignin air-steam gasification

From Figure 2.3-5 it can be observed that tar undergoes through a cracking and polymerization cycle. The final structure is determined not only by the initial raw material but also from the thermodynamic process itself. S2 represents single-ring aromatic compounds formed as intermediates, if more H free radicals were present in the S2 formation step, the aliphatic chain might be stabilised, enhancing gas formation. Therefore the amount of hydrogen free radicals might determine the molecular weight of the tar compounds. S2 compounds further promote the formation of larger molecular weight (MW) compounds. S1 represents 3-ring aromatic compounds with a side-chain, and is formed through parallel reactions; whereas S2 might also result from other intermediaries reacting with water. The cracking reaction from S1 to S2 takes place when the temperature is increased, and also water steam is present.

2.3.1 Syngas tar requirements

The formation and presence of tar in the produced gas or syngas, not only influences its quality but also reduces the overall process yield. The general syngas requirements have been addressed previously in Section 2.2.1., however the tar concentrations and requirements are even more specific. Initially the elevated operational temperatures in turbines, allow most of the tars contained in the syngas to remain in the gaseous phase, however condensation might arise downstream of the process. Once the temperature is reduced in pipelines and other process equipment such as economizers and air-preheaters, tar starts to

condense resulting in fouling and blocking [50, 104]. Therefore syngas aimed for power generation must meet certain criteria in this regard. For example for further use in internal combustion engines the tar concentration limit in syngas is 100mg/Nm³; whereas for gas turbines the tar limit is 5mg/Nm³. Tar and particles requirements for both systems are presented in Table 2.3-3 [76, 104-106].

Table 2.3-3. Syngas requirements for Internal Combustion engines (ICEs) and Gas Turbines (GTs)

Parameter	Units	ICEs	GTs
Particles	mg/Nm ³	<50	<30
Tar		<100	<5

To facilitate syngas transportation the syngas is sometimes compressed, however if the tar content is particularly high, it will deposit in the equipment [105]. Normally the tar limit concentration in the syngas for compressors is 500mg/Nm³, which is about 5 times higher than the one required for internal combustion engines (Table 2.3-3).

2.3.2 Alternatives for tar removal and tar reduction

So far different techniques have been assessed in order to reduce tar formation during the gasification process. For example, novel techniques such as pulse corona discharge in the flue gas have been studied. However high energetic requirements (~400J/L) are reported for tar removal using this method, reducing its economic viability to be considered as an alternative technique [107].

To a large extent two different approaches for tar removal have been investigated in the literature, the first refers to treatments inside the gasifier (known as primary methods), and the second is hot gas cleaning after the gasifier (known as secondary methods). Primary methods include all the measures taken in the gasification to avoid tar formation, for example the design and operation of the gasifier itself. Ideally a very efficient primary method should totally avoid the need of a secondary method. However the

analysis of primary methods is not within the scope of the present work. On the other hand secondary methods include thermally or catalytic tar cracking, or the use of mechanical methods such as cyclones, baffles filters, ceramic/fabric filters, scrubbers, rotating particle, electrostatic precipitators, etc. Any of these chemical or physical treatments are carried out downstream of the gasifier. The use of mechanical devices for hot gas cleaning is not an economically viable alternative as it involves modifications in the facility itself. Although some of these devices have been demonstrated to be effective for gas cleaning, the trend to reduce tar formation is focused on *in situ* treatments as they eliminate the requirement of downstream cleaning systems or devices. The increase of the process temperature and/or residence time was one of the most common methods tested in the past. However, there is current interest in the use of catalysts during the catalytic steam reforming process as it results in a suitable alternative to improve the quality, composition and calorific value of the final gas. In addition, catalysts can modify the hydrogen to carbon monoxide ratio of the syngas by promoting steam reforming, water gas shift, and tar cracking reactions. Additionally the required process temperature is reduced, resulting in an economic and technologically viable alternative to reduce tar formation in the final syngas [9, 50, 59, 64, 77, 80, 86, 108, 109].

2.4 Pyrolysis-catalytic steam reforming process

Abu El-Rub [80], reported two ways to use catalytic reforming, the first option suggests mixing the selected catalyst with the feedstock to achieve a catalytic gasification *in situ*. Whereas the second option suggests that the produced gases are passed through a catalyst bed normally placed in a secondary reactor, the catalyst might be recovered and further recycled making this a more economically viable alternative. This can be achieved by combining pyrolysis and gasification processes, following a series of sequential thermochemical decomposition steps. The first thermochemical step or pyrolysis might be carried out at temperatures around 300 °C up to 700 °C; during this stage the solid waste will be thermally decomposed resulting in the formation of tar, char and volatiles fractions. After this the gaseous fraction is passed directly to the

gasification stage where the gas compounds will further react according to the following catalytic steam reforming reactions (Table 2.4-1) [64].

Table 2.4-1. Catalytic steam reforming reactions

Reaction	Enthalpy ΔH (MJ/kmol)
$C+CO_2 \rightarrow 2CO$	+162.4
$C+H_2O \rightarrow CO+H_2$	+131.3
$CH_4+H_2O \rightarrow CO+3H_2$	+206.3
$Tar+n_1H_2O \rightarrow n_2CO_2+n_3H_2$	$\Delta H_{298K} > 0$

2.4.1 Tar cracking reactions in the catalytic process

The main tar decomposition reactions take place at different stages of the gasification process including cracking, dry and steam reforming. These reactions are included in Table 2.4-2, where C_nH_x represents tar and C_mH_y refers to hydrocarbons [96].

Table 2.4-2. Tar decomposition reactions

Chemical Reaction	Reaction Type
$pC_nH_x \rightarrow qC_mH_y + rH_2$	Cracking
$C_nH_x + nH_2O \rightarrow (n + x/2)H_2 + nCO$	Steam Reforming
$C_nH_x + nCO_2 \rightarrow (x/2)H_2 + 2nCO$	Dry Reforming
$C_nH_x \rightarrow nC + (x/2)H_2$	Carbon formation

C_nH_x : represents tar; C_mH_y : represents hydrocarbon with smaller carbon number than C_nH_x

The general mechanism of catalytic tar reforming starts with the adsorption of hydrocarbons onto the metal site of the catalyst, promoting metal-catalysed dehydrogenation reactions. Then the water steam is also dissociatively adsorbed onto the catalysts' support resulting in hydroxylation of the catalysts' surface. Depending on the process temperature, OH^- radicals migrate to the metal's sites; thus the intermediate fragments of hydrocarbons are oxidized and surface carbons are transformed to CO and H_2 [94].

The kinetics of tar catalytic cracking has been addressed by Dou et al [110], including tar components, primary and secondary gas products and coke. This model is presented in Figure 2.4-1 [110].

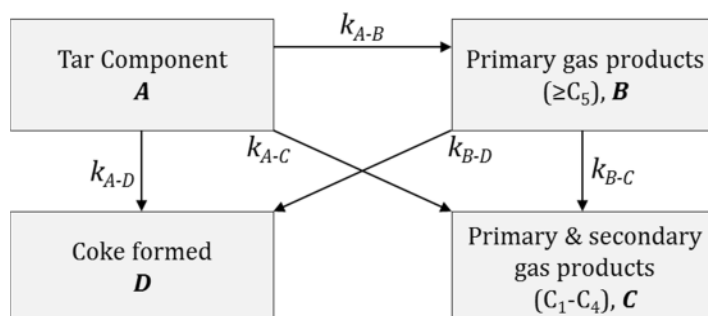


Figure 2.4-1. Kinetic model for cracking of a tar component

From Figure 2.4-1, Dou et al [110] developed the kinetic expressions for the tar compound cracking, considering product yields, deactivation function (catalyst) and the kinetic constant.

In a deeper analysis of the tar behaviour some authors have also studied the thermodynamic properties of tar evaluating the tar heat enthalpy and entropy [96, 111]. According to kinetic and thermodynamic considerations, at gasification temperatures under 800 °C tar cannot be eliminated, including heavy and light hydrocarbons during the reforming stage, resulting in all the tar associated problems [60].

2.4.2 Tar model compounds

To get a better understanding of the decomposition mechanism of tars during thermal processes, and even more when interacting with catalysts during the catalytic steam reforming process, different tar model compounds have been studied and tested under different gasification conditions. For example Elliot et al. [112, 113], studied the catalytic gasification of *p*-cresol in the presence of nickel alumina supported catalyst at 350 °C, to produce methane and CO₂. Additionally other authors have used tar model compounds such as naphthalene [114], methylnaphthalene [79], phenol [115], etc., to study the different decomposition reactions.

In the case of naphthalene, this 2-ring aromatic compound can undergo thermal decomposition to break aromatic rings through naphthoxy formation and further decomposition into indenyl. During the thermal decomposition byproducts such as naphthalene-dione and phthalicanhydride are formed towards an oxidation mechanism of intermediates, following the scheme proposed by Nair et al, shown in Figure 2.4-2 [107, 116].

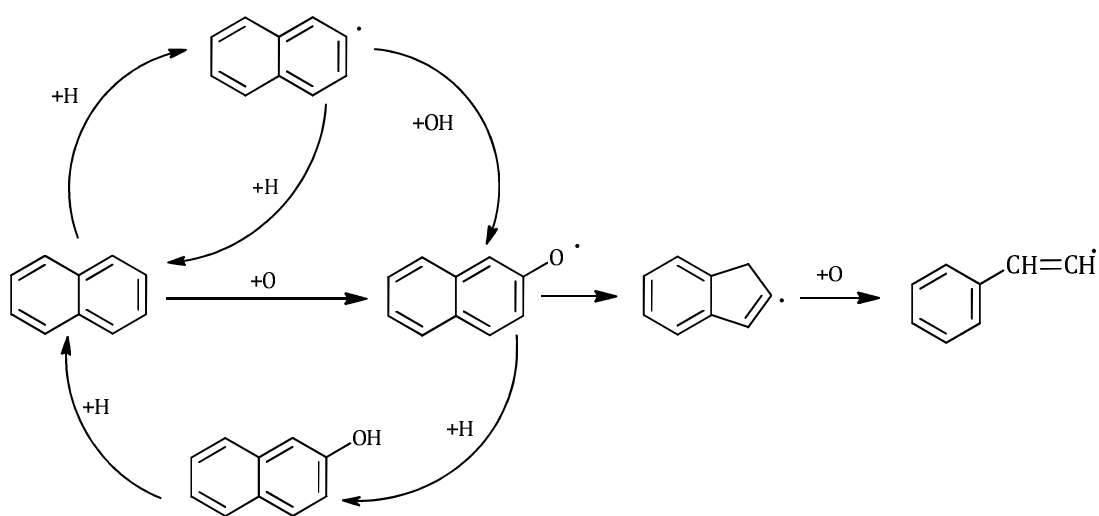


Figure 2.4-2. Naphthalene decomposition mechanism

Jess [88] reported the kinetics involved in the thermal decomposition of aromatic hydrocarbons in the presence of hydrogen and steam, using naphthalene, toluene and benzene as tar model compounds. The conversion yields and the kinetic parameters involved, together with the reaction sequence for methane formation from toluene with hydrogen to benzene were also addressed. Świerczyński et al [109], used toluene as tar model compound to study the tar removal efficiency of Ni/olivine catalyst in a fixed bed reaction system, a high steam reforming of toluene and low carbon formation were achieved.

Güell et al [115] also proposed the decomposition mechanism of oxygen-containing compounds such as phenol during the steam gasification process. This mechanism is shown in Figure 2.4-3 [115].

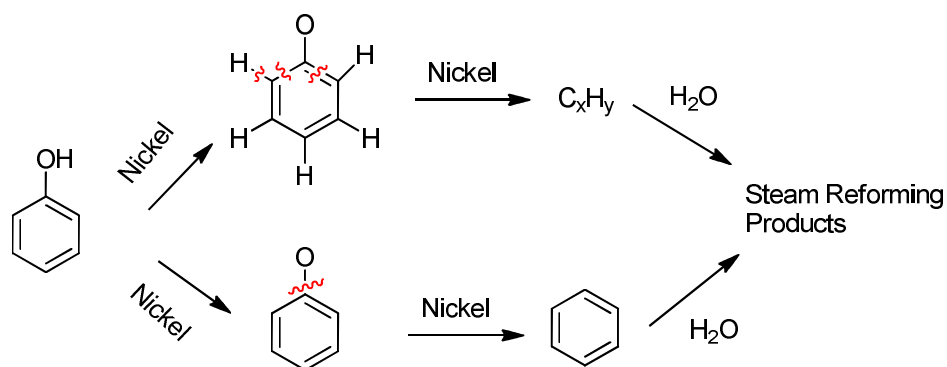


Figure 2.4-3. Steam gasification of phenol over nickel based catalysts

From Figure 2.4-3, it is observed that nickel and steam promote the breakage of the phenol main aromatic ring or the separation of the radical OH, resulting in the formation of lighter aromatic compounds or single ring compounds (benzene) together with other steam reforming products. Similar interactions occur for other polyaromatic and oxygenated tar compounds when subjected to the catalytic steam reforming process using nickel-based catalysts.

2.4.3 Tar sampling methods

There are two ways reported in the literature for tar sampling namely on-line and off-line methods. A general approach to both tar sampling methods is given in Figure 2.4-4 [117].

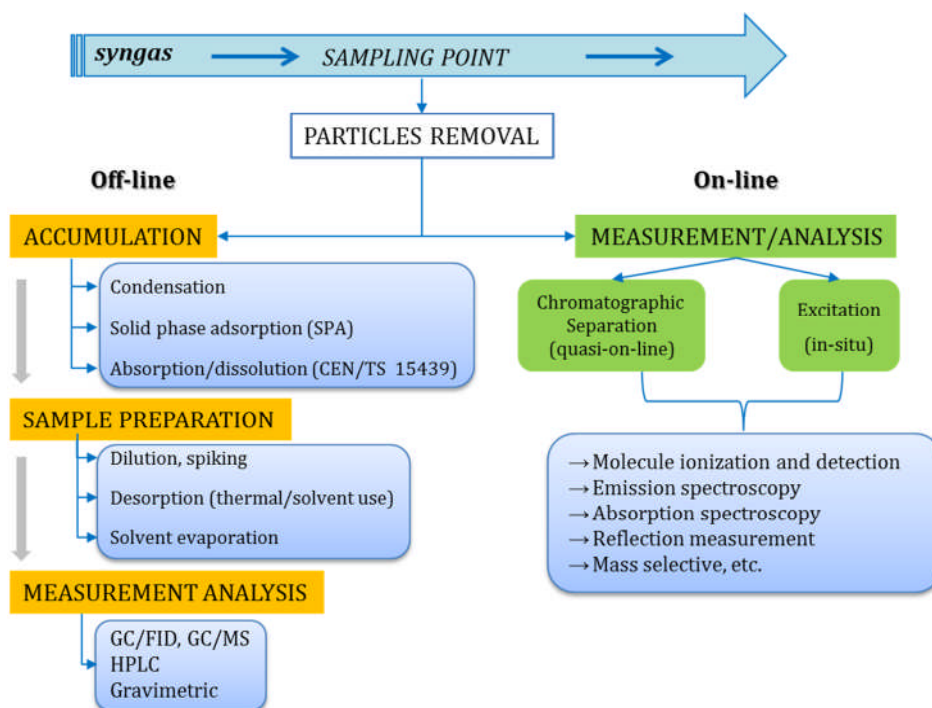


Figure 2.4-4. Diagram of tar sampling and analysis

On-line tar sampling methods include flame ionization detection, photo spectroscopy (laser spectroscopy), light emitting diode spectroscopy, induced laser systems (fluorescence signals), etc. [118, 119]. Unfortunately the use of this technology is associated with elevated costs reducing its further application compared with other simple and efficient off-line methods.

Off-line tar sampling methods are based on the accumulation for example using cold trapping, then the sample preparation stage where a solvent extraction might be used, and finally the analysis that might be focused on weight determination. The selection of each step is based according to the analysis approach and tar analysis requirements. The most common off-line methods are the European Tar Protocol (CEN/TS 15439) and the Solid Phase Adsorption method (SPA) [119-121]. The European tar protocol is based on the absorption of organic contaminants (tars) in an organic solvent. The procedure for tar measurement consists of a gas preconditioning, a filter, tar collection and volume metering. Also different impinger bottles filled with a specific organic solvent are used. Qualitative and quantitative information can be obtained from this method [119].

The Solid Phase Adsorption method (SPA) for tar measurement, is also commonly used and it was firstly reported by Brage et al [122], to monitoring the evolution of tars from biomass gasification. It was initially developed by the Royal Institute of Technology (KTH) to quantify tar compounds with molecular weight ranging from 78 (benzene) to 300 (coronene) [122, 123], and has the advantage of considerable reduction in the sampling time from 60 minutes to up to 1 minute, the sampling is simple and repeatable, also the samples can be well preserved. A schematic of the conventional SPA tar sampling system is presented in Figure 2.4-5 [119, 122].

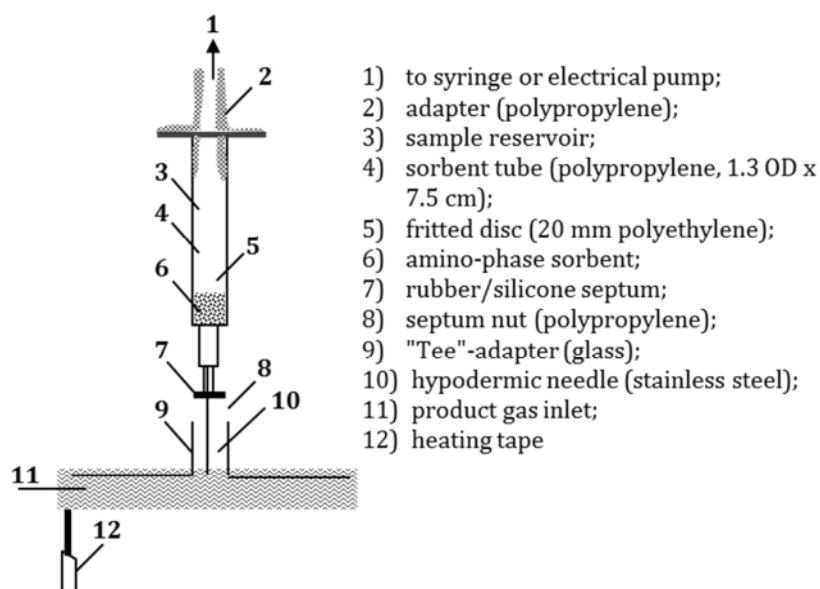


Figure 2.4-5. General diagram SPA tar sampling method in the produced gas

The principle of the SPA method is based on trapping vapour-phase tar compounds in silica bonded amino-phase vapour trap, at room temperature where molecules with polar nature will be retained by the vapour trap active sites. An aliquot of the produced gas is drawn into the sorbent tube, followed by elution and further addition of two internal standards, using a elutropic series to get a neutral aromatic fraction and a polar phenolic fraction [122]. Modifications to the traditional SPA sampling method have been reported in the literature. For example Osipovs [124], used two different solid-phase sorbents for benzene sampling in tar from biomass gasification, and also Masson et al

[125] reported the use of a coupled SPA with a thermal desorption and gas chromatography analyses systems.

2.4.4 Types of catalysts used for catalytic steam reforming

When selecting catalysts, these must meet certain criteria to have an appropriate performance, this means the catalysts must be effective for tar removal; must be resistant to deactivation due to carbon fouling and sintering; should be easily regenerated; should possess good mechanical properties, and should be inexpensive [94, 126]. In the literature it has been reported that several types of catalysts have the potential for cracking tars from the produced gas stream [127-130]. Therefore different catalysts have been evaluated during catalytic steam gasification processes in terms of their nature, precursor, preparation method, activity and selectivity for tar reduction, economic feasibility, attrition resistance, and also about their influence over the quality of the final syngas [50, 131].

Some non-metallic catalysts that have been extensively studied for tar conversion are calcined dolomites or limestone [132-134]. Dolomites have been used as they represent an economic alternative and are widely available. However their resistance to attrition is very low, with low yields for tar conversion. Additionally dolomites require high process temperatures of around 850 °C to be effective for tar removal. Considering the advantages of this material, some other authors such as Corella et al [135], use a guard bed of dolomite followed by a bed of nickel based catalysts to reduce tar content. Other non-metallic material that has been widely used is olivine (magnesium-iron silicate) that has demonstrated a similar activity for tar conversion as dolomite, under similar operation conditions [136, 137]. An advantage of dolomites over olivine is that dolomite has high attrition resistance, therefore it has been used as the primary catalysts and not as a guard bed [109].

Regarding metal-based catalysts, catalysts based on nickel have been largely studied to reduce tar formation, mainly in hydrocracking and biomass

gasification processes [79, 138-146]. Nickel based catalysts are preferred over other metals such as Rh, Ru, or Pt as nickel is widely available, represents a more economic option, and has been proved to be very effective for tar removal during the gasification process [79, 80, 147]. Therefore this work will be focused on the use of nickel based catalysts during the pyrolysis-gasification process.

2.4.5 Nickel-based catalysts during the pyrolysis-gasification process

Nickel has been widely used as the metal base for different catalysts, however one of the main limitations of using nickel as catalysts is the deactivation, which it is mainly originated by carbon deposition on the catalyst surface, sintering and/or metal oxidation [109, 148, 149]. Therefore nickel catalysts are combined with oxide supports such as silica oxide (SiO_2) or alumina (Al_2O_3) oxide in order to improve the catalysts properties, increasing their activity and efficiency when used in the gasification process [150]. Diverse oxide supports have been tested for their efficiency on improving nickel catalysts properties such as surface area and pore distribution; hence a better catalyst performance can be achieved. To get an idea about the oxide supports diversity and other metals that can be used together with nickel based catalysts (metal promoters), in Figure 2.4-6 are presented the most common oxide supports used from the year 1928 up to 2007, based in a detailed report done by Zhang et al [148].

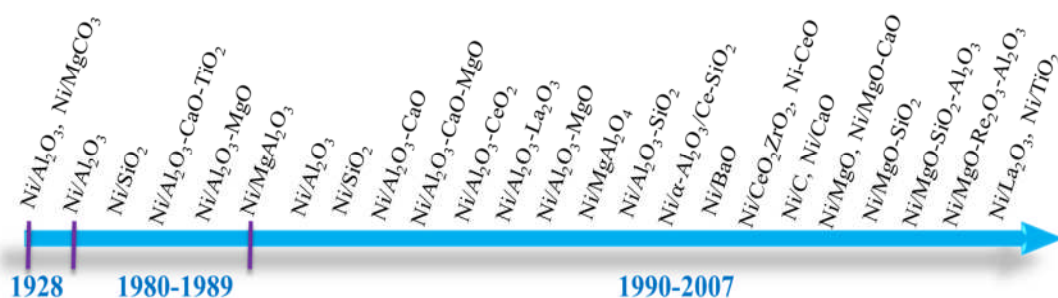


Figure 2.4-6. Timeline of the most common nickel based catalysts synthesized since 1928

A wide variety of synthesis methods have also been reported for catalysts preparation, namely: sol-gel, impregnation, precipitation, co-precipitation,

homogeneous precipitation, phase separation, etc. The preparation of catalysts plays a major role in relation to the final catalysts characteristics and involves a sequence of several complex steps. Each one of these sequential steps has an effect over the final catalyst properties such as surface, area, metal dispersion, pore size, etc. In general the main characteristics sought are good stability, activity and selectivity [151]. A better understanding of both the process and catalysts requirements is required before the selection of the synthesis method.

The catalysts properties and consequently their performance and activity are highly influenced by every step of the preparation method and by the quality of the raw materials. The selection of the preparation method depends on the desired physical and chemical properties of the catalysts together with the desired final composition [152]. Additionally a careful selection of the support is relevant as it can provide a high degree of thermo stability and a high dispersion potential to the catalyst, the effect of diverse supports and their influence over catalyst properties have been also reported in the literature [152].

Gil et al [153], analysed the effect of the preparation method and the nature of the support over the catalyst stability and nickel dispersion. The preparation methods used were incipient wetness, ion exchange, and precipitation deposition, and the supports tested were silica (SiO_2), alumina (Al_2O_3) and silica-alumina ($\text{SiO}_2\text{-Al}_2\text{O}_3$). It was found that the metal-support interaction is highly influenced by the preparation method, and it was found a better metallic dispersion and stability for a Ni/ SiO_2 catalyst prepared by precipitation-deposition method.

The most popular preparation methods for nickel based catalysts are the sol-gel and impregnation methods. The sol-gel method consists of the sequential steps of a solution and further gel formation, colloidal dispersion or organic precursors can be used as raw materials [154]. Whereas the impregnated catalysts are normally obtained from the impregnation of preformed supports and an active phase [152]. For example, Efika et al [155], used a sol-gel method for the synthesis of three nickel based catalysts: NiO/ Al_2O_3 , NiO/ $\text{CeO}_2/\text{Al}_2\text{O}_3$,

NiO/SiO₂ to be later tested in the catalytic steam reforming of biomass waste. Good results were obtained using the sol-gel method for both catalysts properties such as high surface area ($\sim 760\text{m}^2\text{ g}^{-1}$), and for catalyst activity towards hydrogen production ($\sim 44\text{vol.}\%$). Also Wu et al [156], worked in the preparation of nano-Ni/SiO₂ catalysts for hydrogen production during the steam reforming of ethanol. The catalysts was also prepared through a sol-gel method finding good nickel dispersion and high surface area ($>700\text{ m}^2\text{ g}^{-1}$). Other nickel based catalysts (Ni/SiO₂, Ni/Al₂O₃,) have been reported in the literature to be prepared using sol-gel methods with promising results in terms of both catalytic activity and catalysts properties [157, 158]. Other authors such as Tomiyama et al [159], have reported the use of modified sol-gel methods for the preparation of Ni/SiO₂ catalysts. They used a homogeneous precipitation of nickel hydroxide in a wet silica gel (HPG); the catalyst characteristics were compared with those obtained using a conventional incipient wet impregnation process. Larger nickel metal surface area and higher thermal stability were found for the HPG catalyst when compared with the impregnated catalyst; which was attributed to the concurrence of dissolution-reprecipitation of silica and further entrapment of nickel species into the support network.

Additionally other catalysts such as iron-based catalysts have been also used with good performance in terms of hydrogen production. Ermakova et al [160], synthesized Ni/SiO₂ and Fe/SiO₂ catalysts through a heterophase sol-gel method and compared their performance for hydrogen production during methane decomposition. They reported that the effect of silicates over iron is not well understood, although might inhibit and/or promote the process of carbon formation [160]. However Rao et al [161], previously reported a spectroscopic analysis carried out on iron-based catalysts identifying the formation of small particles of ferric oxide, and also the formation of an iron(II) silicate layer that might affect the rate of reduction of the catalysts as tend to partly cover the iron crystallites.

2.4.5.1 Addition of metal promoters to nickel-based catalysts

Diverse metals such as cerium (Ce), magnesium (Mg) and aluminium (Al) have been added to nickel based catalysts in order to improve the catalysts properties, and catalyst performance (Figure 2.4-6).

For example Cai et al [162], reported that the addition of Ce to Ni/Al₂O₃ catalysts resulted in an improvement in the catalyst performance towards hydrogen production in the auto thermal reforming of methane. Also they stated that the prevention of undesirable phases such as NiAl₂O₄ facilitated the formation of NiO crystals; therefore the active sites were increased resulting in higher catalyst activity. Hu and Lu [163], also reported the modification of Ni/Al₂O₃ catalysts by the addition of a range of metals (Li, Na, K, Mg, Fe, Co, Zn, Zr, La, Ce). They reported that the addition of Ce to Al₂O₃ catalysts promoted the methanation reaction, whereas the addition of Mg might increase the number of Ni metallic sites by promoting the reduction of NiO. However a negative effect in relation to catalytic activity was reported when adding Mg as metal promoter. The addition of Mg to Ni/Al₂O₃ catalysts has also been reported by Wu and Williams [164], for hydrogen production during the pyrolysis-gasification of polypropylene. They stated that the addition of Mg significantly increased the amount of reacted steam improving the performance of the catalyst in relation to coke formation. However no positive effects in relation to the hydrogen production were attained.

Wang et al [165], studied the catalytic steam reforming of methane with carbon dioxide, using Ni/Al₂O₃ catalysts promoted with Mg, Ce and other metals. Higher activities were observed for the catalysts promoted with Ce when compared with the catalyst promoted using Mg, additionally the latter also showed a significant deactivation. When compared with the original Ni/Al₂O₃ catalysts, the promoted catalysts suppressed carbon deposition. Also Zapata et al [166], added Ca, K and Ce metals to Ni/SiO₂ catalysts in order to increase the catalyst activity for methane decomposition. The results suggested that the addition of Ce prevents sintering of nickel particles and helped to maintain the distribution

between the silica and cerium oxide also promoting a homogeneous distribution of deposited carbon.

2.4.6 Summary of nickel-based catalysts

A wide range of catalysts have been used and tested during thermochemical decomposition processes such as methane reforming and solid waste gasification. However some of them have become more popular for example Ni/SiO₂ and Ni/Al₂O₃ catalysts due to the higher performance attained either respect to the gas composition or to the improvement in the catalysts properties. The properties and efficiency using other metals such as iron with similar oxide supports (Fe/SiO₂) has been also discussed. The most relevant information regarding the catalysts described above is given next.

1) Ni/SiO₂: for this type of catalyst common nickel loadings range between 10 and 20wt%, with positive effects over catalysts properties such as resistance to deactivation[167] and good catalyst activity towards hydrogen production [168]. The preferred synthesis method for this catalyst is sol-gel, as this results in a good metal dispersion over the silica lattice [157, 169]; although the effects of impregnation or deposition-precipitation have been also studied in the past for metal-support interactions [170]. Ni/SiO₂ catalysts prepared by sol-gel have demonstrated better activity for hydrogen production in processes such as steam reforming of ethanol [156], and pyrolysis/gasification of solid wastes [168], than those prepared by different methods.

2) Ni/Al₂O₃: normal metal loadings used for this catalyst are between 10-20wt.%, also different preparation methods have been reported in the literature. The coprecipitation method and a nickel loading of 15wt.% were reported suitable for hydrogen production during the reforming of ethanol, when compared with the impregnation method [171]. A stable activity for Ni/Al₂O₃ catalyst correlated with the resistance to deactivation due to coke deposition or morphological modifications, during the gasification of biomass was observed when compared with olivine and dolomite performances [141].

3) Fe/SiO₂: the performance of high loaded Fe/SiO₂ catalysts has been evaluated and compared with Ni/SiO₂ catalysts. Different preparation methods have been reported for these catalysts such as (heterophase) sol-gel [160] and impregnation [172]. The metal-support interaction for this catalyst has not been well understood, however good performance and activity have been reported in the literature.

References

1. McDougall, F.R., P.R. White, M. Franke, and P. Hindle, *Integrated solid waste management: a life cycle inventory*. 2nd ed. 2007, GB: Wiley-Blackwell.
2. Tammemagi, H., *The Waste Crisis. Landfills, Incinerators, and the Search for a Sustainable Future*. 1999, New York, USA: Oxford University Press, Inc.
3. Williams, P.T., *Waste Treatment and Disposal*. 2nd ed, ed. J.W.S. Ltd. 2005, Chichester, UK.
4. Christensen, T.H., *Solid Waste Technology and Management*. Solid Waste Technology & Management. Vol. 1. 2010, Malaysia: John Wiley & Sons, Ltd. i-xiv.
5. OECD, *OECD Factbook 2013*: OECD Publishing.
6. Hoornweg, D. and P. Bhada-Tata (2012) *What a waste : a global review of solid waste management*. Urban development series 1.
7. Reddy, P.J., *Municipal Solid Waste Management: Processing - Energy Recovery - Global Examples*. 2011: CRC Press.
8. Tchobanoglous, G., Theisen, H., Vigil, S. A., *Integrated Solid Waste Management: Engineering principles and management issues*. Civil Engineering Series, ed. M.H.I. Editions. 1993, New York.
9. Li, J., J. Liu, S. Liao, X. Zhou, and R. Yan, *Syn-Gas Production from Catalytic Steam Gasification of Municipal Solid Wastes in a Combined Fixed Bed Reactor*, in *International Conference on Intelligent System Design and Engineering Application (ISDEA)*. 2010: Changsha. p. 530-534.
10. Worrell, W.A. and P.A. Vesilind, *Solid Waste Engineering*. 2nd ed. 2002, Stamford, USA: CENGAGE Learning.
11. Dalai, A.K., N. Batta, I. Eswaramoorthi, and G.J. Schoenau, *Gasification of refuse derived fuel in a fixed bed reactor for syngas production*. Waste Management, 2009. 29(1): p. 252-258.
12. Young, G.C., *Municipal solid waste to energy conversion processes : economic, technical, and renewable comparisons*. 2010: John Wiley & Sons Inc. 398.
13. de Souza-Santos, M.L., *Solid Fuels Combustion and Gasification: Modeling, Simulation, and Equipment Operations*. 2nd ed, ed. L. Faulkner. 2010, Boca Raton, Florida. USA.: CRC Press Taylor & Francis Group.
14. Brandt, P., E. Larsen, and U. Henriksen, *High tar reduction in a two-stage gasifier*. Energy & Fuels, 2000. 14(4): p. 816-819.
15. McLaren, R.G. and C.J. Smith, *Issues in the disposal of industrial and urban wastes*, in *Contaminants and the Soil Environment in the Australasia-Pacific Region*, R. Naidu, et al., Editors. 1996, Springer Netherlands. p. 183-212.
16. Cozzani, V., L. Petarca, and L. Tognotti, *Devolatilization and Pyrolysis of Refuse Derived Fuels - Characterization and Kinetic Modeling by a Thermogravimetric and Calorimetric Approach*. Fuel, 1995. 74(6): p. 903-912.

17. Jackson, D.V., *Advances in thermal treatment and RDF*. Resources and Conservation, 1987. 14: p. 1-14.
18. Buah, W.K., A.M. Cunliffe, and P.T. Williams, *Characterization of Products from the Pyrolysis of Municipal Solid Waste*. Process Safety and Environmental Protection, 2007. 85(5): p. 450-457.
19. Buekens, A., *Refuse-Derived Fuel*, in *Incineration Technologies*, A.S.a. Technology, Editor. 2013, Springer New York. p. 71-76.
20. Gupta, B. and P. Shepherd, *Data Summary of Municipal Solid Waste Management Alternatives*. 1992, National Renewable Energy Laboratory, NREL: Menlo Park, California.
21. Wagner, L., *Waste-to-Energy (WtE) technology*. 2007, Mora Associates.
22. Merritt, J.A., *Waste-to-Energy: Comprehensive Recycling's Best Chance?*, in *Recovering Energy from Waste. Various Aspects.*, V.I. Grover, V.K. Grover, and W. Hogland, Editors. 2002, Science Publishers: Enfield, New Hampshire USA. p. 15-20.
23. Piao, G., Aono, S., Kondoh, M., Yamazaki, R., Mori, S., *Combustion test of refuse derived fuel in a fluidized bed*. Waste Management, 2000. 20: p. 443-447.
24. Lin, K.-S., H.P. Wang, S.H. Liu, N.-B. Chang, Y.J. Huang, and H.C. Wang, *Pyrolysis kinetics of refuse-derived fuel*. Fuel Processing Technology, 1999. 60(2): p. 103-110.
25. Cozzani, V., C. Nicolella, L. Petarca, M. Rovatti, and L. Tognotti, *A Fundamental-Study on Conventional Pyrolysis of a Refuse-Derived Fuel*. Industrial & Engineering Chemistry Research, 1995. 34(6): p. 2006-2020.
26. Dou, B., S. Park, S. Lim, T.-U. Yu, and J. Hwang, *Pyrolysis Characteristics of Refuse Derived Fuel in a Pilot-Scale Unit*. Energy & Fuels, 2007. 21(6): p. 3730-3734.
27. Chang, Y.-H., W.C. Chen, and N.-B. Chang, *Comparative evaluation of RDF and MSW incineration*. Journal of Hazardous Materials, 1998. 58(1-3): p. 33-45.
28. Sørum, L., M.G. Grønli, and J.E. Hustad, *Pyrolysis characteristics and kinetics of municipal solid wastes*. Fuel, 2001. 80(9): p. 1217-1227.
29. Williams, P.T. and S. Besler, *The influence of temperature and heating rate on the slow pyrolysis of biomass*. Renewable Energy, 1996. 7(3): p. 233-250.
30. Miles, T.R., *Biomass Preparation for Thermochemical Conversion (Keynote paper)*, in *Thermochemical Processing of Biomass*, A.V. Bridgewater, Editor. 1984, Butterworths: Birmingham, UK. p. 69-90.
31. McKendry, P., *Energy production from biomass (part 2): conversion technologies*. Bioresource Technology, 2002. 83(1): p. 47-54.
32. Malkow, T., *Novel and innovative pyrolysis and gasification technologies for energy efficient and environmentally sound MSW disposal*. Waste Management, 2004. 24(1): p. 53-79.
33. Arena, U., *Process and technological aspects of municipal solid waste gasification. A review*. Waste Management, 2012. 32(4): p. 625-639.
34. Landreth, R.E. and P.A. Rebers, *Municipal solid wastes: problems and solutions*. 1997, Boca Raton: CRC Press.
35. Yaman, S., *Pyrolysis of biomass to produce fuels and chemical feedstocks*. Energy Conversion and Management, 2004. 45(5): p. 651-671.

36. Williams, P.T. and P.A. Horne, *Polycyclic aromatic hydrocarbons in catalytically upgraded biomass pyrolysis oils*. Journal of the Institute of Energy, 1996. 69(481): p. 176-191.
37. Dipple, A., *Polycyclic Aromatic Hydrocarbon Carcinogenesis*, in *Polycyclic Hydrocarbons and Carcinogenesis*. 1985, American Chemical Society. p. 1-17.
38. Astrup, T. and B. Bilitewski, *Pyrolysis and gasification*, in *Solid Waste Technology and Management*, T.H. Christensen, Editor. 2010, John Wiley & Sons, Ltd: Malaysia. p. 502-512.
39. Basu, P., *Pyrolysis and Torrefaction*, in *Biomass Gasification Design Handbook*. 2010, Academic Press: Boston. p. 65-96.
40. Scott, D.S., P. Majerski, J. Piskorz, and D. Radlein, *A second look at fast pyrolysis of biomass--the RTI process*. Journal of Analytical and Applied Pyrolysis, 1999. 51(1-2): p. 23-37.
41. Peters, B., *Thermal Conversion of Solid Fuels*. Developments in heat transfer ser. 2003, Southampton, B., UK: WIT Press.
42. Galvagno, S., S. Casu, T. Casabianca, A. Calabrese, and G. Cornacchia, *Pyrolysis process for the treatment of scrap tyres: preliminary experimental results*. Waste Management, 2002. 22(8): p. 917-923.
43. Bilitewski, B., G. Härdtle, K. Marek, A. Weissbach, and H. Boeddicker, *Waste Management*. 1997, Berlin, Germany: Springer.
44. Horne, P.A. and P.T. Williams, *Influence of temperature on the products from the flash pyrolysis of biomass*. Fuel, 1996. 75(9): p. 1051-1059.
45. Rampling, T.W. and T.J. Hickey, *The laboratory characterisation of Refuse Derived Fuel*. 1988, Warren Spring Laboratory.
46. Williams, E.A. and P.T. Williams, *Analysis of products derived from the fast pyrolysis of plastic waste*. Journal of Analytical and Applied Pyrolysis, 1997. 40-41(0): p. 347-363.
47. Bridgwater, A.V. and S.A. Bridge, *A Review of Biomass Pyrolysis and Pyrolysis Technologies*, in *Biomass Pyrolysis Liquids Upgrading and Utilisation*, A.V. Bridgwater and G. Gassi, Editors. 1991, Elsevier Applied Science: Essex, England.
48. Garcia, A.N., A. Marcilla, and R. Font, *Thermogravimetric Kinetic-Study of the Pyrolysis of Municipal Solid-Waste*. Thermochimica Acta, 1995. 254: p. 277-304.
49. Skoulou, V., A. Zabaniotou, G. Stavropoulos, and G. Sakelaropoulos, *Syngas production from olive tree cuttings and olive kernels in a downdraft fixed-bed gasifier*. International Journal of Hydrogen Energy, 2008. 33(4): p. 1185-1194.
50. Devi, L., K.J. Ptasinski, and F.J.J.G. Janssen, *A review of the primary measures for tar elimination in biomass gasification processes*. Biomass and Bioenergy, 2003. 24(2): p. 125-140.
51. Suksankraisorn, K., S. Patumsawad, and B. Fungtammasan, *Combustion studies of high moisture content waste in a fluidised bed*. Waste Management, 2003. 23(5): p. 433-439.
52. Green, D.W., Perry, R. H., *Perry's Chemical Engineers' Handbook*. 8th ed. 2008: McGraw-Hill.
53. Knoef, H.A.M., *BTG Biomass Gasification*, in *BTG Biomass Technology Group 2008*: Enschede, The Netherlands. p. 14.

54. Phillips, J. *Different Types of Gasifiers and Their Integration with Gas Turbines*. 2010 [cited 2011 13th, June]; Available from: <http://www.netl.doe.gov/technologies/coalpower/turbines/refshelf/handbook/1.2.1.pdf>.
55. Rajvanshi, A.K., *Biomass Gasification*, in *Alternative Energy in Agriculture*, D.Y. Goswami, Editor. 1986, CRC Press: Maharashtra, India. p. 83-102.
56. Warnecke, R., *Gasification of biomass: comparison of fixed bed and fluidized bed gasifier*. *Biomass & Bioenergy*, 2000. 18: p. 489-497.
57. Hotchkiss, R., *Coal gasification technologies*. Proceedings of the Institution of Mechanical Engineers. Part A: Power and Energy, 2003. 217: p. 27-34.
58. Belgiorno, V., G. De Feo, C. Della Rocca, and R.M.A. Napoli, *Energy from gasification of solid wastes*. *Waste Management*, 2003. 23(1): p. 1-15.
59. Bridgwater, A.V., *Catalysis in thermal biomass conversion*. *Applied Catalysis A: General*, 1994. 116: p. 5-47.
60. De Filippis, P., C. Borgianni, M. Paolucci, and F. Pochetti, *Prediction of syngas quality for two-stage gasification of selected waste feedstocks*. *Waste Management*, 2004. 24(6): p. 633-639.
61. Choudhary, T.V. and V.R. Choudhary, *Energy-efficient syngas production through, catalytic oxy-methane reforming reactions*. *Angewandte Chemie-International Edition*, 2008. 47(10): p. 1828-1847.
62. Rostrup-Nielsen, J.R., *Syngas in perspective*. *Catalysis Today*, 2002. 71(3-4): p. 243-247.
63. Edwards, P.P., V.L. Kuznetsov, and W.I.F. David, *Hydrogen energy*. *Philosophical Transactions of the Royal Society A: Mathematical, Physical and Engineering Sciences*, 2007. 365(1853): p. 1043-1056.
64. He, M., Z. Hu, B. Xiao, J. Li, X. Guo, S. Luo, F. Yang, Y. Feng, G. Yang, and S. Liu, *Hydrogen-rich gas from catalytic steam gasification of municipal solid waste (MSW): Influence of catalyst and temperature on yield and product composition*. *International Journal of Hydrogen Energy*, 2009. 34(1): p. 195-203.
65. Sperling, D. and J.S. Cannon, *The Hydrogen Energy Transition: Moving Toward the Post Petroleum Age in Transportation*. 2004, San Diego, California, USA: Elsevier Academic Press.
66. Zuttel, A., A. Borgschulte, and L. Schlapbach, *Hydrogen as a Future Energy Carrier*. 2008, Germany: John Wiley & Sons.
67. Jain, I.P., C. Lal, and A. Jain, *Hydrogen storage in Mg: A most promising material*. *International Journal of Hydrogen Energy*, 2010. 35(10): p. 5133-5144.
68. Jain, I.P., *Hydrogen the fuel for 21st century*. *International Journal of Hydrogen Energy*, 2009. 34(17): p. 7368-7378.
69. Freedonia Group, T., *World Hydrogen to 2016 - Industry Market Research, Market Share, Market Size, Sales, Demand Forecast, Market Leaders, Company Profiles, Industry Trends*. 2012, The Freedonia Group: Cleveland, USA. p. 345.
70. Stoll, R.E. and F. von Linde, *Hydrogen - what are the costs?* *Hydrocarbon Processing*, 2000: p. 42-46.
71. Balat, M., *Possible methods for hydrogen production*. *Energy Sources, Part A: Recovery, Utilization and Environmental Effects*, 2009. 31(1): p. 39-50.

72. Borgschulte, A., A. Zuttel, and U. Wittstadt, *Hydrogen production, in Hydrogen as a Future Energy Carrier*. 2008, John Wiley & Sons: Germany. p. 149-164.
73. US Energy Information Administration, *International Energy Outlook*. 2013: Washington, DC.
74. Klerke, A., C.H. Christensen, J.K. Norskov, and T. Vegge, *Ammonia for hydrogen storage: challenges and opportunities*. Journal of Materials Chemistry, 2008. 18(20): p. 2304-2310.
75. Reichenbach de Sousa, L.C., *Gasification of Wood, Urban Wastewood (Altholz) and other Wastes in a Fluidised Bed Reactor*, in *Technical Sciences*. 2001, Swiss Federal Institute of Technology Zürich: Zürich. p. 286.
76. Milne, T.A., Evans, R. J., *Biomass Gasifier "Tars": Their Nature, Formation and Conversion*. 1998, National Renewable Energy Laboratory.
77. Blanco, P.H., C. Wu, J.A. Onwudili, and P.T. Williams, *Characterization of Tar from the Pyrolysis/Gasification of Refuse Derived Fuel: Influence of Process Parameters and Catalysis*. Energy & Fuels, 2012. 26(4): p. 2107-2115.
78. Pober, K.W. and H.F. Bauer, *The nature of pyrolytic oil from municipal solid waste*, in *Fuels from waste*. 1977, Academic Press, Inc.: New York. p. 73-85.
79. Dou, B.L., J.S. Gao, X.Z. Sha, and S.W. Baek, *Catalytic cracking of tar component from high-temperature fuel gas*. Applied Thermal Engineering, 2003. 23(17): p. 2229-2239.
80. Abu El-Rub, Z., Bramer, E. A., Brem, G. , *Review of Catalysts for Tar Elimination in Biomass Gasification Processes*. Industrial and Engineering Chemistry Research, 2004. 43(22): p. 6911-6919.
81. Maniatis, K. and A.A.C.M. Beenackers, *Tar Protocols. IEA Bioenergy Gasification Task*. Biomass and Bioenergy, 2000. 18(1): p. 1-4.
82. Elliott, D.C., *Analysis and comparison of biomass pyrolysis/gasification condensates: Final report*, in *Other Information: Portions of this document are illegible in microfiche products. Original copy available until stock is exhausted*. 1986. p. Medium: ED; Size: Pages: 100.
83. Phuphuakrat, T., N. Nipattummakul, T. Namioka, S. Kerdsuwan, and K. Yoshikawa, *Characterization of tar content in the syngas produced in a downdraft type fixed bed gasification system from dried sewage sludge*. Fuel, 2010. 89(9): p. 2278-2284.
84. Britt, P.F., A.C. Buchanan, and C.V. Owens, *Mechanistic investigation into the formation of polycyclic aromatic hydrocarbons from the pyrolysis of terpenes*. Abstracts of Papers of the American Chemical Society, 2004. 228: p. U680-U680.
85. Williams, P.T. and S. Besler, *Polycyclic aromatic hydrocarbons in waste derived pyrolytic oils*. Journal of Analytical and Applied Pyrolysis, 1994. 30(1): p. 17-33.
86. Basu, P., *Combustion and Gasification in Fluidized Beds*, ed. T.F. Group. 2005, Florida, USA: CRC Press. 473.
87. van Paasen, S.V.B., Kiel, J. H. A., *Tar formation in a fluidised-bed gasifier, in Primary measures to reduce tar formation in fluidised-bed biomass gasification*, E. Biomass, Editor. 2004, ECN. p. 58.

88. Jess, A., *Mechanisms and kinetics of thermal reactions of aromatic hydrocarbons from pyrolysis of solid fuels*. Fuel, 1996. 75(12): p. 1441-1448.
89. Wolfesberger, U., Aigner, I., Hofbauer, H., *Tar Content and Composition in Producer Gas of Fluidized Bed Gasification of wood - Influence of Temperature and Pressure*. Environmental Progress & Sustainable Energy, 2009. 28(3): p. 8.
90. Andrea, U., R. Luca, F. Marco, and F. Piero, *Microwave pyrolysis of polymeric materials*. Microwave Heating. 2011.
91. Scheer, A.M., C. Mukarakate, D.J. Robichaud, M.R. Nimlos, H.H. Carstensen, and G.B. Ellison, *Unimolecular thermal decomposition of phenol and d(5)-phenol: Direct observation of cyclopentadiene formation via cyclohexadienone*. Journal of Chemical Physics, 2012. 136(4).
92. Kinoshita, C.M., Y. Wang, and J. Zhou, *Tar formation under different biomass gasification conditions*. Journal of Analytical and Applied Pyrolysis, 1994. 29(2): p. 169-181.
93. Yu, Q.Z., C. Brage, G.X. Chen, and K. Sjostrom, *Temperature impact on the formation of tar from biomass pyrolysis in a free-fall reactor*. Journal of Analytical and Applied Pyrolysis, 1997. 40-1: p. 481-489.
94. Han, J. and H. Kim, *The reduction and control technology of tar during biomass gasification/pyrolysis: An overview*. Renewable and Sustainable Energy Reviews, 2008. 12(2): p. 397-416.
95. Morf, P., Hasler, P., Nussbaumer, T., *Mechanisms and kinetics of homogeneous secondary reactions of tar from continuous pyrolysis of wood chips*. Fuel, 2002. 81: p. 843-853.
96. Li, C. and K. Suzuki, *Tar property, analysis, reforming mechanism and model for biomass gasification--An overview*. Renewable and Sustainable Energy Reviews, 2009. 13(3): p. 594-604.
97. Rabou, L.P.L.M., R.W.R. Zwart, B.J. Vreugdenhil, and L. Bos, *Tar in Biomass Producer Gas, the Energy research Centre of The Netherlands (ECN) Experience: An Enduring Challenge*. Energy & Fuels, 2009. 23: p. 6189-6198.
98. Visser, H.J.M., Zwart, R.W.R, Könemann, J.W., Geusebroek, M., *RDF-gasification Part 1: Characterizing the use of RDF as Fuel and Solving the Tar Problem by an in-depth Laboratory Study*, in *2nd International Symposium on Energy from Biomass and Waste*. 2008, Energy Research Centre of the Netherlands (ECN): Venice.
99. ECN-Biomass. *Thersites the ECN tar dew point site*. 2009 June 2009 [cited 23/05/2011]; Available from: <http://www.thersites.nl/tardewpoint.aspx>.
100. Pinto, F., P. Costa, I. Gulyurtlu, and I. Cabrita, *Pyrolysis of plastic wastes. 1. Effect of plastic waste composition on product yield*. Journal of Analytical and Applied Pyrolysis, 1999. 51(1-2): p. 39-55.
101. Desbène, P.L., M. Essayegh, B. Desmazières, and J.J. Basselier, *Contribution to the Analytical Study of Biomass Pyrolysis Oils*, in *Biomass Pyrolysis Liquids Upgrading and Utilization*, A.V. Bridgwater and G. Grassi, Editors. 1991, Springer Netherlands. p. 155-176.
102. Cerniglia, C.E., *Biodegradation of polycyclic aromatic hydrocarbons*. Current Opinion in Biotechnology, 1993. 4(3): p. 331-338.

103. Qin, Y.-H., J. Feng, and W.-Y. Li, *Formation of tar and its characterization during air-steam gasification of sawdust in a fluidized bed reactor*. *Fuel*, 2010. 89(7): p. 1344-1347.
104. Gautam, G., S. Adhikari, S. Thangalazhy-Gopakumar, C. Brodbeck, S. Bhavnani, and S. Taylor, *Tar Analysis in Syngas Derived from Pellitized Biomass in a Commercial Stratified Downdraft Gasifier*. *BioResources*, 2011. 6(4): p. 4652-4661.
105. Spliethoff, H., *Status of biomass gasification for power production*. *IFRF Combustion Journal*, 2001: p. 25.
106. Hasler, P. and T. Nussbaumer, *Sampling and analysis of particles and tars from biomass gasifiers*. *Biomass and Bioenergy*, 2000. 18(1): p. 61-66.
107. Nair, S.A., K. Yan, A.J.M. Pemen, E.J.M. van Heesch, K.J. Ptasinski, and A.A.H. Drinkenburg, *Tar removal from biomass-derived fuel gas by pulsed corona discharges. A chemical kinetic study*. *Industrial & Engineering Chemistry Research*, 2004. 43(7): p. 1649-1658.
108. Luo, S., B. Xiao, X. Guo, Z. Hu, S. Liu, and M. He, *Hydrogen-rich gas from catalytic steam gasification of biomass in a fixed bed reactor: Influence of particle size on gasification performance*. *International Journal of Hydrogen Energy*, 2009. 34(3): p. 1260-1264.
109. Swierczynski, D., S. Libs, C. Courson, and A. Kiennemann, *Steam reforming of tar from a biomass gasification process over Ni/olivine catalyst using toluene as a model compound*. *Applied Catalysis B: Environmental*, 2007. 74(3-4): p. 211-222.
110. Dou, B., W. Pan, J. Ren, B. Chen, J. Hwang, and T.-U. Yu, *Removal of tar component over cracking catalysts from high temperature fuel gas*. *Energy Conversion and Management*, 2008. 49(8): p. 2247-2253.
111. Eisermann, W., P. Johnson, and W.L. Conger, *Estimating Thermodynamic Properties of Coal, Char, Tar and Ash*. *Fuel Processing Technology*, 1980. 3(1): p. 39-53.
112. Elliott, D.C., L.J. Sealock, and E.G. Baker, *Chemical processing in high-pressure aqueous environments. 2. Development of catalysts for gasification*. *Industrial & Engineering Chemistry Research*, 1993. 32(8): p. 1542-1548.
113. Elliott, D.C., G.G. Neuenschwander, T.R. Hart, R.S. Butner, A.H. Zacher, M.H. Engelhard, J.S. Young, and D.E. McCready, *Chemical Processing in High-Pressure Aqueous Environments. 7. Process Development for Catalytic Gasification of Wet Biomass Feedstocks*. *Industrial & Engineering Chemistry Research*, 2004. 43(9): p. 1999-2004.
114. Devi, L., K.J. Ptasinski, and F.J.J.G. Janssen, *Pretreated olivine as tar removal catalyst for biomass gasifiers: investigation using naphthalene as model biomass tar*. *Fuel Processing Technology*, 2005. 86(6): p. 707-730.
115. Matas Güell, B., I.V. Babich, L. Lefferts, and K. Seshan, *Steam reforming of phenol over Ni-based catalysts – A comparative study*. *Applied Catalysis B: Environmental*, 2011. 106(3-4): p. 280-286.
116. Nair, S.A., A.J.M. Pemen, K. Yan, E.J.M. van Heesch, K.J. Ptasinski, and A.A.H. Drinkenburg, *Chemical processes in tar removal from biomass derived fuel gas by pulsed corona discharges*. *Plasma Chemistry and Plasma Processing*, 2003. 23(4): p. 665-680.

117. Knoef, H.A.M., *Handbook Biomass Gasification Second Edition*. 2nd ed ed. 2012: btg biomass technology group. 500.
118. Baumhagl, C. and S. Karellas, *Tar analysis from biomass gasification by means of online fluorescence spectroscopy*. *Optics and Lasers in Engineering*, 2011. 49(7): p. 885-891.
119. Svensson, M.A., *Sampling and Analysis of tars by means of photo ionization detection and solid phase micro extraction*, in *Chemical Engineering and Technology*. 2013, KTH Royal Institute of Technology: Stockholm, Sweden.
120. Simell, P., P. Ståhlberg, E. Kurkela, J. Albrecht, S. Deutsch, and K. Sjöström, *Provisional protocol for the sampling and analysis of tar and particulates in the gas from large-scale biomass gasifiers. Version 1998*. *Biomass and Bioenergy*, 2000. 18(1): p. 19-38.
121. Neeft, J.P.A., H.A.M. Knoef, U. Zielke, K. Sjoström, P. Hasler, and P.A. Simell, *Guideline for sampling and analysis of tar and particles in biomass producer gases in Tar Protocol*. 1999, ECN ERK-CT1999-2002: Petten, Netherlands.
122. Brage, C.Y., Q.; Chen, G.; Rosen, C.; Liliedahl, T.Sjoström, K., *Application of solid-phase adsorption (SPA) to monitoring evolution of biomass tar from different types of gasifiers*, in *Biomass gasification and pyrolysis: state of the art and future prospects Conference, Biomass gasification and pyrolysis: state of the art and future prospects*. 1997, CPL Press. p. 218-227.
123. Brage, C. and K. Sjöström, *Separation of phenols and aromatic hydrocarbons from biomass tar using aminopropylsilane normal-phase liquid chromatography*. *Journal of Chromatography A*, 1991. 538(2): p. 303-310.
124. Osipovs, S., *Sampling of benzene in tar matrices from biomass gasification using two different solid-phase sorbents*. *Analytical and Bioanalytical Chemistry*, 2008. 391(4): p. 1409-1417.
125. Masson, E., S. Ravel, S. Thiery, and A. Dufour, *Tar analysis by Solid Phase Adsorption (SPA) associated with Thermal Desorption and Gas Chromatography analysis*, in *19th European Biomass Conference*. 2011: Berlin.
126. Sutton, D., B. Kelleher, and J.R.H. Ross, *Review of literature on catalysts for biomass gasification*. *Fuel Processing Technology*, 2001. 73(3): p. 155-173.
127. Simell, P.A., Hepola, J. O., Krause, A. O., *Effects of gasification gas components on tare ammonia decomposition over hot gas cleanup catalysts*. *Fuel*, 1997. 76(12): p. 1117-1127.
128. Delgado, J., Aznar, M. P., Corella, J., *Calcined Dolomite, Magnesite, and Calcite for Cleaning Hot Gas from a Fluidized Bed Biomass Gasifier with Steam: Life and Usefulness*. *Industrial and Engineering Chemistry Research*, 1996. 35: p. 3637-3643.
129. Leppälahti, J., P. Simell, and E. Kurkela, *Catalytic conversion of nitrogen compounds in gasification gas*. *Fuel Processing Technology*, 1991. 29(1-2): p. 43-56.

130. Baker, E.G., Mudge, L. K., Brown, M. D., *Steam Gasification of Biomass with Nickel Secondary Catalysts*. Industrial and Engineering Chemistry Research, 1987. 26(7): p. 1335-1339.
131. Park, H.J., S.H. Park, J.M. Sohn, J. Park, J.-K. Jeon, S.-S. Kim, and Y.-K. Park, *Steam reforming of biomass gasification tar using benzene as a model compound over various Ni supported metal oxide catalysts*. Bioresource Technology, 2010. 101(1, Supplement): p. S101-S103.
132. Simell, P.A., J.K. Leppalahti, and J.B.S. Bredenberg, *Catalytic Purification of Tarry Fuel Gas with Carbonate Rocks and Ferrous Materials*. Fuel, 1992. 71(2): p. 211-218.
133. Narvaez, I., A. Orío, M.P. Aznar, and J. Corella, *Biomass gasification with air in an atmospheric bubbling fluidized bed. Effect of six operational variables on the quality of the produced raw gas*. Industrial & Engineering Chemistry Research, 1996. 35(7): p. 2110-2120.
134. Taralas, G., *Catalytic steam cracking of n-heptane with special reference to the effect of calcined dolomite*. Industrial & Engineering Chemistry Research, 1996. 35(7): p. 2121-2126.
135. Corella, J., A. Orío, and J.M. Toledo, *Biomass gasification with air in a fluidized bed: Exhaustive tar elimination with commercial steam reforming catalysts*. Energy & Fuels, 1999. 13(3): p. 702-709.
136. Rapagnà, S., N. Jand, A. Kiennemann, and P.U. Foscolo, *Steam-gasification of biomass in a fluidised-bed of olivine particles*. Biomass and Bioenergy, 2000. 19(3): p. 187-197.
137. Devi, L., K.J. Ptasinski, F.J.J.G. Janssen, S.V.B. van Paasen, P.C.A. Bergman, and J.H.A. Kiel, *Catalytic decomposition of biomass tars: use of dolomite and untreated olivine*. Renewable Energy, 2005. 30(4): p. 565-587.
138. Courson, C., E. Makaga, C. Petit, and A. Kiennemann, *Development of Ni catalysts for gas production from biomass gasification. Reactivity in steam- and dry-reforming*. Catalysis Today, 2000. 63(2-4): p. 427-437.
139. Caballero, M.A., Corella, J. Aznar, M. P. Gil, J., *Biomass gasification with air in fluidized bed. Hot gas cleanup with selected commercial and full-size nickel-based catalysts*. Industrial and Engineering Chemistry Research, 2000. 39(5): p. 1143-1154.
140. Coll, R., J. Salvadó, X. Farriol, and D. Montané, *Steam reforming model compounds of biomass gasification tars: conversion at different operating conditions and tendency towards coke formation*. Fuel Processing Technology, 2001. 74(1): p. 19-31.
141. Miccio, F., B. Piriou, G. Ruoppolo, and R. Chirone, *Biomass gasification in a catalytic fluidized reactor with beds of different materials*. Chemical Engineering Journal, 2009. 154(1-3): p. 369-374.
142. Gebhard, S.C., D. Wang, R.P. Overend, and M.A. Paisley, *Catalytic conditioning of synthesis gas produced by biomass gasification*. Biomass and Bioenergy, 1994. 7(1-6): p. 307-313.
143. Kinoshita, C.M., Wang, Y., Zhou, J., *Effect of Reformer Conditions on Catalytic Reforming of Biomass-Gasification Tars*. Industrial and Engineering Chemistry Research, 1995. 34: p. 2949-2954.
144. Simell, P.A. and J.B.s. Bredenberg, *Catalytic purification of tarry fuel gas*. Fuel, 1990. 69(10): p. 1219-1225.

145. Aznar, M.P., M.A. Caballero, J. Gil, J.A. Martín, and J. Corella, *Commercial Steam Reforming Catalysts To Improve Biomass Gasification with Steam-Oxygen Mixtures. 2. Catalytic Tar Removal*. Industrial & Engineering Chemistry Research, 1998. 37(7): p. 2668-2680.
146. Narvaez, I., Corella, J., Orío, A., *Fresh Tar (from a Biomass Gasifier) Elimination over a Commercial Steam-Reforming Catalyst. Kinetics and Effect of Different Variables of Operation*. Industrial and Engineering Chemistry Research, 1997. 36: p. 317-327.
147. Trimm, D.L., *Coke formation and minimisation during steam reforming reactions*. Catalysis Today, 1997. 37(3): p. 233-238.
148. Zhang, J., *Research and Development of Nickel Based Catalysts for Carbon Dioxide Reforming of Methane*, in *Chemical Engineering*. 2008, University of Saskatchewan: Saskatoon, Saskatchewan. p. 195.
149. Slagtern, Å., U. Olsbye, R. Blom, I.M. Dahl, and H. Fjellvåg, *Characterization of Ni on La modified Al₂O₃ catalysts during CO₂ reforming of methane*. Applied Catalysis A: General, 1997. 165(1-2): p. 379-390.
150. Sutton, D., B. Kelleher, A. Doyle, and J.R.H. Ross, *Investigation of nickel supported catalysts for the upgrading of brown peat derived gasification products*. Bioresource Technology, 2001. 80(2): p. 111-116.
151. Schwarz, J.A., C. Contescu, and A. Contescu, *Methods for Preparation of Catalytic Materials*. Chemical Reviews, 1995. 95(3): p. 477-510.
152. Perego, C. and P. Villa, *Catalyst preparation methods*. Catalysis Today, 1997. 34(3-4): p. 281-305.
153. Gil, A., A. Díaz, L.M. Gandía, and M. Montes, *Influence of the preparation method and the nature of the support on the stability of nickel catalysts*. Applied Catalysis A: General, 1994. 109(2): p. 167-179.
154. Ward, D.A. and E.I. Ko, *Preparing Catalytic Materials by the Sol-Gel Method*. Industrial & Engineering Chemistry Research, 1995. 34(2): p. 421-433.
155. Efika, C.E., C.F. Wu, and P.T. Williams, *Syngas production from pyrolysis-catalytic steam reforming of waste biomass in a continuous screw kiln reactor*. Journal of Analytical and Applied Pyrolysis, 2012. 95: p. 87-94.
156. Wu, C.F. and P.T. Williams, *A Novel Nano-Ni/SiO₂ Catalyst for Hydrogen Production from Steam Reforming of Ethanol*. Environmental Science & Technology, 2010. 44(15): p. 5993-5998.
157. Ermakova, M.A. and D.Y. Ermakov, *High-loaded nickel-silica catalysts for hydrogenation, prepared by sol-gel Route: structure and catalytic behavior*. Applied Catalysis A: General, 2003. 245(2): p. 277-288.
158. Gronchi, P., A. Kaddouri, P. Centola, and R.D. Rosso, *Synthesis of Nickel Supported Catalysts for Hydrogen Production by Sol-Gel Method*. Journal of Sol-Gel Science and Technology, 2003. 26(1-3): p. 843-846.
159. Tomiyama, S., R. Takahashi, S. Sato, T. Sodesawa, and S. Yoshida, *Preparation of Ni/SiO₂ catalyst with high thermal stability for CO₂-reforming of CH₄*. Applied Catalysis A: General, 2003. 241(1-2): p. 349-361.
160. Ermakova, M.A. and D.Y. Ermakov, *Ni/SiO₂ and Fe/SiO₂ catalysts for production of hydrogen and filamentous carbon via methane decomposition*. Catalysis Today, 2002. 77(3): p. 225-235.
161. Rao, K.R.P.M., F.E. Huggins, V. Mahajan, G.P. Huffman, V.U.S. Rao, B.L. Bhatt, D.B. Bukur, B.H. Davis, and R.J. O'Brien, *Mössbauer spectroscopy*

- study of iron-based catalysts used in Fischer-Tropsch synthesis. Topics in Catalysis*, 1995. 2(1-4): p. 71-78.
162. Cai, X., X. Dong, and W. Lin, *Effect of CeO₂ on the catalytic performance of Ni/Al₂O₃ for autothermal reforming of methane*. *Journal of Natural Gas Chemistry*, 2008. 17(1): p. 98-102.
 163. Hu, X. and G. Lu, *Inhibition of methane formation in steam reforming reactions through modification of Ni catalyst and the reactants*. *Green Chemistry*, 2009. 11(5): p. 724-732.
 164. Wu, C. and P.T. Williams, *Investigation of Ni-Al, Ni-Mg-Al and Ni-Cu-Al catalyst for hydrogen production from pyrolysis-gasification of polypropylene*. *Applied Catalysis B: Environmental*, 2009. 90(1-2): p. 147-156.
 165. Wang, S. and G.Q. Lu, *Effects of promoters on catalytic activity and carbon deposition of Ni/ γ -Al₂O₃ catalysts in CO₂ reforming of CH₄*. *Journal of Chemical Technology & Biotechnology*, 2000. 75(7): p. 589-595.
 166. Zapata, B., M.A. Valenzuela, J. Palacios, and E. Torres-Garcia, *Effect of Ca, Ce or K oxide addition on the activity of Ni/SiO₂ catalysts for the methane decomposition reaction*. *International Journal of Hydrogen Energy*, 2010. 35(21): p. 12091-12097.
 167. Aiello, R., J.E. Fiscus, H.-C. zur Loye, and M.D. Amiridis, *Hydrogen production via the direct cracking of methane over Ni/SiO₂: catalyst deactivation and regeneration*. *Applied Catalysis A: General*, 2000. 192(2): p. 227-234.
 168. Blanco, P.H., C. Wu, J.A. Onwudili, and P.T. Williams, *Characterization and evaluation of Ni/SiO₂ catalysts for hydrogen production and tar reduction from catalytic steam pyrolysis-reforming of refuse derived fuel*. *Applied Catalysis B: Environmental*, 2013. 134-135(0): p. 238-250.
 169. Takahashi, R., S. Sato, T. Sodesawa, M. Suzuki, and N. Ichikuni, *Ni/SiO₂ prepared by sol-gel process using citric acid*. *Microporous and Mesoporous Materials*, 2003. 66(2-3): p. 197-208.
 170. Montes, M., C. Penneman de Bosscheyde, B.K. Hodnett, F. Delannay, P. Grange, and B. Delmon, *Influence of metal-support interactions on the dispersion, distribution, reducibility and catalytic activity of Ni/SiO₂ catalysts*. *Applied Catalysis*, 1984. 12(4): p. 309-330.
 171. Akande, A.J., R.O. Idem, and A.K. Dalai, *Synthesis, characterization and performance evaluation of Ni/Al₂O₃ catalysts for reforming of crude ethanol for hydrogen production*. *Applied Catalysis A: General*, 2005. 287(2): p. 159-175.
 172. Cagnoli, M.V., S.G. Marchetti, N.G. Gallegos, A.M. Alvarez, R.C. Mercader, and A.A. Yeramian, *Influence of the Support on the Activity and Selectivity of High dispersion Fe Catalysts in the Fischer-Tropsch Reaction*. *Journal of Catalysis*, 1990. 123(1): p. 21-30.

CHAPTER 3. EXPERIMENTAL METHODOLOGY

3.1 Introduction

This chapter addresses the analytical techniques used to characterise the raw materials, the different catalysts prepared, and products from the pyrolysis/gasification process. The procedures used to carry out the experiments are also described. Additionally the reproducibility of the experimental methodology and analytical techniques used are presented.

3.2 Materials

In this section the characteristics of the raw material used, as well as the synthesis and materials used for the catalysts preparation are described.

3.2.1 Refuse derived fuel (RDF)

Municipal solid waste (MSW) in the form of refuse derived fuel (RDF) was used as raw material during the pyrolysis/gasification process. The original samples in the form of pellets with about 40 mm of length by 20 mm of diameter, were obtained from Byker, a municipal waste treatment plant based in the United Kingdom (UK) (Figure 3.2-1a). To ensure the homogeneity of the material, a certain amount of the RDF was taken, mixed, coned, and quartered repeatedly. Then the sample was further shredded and ground to obtain RDF samples with a particle size of about 1.00mm, as presented in Figure 3.2-1b. The final RDF samples were mainly composed of plastics, paper, board, wood and other textile materials.

3.2.1.1 Elemental Analysis of RDF

The elemental analysis of the RDF sample was carried out using a CE Instrument to determine carbon (C), hydrogen (H), nitrogen (N), and sulphur (S); whereas the oxygen weight fraction (O) was calculated by difference. The results

demonstrated that the RDF sample contained about 44wt.%, 6wt.%, 48wt.%, and 1wt.% of C, H, O, and N respectively. Additionally the proximate analysis was carried out using a thermogravimetric analyser (Schimadzu, Stanton Redcroft 280); about 2mg of RDF were placed in a pan; the sample was heated from room temperature to 125 °C, at a 40 °C min⁻¹ heating rate and 10 minutes dwell time. Then the temperature was increased up to 900 °C with the same heating rate and a further 20 minutes dwell time using nitrogen; after that the gas was switched to air maintaining the temperature at 900 °C for 20 minutes more. The results showed that the RDF sample contained about 7wt.% of moisture, about 15wt.% of ash, around 67wt.% of volatile matter, and about 10wt.% of fixed carbon.

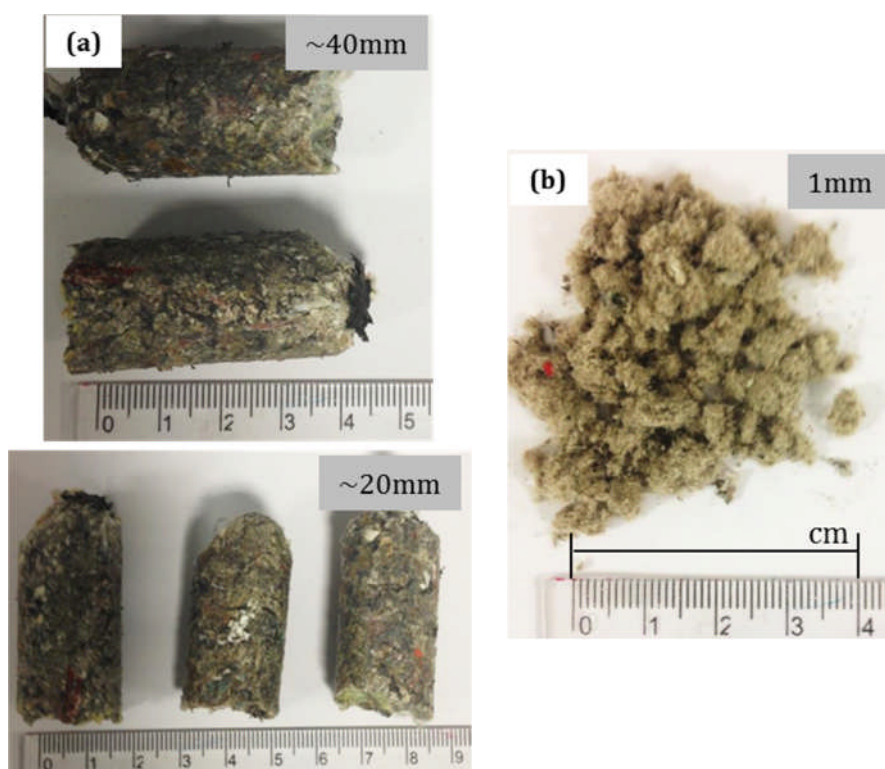


Figure 3.2-1. Appearance of RDF: (a) original pellets, and (b) shredded samples

3.2.1.2 Thermogravimetric Analysis of RDF

Additionally the thermal degradation behaviour of the RDF samples was investigated; this analytical technique is aimed to give information about RDF thermal stability and its fraction of volatile components, details about the weight change of the sample when is heated were obtained. The main

components of a thermogravimetric analyser are a controlled ceramic furnace coupled to a microbalance, and a data recorder [1]. The thermal analysis was carried out using a TGA Schimadzu, Stanton Redcroft 280 analyser; about 10mg of the RDF sample were placed inside of an alumina crucible (1cm diameter and 0.7cm deep), which at the same time was held by a platinum holder that also acted as a thermocouple. A computer system registered the time, temperature, and changes in the weight with the help of the microbalance. For the analysis of thermal decomposition of RDF, the temperature was increased from 25 °C, up to 800 °C with 10 °C min⁻¹ heating rate; and helium flow rate was set as 50 ml min⁻¹. Once the final temperature was achieved, the carrier gas was changed to air to leave the residual ash. The results were displayed as a thermogram showing the weight change against temperature; additionally the first derivative of the TGA thermogram was plotted [2], as shown in Figure 3.2-2.

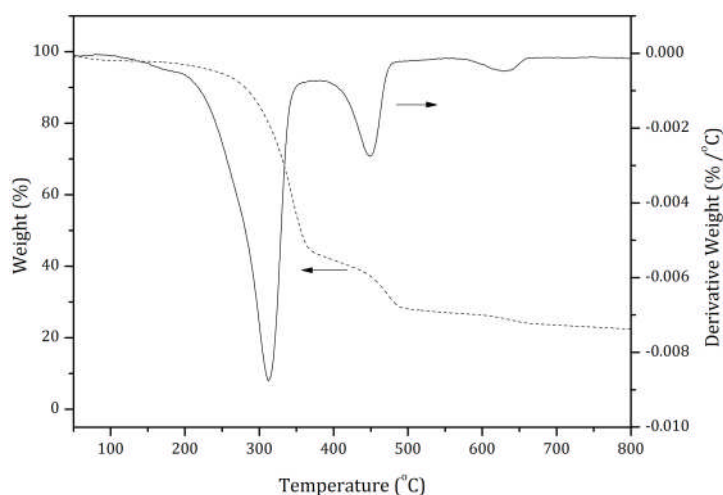


Figure 3.2-2. TGA and DTG thermograms of RDF samples

From the thermogravimetric analysis (Figure 3.2-2), different decomposition stages were identified; the first weight loss before 100 °C was generally associated with water or moisture evaporation. After that it was observed a weight decrease at around 230 °C; some authors have identified this point as the start of the decomposition temperature of the RDF, when some of the volatile compounds start to be released as a result of the temperature increase [3]. From the DTG thermogram also around 300 °C the volatile matter decomposition was observed, followed by higher volatiles released at around

500 °C, and finally after 600 °C the fixed carbon or ash decomposition was observed.

3.2.2 Researched catalysts

The catalyst preparation plays a major role in the catalyst activity, hence in their efficiency for tar reduction and overall gasification yield. Different catalyst preparation methods have been reported in the literature, namely sol-gel [4], impregnation [5], incipient wetness [6], homogenous precipitation [7], etc. The preparation methods and raw materials used in this research work are described below.

3.2.2.1 Ni/Al₂O₃ impregnated catalysts

Two different nickel alumina oxide catalysts were prepared by an impregnation method; the resulting catalysts contained 5wt.% and 10wt.% of metal weight. The oxide support used was α -Al₂O₃, obtained from Sigma-Aldrich (99%), nickel (III) nitrate hexahydrate Ni(NO₃)₂·6H₂O also from Sigma Aldrich was used as metal precursor. An aqueous solution was prepared using a certain amount of the metal precursor and deionised water. The mixture was stirred until complete dissolution, and then the amount oxide was added, followed by drying at 105 °C. After drying, the catalysts were calcined at 750 °C with 20 °C min⁻¹ heating rate, for 3 hours under an air atmosphere. (Refer to Chapter 4).

3.2.2.2 Ni/SiO₂ catalysts by different preparation methods and metal loadings

Four Ni/SiO₂ catalysts were prepared by a sol-gel method using different nickel loadings (5wt.%, 10wt.%, 20wt.%, and 40wt.%). In addition three more catalysts were prepared by adding aluminium (Al), magnesium (Mg), and cerium (Ce) as metal promoters to the 20wt.% Ni/SiO₂ catalyst. The preparation method followed was similar to those reported by Wu and Williams [8, 9]. Ni(NO₃)₂·6H₂O, anhydrous citric acid (Alfa Aesar) deionized water, absolute ethanol (Sigma-Aldrich), and tetraethyl orthosilicate (TEOS: Si(OC₂H₅)₄, Sigma-Aldrich), were used as raw materials. The metal promoters used were obtained

from $\text{Ce}(\text{NO}_3)_3 \cdot 6\text{H}_2\text{O}$ (Aldrich), $\text{Al}(\text{NO}_3)_3 \cdot 9\text{H}_2\text{O}$ (Sigma-Aldrich), and $\text{Mg}(\text{NO}_3)_2 \cdot 6\text{H}_2\text{O}$ (Alfa Aesar). Different amounts of the nickel nitrate, citric acid, and metal promoter (if used) were dissolved into 200 ml of ethanol absolute; the solution was stirred at 60 °C for 3 hours, then a solution containing different volumes of deionised water and 50 ml of absolute ethanol was added to the solution. The resulting mixture was further stirred for about 30 minutes at 60 °C, meanwhile a certain amount of TEOS was added, drop wise into the solution to obtain different Ni:Si ratios. The obtained solution was dried at 80 °C overnight, and finally was calcined at 500 °C for 4 hours (20 °C min^{-1} , heating rate) in the presence of air. (Refer to Chapter 5.1).

Another four Ni/SiO₂ catalysts were prepared by a wet impregnation method, using the same metal loadings (5wt.%, 10wt.%, 20wt.%, and 40wt.%). Different amounts of $\text{Ni}(\text{NO}_3)_2 \cdot 6\text{H}_2\text{O}$ were dissolved into 25 ml of deionised water, and mixed with silicon (IV) oxide amorphous (SiO₂, 99.5% Alfa Aesar). The precursor was stirred at 100 °C for 30 minutes, then dried overnight (105 °C), and further calcined at 500 °C in an air atmosphere for 3 hours. (Refer to Chapter 5.1).

3.2.2.3 Ni/SiO₂ catalysts prepared using different nickel to citric acid (Ni:CA) ratios

Ni/SiO₂ catalysts were prepared by a sol-gel method with a 20wt.% of nickel content and using different nickel to citric acid molar ratios (Ni:CA). The catalysts were prepared according to the method described by Wu and Williams [8], therefore the same raw materials were used. For this preparation method, different amounts of nickel nitrate hexahydrate ($\text{Ni}(\text{NO}_3)_2 \cdot 6\text{H}_2\text{O}$) and citric acid ($\text{C}_6\text{H}_8\text{O}_7$) were dissolved into 200 ml of ethanol, and stirred at 60 °C for 3 hours. Then a solution containing different volumes of deionized water and 50 ml of ethanol was added. A fixed amount of TEOS was added, dropwise, into the solution and stirred for 30 more minutes at 60 °C. The resulting solution was dried and calcined using the conditions described above. The amount of citric acid was varied to obtain Ni:CA ratios of 1:1, 1:2, and 1:3. (Refer to Chapter 5.2).

3.2.2.4 Ni/SiO₂ catalysts prepared by homogeneous precipitation methods

Two different homogeneous precipitation methods were used to prepare a series of six Ni/SiO₂ catalysts, with 10wt.% nickel loading. The preparation methodology was adapted from that reported in the literature for the homogeneous precipitation method (HPG) from Tomiyama and collaborators [7], and for the combined phase separation and HPG methods from that reported by Takahashi et al [10]. For the homogeneous precipitation method (HPG), the raw materials used were tetraethyl orthosilicate (TEOS) as a source of silica; nickel nitrate hexahydrate (Ni(NO₃)₂·6H₂O) as a source of nickel; nitric acid (HNO₃; Aristar), and urea (CH₄N₂O; analytical/reagent grade Fisher Scientific); with an initial composition of TEOS: 0.1mol dm⁻³ HNO₃ aq: Ni(NO₃)₂·6H₂O: urea = 18.7: 20.0: 2.34: 4.09 in wt.%. Initially nickel nitrate and urea were added into the aqueous solution of HNO₃; then TEOS was added into the solution. After continuous stirring a homogenous solution was obtained, this was poured into an open container at room temperature. A wet gel was obtained and kept in a sealed container at 50 °C, after one day the temperature was increased up to 80 °C for 7 days. A dry gel was obtained and it was further dried for 5 days at 80 °C.

A second method was used, adding a phase separation step to the HPG process described above. The same raw materials were used together with polyethylene oxide (PEO; Acros Organics), deionised water and a 60wt.% aqueous solution of nitric acid (HNO₃; Aristar). The initial composition of raw materials was TEOS: Ni(NO₃)₂·6H₂O: PEO: urea: H₂O: 60wt.% HNO₃ aq = 26.6: 3.7: 3.2: 4.0: 32.0: 2.8 in weight; for a final catalyst concentration of 10wt.% NiO. Initially PEO, urea and nitric nitrate hexahydrate were dissolved into the nitric acid aqueous solution; TEOS was added and the solution was stirred until it became homogeneous. The solution was kept in a sealed container for 20 hours at 50 °C, and finally the temperature was increased up to 80 °C for 7 days.

For both methods, the final composites were calcined using three different temperatures: 500 °C, 700 °C, 900 °C for 3 hours in air. A comparative diagram

showing both preparation pathways is shown in Figure 3.2-3. (Refer to Chapter 5.3).

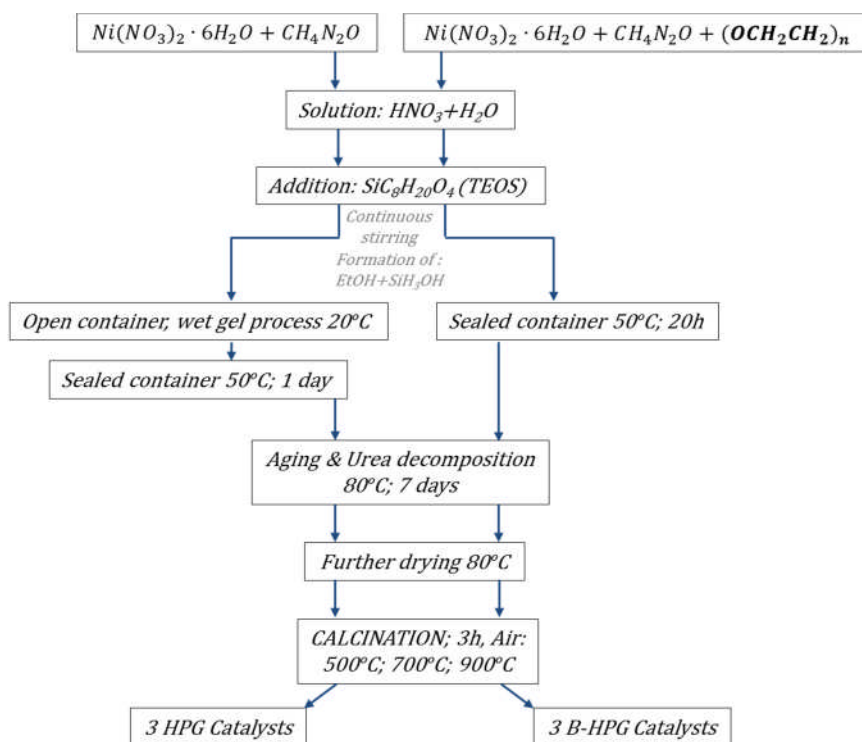


Figure 3.2-3. Comparative of homogeneous precipitation-based preparation methods

3.2.2.5 Fe-Ni/SiO₂ catalysts using a nano-support

A series of catalysts using silica oxide as support and two different metal precursors (nickel or iron), were prepared by a conventional impregnation method. The raw materials used were amorphous silica oxide, ethanol (99%, Sigma-Aldrich), and nickel nitrate hexahydrate ($Ni(NO_3)_2 \cdot 6H_2O$), or iron nitrate nonahydrate ($Fe(NO_3)_3 \cdot 9H_2O$; Sigma Aldrich). A solution with a concentration of 1mol/L was prepared using nickel nitrate hexahydrate or iron nitrate nonahydrate and ethanol. Different volumes of the appropriate solution were mixed with a known amount of amorphous silica, to obtain metal loadings of 2.5wt.%, 5 wt.%, 7 wt.%, 10 wt.%, and 20 wt.%. The solution was stirred for 2 hours at room temperature, then was evaporated overnight at $80^\circ C$ and finally calcined at $550^\circ C$ for 4 hours in air atmosphere. (Refer to Chapter 6).

After calcination, all the prepared catalysts were crushed and sieved to obtain finer particles with a size between 0.05 mm and 0.18 mm. None of the resulting catalysts were reduced as this process took place inside the reaction system, when the catalyst bed came into contact with some of the produced gases from pyrolysis such as hydrogen (H₂) and carbon monoxide (CO) [11]. The activation of the catalyst took place inside the reaction system at the gasification temperature of 800 °C.

3.3 Two-stage fixed bed pyrolysis/gasification reaction system

A two-stage fixed-bed catalytic reaction system was used to carry out various experiments; their physical and operational details are described below.

3.3.1 Reactor Set-up

The reaction system consisted of two stages with a downdraft configuration. The reactor was designed to test the catalytic steam reforming process of different solid waste samples, including RDF. The pyrolysis process takes place within the first stage; whereas the catalytic gasification was carried out downdraft in a second stage. The internal furnace was constructed of one piece of stainless steel, with a length of 26 cm by 5 cm of diameter for the first pyrolysis stage, and 35 cm length by 2.5 cm of diameter for the gasification stage (Figure 3.3-1). Both stages were thermally heated independently, two thermocouples located in each reactor allowed control of the temperature for each stage; the heat transmission from one stage to the other was negligible. The two sections were mounted in a vertical arrangement with the pyrolysis in the upper stage and gasification in the lower stage. The sample container was also made of stainless steel with dimensions of 17.4 cm length and 1.8 cm of diameter. A schematic diagram of the reaction system is presented in Figure 3.3-1.

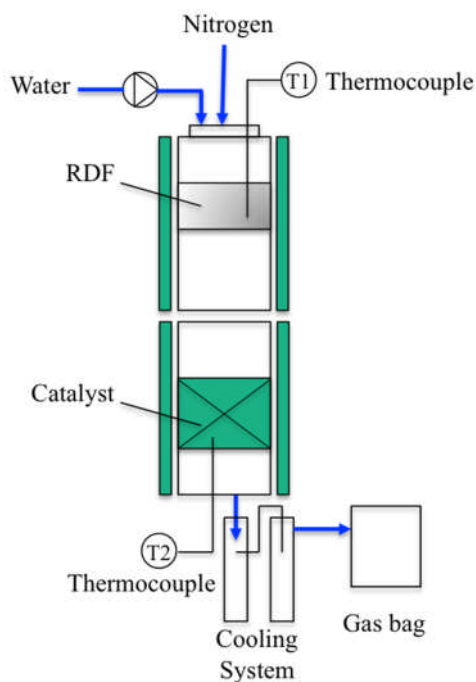


Figure 3.3-1. Schematic diagram of the two-stage fixed-bed catalytic reactor

3.3.2 Experiment Reproducibility and Selection of Process Conditions

The reactor was initially validated and optimised through a series of experiments in order to establish the most suitable operational conditions for the pyrolysis/gasification process. During the blank experiments, a bed of sand was initially used, whose main compound is silicon oxide (SiO_2) [12]. Additionally, some experiments were performed using a prepared 5wt.% Ni/ Al_2O_3 catalyst, whose preparation details can be found in previous Section 3.2.2.1.

The amount of RDF used was varied between 1 and 2 grams, this amount was established considering the very low RDF density, and sample container size. According to Wukovits et al [13], the typical steam/carbon ratio used during steam reforming reactions is between 2.5 and 3.5. However this is not a rule of thumb as this parameter also depends on the type of feedstock used, the reactor configuration, process conditions, etc. For example Franco et al [14], worked with biomass as the feedstock and analysed the effects of varying the steam to biomass ratio over the steam gasification process, and found the most suitable conditions to obtain a gas rich in hydrogen and low in tar was obtained using a

0.6-0.7 w/w steam/biomass ratio. De Filippis et al [15], used a simulation tool to predict the syngas composition during the gasification of different waste. They determined that about 50wt.% of water in relation with RDF was suitable to obtain a final H₂/CO ratio higher than 1.7, which is a desirable value for syngas composition and further use.

Li et al [16], reported that the most suitable temperature for catalyst activation is around 800 °C, also this temperature promotes a high carbon conversion and low tar content in the produced gas. The gasification temperature for the experiments carried out in this research work was initially fixed at 800 °C. Different experiments were carried out varying the pyrolysis temperature and residence time (reaction time); the results were assessed according to the solid conversion of the RDF. The residence time was varied using 10, 20, and 30 minutes, and maintaining other process conditions. Results from these experiments are presented on Table 3.3-1.

Table 3.3-1. Solid decomposition yield at different reaction times

RDF weight (g)	Gasification temperature (°C)	Pyrolysis temperature (°C)	Residence time (min)	Solid conversion (wt.%)
1	800	500	10	65.35
			20	67.39
			30	68.93

From the literature, a normal conversion rate for solid feedstock under similar conditions should be between 60-70wt.%. All the conversion rates in Table 3.3-1 were within this range, but higher RDF conversion was attained using 30 minutes of residence time. However the RDF conversion was further improved by increasing the pyrolysis temperature up to 600 °C (see Table 3.3-2).

The general process conditions established were: 1g of RDF (1.0mm particle size), gasification temperature 800 °C, and N₂ flow rate (carrier gas) 80 ml min⁻¹. The catalyst or sand/RDF ratio was fixed at 1:2 for all the experiments. Conditions such as the bed type, pyrolysis temperature, and H₂O flow rate were varied; the results obtained from this set of experiments, are presented on Table 3.3-2.

Table 3.3-2. Validation of the two-stage pyrolysis/gasification reaction system

	<i>Sand bed</i>										<i>5wt.% Ni/α-Al₂O₃</i>									
	1	2	3	STDV*	RSTDV**	1	2	3	STDV*	RSTDV**	1	2	STDV*	RSTDV**	1	2	3	STDV*	RSTDV**	
<i>General Conditions</i>																				
RDF sample weight (g)	1					1					1					1				
Pyrolysis temperature (°C)	500					600					600					600				
Gasification temperature (°C)	800					800					800					800				
Carrier gas flowrate (ml min ⁻¹)	80					80					80					80				
H ₂ O flow rate (ml h ⁻¹)	—					—					5					5				
<i>Mass Balance</i>																				
RDF conversion rate (wt%)	64.0	67.4	67.0	1.5	2.29%	69.7	68.7	70.0	0.6	0.80%	68.9	69.3	0.2	0.29%	67.5	70.0	70.1	1.2	1.74%	
Gas yield (wt%)	16.4	15.3	17.2	0.8	4.78%	32.0	33.7	34.6	1.1	3.22%	24.1	34.7	5.3	18.03%	37.1	43.5	42.2	2.8	6.75%	
Mass Balance (%)	50.1	47.9	53.0	2.1	4.15%	95.5	95.4	91.9	1.7	1.78%	81.7	92.5	5.4	6.20%	101.1	100.8	100.0	0.5	0.46%	
<i>Gas Composition (N₂ free basis)¹</i>																				
CO (vol.%)	25.6	26.4	26.9	0.5	2.04%	27.2	28.3	23.9	1.9	7.06%	29.7	18.1	5.8	24.27%	16.7	18.1	17.8	0.6	3.43%	
H ₂ (vol.%)	8.4	18.5	12.3	4.2	31.83%	23.2	21.9	26.9	2.1	8.83%	21.3	31.6	5.1	19.47%	39.4	37.0	41.7	1.9	4.85%	
CO ₂ (vol.%)	36.8	29.1	27.8	4.0	12.72%	21.8	22.7	16.5	2.7	13.45%	15.1	20	2.5	13.96%	21.1	25.0	23.2	1.6	7.02%	
CH ₄ (vol.%)	14.7	14.1	18.8	2.1	13.16%	17.7	17.4	20.8	1.5	8.25%	22.8	18.2	2.3	11.22%	12.2	11.1	10.0	0.9	8.05%	
C ₂ -C ₄ (vol.%)	14.5	12.0	14.2	1.1	8.22%	10.1	9.7	11.8	0.9	8.64%	11.1	12.0	0.5	3.90%	10.6	8.8	7.4	1.3	15.02%	

*STDV: standard deviation ; **RSTDV: relative standard deviation

¹ O₂ concentration was 0 vol.% for all the experiments

From Table 3.3-2, it is shown that the experiments are repeatable. The influence of the time collecting gases over the Mass Balance and products yields is presented in Table 3.3-3.

Table 3.3-3. Influence of the gas collection time in general Mass Balance

<i>General Conditions</i>				
Time collecting gases (min)	40.0	40.0	66.0	66.0
RDF sample weight (g)	1.0	1.0	1.0	1.0
Pyrolysis temperature (°C)	600.0	600.0	600.0	600.0
Gasification temperature (°C)	800.0	800.0	800.0	800.0
H ₂ O flow rate (ml min ⁻¹)	0.0	0.0	0.0	0.0
<i>Products Yield</i>				
RDF conversion rate (wt%)	69.2	69.3	69.7	68.7
Gas Yield (wt%)	32.2	30.0	32.0	33.7
Mass Balance	83.0	79.4	95.5	94.5

From Table 3.3-3, it was observed no effect over the RDF or gas yield by changing the gas collection time, but the Mass Balance was considerable improved by increasing the time from 10 to 20 minutes. Blank experiments to calculate the error per cent for water injection and water collection in the condensers (cooling system), were also carried out, the results are presented in Table 3.3-4.

Table 3.3-4. Blank experiments for water yield calculation

Experiment time (min)	30.0	30.0
Pyrolysis temperature (°C)	600.0	600.0
Gasification temperature (°C)	800.0	800.0
Water injected (g)	2.9	4.1
Water condensed (g)	2.5	3.7
Weight difference (g)	0.4	0.4

From Table 3.3-4., it is observed a difference between the total water injected and the water collected in the condensers of less than 10wt.%; this difference was attributed to operational error and system configuration, and was also considered for further calculations regarding the liquid fraction yield. Throughout the whole research programme the experiments were repeated in order to ensure the reliability and accuracy of the research data.

3.3.2.1 Experimental Procedure

Considering the results from the blank experiments, the following general conditions were maintained constant through all the experiments carried out in this research project. Approximately 2 grams of RDF were placed in a stainless steel sample container and placed within the first pyrolysis stage (Figure 3.3-1); a bed of catalyst (or sand) was placed within the second gasification stage, maintaining the catalyst/RDF ratio constant at 0.5g g^{-1} for all the experiments [17]. The experiment was started by heating up the gasification stage up to $800\text{ }^{\circ}\text{C}$ to promote catalyst activation; at the same time the pyrolysis temperature was increased avoiding reach the RDF decomposition temperature, previously identified at around $230\text{ }^{\circ}\text{C}$. Once both temperatures were stable, steam/water was introduced from the top of the reactor using a water syringe pump with a flow rate of 5ml min^{-1} ; at the same time the pyrolysis temperature was increased up to $600\text{ }^{\circ}\text{C}$ with $30\text{ }^{\circ}\text{C min}^{-1}$ heating rate. When both pyrolysis and gasification temperatures reached $600\text{ }^{\circ}\text{C}$ and $800\text{ }^{\circ}\text{C}$ respectively, the operational conditions were maintained constant for about 30 minutes (hold time). The final amount of water supplied was calculated from the weight difference between the initial and final syringe weight, which resulted in steam to RDF ratios of about 1.75:1.0. The pyrolysis gases were conducted through the second gasification stage with the aid of nitrogen as carrier gas continuously supplied with a flow rate of 80 ml min^{-1} . The product gases exit from the bottom of the reactor, and were passed through a cooling system consisting of two condensers cooled by air and dry-ice respectively; a condensed fraction containing water and tar/oil was collected in the condensers. The non-condensed gases were collected in a 10L Tedlar™ gas sample bag, and for about 20 more minutes after the residence time passed to ensure most of the produced gases were collected. All the assembled and main parts of the reaction system are shown in Figure 3.3-2.



Figure 3.3-2. Assembled and main parts of the pyrolysis/gasification reactor.

3.4 Characterisation of materials and products

Different products were obtained from the experiments including solid, liquid and gaseous fractions. All these products were correlated at some extent, and gave different information about the general yield of the process and efficiency of the products and raw materials used. For this reason all these fractions were subjected to different analysis procedures described below.

3.4.1 Analysis of produced gases (GC)

The gases collected in the gas sample bag were analysed by gas chromatography (GC). The aim of using this analytical technique is to obtain qualitative and quantitative information about the gas composition. To carry out this analysis, in general the sample is injected into the chromatograph through an injection port. A carrier gas chemically inert (helium, nitrogen, argon) was used to transport the sample through the oven and then through an analytical column packed with a mesh of specific characteristics. Finally the sample reached the detection system which was either a flame ionization (FID), or thermal conductivity detector (TCD). The main components of a gas chromatograph including a sample injection system, oven, column, thermostat, detector, data interpretation system, and a flow meter; are shown on Figure 3.4-1 [18].

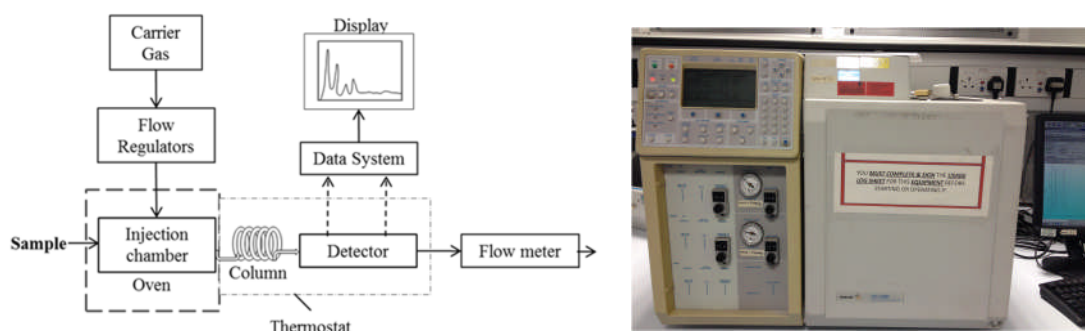


Figure 3.4-1. GC general layout and gas chromatograph equipment

3.4.1.1 Permanent Gas Chromatography (GC) Analysis

Permanent gases including hydrogen (H_2), oxygen (O_2), carbon monoxide (CO), and nitrogen (N_2); were analysed using a Varian CP-3380 GC equipped with a thermal conductivity detector (GC/TCD). The GC was equipped with a column of 2m length by 2mm of diameter, packed with 60-80 molecular sieve; using argon as carrier gas. Carbon dioxide (CO_2) was analysed by another Varian CP-3380 (GC/TCD), a column with 2m length by 2mm diameter was packed with a Hysep 80-100 molecular mesh, and argon was also used as carrier gas. The GC oven temperature was isothermally held at 30 °C; the injector and detector temperatures were set at 120 °C, and the filament temperature at 160 °C.

3.4.1.2 Hydrocarbons Gas Chromatography (GC) Analysis

For the analysis of hydrocarbons C_1 - C_4 , a Varian CP-3380 gas chromatograph equipped with a flame ionisation detector (GC/FID) was used. This GC included a stainless steel column of 2m long by 2mm diameter packed with a Hysep 80-100mesh; nitrogen was used as carrier gas. The oven temperature was set at 60 °C for 3 minutes, then the temperature was increased up to 100 °C with 5 °C min^{-1} heating rate and held for 3 more minutes; finally the temperature was ramped up to 120 °C with 20 °C min^{-1} heating rate and held for 17 minutes.

3.4.1.3 Calibration of Gas Chromatograph instruments

To ensure the values obtained from the GC equipment were accurate, different standard gas mixtures were used. These gases were used to create calibration curves, used as reference for further calculations related with the concentration

of each gas. For the permanent gases, a standard gas containing 1vol.% of each of the following gases H₂, O₂, CO, CO₂, and 96vol.% of N₂, provided by Supelco was used. Whereas for hydrocarbons the calibration curve was created using two different standard gas mixtures for alkanes and alkenes, both balanced with nitrogen. Standard alkane mixture included 1vol.% CH₄, 1vol.% C₂H₆, 1vol.% C₃H₈, and 1vol.% of C₄H₁₀; and alkene hydrocarbons gas mixture contained 1vol.% C₂H₄, 1vol.% C₃H₆, 2vol.% 1-3C₄H₈.

During the calibration, 1ml of each standard was injected into the equipment. The voltage signal obtained for each compound was fed into a digital integrator, which in turn gave a response factor for each compound. A typical chromatogram containing different peaks for permanent and hydrocarbon gases in the gas mixture, expressed as voltage against time is shown on Figure 3.4-2. The obtained sepcode values were later used to calculate a response factor for each gas.

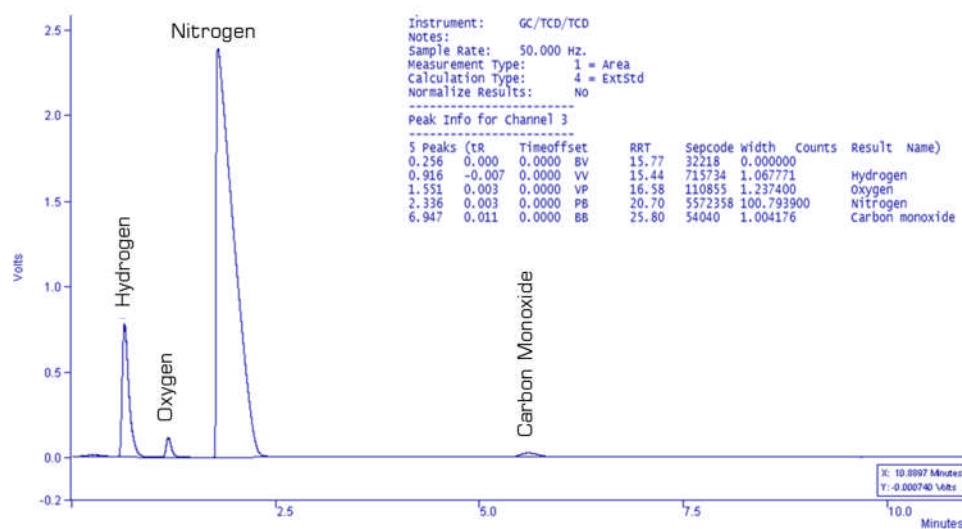


Figure 3.4-2. GC response peaks for a standard gas mixture of permanent gases (H₂, O₂, N₂, CO)

Similar chromatograms were obtained for the hydrocarbons standard gas mixtures. The resulting reference peaks for alkanes and alkenes are shown in Figure 3.4-3.

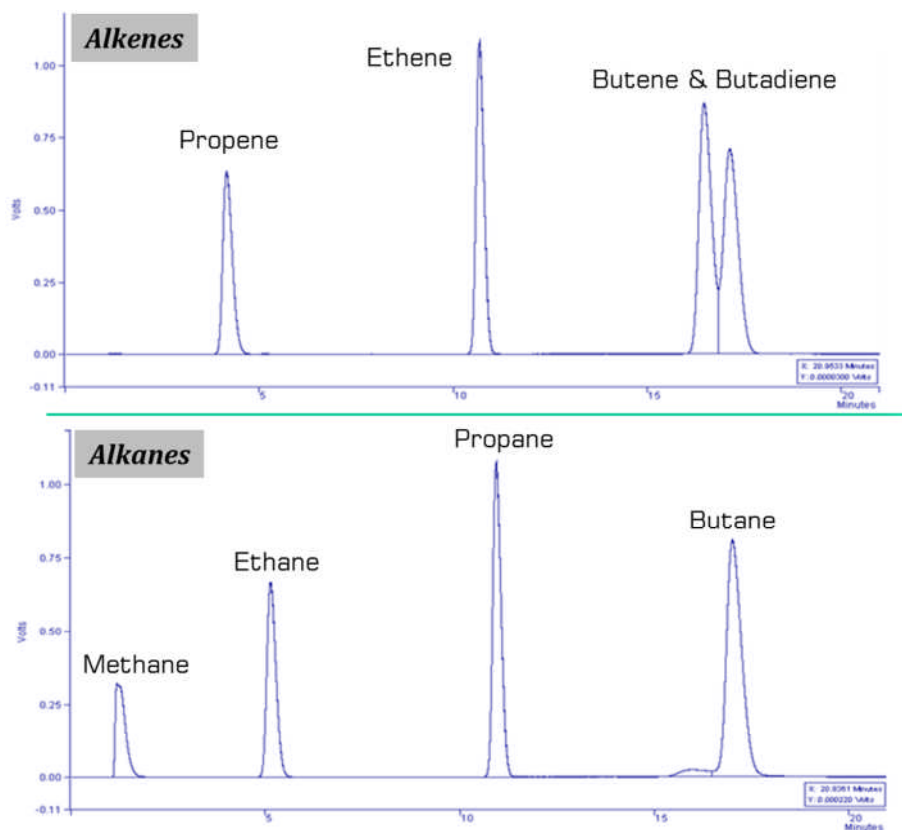


Figure 3.4-3. GC response peaks: standard gas mixture of hydrocarbons (C₁-C₄)

3.4.1.4 Calculation of gas concentration

The response factor values were later used to do a calculation in volume per cent of each analytical gas present in the produced gas, using the following equation:

$$RF = \frac{\text{Peak Area}}{\text{Standard Concentration}} \quad \text{Equation 3.4-1}$$

Where *RF* is defined as the response factor (Volts per unit time per vol.%); *peak area* and *Standard Concentration* correspond to values from the standard gas. Then the volume per cent of each gas can be calculated by using the following equation:

$$xVol. \% = \frac{\text{Peak Area}_x}{RF} \quad \text{Equation 3.4-2}$$

Where x is defined as the gas whose value will be calculated, and RF is the response factor from the standard gases. Once the *vol.%* for each gas was obtained, the mass of each gas can be calculated using the ideal gas law equation:

$$n = \frac{PV}{RT} \quad \text{Equation 3.4-3}$$

Where n is the mole number (mol); V is the volume previously obtained (m^3); P and T are pressure and temperature respectively (Pa, K), and R is a constant value ($8.31441 \text{ J K}^{-1} \text{ mol}^{-1}$) [19].

3.4.1.5 Reproducibility of gas analysis

Values of the concentration of permanent gases and hydrocarbon gases were obtained in *vol.%* (Equation 3.4-2). These values were then used to calculate the mass of an individual component, according to the ideal gas law (Equation 3.4-3). These values were processed into an Excel spread sheet designed to compare and analyse mass and volume concentrations of gaseous products. Analysis of permanent gases and hydrocarbons were repeated in order to ensure data reliability and consistency. An example of the values obtained and how they were collated is presented in Table 3.4-1.

Table 3.4-1. Concentration of permanent gases and hydrocarbons from standard values

General gas data from standard curve				Gas concentrations from GC analysis data									
Gas	Std conc	Peak Area	Rf	Peak Area Sample 1	Con (Vol %)	Peak Area Sample 2	Con (Vol %)	Peak Area Sample 3	Con (Vol %)	Average Conc (Vol %)	STDV	R_STDV* (%)	
CO	0.999	52672	52724.72	201653	3.825	196314	3.723	200207	3.797	3.782	0.05	1.38%	
H ₂	0.994	624273	628041.25	6172455	9.828	6057458	9.645	6126591	9.755	9.743	0.09	0.95%	
O ₂	1.000	104138	104138.00	0	0.000	0	0.000	0	0.000	0.000	0.00	0.00%	
N ₂	96.015	5010103	52180.42	4234086	81.143	4138309	79.308	4191622	80.329	80.260	0.92	1.15%	
CO ₂	0.992	10957	11045.36	43068	3.899	42324	3.832	42249	3.825	3.852	0.04	1.06%	
Methane	CH ₄	0.998	608850	610070.14	816873	1.339	811114	1.330	807937	1.324	1.331	0.01	0.56%
Ethene	C ₂ H ₄	0.991	1202211	1213129.16	854666	0.705	844304	0.696	843584	0.695	0.699	0.01	0.73%
Ethane	C ₂ H ₆	1.010	1177047	1165393.07	92100	0.079	92056	0.079	91954	0.079	0.079	0.00	0.08%
Propene	C ₃ H ₆	0.985	1763656	1790513.71	50880	0.028	50140	0.028	50214	0.028	0.028	0.00	0.81%
Propane	C ₃ H ₈	1.000	1701225	1701225.00	4989	0.003	5544	0.003	4981	0.003	0.003	0.00	0.00%
Butene & Butadiene	C ₄ H ₈	1.958	4434998	2265065.37	25697	0.011	25505	0.011	25603	0.011	0.011	0.00	0.38%
Butane	C ₄ H ₁₀	1.000	2372819	2372819.00	0	0.000	0	0.000	0	0.000	0.00	0.00%	
TOTAL					100.860		98.655		99.848	99.788	1.10	1.11%	

*R_STDV: Relative Standard Deviation

From Table 3.4-1, it was observed that the relative standard deviation (R_STDV), reported for all the data is lower than 2% which is an acceptable value. The more precise data yield the smaller relative standard deviation.

As nitrogen was used as the carrier gas during the experiments, it was assumed the nitrogen flow rate was constant and as observed on Table 3.4-1, the standard nitrogen concentration was higher than 95 vol.%. Also from the ideal gas law equation (Equation 3.4-3), it was assumed that one mole of gas occupies 22.4 L at standard conditions of pressure and temperature. From this, the moles of each gas were calculated using the following expression:

$$X_i = \frac{Vol.\%_i}{Vol.\%_{N_2}} \times n_{N_2} \quad \text{Equation 3.4-4}$$

Where i , represents the gas (different from nitrogen), whose concentration needs to be determined. The other two values ($Vol.\%_{N_2}$, and n_{N_2}) correspond to the volume in per cent and the mole number (Equation 3.4-3) of nitrogen, obtained from experimental and calculated values respectively. To determine the total volume of nitrogen supplied, experimental data from the time collecting the produced gases was included in the spread sheet.

The general gas yield might be calculated considering the total produced mass of the gas (g) divided by the weight of the sample used (g) using the following expression:

$$X_{gas} = \sum_{i=1}^n X_i \quad \text{Equation 3.4-5}$$

Where X_i refers to the calculated weight of each compound of the gas (g), including permanent gases and hydrocarbons (Table 3.4-1), and X_{gas} is the total gas weight in grams. This value will be later used to calculate the total gas yield as follows:

$$Y_{gas} = \frac{X_{gas}}{X_{RDF}} \quad \text{Equation 3.4-6}$$

Where Y_{gas} is the gas yield (g/g), X_{gas} is the total weight of the gas produced (g), and X_{RDF} is the initial sample weight, RDF in this case (g).

3.4.2 Characterization of catalysts (fresh/reacted)

Fresh catalysts were characterised using different analytical techniques to obtain information about their properties. Some of the techniques were also used to characterise reacted catalysts and compare some properties before and after the pyrolysis/gasification process. The analytical techniques used in this research work are described below.

3.4.2.1 Determination of surface area by Brunauer-Emmet-Teller (BET) method

Fresh catalysts were analysed to determine their surface area and porous properties via nitrogen adsorption at liquid gas temperature, which is one of the most widely used methods. However the surface area might be also determined using other techniques such as adsorption from solutions and by heat of adsorption [20].

The BET method has been mainly used to analyse ultra-fine powders and porous materials. The general Brunauer-Emmet-Teller linear equation used for the determination of surface area is as follows [21, 22]:

$$\frac{1}{V(P^0/P - 1)} = \frac{1}{V_m C} + \frac{(C - 1)}{V_m C} \left(\frac{P}{P^0} \right) \quad \text{Equation 3.4-7}$$

Where V is the amount of gas adsorbed at the determined P/P^0 pressure; P^0 refers to the saturation pressure, V_m is the monolayer capacity, and C is an empirical constant. Thereby a linear trend can be constructed using point-by-point adsorption data from the multipoint analysis. The amount of gas adsorbed

is related with the interactions between the gas and the solid, the temperature, and the controlled relative pressure as P/P^0 .

The surface area analysis was carried out using a Quantachrome NOVA 2200e series apparatus (Figure 3.4-4). Prior to the analysis about 90 mg of each catalyst were degassed for 2 hours at 120 °C under a nitrogen atmosphere, in order to remove all previously physisorbed material from the adsorbent surface [21]. Adsorption and desorption isotherms were later obtained using the multipoint data of gas adsorbed or desorbed at different relative pressure.



Figure 3.4-4. BET surface area and pore size analyser: Quantachrome NOVA 2200e

The surface area values obtained of some of the catalysts investigated in this work are presented on Table 3.4-2.

Table 3.4-2. BET Surface area of some nickel and iron-based catalysts

Catalyst	Metal loading (wt.%)	Calcination temperature (°C)	BET surface area (m ² g ⁻¹)
Ni/SiO ₂ *	5.0	500	595.40
	10.0		836.90
	20.0		756.40
	40.0		481.56
Mg-Ni/SiO ₂	20.0		554.40
Fe/SiO ₂	2.5	550	208.50
	5.0		313.70

* Prepared by sol-gel method

As shown in Table 3.4-2, surface areas greater than $800 \text{ m}^2\text{g}^{-1}$ were attained for the Ni/SiO₂ catalyst prepared by a sol-gel method, using a metal loading of 10wt.%. It was also noted that the surface area values were highly influenced by factors such as calcination temperature, metal, loading, and synthesis method. This will be discussed in depth later in this research.

3.4.2.2 Determination of micropore volume by Dubinin-Radushkevich (DR) method

Additional information might be obtained from the adsorption-desorption analysis, using different calculation methods. The Dubinin-Radushkevich (DR) method, relates the temperature, relative pressure and energy with the adsorbed amount of gas per unit of micropore volume, allowing the calculation of micropore volumes, based on Equation 3.4-8 [23, 24]:

$$W/W_0 = \exp[-(RT \ln(x)/E)^2] \quad \text{Equation 3.4-8}$$

Where $x=P/P^0$, E is the characteristic energy for a given system, W is the amount of gas adsorbed, R is the Universal gas constant, and T the temperature (in Kelvin). The values of the adsorbed volume (V_{ads} ; $\text{cm}^3 \text{ STP g}^{-1}$) can be further plotted against the $\{\log(P/P^0)\}^2$. This relationship gives a straight line from which the extrapolation of the 'y intercept' represents the $\log(V_0)$; using this value the volume of gas adsorbed can be obtained. A typical plot is presented in Figure 3.4-5.

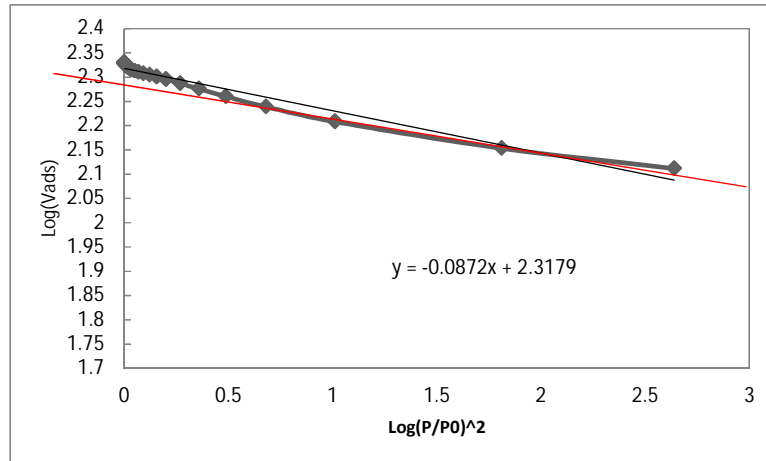


Figure 3.4-5. Diagram used for micropore and mesopore volumes determination

From Figure 3.4-5 the 'y intercept' is used to calculate the micropore volume (V_{micro}). The amount of gas adsorbed at relative pressures closer to unity corresponds to the total amount adsorbed for both micropores (generally filled at low relative pressures), and mesopores (generally filled at relative pressures above 0.2). Therefore the mesopore volume value can be calculated by subtracting the micropore volume (calculated from DR equation) from the total amount of gas adsorbed at the relative pressure $P/P_0=0.95$ (Equation 3.4-9).

$$V_{mesop} = V_{0.95} - V_{microp} \quad \text{Equation 3.4-9}$$

3.4.2.3 Barrett, Joyner & Halenda (BJH) method for total pore volume and pore diameter determination

Additionally using the Barrett, Joyner & Halenda (BJH) method, information about the total pore volume and pore diameter can be obtained. This method was aimed at obtaining information about porous adsorbents with a wide range of pore sizes, but it is also applicable to different solid materials. The method accounts for capillary condensation in pores, based on the classical Kelvin equation. An excess of absorption is given by a surface layer thickness $t(P)$ including an additional pore-filling term, as stated in Equation 3.4-10 [25, 26].

$$\ln \frac{P}{P_0} \geq \frac{-2\gamma V_L}{RT} \frac{1}{r_c} \quad \text{Equation 3.4-10}$$

Where $r_c=r-t(P)$, r is the pore's radius, V_L is the molar volume (liquid), γ is the surface tension and P^0 is the vapour pressure. In the original BJH formulation it was considered the C value of core radius as a constant value [26].

3.4.2.4 Pore size distribution by Density Functional Theory (DFT)

The density functional theory it is based on a regularization method and is based on a molecular model of nitrogen adsorption in porous solids [27]. The use of the DFT method is useful to characterize adsorbents according to their porous structure and surface properties, from experimental adsorption isotherms [28]. Some of the Ni/SiO₂ catalysts prepared within this work were expected to present a broad pore size distribution, thus this method was useful to compare the pore size for different synthesised catalysts. The calculation was carried out using Quantachrome NovaWin software. The pore size distribution was obtained plotting values of the pore size (nm), against dV/dR (cm³/g-nm). This theory has been successfully used for the characterisation of different nanoporous materials, when compared with other methods, and a detailed description of the theory may be found elsewhere as the theoretical development is beyond the scope of this work [29, 30].

3.4.2.5 X-ray Diffraction (XRD)

XRD analyses were carried out in order to identify crystalline phases and the main chemical compounds in the fresh prepared catalysts. A Bruker D-8 diffractometer was used to record the XRD patterns of the samples, using a Cu-K α X-ray source with a Vantec position sensitive detector. Corundum was used as external standard (Figure 3.4-6).

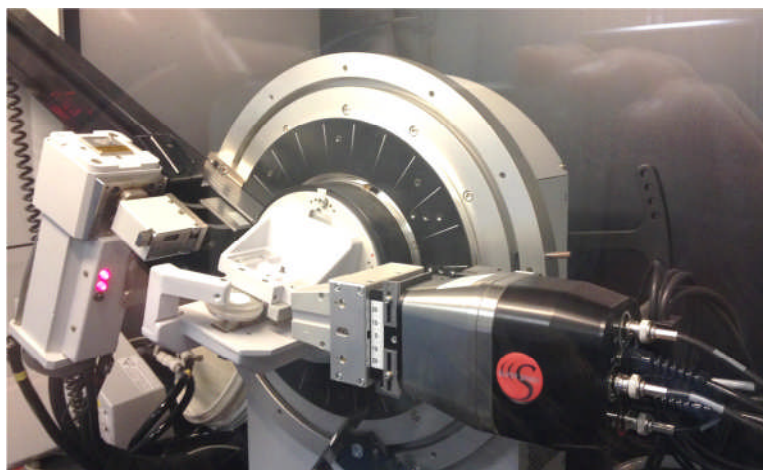


Figure 3.4-6. X-ray Bruker D-8 for diffraction analysis

Diffraction patterns of a crystal lattice generate different reflections occurring at an angular position (2θ), and at an angular wavelength (λ) according to Bragg's law [31]. Diffraction patterns give structural information about the sample, for example the angular position is related with the shape and size of the crystal, whereas the intensity of the pattern is related to the lattice symmetry and electron density [32]. The crystallite size of some samples was also determined according to Scherrer's method, from the broadening of the line [33]. About 2 grams of the sample were placed in an inert sample holder and placed in 63mm support plane. Analysis conditions such as time were set up according to the catalyst to be analysed. The data was recorded using *DIFFRACplus* software. As a result a XRD spectrum containing the different diffraction pattern was obtained as observed in Figure 3.4-7.

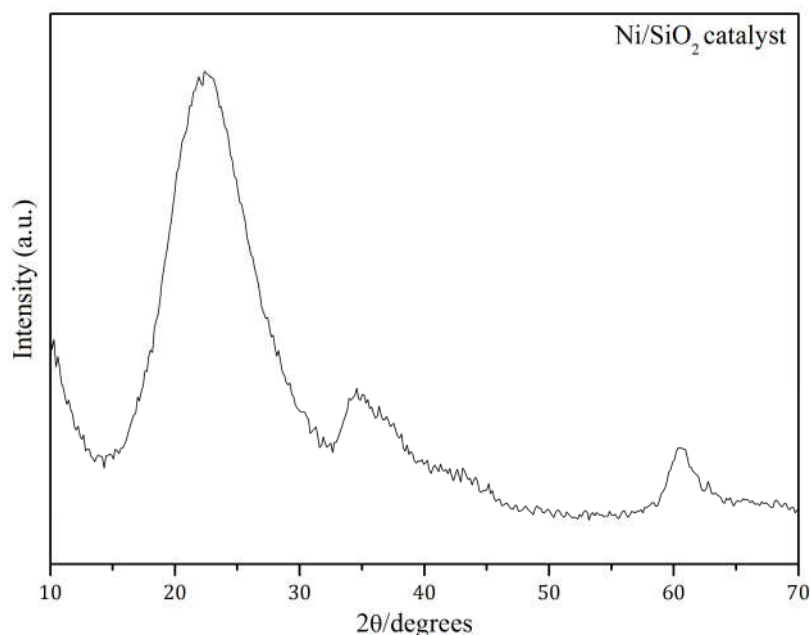


Figure 3.4-7. XRD patterns of Ni-based fresh catalyst, using *DIFFRACplus* software.

3.4.2.6 Temperature programmed oxidation (TGA-TPO)

Reacted catalysts from the pyrolysis-gasification of RDF were analysed using a thermogravimetric method known as temperature programmed oxidation (TGA-TPO). This analytical technique is useful for the analysis of coked and reacted catalysts, based in the TGA analysis previously described for the RDF characterisation (Section 3.2.1.2). A thermogravimetric analyser Shimadzu, Stanton Redcroft 280 was used. About 20 mg of the reacted catalyst were placed in a crucible and heated up to 800 °C at a 15 °C min⁻¹ heating rate, using air with 50 ml min⁻¹ flow rate, and dwell time of 10 minutes. Changes in the catalyst weight represented the combustion of coke deposited over the catalyst surface. The variations in weight were detected by the microbalance and recorded by the computer system. Both the thermogravimetric curve (TGA-TPO) and the differential thermogravimetry (DTG-TPO) were obtained. Three main stages could be identified from the TPO analysis: around 100 °C water vaporization, around 350 °C occurs the Ni or metal oxidation, and above 400 °C might be identified carbon combustion depending on the sample analysed. From Figure 3.4-8 some of these main stages can be identified for a specific 40wt.% Ni/SiO₂ catalyst prepared by an impregnation method.

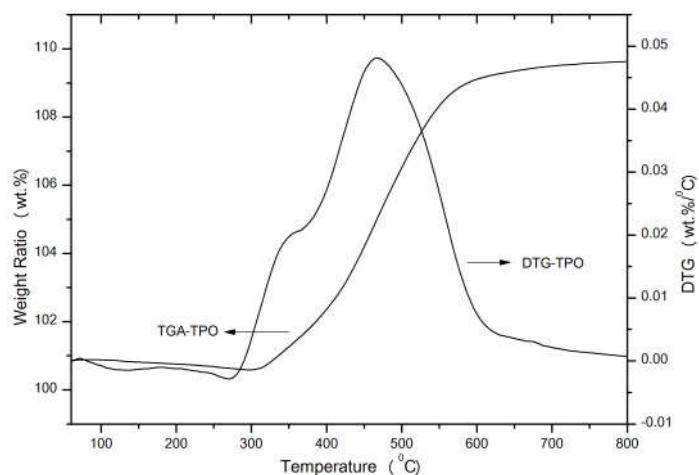


Figure 3.4-8. Thermogravimetric analysis (TPO) of 40wt.% Ni/SiO₂ reacted catalyst

From Figure 3.4-8, the initial mass decrease around 100 °C might be attributed to vaporisation of moisture contained in the catalyst [34]. At around 300 °C the mass gain is likely to be related with the oxidation of metal (in this case nickel) particles, and the final stage is generally associated with the combustion of carbon deposition of the catalyst [8].

3.4.2.7 Scanning Electron Microscopy (SEM) and Transmission Electron Microscopy (TEM)

Two different microscopic techniques were used to characterise and examine the surface of the fresh and reacted catalysts. In addition, since coke formation on the catalyst and indeed the type of carbon deposited influences catalyst deactivation, the analysis of catalyst coke indicates catalyst efficiency. The images of morphologies before and after reaction, together with information obtained from other characterisation techniques, was correlated in order to have a better understanding of the catalysts structure and properties.

The main component of a scanning electron microscope (SEM) is the electron column, which consists of an electron gun and at least two electron lenses. Additionally there is a control console consisting of a cathode ray tube (CRT), screen, and computer system that allows the control of the electron beam. These main components are shown in Figure 3.4-9. An energy filter might be also used, allowing the electron beam to be dispersed according to the electron

energy. Electrons can pass through a diaphragm to form the final image. The main components of an energy filter are shown in Figure 3.4-9 [35].

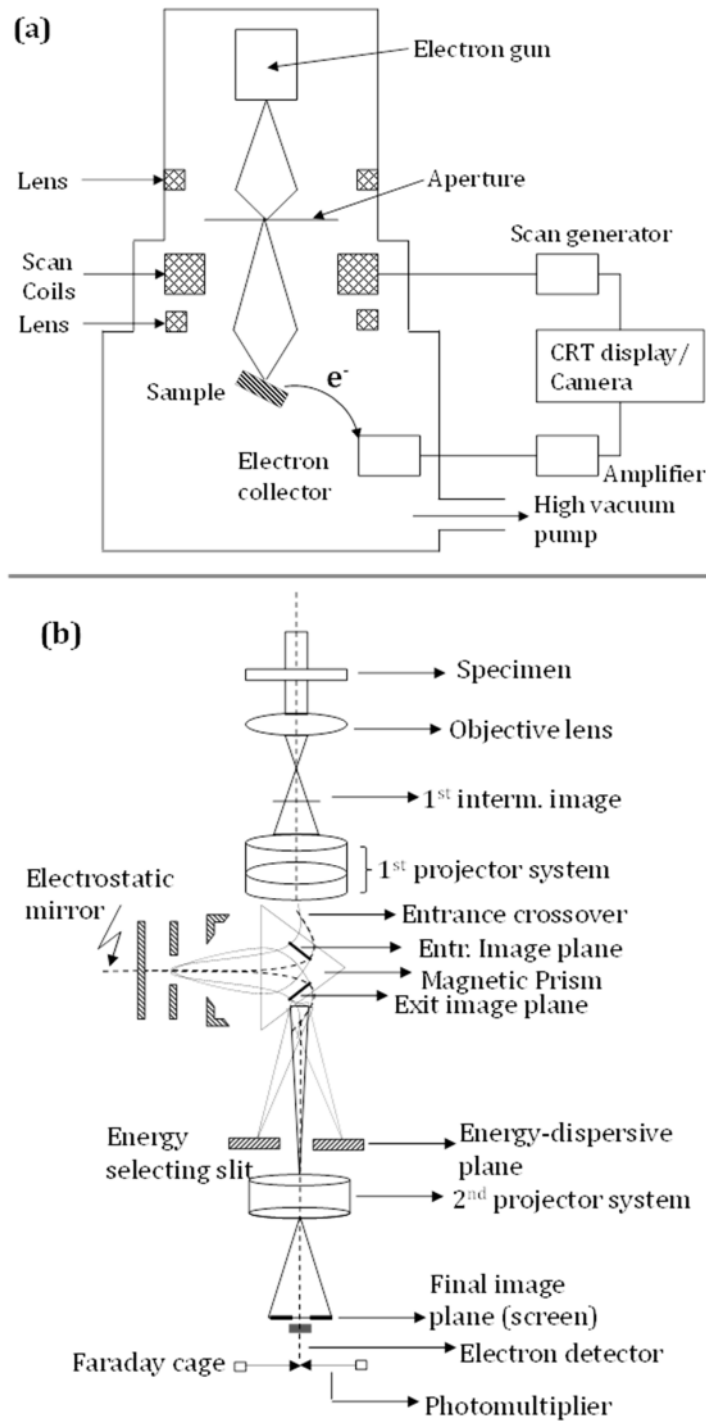


Figure 3.4-9. Main components of an electron column (a) and energy filter diagram (b)

A high resolution scanning electron microscope (LEO 1530), coupled to an energy dispersive X-ray spectrometer (EDXS) was used to carry out SEM-EDXS

analysis. In order to observe the surface of the catalyst, it was necessary to apply a metallic coating to the sample, in this way the charge dissipation was improved [36]; therefore the coating was carried out with Pt/Pt to produce a 5.0 nm layer thickness. An example of a SEM-EDXS result is presented in Figure 3.4-10.

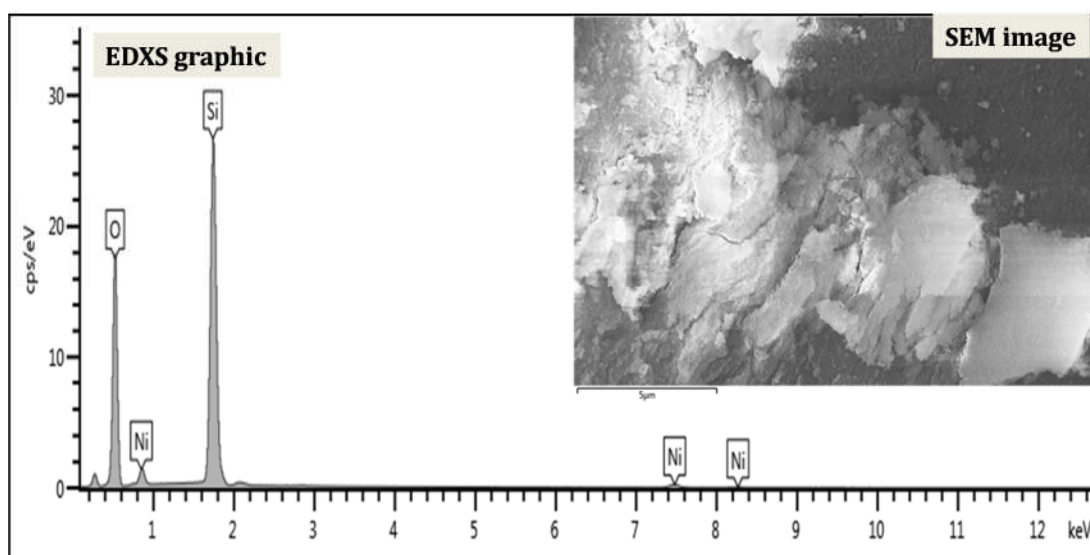


Figure 3.4-10. SEM-EDXS results of 10wt.% Ni/SiO₂ fresh catalyst

Certain features including the electron gun, vacuum system and condenser lenses are the same for both the scanning and transmission microscopes. However a screen with a layer of electron-fluorescent material, and a camera working under vacuum are used for the latter. Also the ways in which the images are produced and magnified are entirely different for both devices [37]. The transmission microscope's column is located vertically and the electrons travel down through a fine tube of about 1mm in diameter. The column is also equipped with two condenser lenses, and four or five projector lenses to magnify the image [38].

Selected samples were prepared by dispersing in ethanol, a Pasteur pipette was used to place drop of the sample over a tiny copper grid. The sample was later carefully introduced into the microscope to be analysed. The transmission electron microscope used was a TEM, Phillips CM200. High magnification

micrographs were obtained for different fresh and reacted catalysts. Examples of TEM micrographs are shown in Figure 3.4-11.

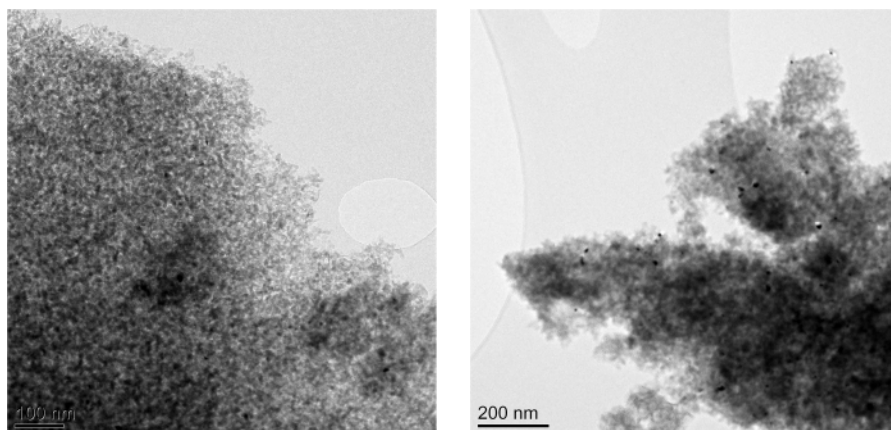


Figure 3.4-11. Micrograph images of fresh 10wt.% Ni/SiO₂ catalyst, obtained by TEM analysis

3.4.2.8 Infrared Spectrometry (FTIR)

Fourier Transform Infrared Spectrometry (FTIR), is a technique used to obtain information about the different functional groups present in liquid and solid samples. The basic components of a FTIR spectrometer are presented in Figure 3.4-12 [39].

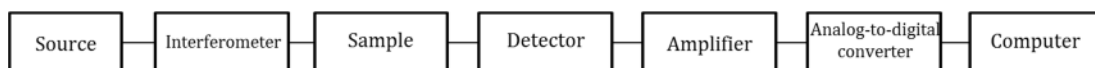


Figure 3.4-12. Basic FTIR spectrometer components

An IR spectrum including the wave number (cm⁻¹) against intensity (% transmittance or absorbance), can be obtained as both parameters are inconvertible by using the mathematical method of Fourier-transformation. On Figure 3.4-13 an example of the spectrum from the analysis of a tar/oil sample obtained from the pyrolysis-gasification of RDF is shown. Different functional groups might be identified from the band location and intensity.

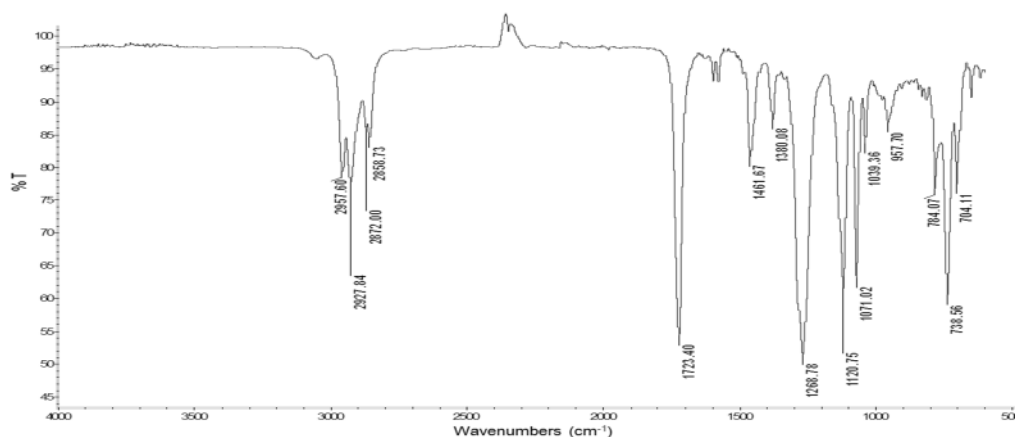


Figure 3.4-13. FTIR spectrum of tar/oil from pyrolysis-gasification of RDF using no catalyst bed or steam

The FTIR analysis was performed using a Thermo Nicolet Corporation *iS10* (Thermo Scientific). The FTIR spectrum was generally recorded within the region comprised from 4000 to 650 cm^{-1} . The sample plate was carefully cleaned *in situ* using acetone before each analysis. Different methodologies were undertaken for sample preparation accordingly (see Section 3.4.3).

3.4.3 Analysis of liquid fraction (tar/oil/ H_2O)

The condensed fraction from the pyrolysis-gasification of RDF was collected at the bottom of the cooling system, consisting of two different condensers. Once the experiment was finished, two different procedures were used for the liquid fraction collection. The first one included the use of dichloromethane (DCM) as organic solvent. As a result a heterogeneous mixture was obtained containing a water fraction and an oil/tar-DCM fraction. Both fractions were separated and the oil/tar-DCM fraction was further subjected to centrifugation. The resulting fraction was subjected to GC-MS analysis to determine PAH and oxygenated compounds contained in the oil/tar fraction. The second technique for liquid fraction collection included the use of DCM and ethanol absolute (HPLC grade) for the samples collection; as a result a homogeneous liquid sample was obtained. The resulting sample was studied to determine its water content, and then was further prepared to identify and quantify the different aromatic and oxygenated compounds in the liquid fraction by GC-MS.

Details about the sample preparation and specific objectives of using each of the above described techniques are given below.

3.4.3.1 Sample preparation: centrifugation for DCM evaporation

The heterogeneous fraction was physically separated by decantation. The tar/oil-DCM fraction was passed through a bed of sodium sulphate (Na_2SO_4), previously dried for 2 hours at 140 °C to remove any moisture content. The DCM was later evaporated by using a Genevac Rocket evaporation system at 30 °C, to obtain a final fraction containing tar/oil. The weight was registered and the samples were further analysed by GC-MS technique.

3.4.3.2 Karl-Fischer Titration

The condensed fraction was collected using different volumes of ethanol (absolute grade), and dichloromethane (DCM, analytical reagent grade, Fischer Scientific), using a ratio of EtOH:DCM of 2:1 v/v. As a result, a homogenous solution containing ethanol, DCM, tar/oils, and water was obtained. The volumes of DCM and ethanol were registered together with the weight of the tar/oil- H_2O fraction collected. The sample was subjected to a titration analysis with the aim to determine the water content. The water determination in the tar/oil samples is a very important characteristic, as it influences the calorific value and viscosity of the oil [40]. It is also useful to determine the amount of water reacted and condensed during the pyrolysis/gasification process. To carry out the water determination in the liquid samples, a device known as Karl-Fischer titration (KFT) was used. The principle of KFT is based on a redox reaction where water is consumed and sulphur dioxide is oxidized by iodine. An organic base is used together with anhydrous methanol as solvent, following the reaction: $\text{SO}_2 + \text{I}_2 + 2\text{H}_2\text{O} \rightleftharpoons \text{H}_2\text{SO}_4 + 2\text{HI}$ [40].

For the determination, an empty syringe was weighed, then about 0.1ml of the sample was taken, and the syringe was weighed. The sample was injected into a flask containing a pair of platinum electrodes immersed into the titration solution, and the syringe was weighed again. The weight difference was

recorded by the instrument software. A stirrer was used to homogenise the solution during the titration, changes in the current are registered using the platinum electrodes. After the sample titration, the excess of iodine solution used is determined by an electrometric end-point detector.

The KF was calibrated by titrating a standard solution containing a mixture of methanol and water with a 3:1 mass ratio. Different measurements were carried out, and a calibration curve was obtained according to the least squares method [18]. The volumetric titrations were carried out using a KF Titrando 890 Metrohm (Switzerland). The titrating agent medium used was a Hydranal[®]-composite 5K one-component solution, and the working medium was a Hydranal[®]-ketosolver (Figure 3.4-14). The end point of the titration (+100mV) was detected with a double platinum electrode (type Pt1400).



Figure 3.4-14. Karl-Fischer Metrohm Titration equipment for moisture determination in liquid samples

The sequential steps followed for the water and tar determination, according to the methodology described above, is shown in Figure 3.4-15.

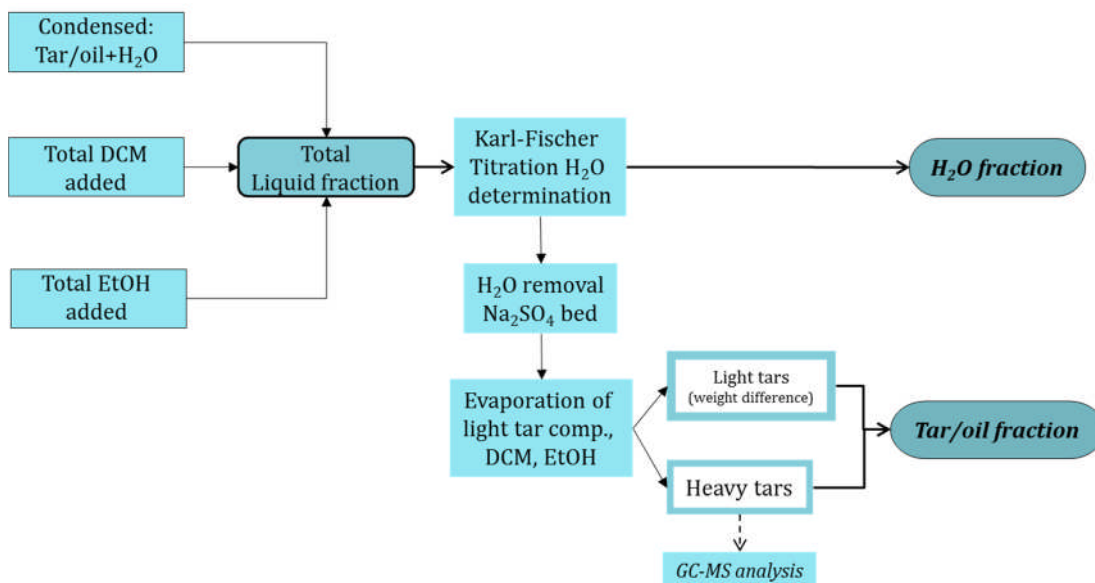


Figure 3.4-15. Sequential steps for water and tar determination in condensed fraction

3.4.3.3 Gas Chromatography/Mass Spectrometry (GC-MS)

The tar/oil fraction mixed with DCM, obtained by any of the two methods described, were analysed using a gas chromatograph coupled to a mass spectrometer (GC-MS). This device combines the benefits of the high resolution separation components from the GC with the very selective and sensitive detection of the MS [41]. The Mass Spectrometer measures the relation of mass and charge ratio (m/z) from the produced ions of the sample. The interaction between the GC and the MS takes place through an inlet system (interface) that must provide an adequate pressure drop from atmospheric pressure (vapour sample from GC) to low pressure (10^{-5} to 10^{-8} torr) by using a vacuum system [18, 42]. A schematic diagram of a typical GC-MS apparatus is presented in Figure 3.4-16.

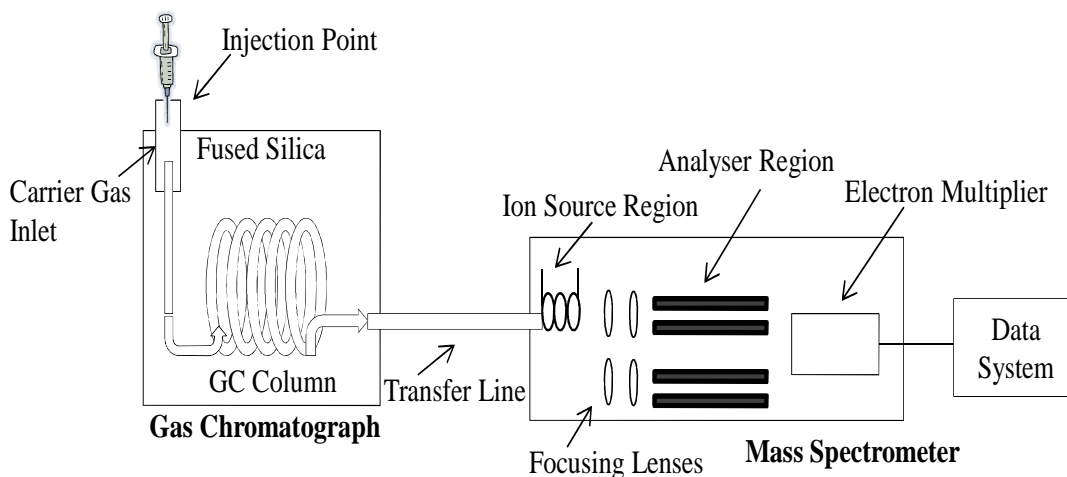


Figure 3.4-16. General diagram of a typical GC-MS system

The GC-MS analyses were carried out using a Varian CP-3800 gas chromatograph, coupled to a Varian Saturn 2200 GC/MS/MS mass spectrometer. An aliquot of 2 μ L of the tar/oil sample dissolved into DCM, was injected into the GC injection port at a temperature of 290 $^{\circ}$ C. The oven programme temperature was 40 $^{\circ}$ C for 2 minutes, and then the temperature was ramped to 280 $^{\circ}$ C at 5 $^{\circ}$ C min $^{-1}$ heating rate, and held for 10 minutes. The transfer line temperature was maintained at 280 $^{\circ}$ C, the manifold was 120 $^{\circ}$ C and the ion trap temperature was held at 200 $^{\circ}$ C. A PAH (polyaromatic hydrocarbon) standard solution, containing mixtures of different aromatic and oxygenated compounds; was created based on the most common compounds reported in the literature for tar/oil samples from the thermal processing of different solid wastes [43, 44]. About 0.1000 \pm 0.0002 g of each aromatic or oxygenated compound was weighed and further dissolved into 10 ml of dichloromethane (DCM, Fischer Scientific). A solution with 1 \times 10 4 ppm of concentration was obtained for each compound, then 1mL of this solution was further dissolved into 100mL of DCM to get a final solution with a concentration of 100 ppm. Parallel dilutions were carried out using the general expression for dilution (Equation 3.4-11) to calculate the amount of stock solution required to obtain solutions with concentrations of 20 ppm, 40 ppm, 80 ppm and 100 ppm.

$$C_1V_1 = C_2V_2$$

Equation 3.4-11

Where C_1 is the original concentration of the solution, C_2 is the final concentration of the solution; V_1 is the unknown volume required to get the final concentration (C_2); and V_2 is the volume that will be prepared or final volume. The sequential steps followed for the preparation of standard solution is presented on Figure 3.4-17.

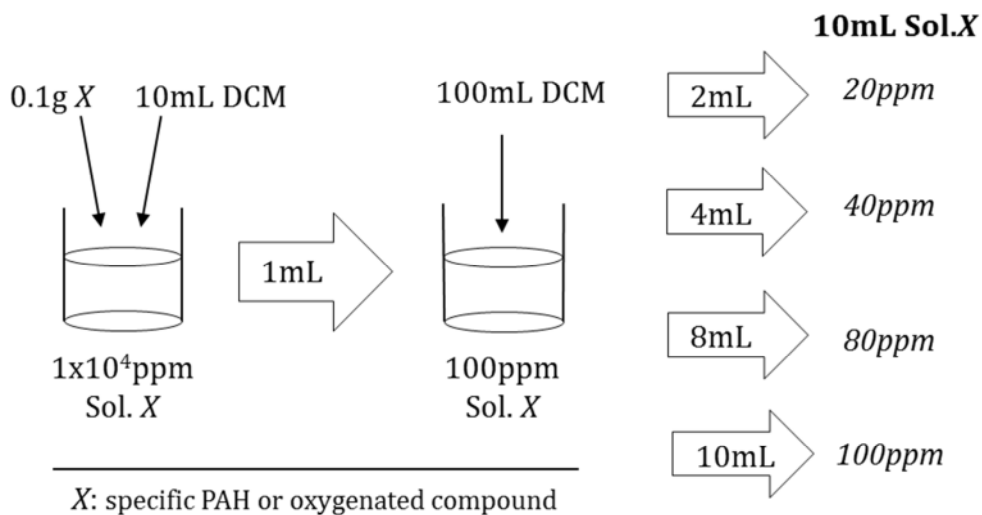


Figure 3.4-17. Methodology followed for the preparation of the PAH and oxygenated standard solution

In Figure 3.4-17, X refers to the different compounds used to prepare standard solutions. In the following Table 3.4-3, are listed the polyaromatic and oxygenated compounds used to calibrate the GC-MS apparatus.

Table 3.4-3. Compounds used for the standard solution (PAH and oxygenated compounds) for GC-MS calibration

	Compound	RT	Response Factor
1	Cyclopentanone	6.11	595.3
2	Furfural	7.35	658.3
3	Ethylbenzene	8.11	692.0
4	<i>p</i> -Xylene	8.57	1033.1
5	<i>m</i> -Xylene	8.53	1230.2
6	Styrene	9.34	1482.7
7	<i>o</i> -Xylene	9.39	788.1
8	Anisole	10.15	2097.3
9	Pyran	11.66	658.3
10	Phenol	12.59	954.0
11	Alphamethylstyrene	12.47	1747.6
12	Betamethylstyrene	13.10	1699.2
13	<i>s</i> -Limonene	14.16	485.2
14	Indane	14.25	2665.6
15	Indene	14.59	2982.2
16	<i>o</i> -Cresol	14.93	1453.5
17	Acetophenone	15.35	1153.4
18	<i>p</i> -Cresol	15.81	3189.2
19	<i>m</i> -Cresol	15.83	2860.6
20	2-Methoxyphenol (guaiacol)	16.04	1677.4
21	2-Methylbenzofuran/2,5-Dimethylanisole	16.78	3752.7
22	1,2,3,4-Tetramethylbenzene	17.03	2649.1
23	3,5-Dimethylanisole	17.15	2036.2
24	2,3-Dimethylanisole	17.51	1512.9
25	2-Ethylphenol	17.57	440.5
26	3,4-Dimethylanisole	17.95	2074.6
27	2,4-Dimethylphenol	17.94	1260.7
28	3-Ethylphenol/4-Ethylphenol	18.60	1207.6
29	2,6-Dimethylphenol	18.66	833.5
30	Naphthalene	19.11	3136.4
31	1,2-Benzenediol (Catechol)	19.26	1702.6
32	2-Isopropylphenol	19.78	468.5
33	2,3,5-Trimethylphenol	19.75	1868.2
34	4-Isopropylphenol	20.35	785.0
35	2-Methylnaphthalene	22.47	2846.7
36	1-Methylnaphthalene	23.00	2846.7
37	Biphenyl	24.48	2614.1
38	2-Ethyl-naphthalene	24.77	631.6
39	1-Ethyl-naphthalene	24.77	295.6
40	2,6-Dimethylnaphthalene	25.03	2267.3
41	1,4-Dimethylnaphthalene	25.65	2471.7
42	Dibenzofuran	27.07	1184.1
43	2,2-Diphenylpropane/4-Phenyphenol	27.32	4440.2
44	Fluorene	27.95	3252.9
45	1,3-Diphenylpropane	28.89	2305.1
46	2-Phenylphenol	29.62	5001.3
47	Phenanthrene	30.49	3005.5
48	1-Phenylnaphthalene	31.29	1591.6
49	<i>o</i> -Terphenyl	31.58	2252.7
50	Fluoranthene	33.42	2115.3
51	Pyrene	33.94	7822.1
52	<i>m</i> -Terphenyl	34.21	3285.0
53	1,3,5-Triphenylbenzene	41.15	3734.7

The corresponding calibration curves were created for each compound by injecting 2 μ L of each concentration (20ppm, 40ppm, 80ppm, 100ppm) into the GC-MS equipment. Examples of some calibration curves obtained for phenol, *p*-cresol, dibenzofuran, ethylbenzene, indane, naphthalene, and fluorene are presented in Figure 3.4-18.

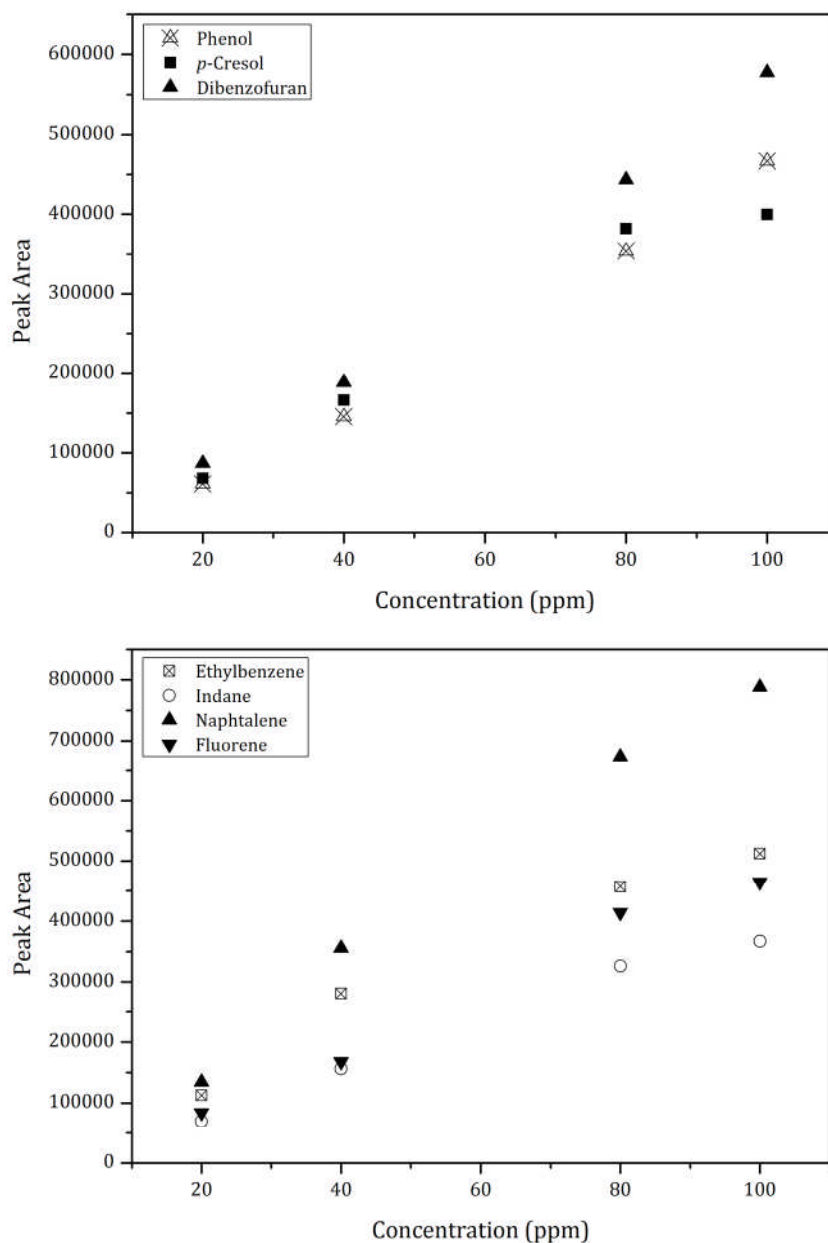


Figure 3.4-18. Calibration curves at different concentration for some oxygenated and PAH compounds in the GC-MS equipment

3.4.3.4 Size Exclusion Chromatography (SEC) and FTIR

Size exclusion chromatography is also referred as gel-permeation chromatography; this analytical technique was used to analyse tar samples and to obtain information about the molecular distribution.

SEC differs from the HPLC technique as largest molecules elute first during the analysis. The SEC equipment used was a Perkin-Elmer Modular, Series 225, equipped with a 5 μ m SEC column from Polymer laboratories. The equipment was calibrated with polystyrene samples with broad molecular weight range from 800-860000; also single ring and PAH standard samples of low molecular mass were used for calibration.

The samples were prepared by dissolving a small amount of oil/tar in tetrahydrofuran (THF), with an approximate concentration of 0.2vol.%. THF was used as mobile phase during the analysis, and the detector used was a Perkin-Elmer 200a refractive index detector. The analytical set-up was connected to an analytical recorder and a computer with processing data software to obtain information on the molecular mass distribution of the tar/oil samples. The results obtained from the SEC analysis were plotted in a graph of intensity against molecular weight. An example from the SEC analysis of the tar/oil from the pyrolysis of RDF is presented in Figure 3.4-19.

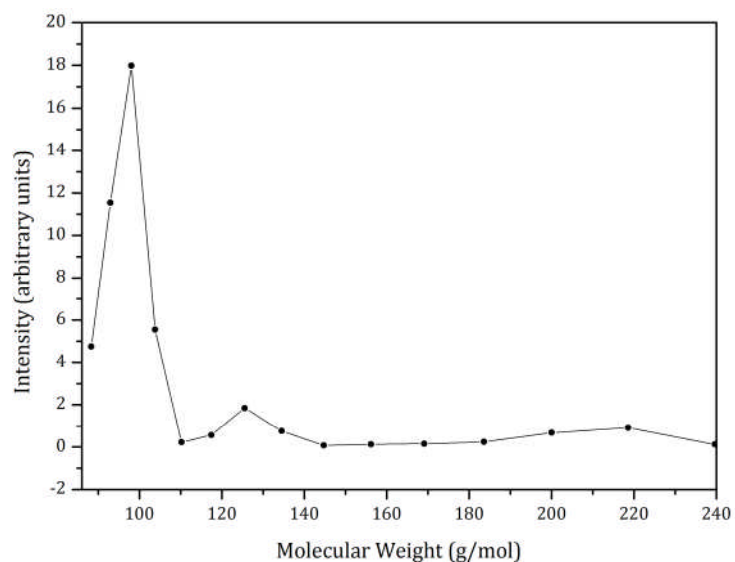


Figure 3.4-19. Size exclusion chromatogram of tar/oil samples

Additionally FTIR analyses were carried out to tar/oil samples with the aim to determine functional groups present in the samples. The FTIR analysis was carried out as described in Section 3.4.2.8.

References

1. Keattch, C.J., *An Introduction to Thermogravimetry*, ed. H. Son. 1969, Philadelphia: Sadtler Reserach Laboratories.
2. Gabbot, P., *Principles and Applications of Thermal Analysis*. 1st ed, ed. L. Blackwell Publishing. 2007, Singapore.
3. Buah, W.K., A.M. Cunliffe, and P.T. Williams, *Characterization of Products from the Pyrolysis of Municipal Solid Waste*. *Process Safety and Environmental Protection*, 2007. 85(5): p. 450-457.
4. Goncalves, G., Lenzi, M. K., Santos, O. A. A., Jorge, L. M. M., *Preparation and characterization of nickel based catalysts on silica, alumina and titania obtained by sol-gel method*. *Journal of Non-Crystalline Solids*, 2006. 352: p. 3697-3704.
5. Lazar, M., Mihet, M., Dan, M., Almasan, V., Marginean, P., *Preparation and characterization of nickel based multicomponent catalysts*, in *Isotopic and Molecular Processes*. 2009, *Journal of Physics: Conference Series*: Cluj-Napoca, Romania. p. 4.
6. Darvell, L.I., K. Heiskanen, J.M. Jones, A.B. Ross, P. Simell, and A. Williams, *An investigation of alumina-supported catalysts for the selective catalytic oxidation of ammonia in biomass gasification*. *Catalysis Today*, 2003. 81(4): p. 681-692.
7. Tomiyama, S., R. Takahashi, S. Sato, T. Sodesawa, and S. Yoshida, *Preparation of Ni/SiO₂ catalyst with high thermal stability for CO₂-reforming of CH₄*. *Applied Catalysis A: General*, 2003. 241(1-2): p. 349-361.
8. Wu, C.F. and P.T. Williams, *A Novel Nano-Ni/SiO₂ Catalyst for Hydrogen Production from Steam Reforming of Ethanol*. *Environmental Science & Technology*, 2010. 44(15): p. 5993-5998.
9. Wu, C. and P.T. Williams, *Hydrogen production from steam reforming of ethanol with nano-Ni/SiO₂ catalysts prepared at different Ni to citric acid ratios using a sol-gel method*. *Applied Catalysis B: Environmental*, 2011. 102(1-2): p. 251-259.
10. Takahashi, R., S. Sato, S. Tomiyama, T. Ohashi, and N. Nakamura, *Pore structure control in Ni/SiO₂ catalysts with both macropores and mesopores*. *Microporous and Mesoporous Materials*, 2007. 98(1-3): p. 107-114.
11. Wu, C. and P.T. Williams, *Hydrogen production by steam gasification of polypropylene with various nickel catalysts*. *Applied Catalysis B: Environmental*, 2009. 87(3-4): p. 152-161.
12. Gil, J., M.A. Caballero, J.A. Martín, M.-P. Aznar, and J. Corella, *Biomass Gasification with Air in a Fluidized Bed: Effect of the In-Bed Use of Dolomite under Different Operation Conditions*. *Industrial & Engineering Chemistry Research*, 1999. 38(11): p. 4226-4235.
13. Wukovits, W., W. Schnitzhofer, and K. Urbaniec, *Process routes of hydrogen production from fossil and renewable sources*, in *Hydrogen production: prospects and processes*, D.R. Honnery and P. Moriarty, Editors. 2012, Nova Science Publishers, Inc.: New York. p. 43-93.

14. Franco, C., Pinto, F., Gulyurtlu, I., Cabrita, I., *The study of reactions influencing the biomass steam gasification process*. Fuel, 2003. 82: p. 835-842.
15. De Filippis, P., C. Borgianni, M. Paolucci, and F. Pochetti, *Prediction of syngas quality for two-stage gasification of selected waste feedstocks*. Waste Management, 2004. 24(6): p. 633-639.
16. Li, X.T., J.R. Grace, C.J. Lim, A.P. Watkinson, H.P. Chen, and J.R. Kim, *Biomass gasification in a circulating fluidized bed*. Biomass and Bioenergy, 2004. 26(2): p. 171-193.
17. Blanco, P.H., C. Wu, J.A. Onwudili, and P.T. Williams, *Characterization of Tar from the Pyrolysis/Gasification of Refuse Derived Fuel: Influence of Process Parameters and Catalysis*. Energy & Fuels, 2012. 26(4): p. 2107-2115.
18. Skoog, D.A., West, D. M., Holler, F. J., Crouch, S. R., *Fundamentals of Analytical Chemistry*. 8th ed, ed. T. Brooks/Cole. 2004, Belmont, CA. USA.
19. Nag, P.K., *Engineering Thermodynamics*. 3rd ed. Mechanical Engineering, 2006, Noida, Dheli: McGraw-Hill.
20. Allen, T., *Particle Size Measurement: Surface Area and Pore Determination*. 5 ed. Vol. 2. 1997, London: Chapman & Hall.
21. Sing, K.S.W., *Adsorption Methods for Surface Area Determination*, in *Particle Size Analysis*, N.G. Stanley-Wood, Lines, R. W., Editor. 1992, Royal Society of Chemistry: Cambridge, UK. p. 13-32.
22. Lowell, S., J.E. Shields, M.A. Thomas, and M. Thommes, *Characterization of Porous Solids and Powders: Surface Area, Pore Size and Density*. 2004, Netherlands: Kluwer Academic Publishers.
23. Nguyen, C. and D.D. Do, *The Dubinin-Radushkevich equation and the underlying microscopic adsorption description*. Carbon, 2001. 39(9): p. 1327-1336.
24. Amphlett, J.C., K.A.M. Creber, J.M. Davis, R.F. Mann, B.A. Peppley, and D.M. Stokes, *Hydrogen production by steam reforming of methanol for polymer electrolyte fuel cells*. International Journal of Hydrogen Energy, 1994. 19(2): p. 131-137.
25. Barrett, E.P., L.G. Joyner, and P.P. Halenda, *The Determination of Pore Volume and Area Distributions in Porous Substances. I. Computations from Nitrogen Isotherms*. Journal of the American Chemical Society, 1951. 73(1): p. 373-380.
26. Gelb, L.D. and K.E. Gubbins, *Pore Size Distributions in Porous Glasses: A Computer Simulation Study*. Langmuir, 1998. 15(2): p. 305-308.
27. Parr, R.G. and W. Yang, *Density-functional theory of atoms and molecules*. International Series of Monographs on Chemistry - 16, ed. O.S. Publications. 1989, Oxford: Oxford University Press.
28. Olivier, J.P., *Improving the models used for calculating the size distribution of micropore volume of activated carbons from adsorption data*. Carbon, 1998. 36(10): p. 1469-1472.
29. Ravikovitch, P.I., G.L. Haller, and A.V. Neimark, *Density functional theory model for calculating pore size distributions: pore structure of nanoporous catalysts*. Advances in Colloid and Interface Science, 1998. 76-77(0): p. 203-226.

30. Lastoskie, C., K.E. Gubbins, and N. Quirke, *Pore size distribution analysis of microporous carbons: a density functional theory approach*. The Journal of Physical Chemistry, 1993. 97(18): p. 4786-4796.
31. Cole, H., *Bragg's law and energy sensitive detectors*. Journal of Applied Crystallography, 1970. 3(5): p. 405-406.
32. Perego, G., *Characterization of heterogeneous catalysts by X-ray diffraction techniques*. Catalysis Today, 1998. 41(1-3): p. 251-259.
33. Langford, J.I. and A.J.C. Wilson, *Scherrer after sixty years: A survey and some new results in the determination of crystallite size*. Journal of Applied Crystallography, 1978. 11(2): p. 102-113.
34. Akande, A.J., R.O. Idem, and A.K. Dalai, *Synthesis, characterization and performance evaluation of Ni/Al₂O₃ catalysts for reforming of crude ethanol for hydrogen production*. Applied Catalysis A: General, 2005. 287(2): p. 159-175.
35. Watt, I.M., *The Principles and Practice of Electron Microscopy*. 2nd ed. 1996, Cambridge, UK: Cambridge University Press.
36. Datye, A.K., *Electron microscopy of catalysts: recent achievements and future prospects*. Journal of Catalysis, 2003. 216: p. 144-154.
37. Goodhew, P.J., J. Humpreys, and R. Beanland, *Electron microscopy and analysis*. 3rd ed. 2001, London: Taylor and Francis Publisher.
38. Goldstein, J., D. Newbury, D. Joy, C. Lyman, P. Echlin, E. Lifshin, L. Sawyer, and J. Michael, *Scanning Electron Microscopy and X-Ray Microanalysis*. 3rd ed. 2003, New York: Kluwer Academic/Plenum.
39. Stuart, B.H., *Infrared Spectroscopy: Fundamentals and Applications*. Analytical Techniques in the Sciences. 2004, Chichester, England: Wiley.
40. Smets, K., P. Adriaensens, J. Vandewijngaarden, M. Stals, T. Cornelissen, S. Schreurs, R. Carleer, and J. Yperman, *Water content of pyrolysis oil: Comparison between Karl Fischer titration, GC/MS-corrected azeotropic distillation and 1H NMR spectroscopy*. Journal of Analytical and Applied Pyrolysis, 2011. 90(2): p. 100-105.
41. Grob, R.L., *Modern Practice of Gas Chromatography*. 3rd ed. 1995, New York, USA.: Wiley.
42. Pool, C.F., *The Essence of Chromatography*. 1st ed, ed. B.V. Elsevier Science. 2003, USA.
43. Kinoshita, C.M., Y. Wang, and J. Zhou, *Tar formation under different biomass gasification conditions*. Journal of Analytical and Applied Pyrolysis, 1994. 29(2): p. 169-181.
44. Li, C. and K. Suzuki, *Tar property, analysis, reforming mechanism and model for biomass gasification--An overview*. Renewable and Sustainable Energy Reviews, 2009. 13(3): p. 594-604.

CHAPTER 4. EFFECTS OF OPERATIONAL PARAMETERS ON GAS AND LIQUID YIELDS AND COMPOSITION

4.1 Effects of bed type and gasification temperature, on gas and liquid products during pyrolysis-gasification of RDF

A series of experiments were carried out in the two-stage pyrolysis-gasification catalytic reaction system described in Chapter 3, Section 3.3. Refuse derived fuel (RDF) was used as raw material and also nickel-based catalysts were tested during the gasification stage in order to promote catalytic steam reforming reactions. The high calorific value of RDF make it suitable to be used for pyrolysis-gasification, and furthermore to be a candidate for the generation of a hydrogen-rich syngas. This section will address the selection, characterisation and activity of nickel-based catalysts when used for the production of a hydrogen-rich syngas. Some of the catalysts were also tested according to their ability to reduce tar formation during the process, through the analysis of the condensed fraction.

4.1.1 Ni/Al₂O₃ catalysts

Initially two Ni/Al₂O₃ catalysts were prepared according to the impregnation method described in Chapter 3 Section 3.2.2. The metal loading was varied such that the final metal loading of the catalysts contained 5 and 10wt.% of nickel loading respectively. The activity of these catalysts and the influence of the nickel loading were measured in terms of their influence on the tar and syngas compositions. The results were compared with experiments carried out using a bed of sand (silica based material) with and without water steam. The effect of the gasification temperature was also measured for the experiments carried out using the bed of sand and steam.

4.1.2 Gas composition and Mass Balance

The yield of each fraction (solid, liquid and gas) was calculated considering the inlet products and the resulting fractions. The following expression was developed considering the fractions involved during the experiments:

$$\text{Mass Balance} = \frac{\text{gas} + \text{oil} + \text{char}(\text{residue}) + \text{lost water}}{\text{sample} + \text{water}(\text{wt. \%})} \quad \text{Equation 4.1-1}$$

The conversion rate of the raw material (RDF) was calculated considering the initial and the final weight, using the following expression:

$$\text{Conversion rate}_{RDF} = 100 - \text{residue}(\text{wt. \%}) \quad \text{Equation 4.1-2}$$

For most of the experiments, the conversion rate was around 70wt.%, which means that just about 30% of the raw material remained as solid residue in the form of char. The composition of the gases was measured and calculated according to the methodology described in Chapter 3, Section 3.4.1.4. The results regarding the product yield, gas composition and mass balance are presented in Table 4.1-1.

Table 4.1-1. Results of pyrolysis-gasification of RDF in terms of product yield and gas composition using different bed materials

Catalyst Bed	Sand Bed				Ni/ α -Al ₂ O ₃	
	No steam		Steam		5wt%	10wt%
Temperature	800°C	600°C	700°C	800°C	800°C	800°C
Water flow rate (g h ⁻¹)	0.00	5.00	5.00	5.00	5.00	5.00
<i>Gas composition (vol. %)</i>						
CO	27.09	20.90	21.00	18.15	16.70	17.00
H ₂	18.70	21.70	20.10	31.61	39.42	45.54
CO ₂	20.58	27.20	19.50	20.04	21.06	23.81
CH ₄	20.58	12.60	15.80	18.23	12.19	7.52
C ₂ -C ₄	11.01	17.50	23.50	11.98	10.64	6.13
H ₂ /CO ratio	0.69	1.04	0.96	1.74	2.36	2.68
<i>Products Yield (wt. %)</i>						
Gas Yield (wt. %)	30.85	25.40	31.50	34.71	37.08	45.89
Conversion to gas/oil (wt%)	69.81	70.20	71.50	69.26	67.51	69.11
Mass Balance (%)	84.85	92.10	91.37	92.54	101.14	102.30

When comparing the experiments carried out at 800 °C with and without steam, it was found that the addition of steam increased the gas yield, however there was no effect on the conversion to gas/oil ratio. Furthermore the gas composition was highly influenced by the addition of steam, as the hydrogen concentration in the produced gas increased from 18vol.% up to 31vol.%, whereas the CO and CH₄ concentrations were reduced. This is due to the water-gas and steam reforming reactions taking place, resulting in the formation of carbon dioxide and hydrogen.

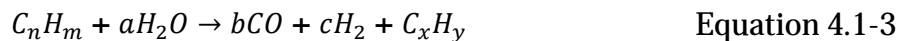
For the experiments carried out with steam at different gasification temperatures, as shown in Table 4.1-1 it was observed that the gas yield increased from 25wt.% up to about 35wt.% as the gasification temperature increased from 600 °C to 800 °C. The H₂ content in the produced gas was also increased from 21vol.% up to 31vol.% with the increasing temperature, whereas the CO₂ was reduced from 27vol.% to 20vol.%. This was attributed to a promotion of gasification reactions involving steam as the temperature was increased. Li et al [1] previously reported similar results in the literature; they observed that an increase in the gasification temperature from 750 °C up to 900 °C, resulted in an increase in the H₂ and CO₂ concentrations, and also an increase in the gas yield from 10wt.% up to 50wt.%. The effect of using different process conditions on the syngas composition during the gasification of RDF, has been also reported by Galvagno et al [2]. They reported that the produced gas contained up to 43vol.% of H₂, about 18vol.% CO, 17.63vol.% CO₂, and about 16vol.% CH₄; these concentrations are similar to those reported in this work (Table 4.1-1), when the gasification temperature was set at 800°C and using a bed of sand.

Comparing the experiments with and without catalysts it could be seen in Table 4.1-1 that the gas yield was slightly increased using the 5wt.%Ni/Al₂O₃ catalyst, but was further improved reaching about 46wt.% by using the 10wt.%Ni/Al₂O₃ catalyst. The hydrogen and CO₂ concentrations were also increased to 45.5vol.% and 23vol.% respectively. By adding the catalyst, reactions such as water-gas

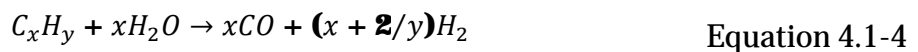
and tar cracking were further enhanced as the produced pyrolysis gases were passed through the catalytic bed. The promotion of decomposition reactions of tars and hydrocarbons using the nickel based catalysts can be seen in Table 4.1-1. The data show that the concentrations of CH₄ and light hydrocarbons (C₂-C₄) in the syngas were markedly reduced as a result of this decomposition. Much work has been done to analyse the effects of nickel-based catalysts during biomass gasification. For example Miccio and collaborators [3], used a fluidized bed gasification system, using biomass as raw material. They reported a maximum hydrogen concentration of about 30vol.% using two different nickel-alumina catalysts. Also Liu et al [4], and collaborators stated that the use of a specific nano-nickel-based catalyst can increase the quality of the syngas during the gasification steam reforming of MSW carried out at 800 °C. In addition the resulting gas contained 50vol.% H₂, 21.4vol.% of CO, and about 20vol.% of CO₂.

From Table 4.1-1 it was also observed that the gas yield was increased to about 2vol.% when the bed of catalyst was changed from sand to catalyst and was further increased to about 8vol.% when the metal loading of the catalyst was increased from 5wt.% up to 10wt.%. Further increasing the metal loading might be useful to maximise gas yield using this specific catalyst.

The use of nickel-based catalysts influences the tar formation and kinetics during the gasification stage. A general expression for tar formation, based on the evolution of light hydrocarbons has been suggested as follows [5]:



Where C_nH_m and C_xH_y represent tar and light hydrocarbons respectively. Light hydrocarbon can further evolve to release hydrogen according to the following chemical reaction:



The calorific value and hydrogen concentration of the syngas can be also improved through the promotion of hydrogenation reactions [6], by using Ni/Al₂O₃ catalysts, which might explain the increase in the hydrogen concentration from 18vol.% up to 45vol.% shown in Table 4.1-1.

4.1.3 Tar Analysis

The characterisation of tar samples collected from the pyrolysis/gasification of RDF was carried out by using GC-MS, SEC, and FTIR analytical techniques. As described in Chapter 3.

4.1.3.1 GC-MS analysis of the collected tar

The tars collected from the experiments were analysed by gas chromatography coupled to mass spectrometry (GC-MS), and the resulting chromatograms are shown in Figure 4.1-1.

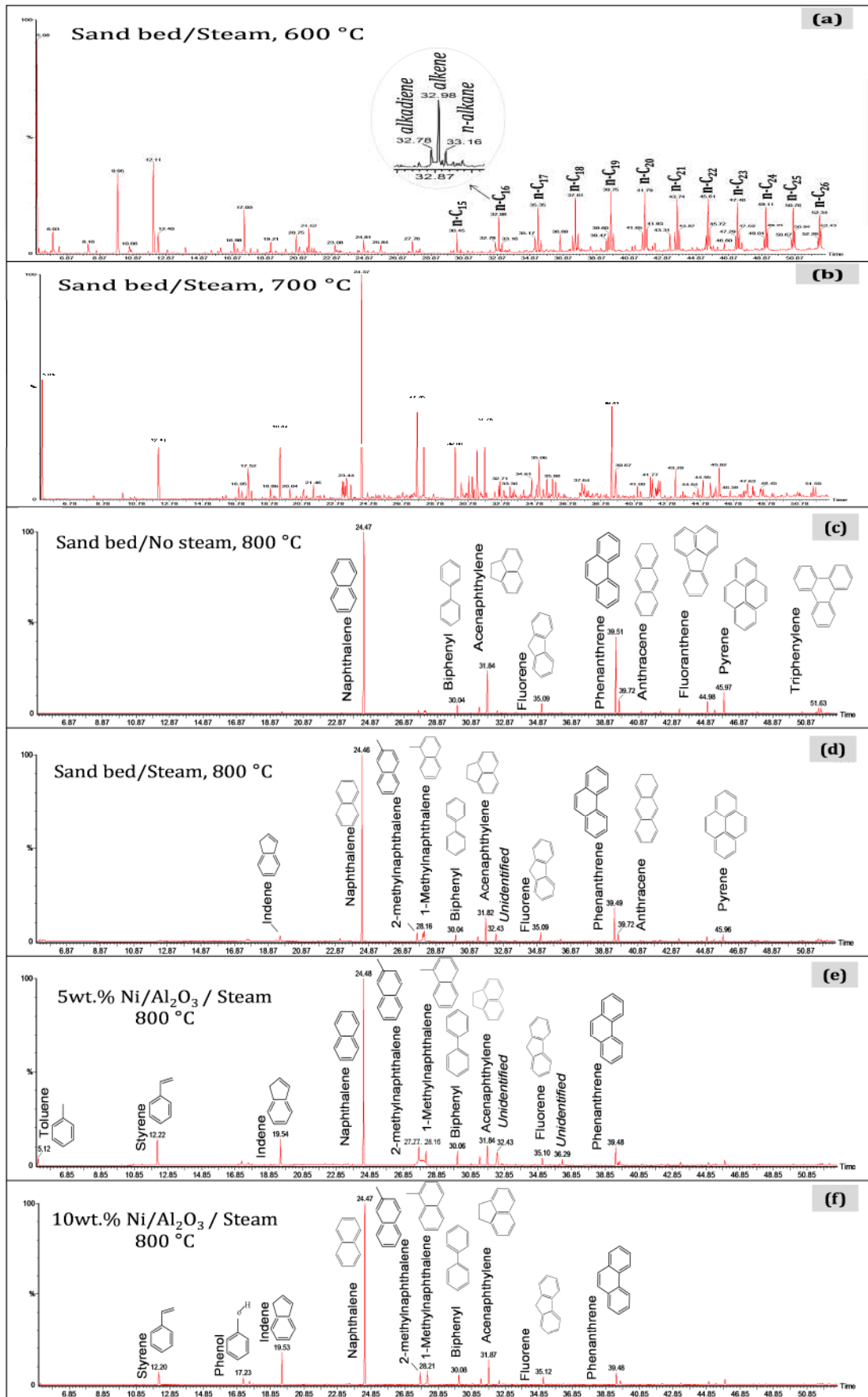


Figure 4.1-1. Chromatograms of tar samples showing the effect of gasification temperature (a, b); and bed type (c, d, e, f).

Some of the identified PAHs shown in Figure 4.1-1 such as acenaphthylene, fluorene, phenanthrene, anthracene, pyrene, and fluoranthene, represent concern due to their associated mutagenic characteristics. Phenanthrenes and methylphenanthrenes have shown mutagenic characteristics in both human and bacterial cell tests [7]; in addition some compounds such as chrysene, tri- and tetramethylphenanthrenes, and benzo pyrenes have exhibited certain carcinogenic activity [8]. Therefore some of these compounds together with other PAHs have been classified by the Environmental Protection Agency (EPA) as priority pollutants [9]. Thus the reduction in the formation of these compounds is a priority when analysing the effectiveness of a catalyst.

Figure 4.1-1(a), correspond to the chromatogram obtained from the tar collected after the experiment carried out with a sand bed and no steam introduced into the reactor. For this tar sample it was observed a typical trend of peak triplets related with the presence of alkadienes, alkenes and n-alkenes. Similar trends have been previously reported in the literature by Williams and Williams [10], when analysing wax derived from the pyrolysis at 500 °C of low density polyethylene (LDPE). Also Predel and Kaminsky [11], reported similar chromatograms from the analysis of light wax from the pyrolysis at 500 °C of high density polyethylene. Therefore the presence of this pattern in the chromatogram shown in Figure 4.1-1(a), might be attributed to the presence of some plastics present in the RDF material subjected to pyrolysis and further gasification at 600 °C. Comparing the chromatograms obtained at 600 °C (Figure 4.1-1(a)), 700 °C (Figure 4.1-1(b)) and 800 °C (Figure 4.1-1(d)), a large decrease in the number of compounds present in the tar samples was observed; which indicates that the tar composition is directly related to the gasification temperature, which has been also previously observed and reported in the literature [12, 13].

A list of the identified compounds at different gasification temperatures 600 °C (Figure 4.1-1(a)), 700 °C (Figure 4.1-1(b)) and 800 °C (Figure 4.1-1(d)), is shown in Table 4.1-2.

Table 4.1-2. Identified compounds in tars from the gasification of RDF at 600, 700 and 800°C

Retention time (min)	Gasification 600°C	Gasification 700°C	Gasification 800°C
5.08-5.09	Toluene	Toluene	—
6.03	1,2,3-Trimethylcyclopentane	—	—
8.16	2,5- dimethylfuran	2,5- dimethylfuran	—
9.95	Ethylbenzene	Ethylbenzene	—
10.66	<i>o</i> -xylene	<i>o</i> -xylene	—
12.11	Styrene	Styrene	—
12.40	Benzene, (1-methylethyl)-	—	—
16.95-16.98	Alpha-methylstyrene	Alpha-methylstyrene	—
17.52-17.60	Benzene-propyl	Benzene-propyl	—
18.86	—	Benzene-2-propenyl	—
19.21	5-butyl,1,3-cyclohexadiene	—	—
19.44	—	Indene	Indene
20.04	—	2-methylphenol	—
20.75	Benzene, 1-ethyl-2-methyl	—	—
21.46	—	4-methylphenol	—
21.52	2-furancarboxaldehyde, 5-methyl	—	—
23.08	1,3,5-trimethylbenzene	—	—
23.44	—	Naphthalene, 2-dihydro	—
24.37	—	Naphthalene	Naphthalene
24.81	1,2-benzenediol	—	—
25.84	2-furancarboxaldehyde	—	—
27.70	—	2-methylnaphthalene	2-methylnaphthalene
27.76	Benzyl Alcohol	—	—
28.16	—	1-methylnaphthalene	1-methylnaphthalene
30.00	—	Biphenyl	Biphenyl
30.30	—	Naphthalene, 1-ethyl	—
30.45	n-C ₁₅	—	—
31.33	—	Acenaphthene	—
31.78	Acenaphthylene	Acenaphthylene	Acenaphthylene
32.71	—	2-methyl-1,1'-biphenyl	—
32.98	n-C ₁₆	—	—
33.30	—	2-naphthalenol	—
34.61	—	1-naphthol	—
35.06	—	Naphthalene, 1-(2-propenyl)	—
35.35	n-C ₁₇	—	—
35.88	—	Fluorene	Fluorene
36.69	<i>Unidentified</i>	—	—
37.61	n-C ₁₈	—	—
37.64	—	9H-Fluorene, 1-methyl	—
39.44	—	Phenanthrene	Phenanthrene
39.67	—	Anthracene	Anthracene
39.75	n-C ₁₉	—	—
41.00	—	2-methylanthracene	—
41.77	—	1-methylanthracene	—
41.79	n-C ₂₀	—	—
43.29	—	2-phenylnaphthalene	—
43.74	n-C ₂₁	—	—
44.64	—	4,5,9,10-tetrahydropyrene	—
44.95	—	Fluoranthene	—
45.61	n-C ₂₂	—	—
45.92	—	Pyrene	Pyrene
46.60	—	<i>m</i> -Terphenyl	—
47.40	n-C ₂₃	—	—
47.63	—	Benzanthrene	—
48.45	—	Benzo[c]fluorene	—
49.11	n-C ₂₄	—	—
50.76	n-C ₂₅	—	—
51.59	—	Triphenylene	—
52.34	n-C ₂₆	—	—

From Table 4.1-2, it was observed that at 600 °C the oxygenated compounds identified were benzenediols, alcohols and decanols, at 700 °C some phenol derivatives such as naphthols, and naphthalenols were detected, whereas at 800 °C the tar composition was dominated by polycyclic aromatic compounds (Table 4.1-2 and Figure 4.1-1).

Changes in the chromatograms according to different bed materials used are shown in Figure 4.1-1(d)-(f). Additionally in Table 4.1-3, are shown the tar compounds and concentrations found in the analysed tar samples obtained using different bed types and a constant gasification temperature of 800 °C.

Table 4.1-3. Influence of the bed type over the tar composition during gasification at 800°C ^a

Retention time (min)	M _w (g mol ⁻¹)	Identified Component	Boiling Point (°C)	Sand / No Steam	Sand/ Steam	5wt% Ni/Al ₂ O ₃	10wt% Ni/Al ₂ O ₃
5.1	92	Toluene	110.6			*	
12.2	104	Styrene	145			**	*
17.2	94	Phenol	181				*
19.5	116	Indene	183		*	**	**
24.4	128	Naphthalene	218	***	***	***	***
27.7	142	2-methylnaphthalene	241-243		*	*	*
28.2	142	1-methylnaphthalene			*	*	*
30.0	154	Biphenyl	256	*	*	*	*
31.8	152	Acenaphthylene	279-280	**	**	**	**
32.4	--	<i>Unidentified</i>	--		*	*	
35.1	166	Fluorene	295	*	*	*	*
36.3	--	<i>Unidentified</i>	--			*	
39.5	178	Phenanthrene	340	**	**	**	*
39.7	178	Anthracene	340	*	*		
44.9	202	Fluoranthene	375	*			
45.9	202	Pyrene	404	*	*		
51.6	228	Triphenylene	425	*			

^a More asterisks mean higher concentration; No asterisks means compound no detected/no present in the sample

In Table 4.1-3 a relative yield is shown by using different asterisks, for the experiments carried out with sand there are no signals from single ring compounds, but the presence of higher aromatic compounds such as pyrene and triphenylene is clear. From Table 4.1-3 and Figure 4.1-1 it was also noted the presence of other aromatic and polyaromatic hydrocarbons such as naphthalene and phenanthrene. Compounds with 3 and 4 aromatic rings (anthracene, fluoranthene, pyrene and triphenylene) were identified in the tar

from the experiments carried out with the sand bed, whereas single ring compounds such as styrene were detected in the tar samples from experiments carried out using catalysts. The change in the presence of 3-4 aromatic ring compounds to a dominance of single ring aromatic compounds could be due to higher molecular weight hydrocarbons which were thermally degraded into lighter hydrocarbons. The lighter hydrocarbons could have been subsequently aromatised via Diels-Alder type reactions due to the thermal degradation of alkanes into alkenes resulting in the formation of single ring compounds such as toluene and styrene [6, 14]. An example of a cycloaddition reaction between a conjugated diene and an alkene to form a single ring structure is shown in Figure 4.1-2.

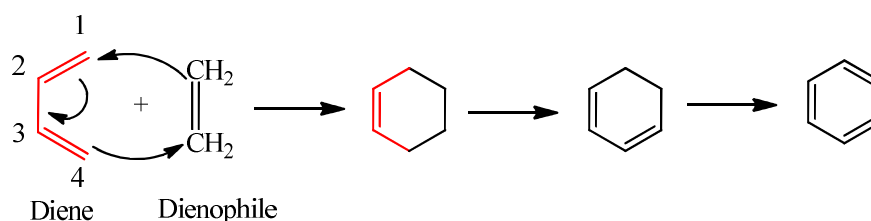


Figure 4.1-2. Diels-Alder cyclo-addition reaction for a single ring structure formation

From Figure 4.1-2, it is observed an overlap between positions 1 and 4 which ends up with the formation of sigma bonds, and a new bond formed between the positions 2 and 3 of the diene.

From Table 4.1-3 and Figure 4.1-1(e)-(f), it was also observed that the use of nickel-based catalysts during the pyrolysis/gasification of RDF, favoured the formation of phenanthrene rather than anthracene, which has been also reported in the literature [7]. It has also been reported the reduction of oxygenated species via de-oxygenation reactions, resulting in an increase in aromatic species [15]. Single ring aromatic compounds identified included benzene and toluene, in addition some PAH compounds such as naphthalene, phenanthrene, fluorene and their alkylated homologues were also identified. From Figure 4.1-1(e)-(f), the small peak shown between biphenyl and acenaphthylene might be due to the presence of acenaphthene, while the peak

that elutes after acenaphthylene labelled as unidentified, might be attributed to dibenzofuran. Both assumptions were based on the m/z spectra reported for both peaks. From the chromatograms reported in Figure 4.1-1, it can also be observed that when catalysts were used, aromatic compounds such as anthracene and pyrene were not present in the tar samples, whereas some single ring aromatic compounds such as styrene and toluene were formed (Figure 4.1-1(e), and Figure 4.1-1(f)).

For all the tar samples analysed the major compounds identified were indene, naphthalene, methylnaphthalenes, biphenyl, acenaphthylene, fluorene, and phenanthrene (Table 4.1-3). These aromatic species have been reported as tar compounds from different thermal processes such as pyrolysis and gasification of both biomass and wastes [3, 16-19]. For example major tertiary tar compounds such as naphthalene, fluorene, phenanthrene, and pyrene have been reported in samples from the pyrolysis of biomass [20]. Benzene has also been reported as tar compound; however as it is highly volatile it might not be captured during the collection and analysing process in our work, hence the resulting samples were deficient in lighter compounds such as benzene.

4.1.3.2 Size Exclusion Chromatography (SEC)

Size exclusion chromatography (SEC) was used to determine the molecular mass of the tar compounds. The SEC chromatograms were plotted as a linear function of the molecular weight in the region between 88 and 240 g mol⁻¹. From the molecular weight distributions obtained, three major regions were identified. The molecular weights of these regions were associated and compared with those compounds identified through GC-MS. In Figure 4.1-3 is shown the molecular mass distribution and their associated compounds for each region.

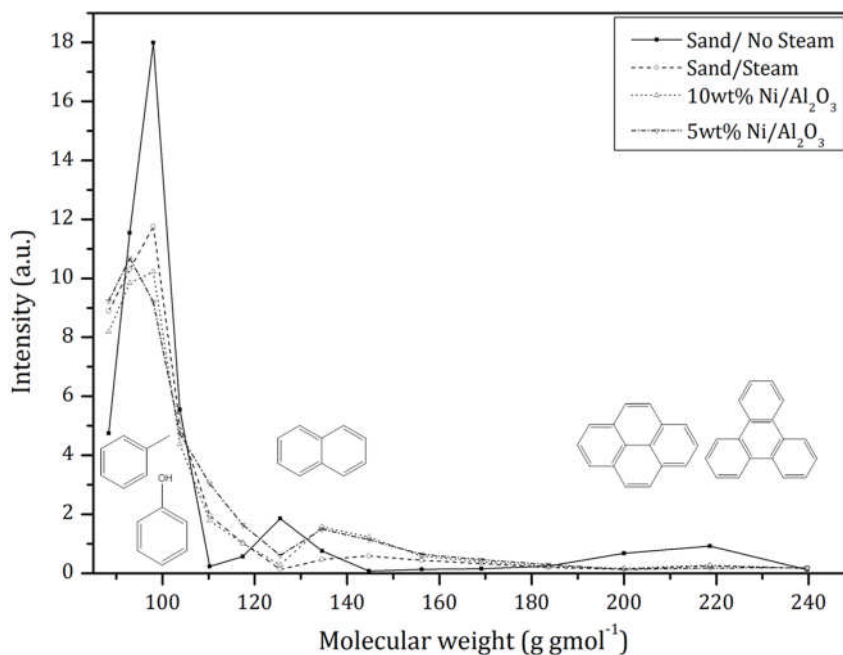


Figure 4.1-3. Size exclusion chromatograms (SEC) of tar samples

The presence of some peaks around 95 g mol⁻¹, was attributed to the presence of toluene and phenol. In the region between 126-135 g mol⁻¹ the data suggest the presence of naphthalene, whereas the peaks shown ~219 g mol⁻¹ might be due to large-molecular mass compounds such as pyrene and triphenylene. The addition of Ni-alumina catalyst into the gasification stage promoted the formation of single and 2-ring aromatic compounds of lower molecular weight as shown within the first region. The SEC from the experiment carried out without steam showed the presence of higher MW species, which might be related to the presence of some 4-ring aromatic compounds such as anthracene, pyrene, and triphenylene.

The molecular weight of the compounds found by SEC (Figure 4.1-3), compared with the identified compounds by GC-MS (Figure 4.1-1) are in good agreement. The molecular weights reported by SEC were compared with possible compounds reported in the literature and a probable match and comparison is shown in Figure 4.1-4.

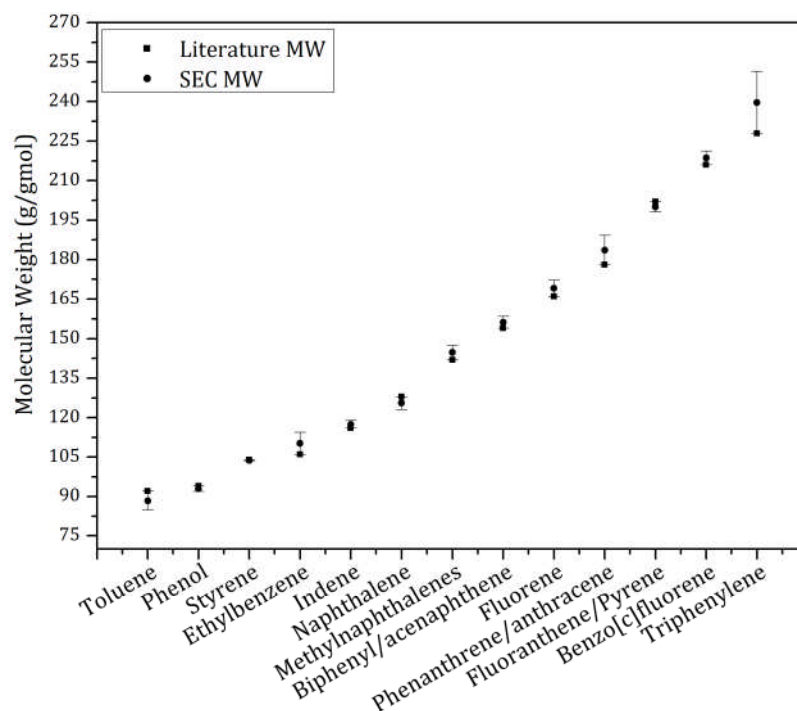


Figure 4.1-4. Possible assignment of MW reported by SEC

4.1.3.3 FTIR Analysis

The FTIR analysis of tar samples was carried out with the aim to identify the chemical functional groups present in the samples derived from different Ni catalysts. In order to carry out the FTIR analysis it was necessary to prepare the tar samples; the preparation pathway is shown in Figure 4.1-5.

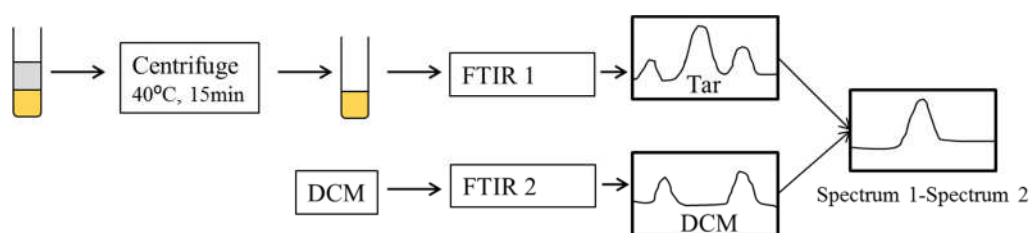


Figure 4.1-5. Sample preparation, FTIR analysis and interpretation

The original sample was a heterogeneous mixture containing tar/oil/H₂O/dichloromethane (DCM) in different proportions. The water was separated from the original sample by simple decantation; afterwards the remaining sample was subjected to a centrifuge process at 40 °C for 15 minutes, as the boiling point of the DCM is around 40 °C. The resulting liquid sample was subjected to FTIR analysis. As some traces of the DCM might have remained in

the original sample after the centrifuge process, a parallel FTIR analysis for DCM was carried out. The resulting spectra were compared and a final spectral pattern for each sample was obtained.

The bands in the FTIR spectrum resulted from different vibrations and rotations in the bonds of a molecule. Vibrational motions can be stretching and bending, and usually occur in diatomic or triatomic molecules. Stretching vibrations are related with changes in the interatomic distance along the axis of the bond, whereas bending vibrations are related with changes in the angle of the bonds. Bending vibrations include wagging, twisting, rocking, and scissoring. Examples of some of these vibrations for CH₂ groups, are graphically shown in Figure 4.1-6 [21].

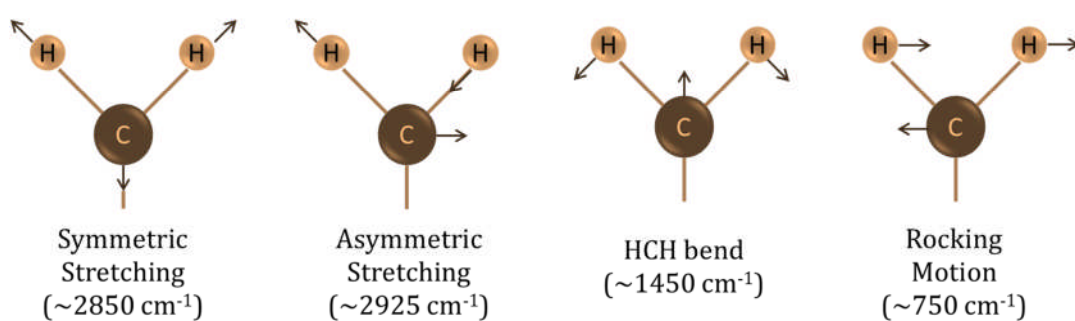


Figure 4.1-6. Types of CH₂ vibrations

The FTIR results obtained from the analysis of tar samples are shown in Figure 4.1-7.

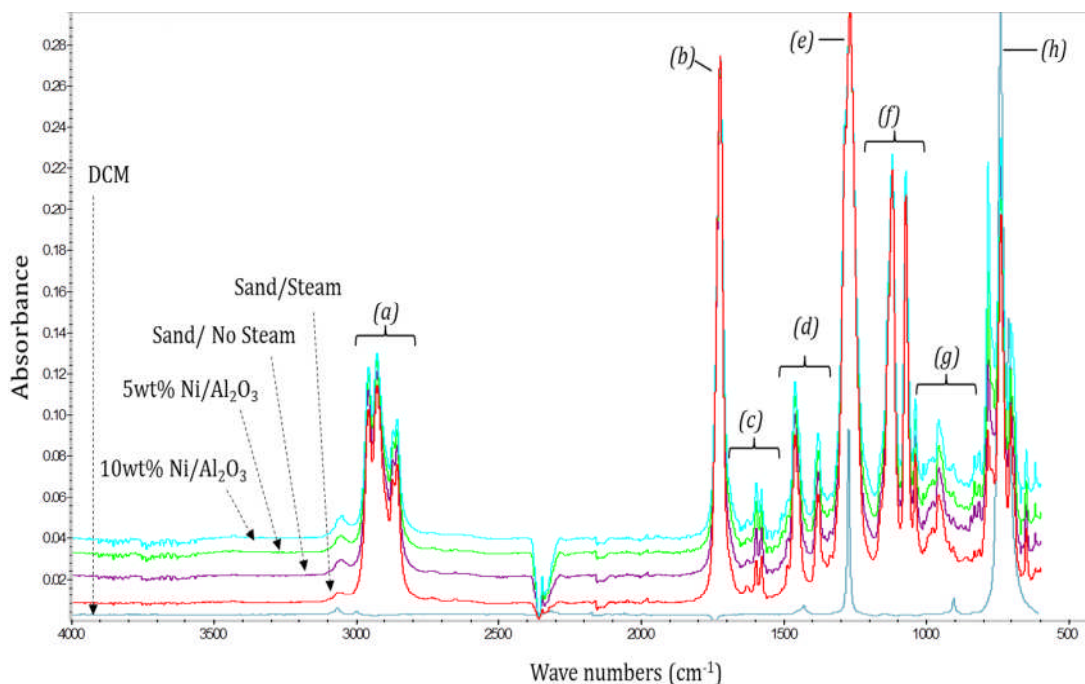


Figure 4.1-7. Fourier transform infrared spectra (FTIR) of tar from pyrolysis-gasification of RDF at frequency of 4000-650cm⁻¹

A difference from the GC-MS chromatograms, the absorption bands from the FTIR spectra analysis are assigned to functional groups instead of specific compounds. An example of the correlation of bond stretching and IR absorption bands is shown in the following Table 4.1-4 [22].

Table 4.1-4. Bond stretching and IR absorption

Type of Bond	Functional Group	Family of compounds	Wavenumber range (cm ⁻¹)
<i>Single</i>	-C - H	Alkanes	2850-3300
	= C - H	Alkenes, aromatics	3000-3100
	≡ C - H	Alkynes	3300-3320
	O - H	Alcohols	3200-3600
	N - H	Amines	3300-3500
<i>Double</i>	C = C	Alkenes, aromatics	1600-1680
	C = O	Carbonyls	1680-1750
		Aldehydes, ketones	1710-1750
		Carboxylic acids	1700-1725
		Esters, amides	1680-1750
		C = N	Imines
<i>Triple</i>	C ≡ C	Alkynes	2100-2200
	C ≡ N	Nitriles	2200-2300

From Figure 4.1-7 it was observed that the tar samples showed a similar pattern, which indicates a similarity among the functional groups present in the samples. The peaks observed between the region 3000 and 2850 cm^{-1} (a) correspond to aliphatic hydrocarbons, specifically to stretching of the type C-H bonds, the peaks between 1450 and 1350 cm^{-1} (d) represent C-H deformation vibrations that might be related with $-\text{CH}_3$, CH_2 and C-H groups [23]. The absorption peaks detected around 1625 and 1575 cm^{-1} (c) as well as those between 950-800 cm^{-1} (g) indicate the presence of mono and polycyclic aromatic compounds. It has been reported that the double bond C=C stretching vibrations from aromatic compounds appear within the region 1430-1650 cm^{-1} [24]. The peak between 1675-1352 cm^{-1} (b) represents double carbon bonds (C=C) from the alkene functional group. Alkanes, alkenes and alkynes functional groups have been previously reported in the literature, for example when analysing pyrolytic oils from the thermochemical conversion of waste paper [25]. The signal around 1100 cm^{-1} (f) might correspond to single bond interactions between carbon and hydrogen. The region between 500-1500 cm^{-1} normally contains overlapped absorption bands from both bending and stretching vibrations, this region is known as fingerprint region and sometimes is complicated to assign them to an specific functional group (e, f, g, h).

The functional groups identified in the FTIR spectra support the GC-MS results, as it was confirmed the aromatic nature of the analysed tar samples.

4.1.4 Summary

In this section of the work, the effects of both the gasification temperature and the catalyst bed type were studied regarding the yield and composition of the gas fraction and tar by-product. It was found that the composition of the produced syngas was highly influenced by the addition of steam into the gasification stage. Even more it was found that the type of material used to promote catalytic reactions in the second gasification stage also modified the hydrogen content in the produced gas. For example by using a 10wt.% Ni/ α - Al_2O_3 catalyst, the hydrogen concentration was increased by almost 14%

compared with the experiments carried out using a silica-sand bed under similar conditions. Also it was noted that methane and C₂-C₄ gas concentrations were reduced by about 10% and 5% respectively.

By combining the techniques of GC-MS, SEC, and FTIR for tar characterisation, it was possible to obtain a general idea about the different compounds contained in the tar samples derived from the pyrolysis-gasification of RDF. Additionally the effects of both the gasification temperature and catalyst bed on the liquid fraction were also studied. The tar obtained at gasification temperatures around 800 °C was found to contain PAH, consisting mainly of naphthalene, biphenyl, acenaphthylene, fluorene, and phenanthrene. The PAH were assumed to be formed via Diels-Alder reactions and deoxygenation reactions. The use of nickel-alumina catalysts promoted the reduction of 3 and 4-ring aromatic compounds and helped to increase the hydrogen yield in the syngas. It was found that lower gasification temperatures of 600 °C promoted the formation of oxygenated compounds; whereas at higher temperatures the formation of aromatic compounds was preferred.

References

1. Li, J., J. Liu, S. Liao, X. Zhou, and R. Yan, *Syn-Gas Production from Catalytic Steam Gasification of Municipal Solid Wastes in a Combined Fixed Bed Reactor*, in *International Conference on Intelligent System Design and Engineering Application (ISDEA)*. 2010: Changsha. p. 530-534.
2. Galvagno, S., Casu, E., Casciaro, G., Martino, M., Russo, A., Portofino, S., *Steam Gasification of Refuse-Derived Fuel (RDF): Influence of Process Temperature on Yield and Product Composition*. *Energy Fuels*, 2006. 20(5): p. 2284-2288.
3. Miccio, F., B. Piriou, G. Ruoppolo, and R. Chirone, *Biomass gasification in a catalytic fluidized reactor with beds of different materials*. *Chemical Engineering Journal*, 2009. 154(1-3): p. 369-374.
4. Liu, J., J. Li, and S. Liao. *Fuel gas production from catalytic steam gasification of municipal solid wastes*. in *2010 2nd Conference on Environmental Science and Information Application Technology (ESIAT)*. 2010: IEEE.
5. Zhang, Q., L. Dor, D. Fenigshtein, W. Yang, and W. Blasiak, *Gasification of municipal solid waste in the Plasma Gasification Melting process*. *Applied Energy*, 2012. 90(1): p. 106-112.
6. Depeyre, D., C. Flicoteaux, and C. Chardaire, *Pure n-hexadecane thermal steam cracking*. *Industrial & Engineering Chemistry Process Design and Development*, 1985. 24(4): p. 1251-1258.
7. Williams, P.T. and P.A. Horne, *The influence of catalyst type on the composition of upgraded biomass pyrolysis oils*. *Journal of Analytical and Applied Pyrolysis*, 1995. 31(0): p. 39-61.
8. Williams, P.T. and P.A. Horne, *Analysis of aromatic hydrocarbons in pyrolytic oil derived from biomass*. *Journal of Analytical and Applied Pyrolysis*, 1995. 31: p. 15-37.
9. Dabestani, R. and I.N. Ivanov, *A Compilation of Physical, Spectroscopic and Photophysical Properties of Polycyclic Aromatic Hydrocarbons*. *Photochemistry and Photobiology*, 1999. 70(1): p. 10-34.
10. Williams, P.T. and E.A. Williams, *Fluidised bed pyrolysis of low density polyethylene to produce petrochemical feedstock*. *Journal of Analytical and Applied Pyrolysis*, 1999. 51(1-2): p. 107-126.
11. Predel, M. and W. Kaminsky, *Pyrolysis of mixed polyolefins in a fluidised-bed reactor and on a pyro-GC/MS to yield aliphatic waxes*. *Polymer Degradation and Stability*, 2000. 70(3): p. 373-385.
12. Elliott, D.C., *Relation of Reaction Time and Temperature to Chemical Composition of Pyrolysis Oils*, in *Pyrolysis Oils from Biomass*. 1988, American Chemical Society. p. 55-65.
13. Gilbert, P., C. Ryu, V. Sharifi, and J. Swithenbank, *Tar reduction in pyrolysis vapours from biomass over a hot char bed*. *Bioresource Technology*, 2009. 100(23): p. 6045-6051.
14. Cyprés, R., *Aromatic hydrocarbons formation during coal pyrolysis*. *Fuel Processing Technology*, 1987. 15: p. 1-15.

15. Pattiya, A., J.O. Titiloye, and A.V. Bridgwater, *Fast pyrolysis of cassava rhizome in the presence of catalysts*. Journal of Analytical and Applied Pyrolysis, 2008. 81(1): p. 72-79.
16. Dufour, A., E. Masson, P. Girods, Y. Rogaume, and A. Zoulalian, *Evolution of Aromatic Tar Composition in Relation to Methane and Ethylene from Biomass Pyrolysis-Gasification*. Energy & Fuels, 2011. 25(9): p. 4182-4189.
17. Williams, P.T. and S. Besler, *Polycyclic aromatic hydrocarbons in waste derived pyrolytic oils*. Journal of Analytical and Applied Pyrolysis, 1994. 30(1): p. 17-33.
18. Garcia-Perez, M., *The formation of Polyaromatic Hydrocarbons and Dioxins During pyrolysis: A review of the Literature with descriptions of Biomass Composition, Fast pyrolysis Technologies and Thermochemical Reactions*. 2008, Washington State University: Washington. p. 57.
19. Bangala, D.N., N. Abatzoglou, J.-P. Martin, and E. Chornet, *Catalytic Gas Conditioning: Application to Biomass and Waste Gasification*. Industrial & Engineering Chemistry Research, 1997. 36(10): p. 4184-4192.
20. Su, Y., Y. Luo, Y. Chen, W. Wu, and Y. Zhang, *Experimental and numerical investigation of tar destruction under partial oxidation environment*. Fuel Processing Technology, 2011. 92(8): p. 1513-1524.
21. Lee, M., *Identifying an Unknown Compound by Infrared Spectroscopy*, in *Modular laboratory program in Chemistry*, J. Jeffers, Editor. 1997, Chemical Education Resources, Inc.: Palmyra, Pennsylvania. p. 12.
22. Johnson, A.W., *Invitation to Organic Chemistry*. 1999: Jones and Bartlett Publishers.
23. Williams, E.A. and P.T. Williams, *Analysis of products derived from the fast pyrolysis of plastic waste*. Journal of Analytical and Applied Pyrolysis, 1997. 40-41(0): p. 347-363.
24. Krishnakumar, V., N. Surumbarkuzhali, and S. Muthunatesan, *Scaled quantum chemical studies on the vibrational spectra of 4-bromo benzonitrile*. Spectrochimica Acta Part A: Molecular and Biomolecular Spectroscopy, 2009. 71(5): p. 1810-1813.
25. Nurul Islam, M., M. Rafiqul Alam Beg, and M. Rofiqul Islam, *Pyrolytic oil from fixed bed pyrolysis of municipal solid waste and its characterization*. Renewable Energy, 2005. 30(3): p. 413-420.

CHAPTER 5. PREPARATION, CHARACTERIZATION AND EVALUATION OF NICKEL BASED CATALYSTS

This Chapter was divided in three different sections, each one mostly dedicated to the study of nickel-based catalysts for the hydrogen production. The catalytic activity was assessed using a two-stage pyrolysis-gasification reaction system described in Chapter 3, Section 3.3. A brief description of each section is given next.

Section 5.1., includes results obtained from the preparation of diverse Ni/SiO₂ catalysts prepared by sol-gel and impregnation methods. Some properties such as metal loading and the addition of metal promoters were also studied regarding the catalysts properties. The catalytic activity towards hydrogen production, tar composition and formation was evaluated for all the catalysts.

Section 5.2., was dedicated to the analysis of varying the nickel to citric acid ratio (Ni:CA) into the final characteristics of a series of three Ni/SiO₂ catalysts. The catalytic performance was evaluated in a similar way as in the previous section, considering the hydrogen and tar yields.

Finally the Section 5.3., was focused on the characterisation of a series of Ni/SiO₂ catalysts obtained using two different homogeneous precipitation (HGP) methods. The final properties of the catalysts were correlated with their performance for hydrogen production.

5.1 Ni/SiO₂ catalysts: Influence of metal loading, metal promoters and preparation method on catalyst characteristics

There are diverse parameters influencing the properties of the final catalysts, such as the preparation method, and the type of oxide support namely Al₂O₃ [1, 2], and SiO₂ [3-5]. Al₂O₃ was used as oxide support in the previous Chapter 4, however SiO₂ has been also largely used as oxide support due to promotes a higher metallic surface area and higher sintering resistance compared with other oxide supports [6]. In addition some authors have reported that the use of silica oxide as support also contributes to improvement of the thermal stability and porous properties of the resulting catalyst [4, 7, 8]. In order to further improve the catalytic activity and selectivity of catalysts, diverse metals such as Ce, Al, and Mg have been added to Ni/SiO₂ catalysts as metal promoters. The enhancement of steam adsorption and the reduction in carbon deposition over the catalyst surface have been reported in the literature as positive effects of adding metal promoters [9-11].

This section describes and compares the influence of impregnation and sol-gel preparation methods, on Ni/SiO₂ catalyst characteristics. In addition the influence of the nickel loading (5wt%, 10wt%, 20wt%, and 40wt%) and the further addition of Mg, Al, and Ce as metal promoters were studied over catalysts properties. Furthermore the catalysts were analysed for their efficiency towards hydrogen production and tar reduction during the pyrolysis-gasification of RDF.

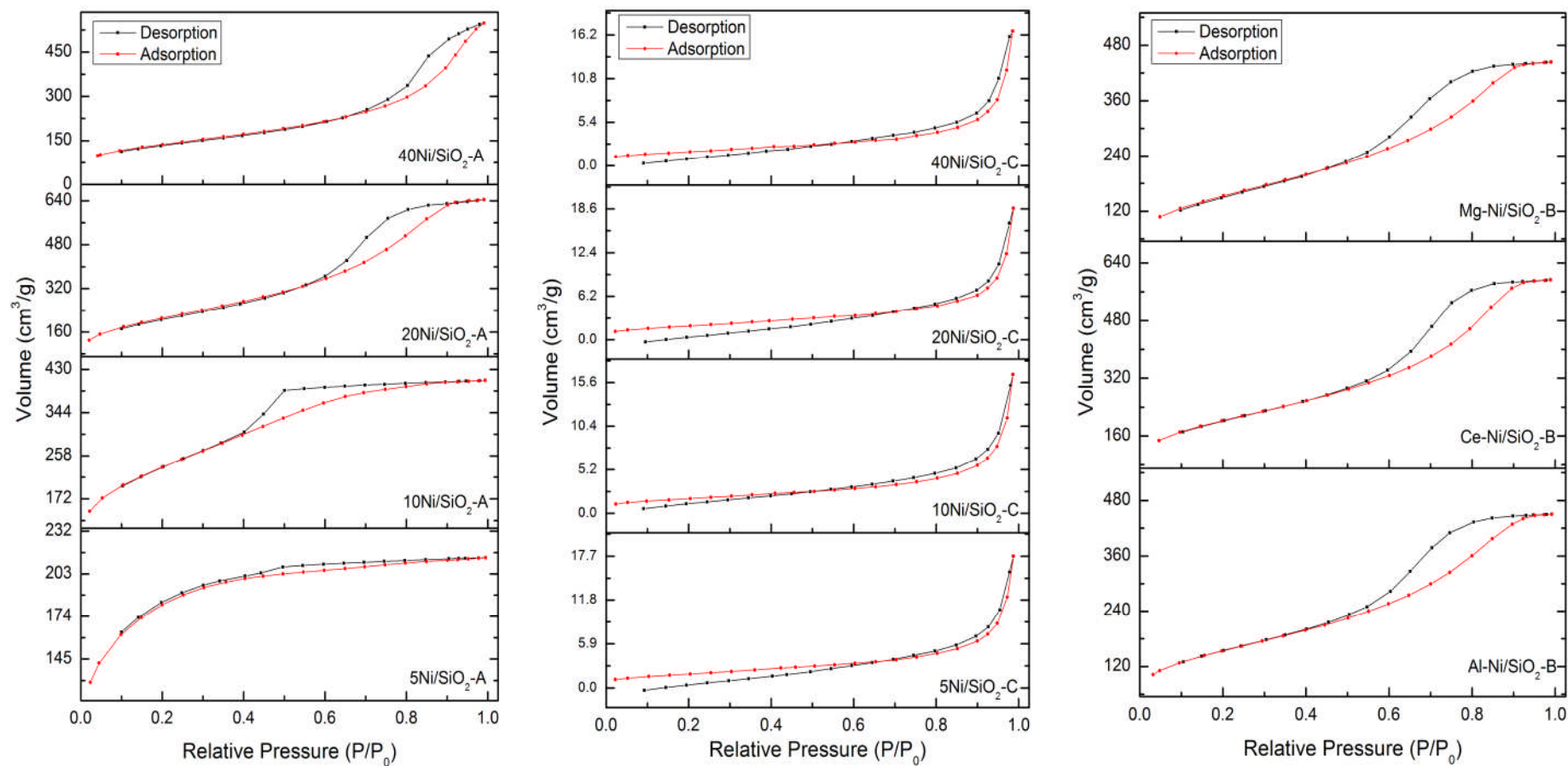
5.1.1 Characterization of fresh Ni/SiO₂ catalysts

The details about the Ni/SiO₂ catalysts used in this section are described in Chapter 3, Section 3.2.2.2. The identification and properties of the catalyst used for this section of the work are detailed in Table 5.1-1.

Table 5.1-1. Description and properties of the prepared Ni/SiO₂ catalysts

Catalyst ID	Ni loading	Metal addition	Preparation method
5Ni/SiO ₂ -A	5 wt%		<i>SOL-GEL</i>
10Ni/SiO ₂ -A	10 wt%		
20Ni/SiO ₂ -A	20 wt%	—	
40Ni/SiO ₂ -A	40 wt%		
Mg-Ni/SiO ₂ -B		<i>Mg</i>	
Al-Ni/SiO ₂ -B	20 wt%	<i>Al</i>	
Ce-Ni/SiO ₂ -B		<i>Ce</i>	
5Ni/SiO ₂ -C	5 wt%		<i>IMPREGNATION</i>
10Ni/SiO ₂ -C	10 wt%		
20Ni/SiO ₂ -C	20 wt%	—	
40Ni/SiO ₂ -C	40 wt%		

The fresh catalysts listed in Table 5.1-1, were analysed to determine their surface area and porous properties according to the BET technique described in Chapter 3, Section 3.4.2. The N₂ adsorption and desorption isotherms were obtained at 77K, the resulting curves for the catalysts are shown in Figure 5.1-1.



(a) 5-40wt% Ni/SiO₂ SOL-GEL

(b) 5-40wt% Ni/SiO₂ IMPREGNATION

(c) 20wt% Ni/SiO₂ Mg, Ce, Al

Figure 5.1-1. BET Adsorption-desorption isotherms from fresh Ni/SiO₂ catalysts

The surface area of the catalysts was calculated using the MultiPoint Brunauer, Emmett & Teller (BET) method, the micropore and mesoporous volumes were calculated using the Dubinin-Radushkevich (DR) method, and the total pore volume and pore diameter were obtained by the Barrett, Joyner & Halenda (BJH) method. The amount of N₂ adsorbed at relative pressures near unity corresponds to the total amount adsorbed for both micropores (generally filled at low relative pressures) and mesopores (filled by capillary condensation at relative pressures above 0.2). Therefore, the mesopore volume might be obtained by subtracting the micropore volume (obtained using the D-R equation), from the total amount adsorbed determined at P/P₀=0.95 [12-14]. The results from these calculations are shown in Table 5.1-2.

Table 5.1-2. Surface area and porous properties of fresh Ni/SiO₂ catalysts

Catalyst	Surface area ¹ (m ² g ⁻¹)	Micropore volume ² (cm ³ g ⁻¹)	Mesoporous volume ² (cm ³ g ⁻¹)	Total pore volume ³ (cm ³ g ⁻¹)	Pore diameter ³ (nm)
5Ni/SiO ₂ -A	595.4	0.322	0.008	0.034	3.776
10Ni/SiO ₂ -A	836.9	0.398	0.231	0.315	3.820
20Ni/SiO ₂ -A	756.4	0.389	0.602	0.884	6.608
40Ni/SiO ₂ -A	481.6	0.260	0.492	0.755	12.612
Mg-Ni/SiO ₂ -B	554.4	0.281	0.400	0.583	5.660
Al-Ni/SiO ₂ -B	552.6	0.281	0.410	0.587	5.654
Ce-Ni/SiO ₂ -B	717.9	0.389	0.524	0.771	6.606
5Ni/SiO ₂ -C	6.9	0.003	0.010	0.029	3.172
10Ni/SiO ₂ -C	6.4	0.003	0.009	0.025	3.796
20Ni/SiO ₂ -C	9.7	0.003	0.010	0.019	3.374
40Ni/SiO ₂ -C	6.3	0.003	0.010	0.026	3.764

¹ MultiPoint Brunauer, Emmett & Teller (BET) Method

² Dubinin-Radushkevich (DR) Method

³ Barrett, Joyner & Halenda (BJH) Method

From Figure 5.1-1(a), the isotherm given by the 5Ni/SiO₂-A catalyst was identified as Type I, based on the IUPAC classification [15]. This type of isotherm generally shows no hysteresis loop and is associated with microporous solids with relatively small external surface area. The limiting uptake of this isotherm is normally governed by the accessible micropore rather than by the internal surface area. Table 5.1-2 shows the surface area for the

5Ni/SiO₂-A catalyst was around 600m² g⁻¹ with a very low mesoporous volume (0.008cm³ g⁻¹) and low total pore volume (0.034cm³ g⁻¹); which confirms the microporous properties of this catalyst. The resulting trend from the isotherm from the 10Ni/SiO₂-A catalyst seems to be a combination of the isotherms Type I and Type IV (Figure 5.1-1(a)). It was also distinguished by a hysteresis loop of the type H2 indicating the multilayer region of the isotherm, around P/P₀=0.5. This trend is associated with very complex structures and interconnected pores with different shapes and sizes [16]. The higher value of the surface area for sol-gel catalysts (Table 5.1-2), was around 800m² g⁻¹ for the 10Ni/SiO₂ catalyst. However, this catalyst also showed lower values for mesopores and total pore volume compared with the catalysts prepared using nickel loadings of 20wt.% and 40wt.%. Both 20Ni/SiO₂-A and 40Ni/SiO₂-A catalysts showed isotherms of the Type IV (Figure 5.1-1(a)) generally associated with well-defined mesoporous materials with fairly narrow pore size distribution [17]. Additionally from Figure 5.1-1(a), two main stages in the adsorption-desorption isotherms might be identified for both 20Ni/SiO₂-A and 40Ni/SiO₂-A catalysts; the first one appears at low pressures indicating an adsorbate monolayer formation on the pore surface; then a second stage takes place related to the multilayer formation at higher pressures [18]. The upward deviation observed into the multilayer region for 20Ni/SiO₂-A and 40Ni/SiO₂-A isotherms (top Figure 5.1-1(a)), corresponds to hysteresis of the H1-Type, which is characteristic of mesoporous solids having uniform pore structures [19, 20]. In addition, the beginning of the capillary condensation in the pores was indicated by the onset of the hysteresis loop [18]. In Table 5.1-2 relatively high mesoporous volumes of around 0.6 and 0.5cm³ g⁻¹ for the 20Ni/SiO₂-A and 40Ni/SiO₂-A catalysts respectively, were obtained from the DR calculation method. Kim et al [21], reported that mesoporous materials tend to have ordered pore structures with narrow pore size distribution, high surface area and large pore volumes. For the sol-gel catalysts it was observed that as the Ni loading increased from 10wt.% up to 40wt.%, the total pore volume and mesoporous volume of the catalysts were increased (Table 5.1-2). It was also observed that the hysteresis loop became more pronounced and was slightly shifted to higher pressures in the multilayer region (Figure 5.1-1(a)), as the

metal loading was increased; this trend is related to a displacement of the beginning of the capillary condensation in pores [18].

From Table 5.1-2, the Ni/SiO₂ sol-gel catalysts presented a wide pore diameter distribution, especially at higher Ni loadings, leading to larger pore diameters. The pore diameter distribution for the catalysts prepared by sol-gel increased from 3.77nm to 12.61nm as the Ni loading was increased. Wu and Williams [3], also reported that the average pore size of sol-gel Ni/SiO₂ catalysts seemed to increase as the Ni loading was increased from 10 wt.% to 50 wt.%.

All the isotherms plotted for the impregnated catalysts (Figure 5.1-1(b)), are from the Type III with no hysteresis loop which might be indicative of catalysts with weak adsorbent-adsorbate interactions [16]. From Table 5.1-2, it was also observed a major reduction in the surface area values reported for the impregnated catalysts when compared with those values obtained from the sol-gel catalysts. Also similar values for pore diameter were observed for all the impregnated catalysts, this might be due to the similar trends shown in the isotherms, which means very similar characteristics for the impregnated catalysts, and very low influence of the metal loading.

Comparing the isotherms plotted for the 20wt.% catalysts prepared by both impregnation and sol-gel methods (Figure 5.1-1(a) and (b)), the difference observed in the trends could be related with both the preparation method and the raw materials used during the catalysts preparation. For example the silica gel in the sol-gel catalysts, was formed through the interaction between TEOS and citric acid, which has been reported to provide mesoporous amorphous silica with high specific surface areas. On the other hand, the silica source used during the catalysts preparation by impregnation came directly from silicon (IV) oxide, which typically leads in a material with weak adsorbent-adsorbate interactions. Pina and collaborators [22], have reported weak interactions in the substrate and a great tendency to agglomeration for Ni/SiO₂ catalysts prepared by the impregnation method. The effect of the preparation method has been previously studied on catalysts used for ethanol and methanol reforming,

reporting better characteristics and performance for sol-gel prepared catalysts [3, 7]. Tomiyama et al [4], also reported larger surface areas for Ni/SiO₂ catalysts prepared by sol-gel, compared with the same catalysts prepared by incipient wet impregnation; which is in accordance to the values reported in the present work (Table 5.1-2).

In Figure 5.1-1c, are depicted the isotherms for the catalysts impregnated with Mg, Ce, and Al. From Figure 5.1-1(c) similar trends were observed for the three catalysts and were identified as isotherms of the type IV, which are characteristic of mesoporous materials. From Table 5.1-2, similar BET surface areas around 550m² g⁻¹ and pore diameter values about 5.6nm, were reported for both Mg and Al-Ni/SiO₂-B catalysts. Whereas the Ce-Ni/SiO₂-B catalyst reported a surface area higher than 700m² g⁻¹, and 6.6nm pore diameter. This difference suggests that the addition of cerium has a minor influence on the surface area or pore size of the prepared catalysts; but a reduction in these two parameters can be noticed with the addition of Mg and Al. Also the addition of Mg and Al could lead to the modification of active sites on the metal surface or in changes of the geometric structure of the catalyst surface, as has been reported by Wang et al [23]. From Table 5.1-2, a reduction in the mesoporous volume of this series of metal-promoted catalysts was observed, when compared with the mesoporous volume of the 20Ni/SiO₂-A catalyst. This reduction effect in the mesopore volume, has been previously reported by Ding and Yan [24], during the addition of oxide promoters to Ni/Al₂O₃ catalysts. They suggested that the oxide promoters, MgO and CeO₂, might be concentrated on the outer layer of the support, whereas the nickel metal was dispersed in the support pores; as a result a reduction in mesopore volume might be promoted.

5.1.2 Test of the catalytic activity of Ni/SiO₂ catalysts

Once all the Ni/SiO₂ catalysts were characterised, all of them were tested in the two-stage gasification system previously described in Chapter 3, Section 3.3. The activity of the catalysts was tested regarding the composition of the final syngas, specifically towards hydrogen production, and also this was related to

their efficiency to promote tar cracking reactions during the steam reforming stage. The gas composition of the gases derived from the pyrolysis-gasification of RDF was analysed and reported on a N₂ free basis. The gas yield included the initial sample weight and the injected water for each experiment. The gas composition and gas yields are presented in Table 5.1-3.

Table 5.1-3. Gas yield and composition using diverse Ni/SiO₂ catalysts

Catalyst	Gas composition (Vol.%, N ₂ free)					Gas Yield (wt.%)	Mass Balance (wt.%)
	CO	H ₂	CO ₂	CH ₄	C ₂ -C ₄		
5Ni/SiO ₂ -A	28.6	41.2	15.4	8.8	6.1	45.7	94.8
10Ni/SiO ₂ -A	24.1	47.4	16.5	8.1	3.8	58.6	98.0
20Ni/SiO ₂ -A	18.4	57.9	20.7	2.2	0.8	68.7	91.6
40Ni/SiO ₂ -A	16.5	56.2	25.6	1.4	0.4	72.6	98.7
Ce-Ni/SiO ₂ -B	19.0	53.6	24.1	2.6	0.7	64.9	98.1
Mg-Ni/SiO ₂ -B	20.1	54.3	22.4	2.6	0.6	58.6	98.5
Al-Ni/SiO ₂ -B	21.6	49.6	22.0	5.3	1.5	46.4	94.2
5Ni/SiO ₂ -C	27.6	35.6	22.3	9.7	4.8	39.9	93.9
10Ni/SiO ₂ -C	29.2	37.7	20.5	8.8	3.8	46.8	94.6
20Ni/SiO ₂ -C	21.7	40.6	26.6	7.2	3.9	51.9	99.0
40Ni/SiO ₂ -C	22.3	44.1	25.8	5.7	2.1	55.4	98.6

From Table 5.1-3, it was observed that the H₂ concentration of the produced gases for the series of sol-gel catalysts (series A), was increased as the Ni loading was increased. However for the 40Ni/SiO₂-A catalyst, the hydrogen concentration was slightly decreased. This effect might be related to the catalyst properties, for example the mesoporous volume for the 40Ni/SiO₂-A catalyst was 0.49 cm³ g⁻¹, whereas for the 20Ni/SiO₂-A catalyst it was 0.60 cm³ g⁻¹ (Table 5.1-2). This difference might be due to the promotion of steam reforming reactions as the Ni loading increased. Therefore it was an increase in the hydrogen production for the sol-gel series of catalysts. From Table 5.1-3, it was also noted that the concentration of CO₂ increased as the Ni loading was increased. In this case the pore size of the catalyst may influence the CO₂ concentration, which coincides with the trend reported in Table 5.1-2 for the pore size of the sol-gel catalysts. Thus the highest pore size and highest CO₂ concentration of about 12nm, and 25.6 vol.% respectively, corresponded to the

40Ni/SiO₂-A catalyst. Methane (CH₄) and light hydrocarbon (C₂-C₄) concentrations were considerably reduced as the Ni loading was increased; again this trend was related to the catalysts physical properties, specifically with the pore size. From Table 5.1-2 it can be seen that there was an increase in the pore size as the metal loading was increased, whereas the concentrations of both CH₄ and C₂-C₄ decreased up to 1.4 vol.% and 0.4 vol.% respectively. The increase in the H₂ and CO₂ concentrations and the decrease in the concentration of CH₄ and C₂-C₄ (Table 5.1-3), might be due to the conversion of CO into CO₂ by water-gas shift and hydrocarbon reforming reactions, including methane reforming [25].

Zapata et al [26], reported that the addition of Ce to Ni/SiO₂ catalyst resulted in the promotion of methane reforming reactions and also in an improvement in the stability of the catalyst. Also the addition of Mg to different supported Ni-based catalysts has been reported by Choudhary et al [11], in order to enhance the steam adsorption capability, to stabilize the Ni and to prevent catalyst sintering. In this work Mg, Ce, and Al were used as metal promoters in order to improve the catalysts activity towards hydrogen production. From Table 5.1-3 it can be observed that about 54vol.% of hydrogen was obtained in the produced gas when using Ce-Ni/SiO₂-B and Mg-Ni/SiO₂-B catalysts, whereas less than 50vol.% of H₂ was attained using the Al-Ni/SiO₂-B catalyst. A similar trend was reported for the CH₄ concentration as Ce-Ni/SiO₂-B and Mg-Ni/SiO₂-B catalysts resulted in concentrations of 2.6vol%, while using the Al-Ni/SiO₂-B catalyst a CH₄ concentration of 5.3 vol.% was obtained. In addition, similar CO₂ concentrations (~22 vol.%), were obtained using Mg and Al added Ni/SiO₂-B catalysts, whereas Ce addition showed a CO₂ concentration of 24 vol.%. From the catalysts properties shown in Table 5.1-2, it was expected that the addition of Mg and Al to the Ni/SiO₂-B catalyst would produce a similar performance regarding gas composition based on surface area and porosity characteristics. However, a more similar catalytic activity for both Ce and Mg added Ni/SiO₂-B catalysts was observed, whereas using the Al-Ni/SiO₂-B catalyst resulted in lower H₂, and higher CH₄ and C₂-C₄ compositions. A better performance was observed when using Mg and Ce as metal promoters instead of using Al.

However, there was not an improvement towards hydrogen production by using any of these three metal promoters, when compared with the original 20Ni/SiO₂-A catalyst prepared by conventional sol-gel method.

The influence of the preparation method was also studied by using the impregnation method and varying the metal loadings from 5-40wt%, and these catalysts were assigned as C series (Table 5.1-1). From Table 5.1-3, the highest H₂ concentration of about 44vol.% was obtained using the 40Ni/SiO₂-C catalyst. The use of 10Ni/SiO₂-C and 20Ni/SiO₂-C catalysts resulted in H₂ concentrations of ~40 vol.%, whereas a hydrogen concentration of 36vol.% was obtained using the 5Ni/SiO₂-C. The CH₄ and C₂-C₄ concentrations were found to be reduced for all the impregnated catalysts, when the Ni loading was increased.

From Table 5.1-3, the gas yield of the sol-gel catalysts (series A), was increased from 45.7 to 72.6 wt.% as the nickel loading was increased from 5 to 40 wt.%. A similar trend was observed for the impregnated catalysts (series C), but with lower gas yields, increasing from 39.9 to 55.4 wt.% as the Ni loading was increased from 5 to 40 wt.%. Slight differences in the gas yield can also be attributed to changes in the amount of water steam injected during each experiment. It was expected that the addition of Ce, Mg, and Al as metal promoters into the Ni/SiO₂ sol-gel catalyst, would increase the gas yield; however using the Al-Ni/SiO₂-B catalyst resulted in a reduction in the gas yield (46.4 wt.%), that was similar to that obtained using the 5Ni/SiO₂-A and 10Ni/SiO₂-C catalysts. The addition of Ce and Mg into the Ni/SiO₂ catalyst, resulted in gas yields of between 60 and 65 wt.% that were lower than the gas yield obtained using the 20Ni/SiO₂-A catalyst (~69 wt.%). The reduction in the catalytic activity of the Al-Ni/SiO₂-B catalyst, in terms of gas yield and hydrogen production, might be related to a lower Ni metal dispersion; as this property can be sometimes decreased by the addition of inappropriate promoters [24], thus the catalytic activity might also be influenced [27]. There has been much research on the influence of metal promoters in relation to Ni/SiO₂ catalysts properties and activity for methane and CO₂ conversion [9, 28-30]. For example Garcia et al [9], reported that the addition of MgO into nickel-based catalysts can

lead to a H₂ yield of 40% stoichiometric during the steam reforming of bio-oil, whereas methane conversions higher than 90% can be attained using similar catalysts [11, 31]. The addition of the CeO promoter was also studied during the autothermal reforming of methane and partial oxidation of methane to syngas, leading to a CH₄ conversion up to 100% and attaining a H₂/CO maximum of 3.5 using Ni/Ce₃₀Al₇₀O₈ catalyst [10].

5.1.2.1 Performance of Ni/SiO₂ catalysts towards hydrogen production

In terms of hydrogen production, it was observed that the series of sol-gel catalysts (series A), exhibited a better performance when compared with the catalysts prepared by the impregnation method (series C). Similar results have been reported by Wu and Williams during the steam reforming of ethanol [3]. Also Goncalves et al [7], reported a better performance for Ni/SiO₂ sol-gel catalysts during the CO₂ reforming of CH₄ when compared with Ni/SiO₂ catalysts prepared by impregnation. The promotion of the catalytic activity by adding metals, Ce, Mg, Al, to the 20Ni/SiO₂ sol-gel catalyst has not been observed in this work for the pyrolysis/gasification of RDF; as the H₂ concentrations obtained for the metal-promoted catalysts (series B) were lower than the hydrogen concentration attained using the 20Ni/SiO₂-A catalyst.

5.1.3 GC-MS analysis of the condensed tar fraction

After each experiment using the catalysts shown in Table 5.1-1, the condensed fraction coming from the main exit gas stream was collected from the bottom of the condensers cooled by air and dry-ice respectively. The liquid sample was analysed by gas chromatography coupled to mass spectrometry (GC-MS), in order to obtain both qualitative and quantitative information about this fraction. Details about the sample preparation and GC-MS analysis are given in the Chapter 3, Section 3.4.3 of this work; however a brief description is given next.

The samples contained in the condensers were collected using dichloromethane (DCM analytical reagent grade, Fischer Scientific). A heterogeneous sample was obtained containing a fraction of tar mixed with DCM and a second fraction

mainly containing water; afterwards both fractions were separated by simple decantation. The water traces contained in the tar/oil mixed with the DCM samples was extracted using a sodium sulphate bed (Na_2SO_4); the salt was previously dried for 2 hours at 140 °C. The DCM contained in the samples was then evaporated at around 30 °C using a Genevac Rocket Evaporation system, to obtain concentrated samples at the same volume. The tar composition was determined by injecting 2 microliters of the sample into a Varian CP-3800 gas chromatograph coupled with a Varian Saturn 2200 GC/MS/MS mass spectrometer. Further details about the programme used for the analysis of tar/DCM samples can be found in Chapter 3, Section 3.4.3 of this work. The results from this analysis including the retention times of the eluted peaks, the compounds assigned and concentration expressed as $\mu\text{g}_{\text{compound}}/\text{g}_{\text{RDF}}$, are presented in Table 5.1-4.

Table 5.1-4. Identified compounds from GC-MS analysis of tar samples ($\mu\text{g}_{\text{compound}}/\text{g}_{\text{RDF}}$)

RT (min)	Assigned Peak	MW (g mol^{-1})	5Ni/SiO ₂ -A	10Ni/SiO ₂ -A	20Ni/SiO ₂ -A	40Ni/SiO ₂ -A	Ce-Ni/SiO ₂ -B	Mg-Ni/SiO ₂ -B	Al-Ni/SiO ₂ -B	5Ni/SiO ₂ -C	10Ni/SiO ₂ -C	20Ni/SiO ₂ -C	40Ni/SiO ₂ -C
7.84	Furfural	96	–	3.4	1.5	0.5	1.2	0.3	2.0	12.7	5.1	3.7	7.1
7.81	Cyclopentanone	84	–	7.4	1.5	0.5	1.2	0.0	2.1	13.4	3.6	3.7	7.0
8.67	Ethylbenzene	106	4.8	0.2	–	1.2	0.6	0.2	1.1	–	1.3	1.1	4.1
9.02	<i>p</i> -Xylene	106	–	1.0	3.1	1.8	8.5	2.5	5.0	0.4	4.1	5.4	7.1
9.02	<i>m</i> -Xylene	106	12.9	1.0	3.2	1.8	8.3	2.4	4.8	0.6	4.1	5.3	6.9
9.86	Styrene	104	116.0	21.3	1.4	8.5	31.1	15.2	27.1	3.1	44.3	43.8	43.0
9.89	<i>o</i> -Xylene	106	2.8	–	–	–	2.4	1.6	2.7	–	–	–	–
13.36	Phenol	94	867.1	408.0	183.8	130.0	404.5	160.3	377.1	1019.0	419.7	607.9	706.5
13.78	para-methylstyrene	118	7.1	–	–	–	–	–	–	1.3	–	–	–
14.97	Indane	118	2.3	1.4	–	0.2	0.2	0.3	0.2	0.3	1.0	0.9	0.5
15.35	Indene	116	182.2	95.3	1.2	8.3	11.0	21.5	9.1	5.9	56.0	68.1	28.2
15.69	<i>o</i> -Cresol	108	27.4	15.8	2.7	2.5	5.0	1.3	7.9	–	28.4	10.7	12.5
16.14	Acetophenone	120	1.2	5.1	1.0	1.2	–	0.4	1.0	3.7	–	1.2	1.7
16.47	<i>p</i> -Cresol	108	71.5	–	5.6	6.5	15.6	5.0	15.1	105.6	81.0	27.8	35.2
16.48	<i>m</i> -Cresol	108	34.3	5.0	5.3	6.0	11.0	4.6	18.1	72.6	64.0	23.8	32.8
17.38	2-Methylbenzofuran	132	6.6	–	–	0.8	–	0.4	0.3	–	–	1.6	1.5
18.29	2-Ethylphenol	122	1.5	–	–	–	–	–	–	2.2	1.8	–	2.5
18.66	2,4-Dimethylphenol	122	4.6	1.2	–	1.1	–	–	1.3	–	5.6	–	–
19.32	4-Ethylphenol	122	4.7	2.4	–	–	–	–	1.5	–	5.8	–	–
19.32	3-Ethylphenol	122	5.1	2.7	–	1.3	–	–	1.6	–	6.3	–	–

RT (min)	Assigned Peak	MW (g mol ⁻¹)	5Ni/SiO ₂ -A	10Ni/SiO ₂ -A	20Ni/SiO ₂ -A	40Ni/SiO ₂ -A	Ce-Ni/SiO ₂ -B	Mg-Ni/SiO ₂ -B	Al-Ni/SiO ₂ -B	5Ni/SiO ₂ -C	10Ni/SiO ₂ -C	20Ni/SiO ₂ -C	40Ni/SiO ₂ -C
19.32	2,6-Dimethylphenol	122	5.2	2.7	–	1.5	–	–	1.7	–	6.5	–	–
19.93	Naphthalene	128	70.4	35.2	4.1	39.0	17.1	10.3	10.6	35.2	123.7	46.6	42.4
20.93	4-Isopropylphenol	136	–	–	–	–	–	–	–	–	–	–	2.5
23.16	2-Methylnaphthalene	142	17.2	16.2	1.6	3.3	2.7	2.3	3.2	17.2	24.6	8.0	9.1
25.08	Biphenyl	154	19.1	20.9	2.1	1.7	2.8	2.9	3.5	42.5	45.5	9.2	18.2
25.32	2-ethylnaphthalene	156	1.8	1.0	–	1.1	0.8	–	0.7	2.7	2.0	2.0	–
25.32	1-ethylnaphthalene	156	–	0.8	–	0.5	0.4	–	0.4	1.5	1.8	–	–
25.54	2,6-dimethyl naphthalene	156	2.1	1.1	–	–	0.7	–	0.7	3.7	2.8	1.9	3.4
26.16	1,4-dimethylnaphthalene	156	–	–	1.2	0.8	0.6	–	–	3.3	–	–	–
27.47	Dibenzofuran	168	–	–	–	1.5	–	3.5	3.6	–	–	7.0	18.7
28.51	Fluorene	166	42.0	51.1	4.5	–	5.2	5.6	7.5	136.4	58.5	15.0	37.2
29.28	1,3-diphenylpropane	196	–	–	1.4	–	–	–	–	–	–	–	2.8
31.06	Phenanthrene	178	83.8	41.8	3.8	10.9	27.0	19.3	18.1	144.8	71.4	10.4	–
31.97	<i>o</i> -Terphenyl	230	1.5	0.7	1.5	0.9	0.7	0.6	0.6	2.3	1.6	1.6	2.7
34.17	Fluoranthene	202	24.3	5.5	2.8	5.6	2.8	2.5	2.0	11.1	9.5	3.1	8.1
34.48	Pyrene	202	32.8	23.1	3.2	7.8	13.6	3.9	2.8	24.2	12.8	2.9	28.9
34.62	<i>m</i> -Terphenyl	230	3.5	2.1	2.5	2.1	1.9	1.1	1.1	4.8	3.2	2.6	5.9
41.98	1,3,5-triphenylbenzene	306	2.4	2.5	2.1	1.6	1.2	–	–	2.9	–	–	3.3
Tar Concentration ($\mu\text{g}_{\text{tar}}/\text{g}_{\text{RDF}}$)			1660.8	775.7	241.0	250.3	577.8	268.0	534.3	1673.2	1095.6	915.0	1079.5
Tar Concentration ($\text{mg}_{\text{tar}}/\text{g}_{\text{RDF}}$)			1.7	0.8	0.2	0.3	0.6	0.3	0.5	1.7	1.1	0.9	1.1

From Table 5.1-4, it is observed that the major compounds in terms of concentration ($\mu\text{g}_{\text{comp}}/\text{g}_{\text{RDF}}$), for most of the analysed samples were: styrene, phenol, indene, p-cresol, m-cresol, naphthalene, fluorene, and phenanthrene. In the previous Chapter 4 of the present work a qualitative GC-MS analysis of the tar samples from the pyrolysis-gasification of RDF using Ni/ Al_2O_3 catalysts was reported. In Chapter 4 tar compounds such as naphthalene, biphenyl, fluorene, phenanthrene, methylnaphthalene, catechols and alcohols were identified in the analysed tar samples. From those compounds naphthalene, fluorene and phenanthrene were also identified and reported in Table 5.1-4. Some other authors have also identified similar compounds when analysing tars from the pyrolysis of RDF [32], and tars derived from biomass gasification using a secondary tar cleaning system [33]. From the major tar compounds identified in the analysed samples (Table 5.1-4), the following Figure 5.1-2, shows the trends observed in terms of concentration ($\mu\text{g}_{\text{compound}}/\text{g}_{\text{RDF}}$).

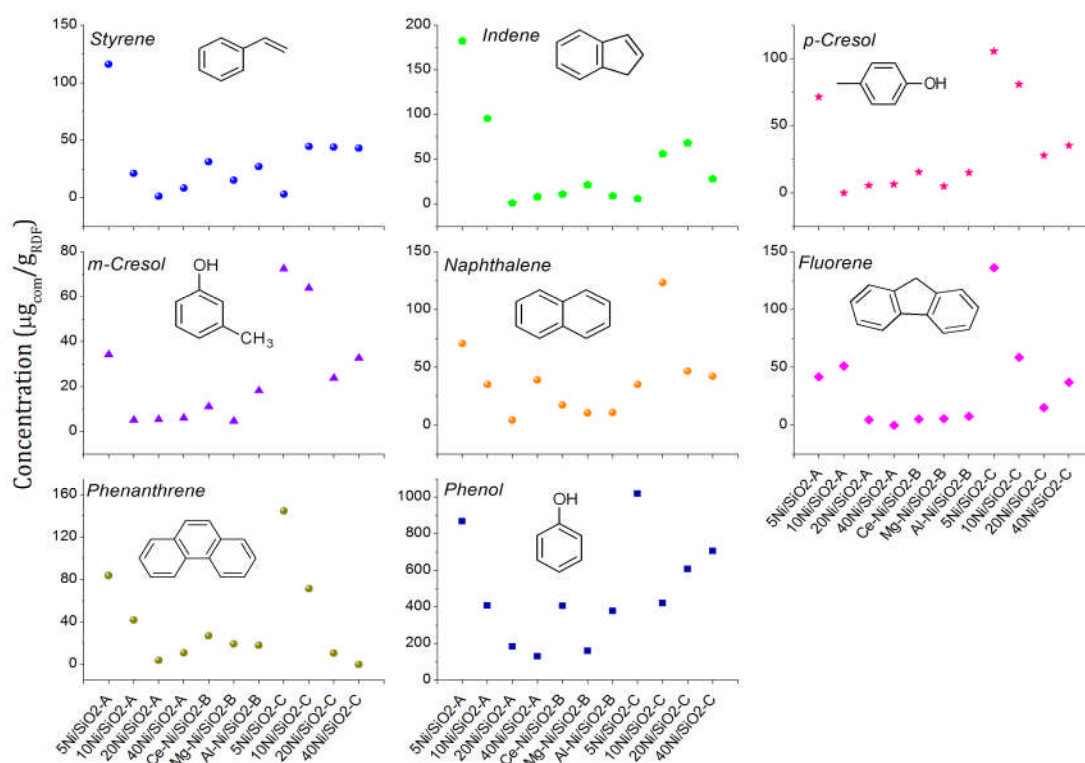


Figure 5.1-2. Trends in concentrations for major tar compounds identified in the analysed samples

From Figure 5.1-2, it was observed that major concentrations for the reported tar compounds were obtained when using the low nickel loading for the sol-gel

catalyst (5Ni/SiO₂-A), and all the series of catalysts prepared by impregnation method (series C).

Also from the concentration values shown in Table 5.1-4, a reduction in the total tar concentration from 1.66 to 0.24 mg_{tar}/g_{RDF} as the nickel loading was increased for the sol-gel catalysts (series A). The tar concentration for the 20Ni/SiO₂-A and 40Ni/SiO₂-A catalysts was quite similar (~0.25 mg_{tar}/g_{RDF}), this indicates that no major tar reduction was attained for a nickel loading higher than 20wt.% for the catalysts prepared by the sol-gel method. For the series of sol-gel catalysts, it was also observed a remarkable reduction from 1.66 mg_{tar}/g_{RDF} to 0.24mg_{tar}/g_{RDF}, when increasing the nickel loading in the Ni/SiO₂ catalysts from 5 up to 20wt.%. However it was noted a slight increase in the tar concentration to 0.25mg_{tar}/g_{RDF} when the nickel loading was further increased to 40wt.%.

It was expected that a further reduction in the tar formation might occur when adding Al, Mg, or Ce to the 20Ni/SiO₂ catalyst (Table 5.1-4). This forecast was based on a reported increase in the catalytic activity by adding metal-promoters, through the promotion of cracking reactions, for example during the partial oxidation of methane [34]. Among the three metal-promoters added, the highest activity in terms of tar reduction was shown by the Mg-Ni/SiO₂ catalyst (Figure 5.1-3), resulting in a tar content of 0.25 mg_{tar}/g_{RDF} (Table 5.1-4), whereas Al and Ce-Ni/SiO₂ catalysts reported about twice that value. It has been reported that the addition of CeO₂ to nickel-based catalysts promoted major tar removal during biomass gasification, when compared with a conventional nickel-based catalyst [35, 36]. For example Kimura et al [35], reported that the addition of CeO₂ to a Ni/Al₂O₃ catalyst, promoted the conversion of tar and coke to CO, H₂ and CH₄ during the biomass steam gasification of biomass. Also Wang et al [29], reported that the addition of MgO to Ni/SiO₂ catalyst improved coke resistance and reduced the sintering of nickel particles; hence the catalytic activity of the catalyst was improved. However in this work the production of tar of hydrogen were not improved by adding Mg, Al or Ce as metal promoters to the sol-gel Ni based catalyst, which might be due to the reduction in the surface area for these

catalysts not allowed an even dispersion of both metals, resulting in a reduction in the promotion of cracking and reforming reactions.

From Table 5.1-4, it was observed that for the Ni/SiO₂ catalysts prepared by impregnation method (series C), the tar concentration was reduced from 1.67 up to 0.60 mg_{tar}/g_{RDF} when the Ni loading was increased from 5 to 20 wt.%, but increased again up to 0.98 mg_{tar}/g_{RDF} when using the 40Ni/SiO₂-C catalyst. This trend might be related to the sintering of nickel particles due to the high nickel loading, resulting in lower catalytic activity. Mark and Maier [37], reported that increasing the metal content in catalysts could lead to a decrease in the metal dispersion. Therefore, it was suggested that for the 40Ni/SiO₂-C catalyst a nickel loading of 40wt.% was too high to improve the catalyst's activity towards hydrogen production from pyrolysis/gasification of RDF. Besides by increasing the nickel loading from 20 to 40wt.%, some of the catalyst properties were negatively influenced, such as the surface area that was reduced 9.7 and 6.3m² g⁻¹ (Table 5.1-2).

Diverse classifications of tar compounds have been previously reported in the literature by different authors [38-41], most of these classifications are based on the number of aromatic rings of the different compounds found in tar samples from different sources. Based on this classification the identified tar compounds shown in Table 5.1-4, were grouped and are presented in Table 5.1-5.

Table 5.1-5. Classification of tar compounds found in analysed tar samples

CLASS 2 Heterocyclic Aromatics	CLASS 3 Aromatics 1-Ring	CLASS 4 Light PAH 2-3 Rings	CLASS 5 Heavy PAH 4-7 Rings
<i>Tars with hetero atoms; highly water soluble compounds</i>	<i>Light hydrocarbons; no condensability or solubility problems</i>	<i>Compounds that condense at low temperature even at very low concentration</i>	<i>Components condense at high temperatures at low concentrations</i>
Furfural Phenol o-Cresol p-Cresol m-Cresol 2-Methylbenzofuran Cyclopentanone Acetophenone 2-ethylphenol 2,4-dimethylphenol 4-ethylphenol 3-ethylphenol 2,6-dimethylphenol 4-isopropylphenol Dibenzofuran	Ethylbenzene p-Xylene m-Xylene o-Xylene Styrene Para-methyl Styrene	Naphthalene 2-Methylnaphthalene Biphenyl 2-ethylnaphthalene 1-ethylnaphthalene 2,6-dimethylnaphthalene 1,4-dimethylnaphthalene Fluorene 1,3-diphenylpropane Phenanthrene o-Terphenyl m-Terphenyl Indane Indene	Fluoranthene Pyrene 1,3,5-Triphenylbenzene

There is also a tar Class 1 normally referred to as GC-undetectable compounds, thus it was not considered in the classification shown in Table 5.1-5. Tar Class 2 mainly includes heterocyclic compounds; compounds with 1 aromatic ring were grouped in Class 3; light polyaromatic compounds in Class 4, and tar Class 5 grouped heavy polyaromatic compounds. Once the identified compounds were grouped, general tar concentrations per Class were calculated and these values are shown in Figure 5.1-3.

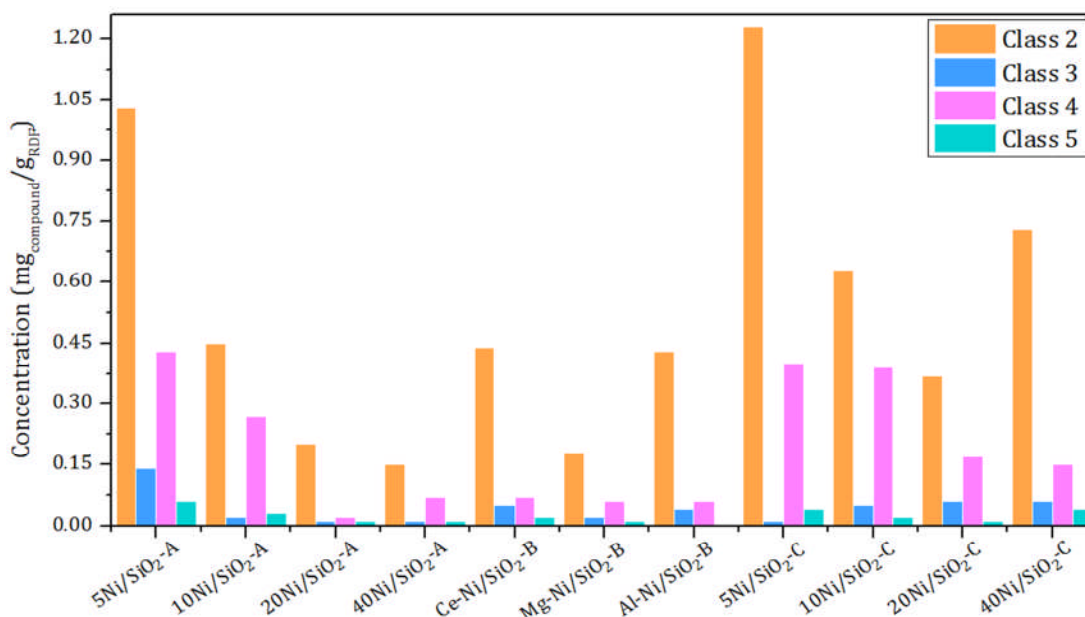


Figure 5.1-3. Concentration of tar classes using different catalysts

From Figure 5.1-3 it was noted that for all the analysed samples the major tar contribution came from tar Class 2; these tars are sometimes referred to as primary tars and are known to contain mainly oxygenated compounds with aromatic and aliphatic structures [42]. Among the compounds grouped in tar Class 2, the major contribution came from the compound phenol for all the analysed samples (Table 5.1-4 and Figure 5.1-2). In general it was noted that for the sol-gel catalysts (A series), the concentration of the tar Class 2 was reduced as the Ni loading was increased (Figure 5.1-3), also the concentration of phenol followed a similar trend (Figure 5.1-2). This reduction can be related to the pore diameter of the sol-gel catalysts because the pore diameter was increased as the Ni loading was increased (Table 5.1-2), and also with the promotion of cracking of the heterocyclic aromatic compounds. From Table 5.1-4, for the metal-promoted catalysts (series B), the highest phenol concentration was obtained for the Ce-Ni/SiO₂-B catalyst, and the lowest concentration was attained using the Mg-Ni/SiO₂-B catalyst (Figure 5.1-2). From Figure 5.1-3, the lower concentration of tar Class 2, was attained using the Ce and Al Ni/SiO₂-B catalysts, whereas a remarkable reduction was attained using Mg as the metal promoter. This difference might be attributed to the long-term stability of the catalyst due to the addition of metal-promoters to the Ni/SiO₂ catalysts, and also to the low sintering of Ni particles and high coke resistance reported previously by Wang and Lu [29].

From Figure 5.1-3 it was also observed that the concentration of tar Class 3, from single ring aromatic compounds, was reduced as the Ni loading was increased for the sol-gel catalysts (series A). A concentration of 0.1 mg_{tar-Class3}/g_{RDF} for the tar Class 3, was obtained using both 20 and 40Ni/SiO₂-A catalysts. This might suggest that the increase in the Ni loading from 20 wt.% to 40 wt.% for the sol-gel catalyst, does not have a positive effect over the reduction of single ring aromatic compounds (Class 3). For metal-promoted catalysts (series B) the concentration of tar Class 3 was 0.04 mg_{tar-Class3}/g_{RDF} for both Ce and Al Ni/SiO₂-B catalysts, whereas a lower concentration of 0.02 mg_{tar-Class3}/g_{RDF} was obtained using the Mg-Ni/SiO₂-B catalyst. This reduction might be related to the nature of the metal that might be promoting more of the

cracking of single ring aromatic compounds. For example, it has been reported that the addition of Mg might stabilize the Ni crystallite, improving in this way the catalytic activity of the catalyst [43]. For the catalysts prepared by the impregnation method, the lowest concentration of the tar Class 3 was attained using the 5Ni/SiO₂-C catalyst; while somewhat similar concentrations were reported using the 10, 20 and 40 Ni/SiO₂-C catalysts. Therefore no major effect of the metal loading over the catalytic activity towards reduction of tar Class 3 was observed for the impregnated catalysts (Figure 5.1-3).

Naphthalene was included in the tar Class 4, which contributed significantly to the concentration of tar for all the analysed samples (Figure 5.1-3). Naphthalene has been identified as one of the major tar compounds in tar samples from the pyrolysis and/or gasification process [44, 45]. For example Abu El-Rub et al [46], used naphthalene and phenol as tar model compounds to measure tar reduction during the gasification process, using different catalyst types. Devi and collaborators [47], used naphthalene as a tar model compound, with olivine as the catalyst in order to improve the naphthalene conversion. Considering this, the reduction of naphthalene can be used as a measure of the efficiency of the prepared catalysts. From Figure 5.1-2, a reduction in the naphthalene concentration was observed as the Ni loading was increased for the sol-gel catalysts (series A), however a considerable increase was noted when using the highest nickel loading of 40wt.%. A similar increase in the concentration of other compounds such as styrene, indene, and phenanthrene; was also observed using the 40Ni/SiO₂-A catalyst which indicates that the reduction of these major compounds is not as effective as using the 20Ni/SiO₂-A catalyst (Figure 5.1-2). This might also be related to the lower surface area and mesoporous volume reported for the 40Ni/SiO₂-A catalyst (Table 5.1-2). By using the metal promoters Ce, Mg, and Al (series B), different concentrations of naphthalene were obtained with a better conversion using both Mg and Al Ni/SiO₂-B catalysts. However, the general concentrations of tar Class 4 using these metal-promoted catalysts were similar at 0.06 mg_{tar-Class4}/g_{RDF}, which was slightly higher compared with the concentration of 0.02 mg_{tar-Class4}/g_{RDF} obtained using the 20Ni/SiO₂-A catalyst. For the series of impregnated catalysts

a reduction of naphthalene was observed for the 10Ni/SiO₂-C catalyst (Figure 5.1-2), but it is noted that using the 5Ni/SiO₂-C catalyst the lowest naphthalene concentration was attained. This effect can also be observed for other low molecular weight compounds such as styrene, and indene, but for higher molecular weight compounds such as fluorene and phenanthrene, higher concentrations were obtained using the 5Ni/SiO₂-C catalyst (Figure 5.1-2). The total concentration of tar Class 4 was reduced as the Ni loading was increased for the impregnated catalysts (series C). The lowest tar concentration attained for the impregnated catalysts, it was 0.15 mg_{tar-Class4}/g_{RDF}, when using the 40Ni/SiO₂-C catalyst (Figure 5.1-3 and Table 5.1-4).

Fluoranthene, pyrene and 1,3,5-triphenylbenzene were identified and included in tar Class 5; the concentration of these compounds for all the samples was very low with a maximum tar concentration of 0.06 mg_{tar-Class5}/g_{RDF} using the 5Ni/SiO₂-A catalyst (Figure 5.1-3). A total conversion of tar Class 5 was attained using the Al-Ni/SiO₂-B catalyst, while very low concentrations of around 0.01 mg_{tar}/g_{RDF} were obtained using 20Ni/SiO₂-A, 40Ni/SiO₂-A, Mg-Ni/SiO₂-B, and 20-Ni/SiO₂-C catalysts (Figure 5.1-3). This suggests that the conversion of higher molecular weight compounds (>200 g mol⁻¹) included in Class 5, can be attained using Ni loadings from 20 wt.%, but also the influence of the preparation method should be considered, as for the 40-Ni/SiO₂-C catalyst a higher concentration of the tar Class 5 was attained (Figure 5.1-3).

From Table 5.1-4, the best catalytic activity towards tar reduction was attained using the 20-Ni/SiO₂-A, 40-Ni/SiO₂-A, and Mg-Ni/SiO₂-B catalysts, resulting in tar concentrations lower than 0.3 mg_{tar}/g_{RDF}. These catalysts were also found to have better performance in terms of hydrogen production as shown in Table 5.1-3.

The highest styrene, indene, and naphthalene conversions were obtained using the 20Ni/SiO₂-A catalyst (Figure 5.1-2), while the best phenol and fluorene conversions were obtained using the 40-Ni/SiO₂-A catalyst (Figure 5.1-2). The

highest fluoranthene and phenanthrene conversions were attained using the Al-Ni/SiO₂-B and 40-Ni/SiO₂-C catalysts respectively (Table 5.1-4 and Figure 5.1-2).

In general, the conversion of hydrocarbons during the gasification process might be attributed to steam cracking and CO₂ reforming reactions; the decrease in hydrocarbons is associated with an increase in hydrogen with a more effective catalyst [25].

5.1.4 Analysis of reacted Ni/SiO₂ catalysts

The reacted catalysts were analysed by temperature-programmed oxidation (TPO) and SEM, in order to characterize the carbon deposited over the catalysts surfaces.

5.1.4.1 Thermogravimetric analysis (TGA)

In order to carry out the thermogravimetric analysis of coked carbons deposited over the surface of reacted catalysts, a Stanton-Redcroft thermogravimetric analyser (TGA) was used; their respective differential thermogravimetric (DTG) results were also obtained. Details about thermogravimetric analysis carried out on the reacted catalysts, have been described in Chapter 3, Section 3.4.2.6 of this work. However a brief description is as follows. Around 20 mg of the used catalyst was placed in the TGA sample crucible, and heated in an air atmosphere at 15 °C min⁻¹ to a final temperature of 800 °C, with a dwell time of 10 minutes. The TGA curves and their respective differential curves are shown in Figure 5.1-4.

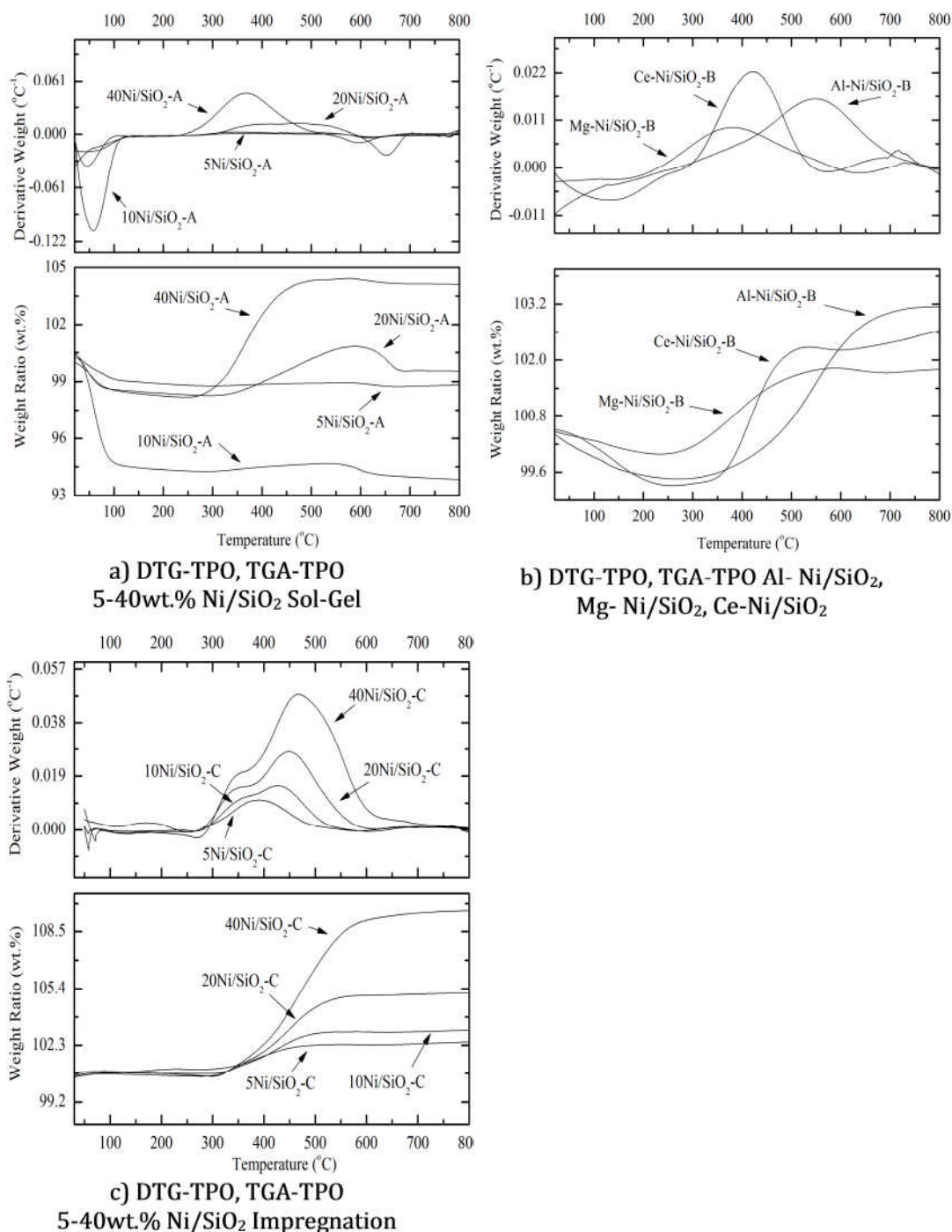


Figure 5.1-4. DTG-TPO and TGA-TPO analysis from reacted Ni/SiO₂ catalysts

In general it has been reported in the literature that at least three different stages can be identified in thermogravimetric curves from reacted catalysts [3, 48, 49]. The first stage from 0 °C to 100 °C, is normally related with a mass decrease associated with water vaporization or moisture contained in the sample [1]. The second stage is normally around 350 °C and is related with the Ni phase oxidation, and the final stage of the thermogram comes from the

carbon combustion normally after 400 °C [3]. The TGA curves can also give information about the type of carbon formed within the surface of the catalyst. For example the thermograms corresponding to amorphous type carbons are suggested to initiate oxidation, and therefore weight loss, at around 500 °C, whereas those from filamentous carbons can be identified from their oxidation at a temperature of 600 °C [48, 50].

The DTG-TPO thermogram plotted for the reacted 5Ni/SiO₂-A sol-gel catalysts (Figure 5.1-4(a)), showed almost a straight line, which might be due to the low Ni loading and also due to the small amount of carbon deposition over this catalyst. In the TGA-TPO thermograms, a weight decrease before 100 °C was initially observed for the 5, 10 and 20 wt.% Ni/SiO₂-A reacted catalysts, which might be related to initial water vaporization. The DTG-TPO curves for the reacted 10, 20 and 40 wt.% Ni/SiO₂-A catalysts presented different peaks at different temperatures, the initial weight increase at around 350 °C was attributed to Ni oxidation, as this peak seemed to increase as the Ni loading in the catalysts was increased. From Figure 5.1-4(a), at least two peaks can be identified around 600 °C for the DTG-TPO thermogram of 10Ni/SiO₂-A, and 20Ni/SiO₂-A reacted catalysts. This might suggest the deposition of filamentous carbon on to the catalysts after pyrolysis-gasification of RDF, as the oxidation of filamentous carbon was suggested to start to be formed around 600 °C [3]. It is suggested that cracking of hydrocarbons and tars, resulted in the formation and further deposition of carbons in the reacted catalysts. From Figure 5.1-4(a), it seems that the carbon deposition is increased as the Ni loading was increased from 5 up to 20wt.%, however for the nickel loading of 40wt.% the coke deposition seemed to be decreased which might be related with lower promotion of coke-steam reactions when using the latter catalyst.

Figure 5.1-4(b), shows the thermograms for the Mg, Ce, and Al Ni/SiO₂-B metal-added catalysts; the initial decrease in both TGA and DTG thermograms was mainly attributed to moisture loss. After that the weight increase was related to metal oxidation in the catalysts. The three catalysts presented similar thermogravimetric curves however two peaks from the Mg and Ce Ni/SiO₂-B

catalysts appear at around 400 °C (DTG-TPO), while the Al-Ni/SiO₂-B reacted catalyst peak appear around 600 °C. This difference can be related to the nature of the promoter added as for example Wang and Lu [23], reported that the addition of metal oxides might influence the activity of the supported metal catalyst and also the coke formation on the catalyst surface. They stated that the addition of alkaline-earth metal promoters such as Mg to Ni/Al₂O₃ catalysts could significantly reduce coke formation on the catalyst surface during the CO₂ reforming of methane. Probably due to this, the reacted Mg-Ni/SiO₂-B catalyst has a smaller oxidation peak when compared with the other metal-promoted catalysts. Also from the DTG-TGA thermograms (Figure 5.1-4(b)), two different peaks can be observed which was probably due to the deposition of different types of carbon over the reacted catalysts. Most likely amorphous carbon was formed on the Ce and Mg-Ni/SiO₂-B catalysts, whereas filamentous carbon could be found in the Al-Ni/SiO₂-B reacted catalyst.

From Figure 5.1-4(c), it can be noted that both TGA-TPO and DTG-TPO thermograms for the reacted impregnated catalysts, were displaced as the nickel loading was increased. This was probably due to more nickel particles being available for oxidation at higher Ni loadings. When comparing the TPO thermograms for the 20Ni/SiO₂-A and 20Ni/SiO₂-C catalysts prepared by the sol-gel and impregnation methods respectively (Figure 5.1-4(a), and Figure 5.1-4(c)), the carbon combustion for the sol-gel catalyst appeared after 600 °C (Figure 5.1-4(a)), whereas for the impregnated catalyst (Figure 5.1-4(c)) was immediately after 400 °C. Therefore it was suggested that for reacted impregnated catalysts, amorphous carbons were formed; while for the reacted sol-gel catalysts the deposition of filamentous carbon was preferential.

5.1.4.2 Scanning electron microscopy (SEM)

A high-resolution scanning electron microscope (SEM, LEO 1530) was used to characterize and examine the carbon deposited on the reacted catalysts (Chapter 3, Section 3.4.2.7). The results are shown in Figure 5.1-5.

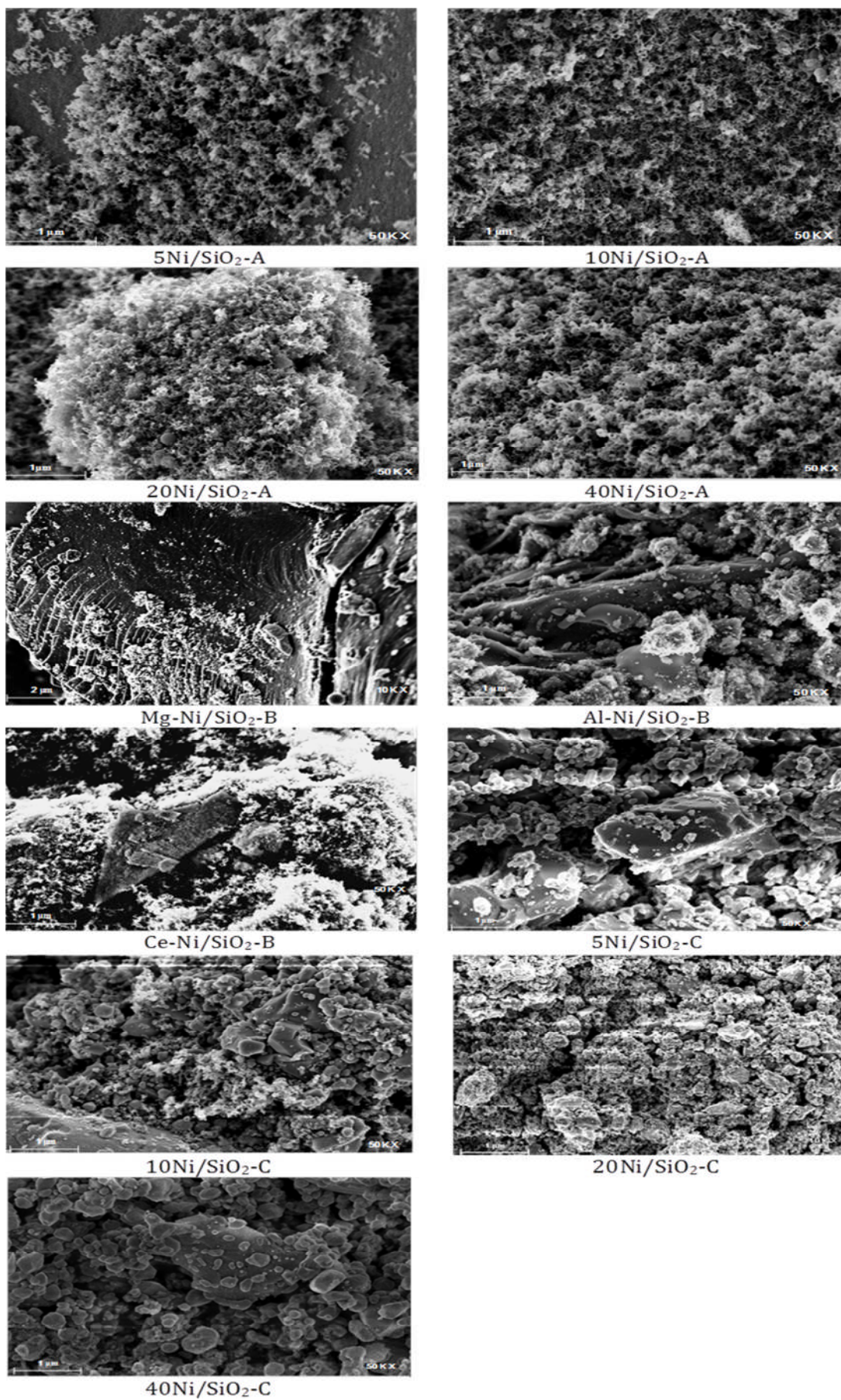


Figure 5.1-5. Scanning electron images (SEM) of reacted Ni/SiO₂ catalysts

From Figure 5.1-5, some filamentous carbons were observed over the surface of the reacted sol-gel catalysts (5, 10, 20, 40 Ni/SiO₂-A), this observation was consistent with the results from the thermogravimetric analysis (Figure 5.1-4(a)). For the SEM analysis of the reacted metal-promoted catalysts it was observed that different amounts of filamentous and probably amorphous carbon were deposited over the surface of the Mg-Ni/SiO₂-B, Al-Ni/SiO₂-B, and Ce-Ni/SiO₂-B catalysts. The images of the Mg-Ni/SiO₂-B and Ce-Ni/SiO₂-B catalysts were more similar, whereas the SEM image of the Al-Ni/SiO₂ catalyst differs regarding the type of coke deposited. Comparing this with the thermogravimetric analysis results shown in Figure 5.1-4(b), the DTG-TPO curve of the Al-Ni/SiO₂-B catalyst showed the main peak at higher temperatures when compared with the other two reacted catalysts (series B); which might suggest the formation of two different carbon types over the surface of the Al-Ni/SiO₂-B reacted catalyst. Finally the images obtained from the SEM analysis of reacted impregnated catalysts, showed very little coke deposition which was mainly from amorphous type carbon.

When comparing both thermogravimetric and SEM results (Figure 5.1-4, and Figure 5.1-5), it was observed that filamentous carbons tend to be deposited over the reacted Ni/SiO₂ sol-gel catalysts, whilst amorphous carbons are deposited over the reacted catalysts prepared by the impregnation method. Also two different types of carbon (filamentous and amorphous) were identified over the metal-promoted reacted catalysts; however the amount of each one influenced the trends in the DTG-TPO thermogram.

5.1.5 Summary of Ni/SiO₂ characteristics and performance

In Section 5.1, a series of Ni/SiO₂ catalysts were prepared using different metal promoters and preparation methods. In addition the resulting catalysts were characterised and investigated for their efficiency in relation to hydrogen production and tar reduction during the pyrolysis/gasification of RDF in a two-stage reaction system.

It was found that the series of Ni/SiO₂ catalysts prepared by the sol-gel method were effective to promote an increase in the hydrogen concentration, an increase in the produced syngas, and to reduce the tar formation. The best performance for this series of sol-gel catalysts was attained using the Ni/SiO₂ catalyst prepared using a nickel loading of 20 wt.%. Also Ni/SiO₂ catalysts prepared by sol-gel showed better characteristics such as high surface area, mesoporous volume, and particle size, when compared with the catalysts prepared by impregnation method.

It was expected that the addition of metal-promoters such as Ce, Mg or Al to the 20 wt.% Ni/SiO₂ sol-gel catalyst, would result in an improvement on catalysts properties, hydrogen production and tar reduction; nevertheless from experimental data there was no significant positive influence.

When analysing the reacted Ni/SiO₂ catalysts through thermogravimetric analysis and scanning electron microscopy techniques, it was found that filamentous carbons were more likely to be deposited over reacted sol-gel catalysts, whereas amorphous carbons were identified over the surface of reacted impregnated catalysts. Both types of carbon were found to be deposited over the reacted metal-promoted catalysts, depending on the metal nature and on its interaction with the Ni phase.

In general the tar from the pyrolysis-gasification of RDF was found to contain mainly styrene, phenol, indene, cresols, naphthalene, fluorene, and phenanthrene, from the alkene and alcohol functional groups.

References

1. Akande, A.J., R.O. Idem, and A.K. Dalai, *Synthesis, characterization and performance evaluation of Ni/Al₂O₃ catalysts for reforming of crude ethanol for hydrogen production*. Applied Catalysis A: General, 2005. 287(2): p. 159-175.
2. Darvell, L.I., K. Heiskanen, J.M. Jones, A.B. Ross, P. Simell, and A. Williams, *An investigation of alumina-supported catalysts for the selective catalytic oxidation of ammonia in biomass gasification*. Catalysis Today, 2003. 81(4): p. 681-692.
3. Wu, C.F. and P.T. Williams, *A Novel Nano-Ni/SiO₂ Catalyst for Hydrogen Production from Steam Reforming of Ethanol*. Environmental Science & Technology, 2010. 44(15): p. 5993-5998.
4. Tomiyama, S., R. Takahashi, S. Sato, T. Sodesawa, and S. Yoshida, *Preparation of Ni/SiO₂ catalyst with high thermal stability for CO₂-reforming of CH₄*. Applied Catalysis A: General, 2003. 241(1-2): p. 349-361.
5. Tang, N.J., W. Zhong, W. Liu, H.Y. Jiang, X.L. Wu, and Y.W. Du, *Synthesis and complex permeability of Ni/SiO₂ nanocomposite*. Nanotechnology, 2004. 15(12): p. 1756-1758.
6. Gil, A., A. Díaz, L.M. Gandía, and M. Montes, *Influence of the preparation method and the nature of the support on the stability of nickel catalysts*. Applied Catalysis A: General, 1994. 109(2): p. 167-179.
7. Goncalves, G., Lenzi, M. K., Santos, O. A. A., Jorge, L. M. M., *Preparation and characterization of nickel based catalysts on silica, alumina and titania obtained by sol-gel method*. Journal of Non-Crystalline Solids, 2006. 352: p. 3697-3704.
8. Satterfield, C.N., *Heterogeneous catalysis in practice*. 2nd ed. McGraw-Hill chemical engineering series. 1980, London: McGraw-Hill.
9. Garcia, L.a., R. French, S. Czernik, and E. Chornet, *Catalytic steam reforming of bio-oils for the production of hydrogen: effects of catalyst composition*. Applied Catalysis A: General, 2000. 201(2): p. 225-239.
10. Cai, X., X. Dong, and W. Lin, *Effect of CeO₂ on the catalytic performance of Ni/Al₂O₃ for autothermal reforming of methane*. Journal of Natural Gas Chemistry, 2008. 17(1): p. 98-102.
11. Choudhary, V.R., B.S. Uphade, and A.S. Mamman, *Oxidative Conversion of Methane to Syngas over Nickel Supported on Commercial Low Surface Area Porous Catalyst Carriers Precoated with Alkaline and Rare Earth Oxides*. Journal of Catalysis, 1997. 172(2): p. 281-293.
12. Hsieh, C.T. and H.S. Teng, *Influence of mesopore volume and adsorbate size on adsorption capacities of activated carbons in aqueous solutions*. Carbon, 2000. 38(6): p. 863-869.
13. Rodríguez-Reinoso, F., M. Molina-Sabio, and M.T. González, *The use of steam and CO₂ as activating agents in the preparation of activated carbons*. Carbon, 1995. 33(1): p. 15-23.
14. Teng, H.S. and C.T. Hsieh, *Influence of surface characteristics on liquid-phase adsorption of phenol by activated carbons prepared from*

- bituminous coal*. Industrial & Engineering Chemistry Research, 1998. 37(9): p. 3618-3624.
15. Sing, K.S.W., D.H. Everett, R.A.W. Haul, L. Moscou, R.A. Pierotti, J. Rouquerol, and T. Siemieniewska, *Reporting Physisorption Data for Gas Solid Systems with Special Reference to the Determination of Surface-Area and Porosity (Recommendations 1984)*. Pure and Applied Chemistry, 1985. 57(4): p. 603-619.
 16. Rouquerol, F., J. Rouquerol, and K.S.W. Sing, *Adsorption by Powders and Porous Solids*. 1999, London: Academic Press.
 17. Kim, P., Y. Kim, H. Kim, I.K. Song, and J. Yi, *Synthesis and characterization of mesoporous alumina with nickel incorporated for use in the partial oxidation of methane into synthesis gas*. Applied Catalysis A: General, 2004. 272(1-2): p. 157-166.
 18. Naumov, S., *Hysteresis Phenomena in Mesoporous Materials*, in *Physics and Earth Sciences*. 2009, University of Leipzig: Leipzig.
 19. Chiou, C.T., *Partition and Adsorption of Organic Contaminants in Environmental Systems*. 2002, Hoboken, New Jersey: John Wiley & Sons, Inc.
 20. Sing, K.S.W., *Adsorption Methods for Surface Area Determination*, in *Particle Size Analysis*, N.G. Stanley-Wood, Lines, R. W., Editor. 1992, Royal Society of Chemistry: Cambridge, UK. p. 13-32.
 21. Kim, P., Y. Kim, T. Kang, I. Song, and J. Yi, *Preparation of nickel-mesoporous materials and their application to the hydrodechlorination of chlorinated organic compounds*. Catalysis Surveys from Asia, 2007. 11(1): p. 49-58.
 22. Pina, G., C. Louis, and M.A. Keane, *Nickel particle size effects in catalytic hydrogenation and hydrodechlorination: phenolic transformations over nickel/silica*. Physical Chemistry Chemical Physics, 2003. 5(9): p. 1924-1931.
 23. Wang, S. and G.Q. Lu, *Effects of promoters on catalytic activity and carbon deposition of Ni/ γ -Al₂O₃ catalysts in CO₂ reforming of CH₄*. Journal of Chemical Technology & Biotechnology, 2000. 75(7): p. 589-595.
 24. Ding, R.G. and Z.F. Yan, *Adsorption properties studies of the nickel catalysts for carbon dioxide reforming of methane*. Abstracts of Papers of the American Chemical Society, 2002. 223: p. U563-U563.
 25. Pinto, F., R.N. André, C. Franco, H. Lopes, I. Gulyurtlu, and I. Cabrita, *Cogasification of coal and wastes in a pilot-scale installation 1: Effect of catalysts in syngas treatment to achieve tar abatement*. Fuel, 2009. 88(12): p. 2392-2402.
 26. Zapata, B., M.A. Valenzuela, J. Palacios, and E. Torres-Garcia, *Effect of Ca, Ce or K oxide addition on the activity of Ni/SiO₂ catalysts for the methane decomposition reaction*. International Journal of Hydrogen Energy, 2010. 35(21): p. 12091-12097.
 27. Zhang, Z.L., V.A. Tsipouriari, A.M. Efstathiou, and X.E. Verykios, *Reforming of Methane with Carbon Dioxide to Synthesis Gas over Supported Rhodium Catalysts: I. Effects of Support and Metal Crystallite Size on Reaction Activity and Deactivation Characteristics*. Journal of Catalysis, 1996. 158(1): p. 51-63.

28. Al-Fatesh, A.S.A., A.H. Fakeeha, and A.E. Abasaeed, *Effects of promoters on methane dry reforming over Ni catalyst on a mixed (α-Al₂O₃+TiO₂-P25) support*. International Journal of the Physical Sciences, 2011. 6(36): p. 8083-8092.
29. Wang, S. and G.Q.M. Lu, *CO₂ reforming of methane on Ni catalysts: Effects of the support phase and preparation technique*. Applied Catalysis B: Environmental, 1998. 16(3): p. 269-277.
30. Miao, Q., G. Xiong, S. Sheng, W. Cui, L. Xu, and X. Guo, *Partial oxidation of methane to syngas over nickel-based catalysts modified by alkali metal oxide and rare earth metal oxide*. Applied Catalysis A: General, 1997. 154(1-2): p. 17-27.
31. Choudhary, V.R., B.S. Uphade, and A.S. Mamman, *Large enhancement in methane-to-syngas conversion activity of supported Ni catalysts due to precoating of catalyst supports with MgO, CaO or rare-earth oxide*. Catalysis Letters, 1995. 32(3): p. 387-390.
32. Williams, P.T. and S. Besler, *Polycyclic aromatic hydrocarbons in waste derived pyrolytic oils*. Journal of Analytical and Applied Pyrolysis, 1994. 30(1): p. 17-33.
33. Lind, F., M. Seemann, and H. Thunman, *Continuous Catalytic Tar Reforming of Biomass Derived Raw Gas with Simultaneous Catalyst Regeneration*. Industrial & Engineering Chemistry Research, 2011. 50(20): p. 11553-11562.
34. Ma, D., D.J. Mei, X. Li, M.C. Gong, and Y.Q. Chen, *Partial oxidation of methane to syngas over monolithic Ni/γ-Al₂O₃ catalyst - Effects of rare earths and other basic promoters*. Journal of Rare Earths, 2006. 24(4): p. 451-455.
35. Kimura, T., T. Miyazawa, J. Nishikawa, S. Kado, K. Okumura, T. Miyao, S. Naito, K. Kunimori, and K. Tomishige, *Development of Ni catalysts for tar removal by steam gasification of biomass*. Applied Catalysis B: Environmental, 2006. 68(3-4): p. 160-170.
36. Tomishige, K., T. Kimura, J. Nishikawa, T. Miyazawa, and K. Kumori, *Promoting effect of the interaction between Ni and CeO₂ on steam gasification of biomass*. Catalysis Communications, 2007. 8(7): p. 1074-1079.
37. Mark, M.F. and W.F. Maier, *CO₂-Reforming of Methane on Supported Rh and Ir Catalysts*. Journal of Catalysis, 1996. 164(1): p. 122-130.
38. Devi, L., K.J. Ptasinski, F.J.J.G. Janssen, S.V.B. van Paasen, P.C.A. Bergman, and J.H.A. Kiel, *Catalytic decomposition of biomass tars: use of dolomite and untreated olivine*. Renewable Energy, 2005. 30(4): p. 565-587.
39. Han, J. and H. Kim, *The reduction and control technology of tar during biomass gasification/pyrolysis: An overview*. Renewable and Sustainable Energy Reviews, 2008. 12(2): p. 397-416.
40. Brage, C., Q. Yu, and K. Sjöström, *Characteristics of evolution of tar from wood pyrolysis in a fixed-bed reactor*. Fuel, 1996. 75(2): p. 213-219.
41. Ponzio, A., S. Kalisz, and W. Blasiak, *Effect of operating conditions on tar and gas composition in high temperature air/steam gasification (HTAG) of plastic containing waste*. Fuel Processing Technology, 2006. 87(3): p. 223-233.

42. Morf, P., *Secondary Reactions of Tar during Thermochemical Biomass Conversion*. 2001, Swiss Federal Institute of Technology Zurich: Zurich. p. 177.
43. Richardson, S.M. and M.R. Gray, *Enhancement of Residue Hydroprocessing Catalysts by Doping with Alkali Metals*. *Energy & Fuels*, 1997. 11(6): p. 1119-1126.
44. Sato, K. and K. Fujimoto, *Development of new nickel based catalyst for tar reforming with superior resistance to sulfur poisoning and coking in biomass gasification*. *Catalysis Communications*, 2007. 8(11): p. 1697-1701.
45. Srinakruang, J., K. Sato, T. Vitidsant, and K. Fujimoto, *Highly efficient sulfur and coking resistance catalysts for tar gasification with steam*. *Fuel*, 2006. 85(17-18): p. 2419-2426.
46. Abu El-Rub, Z., E.A. Bramer, and G. Brem, *Experimental comparison of biomass chars with other catalysts for tar reduction*. *Fuel*, 2008. 87(10-11): p. 2243-2252.
47. Devi, L., K.J. Ptasinski, and F.J.J.G. Janssen, *Pretreated olivine as tar removal catalyst for biomass gasifiers: investigation using naphthalene as model biomass tar*. *Fuel Processing Technology*, 2005. 86(6): p. 707-730.
48. Wu, C. and P.T. Williams, *Hydrogen production by steam gasification of polypropylene with various nickel catalysts*. *Applied Catalysis B: Environmental*, 2009. 87(3-4): p. 152-161.
49. Wang, S. and G.Q. Lu, *Role of CeO₂ in Ni/CeO₂-Al₂O₃ catalysts for carbon dioxide reforming of methane*. *Applied Catalysis B: Environmental*, 1998. 19(3-4): p. 267-277.
50. Wu, C. and P.T. Williams, *Investigation of coke formation on Ni-Mg-Al catalyst for hydrogen production from the catalytic steam pyrolysis-gasification of polypropylene*. *Applied Catalysis B: Environmental*, 2010. 96(1-2): p. 198-207.

5.2 Effects of nickel to citric acid ratio (Ni:CA)

The effects of modifying the catalyst preparation method and raw materials over both catalysts properties and catalysts activity were addressed in the previous Section 5.1. When preparing Ni/SiO₂ catalysts through the sol-gel method, TEOS and citric acid are normally used to generate the silica gel; in addition the variation of the nickel to citric acid ratio (Ni:CA) has been reported to influence both the catalyst properties and catalyst activity. For example it has been reported [1], that varying the Ni:CA ratio influenced the catalytic activity for hydrogen production, during the steam reforming of ethanol. Takahashi et al [2], have also reported the effects of varying the amount of citric acid, on the formation of mesoporous amorphous silica during the preparation of Ni/SiO₂ catalysts. This section therefore examines the effects of modifying the Ni:CA ratio in relation to the catalysts properties. A series of three different catalysts were prepared using Ni:CA ratios of 1:1, 1:2, and 1:3, the resulting catalysts were assigned to Ni/SiO₂-A, Ni/SiO₂-B, and Ni/SiO₂-C, respectively.

Furthermore, the catalyst performance was studied for hydrogen production and tar reduction during the pyrolysis-gasification of RDF. The results from the investigations of these two parameters were compared with results obtained from blank experiments using a silica bed instead of catalysts. The catalytic activity was studied using the two-stage reactor system (Chapter 3).

5.2.1 Catalysts preparation and characterization

Details regarding the preparation method of the Ni/SiO₂ catalysts used in this Section can be found in Chapter 3, Section 3.2.2.3. Three different Ni/SiO₂ catalysts were prepared by a sol-gel method, the amount of citric acid was varied to obtain Ni:CA ratios of 1:1, 1:2, and 1:3. Initially the catalysts were characterised to identify their surface area and porous properties using the BET analysis (Brunauer, Emmet and Teller), and the obtained results are shown in Table 5.2-1.

Table 5.2-1. Surface area and porous properties Ni/SiO₂ catalysts

Catalyst	Ni content (wt%)	Ni:CA ratio	Surface area ¹ (m ² g ⁻¹)	Micropore volume ² (cm ³ g ⁻¹)	Mesoporous volume ² (cm ³ g ⁻¹)	Total pore volume ³ (cm ³ g ⁻¹)	Pore diameter ³ (nm)
Ni/SiO ₂ -A	20	1:1	547.5	0.270	0.090	0.150	3.818
Ni/SiO ₂ -B	20	1:2	788.2	0.390	0.363	0.548	4.312
Ni/SiO ₂ -C	20	1:3	756.4	0.389	0.602	0.884	6.608

¹ MultiPoint Brunauer, Emmett & Teller (BET) Method

² Dubinin-Radushkevich (DR) Method

³ Barrett, Joyner & Halenda (BJH) Method

From Table 5.2-1, it was observed that the lowest surface area value was reported for the Ni/SiO₂-A catalyst, then it was increased to more than 700 m² g⁻¹ as the Ni:CA ratio was increased. However a reduction in the surface area was noted by changing the Ni:CA from 1:2 to 1:3; this effect might be due to the higher amount of citric acid which generated polymeric networks rather than particle aggregates promoting a higher swelling of the wet silica gel [2]. During the catalyst preparation the citric acid also altered the pH of the solution, which would also influence the nickel aggregation and the formation of SiO₂ particles.

The micropore and mesoporous volumes of the catalysts were obtained using the Dubinin-Radushkevich (DR) method [3]; whereas the total pore volume and the pore diameter were obtained using the Barrett, Joyner & Halenda (BJH) method [4]. The methodology used has been previously described in the Chapter 3, Section 3.4.2.1. Table 5.2-1, showed that the mesoporous volume, the total pore volume and pore diameter increased as the Ni:CA ratio was increased. This trend was attributed to the variation in the citric acid during the preparation as the nickel loading was maintained constant. For example changes in the pore volume of Ni/SiO₂ catalysts, have been associated to variations in the volume of citric acid during the catalysts preparation [5]. The original spaces occupied by the citric acid turned into pores after the citric acid elimination during the calcination process, resulting in changes in the pore diameter. An increase in the pore size might also indicate that the citric acid is well dispersed in CA-silica composites in the form of nanocomposites [2].

From the pore diameter values shown in Table 5.2-1, it was noted that the resulting Ni/SiO₂ catalysts are considered mesoporous materials since the pore

diameter values are within 2-50 nm [6]. The N₂ adsorption-desorption isotherms from the analysis of fresh catalysts, are shown in Figure 5.2-1.

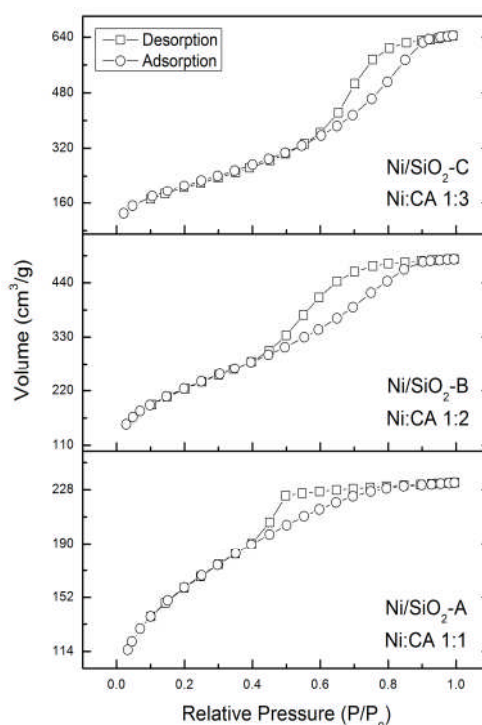


Figure 5.2-1. BET adsorption-desorption isotherms of Ni/SiO₂ catalysts

From Figure 5.2-1, it was noted a displacement of the characteristic hysteresis loop into the multilayer region at higher pressures, as the Ni:CA ratio was increased. Based on the International Union of Pure & Applied Chemistry (IUPAC) classification of isotherms [6], the isotherm from the Ni/SiO₂-A catalyst (Ni:CA 1:1), seems to be a combination between type I and type IV isotherms, with a hysteresis loop of the H2 type. The combination of these types of isotherms might suggest a material with limited pore size and very small external surface area, whereas the hysteresis loop might result from a complex pore structure and a network with pores of different shapes and sizes [7]. On the other hand, the isotherms from the Ni/SiO₂-B and Ni/SiO₂-C catalysts depicted a similar trend with an isotherm of type IV, as a result of the filling and emptying of mesopores by capillary condensation. Moreover the hysteresis loop of the H1 type, is normally associated with adsorbents with a narrow distribution of uniform pores [7].

5.2.2 Study of the catalytic activity

The synthesised catalysts were tested for their ability toward hydrogen production and tar reduction during the pyrolysis-gasification of RDF. The experimental conditions have been previously described in Chapter 3, Section 3.3. The catalytic activity was examined in relation to hydrogen production. The produced gases were subjected to gas chromatography analysis, and the concentration of permanent and light hydrocarbons was determined on a N₂ free basis. In addition the gas and residue yields were also calculated together with the general mass balance for each experiment. The results from the GC analysis and other results obtained are shown in Table 5.2-2.

Table 5.2-2. Gas composition, product yields and mass balance

Catalyst	Gas composition (Vol.%, N ₂ free)					Gas Yield (wt.%)	Residue Yield (%)	Mass Balance (wt.%)
	CO	H ₂	CO ₂	CH ₄	C ₂ -C ₄			
Ni/SiO ₂ -A	17.7	56.6	21.3	3.1	1.3	71.1	29.5	96.3
Ni/SiO ₂ -B	18.8	57.8	20.1	2.4	0.9	71.2	30.3	93.7
Ni/SiO ₂ -C	18.4	57.9	20.7	2.2	0.8	68.7	29.8	91.6
Sand	22.3	24.3	20.7	19.0	13.7	50.0	30.5	96.5

From Table 5.2-2, the gas yield was calculated considering the final weight of the produced gas, the tar/oil fraction collected, and the RDF residue, divided by the initial weight of the RDF sample plus the steam added during the experiment, as shown in Equation 5.2-1.

$$mass\ balance = \frac{gas\ products + liquid\ products + char\ (residue)}{RDF + Supplied\ water} \quad \text{Equation 5.2-1}$$

From Table 5.2-2, it was noted that the residue yield was around 30%, which is related with the constant amount of initial RDF sample used for all the experiments. The aforementioned yield means that about 70wt.% of the initial RDF sample was converted into liquid and/or gaseous products. For the experiment carried out with the sand bed, about 50wt.% of gas yield was attained; whereas the gas yield was increased up to 71wt.% in the presence of the Ni/SiO₂ catalysts. About 24vol.% of hydrogen concentration was obtained

using the sand bed, however when using the Ni/SiO₂ catalyst bed, the H₂ concentration increased up to about 58vol.%. CO and CH₄ concentrations were reduced, also a remarkable reduction in the concentration of light hydrocarbons (C₂-C₄) from about 14vol.% to less than 1vol.% was obtained when changing the bed from sand to the prepared Ni/SiO₂ catalysts. CO concentrations were about 22vol.% when using the sand bed and was further reduced to less than 18vol.% in the presence of the Ni/SiO₂ catalysts. Changes in the concentration of the produced gas can be explained due to the promotion of certain reactions taking place during the thermal decomposition of RDF, some of these main reactions are shown in Table 5.2-3 [8, 9].

Table 5.2-3. Reactions taking place during gasification

Reaction Type	Reaction	
Steam Reforming	$C_nH_m + nH_2O \leftrightarrow nCO + \left(n + \frac{m}{2}\right)H_2$	(1)
Dry Reforming	$C_nH_m + nCO_2 \leftrightarrow 2nCO + \left(\frac{m}{2}\right)H_2$	(2)
Thermal cracking	$C_nH_m \leftrightarrow C^* + C_xH_y + gas$	(3)
Tars hydrocracking	$C_nH_m + H_2 \leftrightarrow CO + H_2 + CH_4 + \dots + coke$	(4)
Water-gas shift reaction	$CO + H_2O \leftrightarrow CO_2 + H_2$	(5)

C_nH_m are hydrocarbons representing tars; C_xH_y hydrocarbons representing lighter tars.

The increase in the H₂ concentration from the experiment using the sand bed compared with those using Ni/SiO₂ catalysts (Table 5.2-2), can be explained due to the promotion of steam reforming and water-gas reactions (Reactions 1 and 5, Table 5.2-3). Also the promotion of cracking reactions (Reactions 3 and 4, Table 5.2-3) might have contributed to the reduction in the concentrations of CH₄ and C₂-C₄ in the presence of Ni/SiO₂ catalysts [10]. The similarity in the concentrations of CO₂ (~20 vol.%) for all the experiments, might be related with a similar promotion of the water-gas shift reaction (Reaction 5, Table 5.2-3), however when using the catalysts other reactions were also promoted, resulting in changes in the concentrations of other gas compounds.

From Table 5.2-2, it was noted that there was a little influence by modifying the Ni:CA ratio over the gas yield and also in the concentration of some gases. As for example the H₂ concentration attained was around 57wt.%, CO concentration

about 18wt.%, and CO₂ concentrations around 20wt.% for all the Ni/SiO₂ catalysts. However using the Ni/SiO₂-A catalyst about 3wt.% and 1wt.% concentrations for CH₄ and C₂-C₄ were obtained, and were further reduced up to ~2wt.% and 0.8wt.% respectively, as the Ni:CA ratio was increased up to 1:3. This reduction in the concentration might be related with a higher promotion of cracking reactions (Reactions 3 and 4, Table 5.2-3), followed by a release of H₂, and hence an increase in its concentration when using higher citric acid during the catalysts preparation [11].

Wu et al [1], have previously studied the variation of Ni:CA ratios during the Ni/SiO₂ preparation, specifically the effects over the catalytic activity during ethanol steam reforming. They found an increase in both hydrogen concentration and gas yield as the nickel to citric acid ratio was increased from 1:0.5 to 1:1; however they reported that the further increase in the Ni:CA, resulted in a decrease in the gas yield. This is in accordance with the present results (Table 5.2-2), as it seems the gas yield was slightly reduced when the Ni:CA ratio was increased from 1:2 to 1:3.

5.2.3 Analysis of the tar fraction

Tar/oil samples were collected from the condensers after each experiment using dichloromethane. The details about the sample collection, preparation and analysis are given in the Chapter 3, Section 3.4.3. The samples were prepared using centrifugation in order to evaporate the organic solvent (dichloromethane, DCM); afterwards the samples were analysed using gas chromatography and mass spectrometry (GC-MS). The assigned compounds, elution retention time, molecular weight, compound concentration ($\mu\text{g}_{\text{compound}}/\text{g}_{\text{RDF}}$), and global tar concentration values ($\text{mg}_{\text{tar}}/\text{g}_{\text{RDF}}$), are shown in Table 5.2-4.

Table 5.2-4. Identification of tar compounds using GC-MS analysis

(µg _{compound} /g _{RDF})						
RT (min)	Assigned Peak	MW (g mol ⁻¹)	Ni/SiO ₂ -A	Ni/SiO ₂ -B	Ni/SiO ₂ -C	SAND
7.84	Furfural	96	—	5.39	1.52	28.77
7.81	Cyclopentanone	84	—	5.40	1.45	—
8.67	Ethylbenzene	106	—	—	—	16.75
9.02	p-Xylene	106	4.51	—	3.06	43.61
9.02	m-Xylene	106	4.42	—	3.18	42.11
9.86	Styrene	104	1.08	2.46	1.41	141.50
9.89	o-Xylene	106	—	—	—	11.95
12.45	Alphamethylstyrene	118	—	—	—	15.20
13.12	Betamethylstyrene	118	—	—	—	9.11
13.36	Phenol	94	61.68	255.09	183.82	613.56
14.78	s-Limonene	136	—	—	—	15.24
14.97	Indane	118	—	0.20	—	1.54
15.35	Indene	116	4.88	11.31	1.23	90.34
15.69	o-Cresol	108	2.07	6.82	2.72	36.10
16.14	Acetophenone	120	1.22	—	0.99	—
16.47	p-Cresol	108	3.53	16.2	5.58	65.16
16.48	m-Cresol	108	3.41	14.65	5.34	63.66
16.58	2-methoxyphenol	124	—	—	—	24.79
17.38	2-Methylbenzofuran	132	0.78	—	—	—
18.61	2,4-Dimethylphenol	122	—	—	—	5.63
19.27	Ethylphenol	122	—	—	—	13.59
19.27	2,6-Dimethylphenol	122	—	—	—	17.75
20.98	Naphthalene	128	19.14	79.20	4.11	58.18
20.98	2,3,5-Trimethylphenol	136	—	—	—	2.08
23.16	2-Methylnaphthalene	142	2.27	6.66	1.62	97.00
25.08	Biphenyl	154	2.06	4.61	2.06	69.20
25.32	2-ethylnaphthalene	156	—	—	—	—
25.54	2,6-dimethyl naphthalene	156	—	—	—	1.04
26.16	1,4-dimethylnaphthalene	156	—	1.43	1.21	0.95
27.47	Dibenzofuran	168	3.37	3.70	—	24.13
28.51	Fluorene	166	6.59	10.62	4.51	50.10
29.28	1,3-diphenylpropane	196	—	—	1.36	1.19
29.34	2-Phenylphenol	170	—	—	—	13.32
31.06	Phenanthrene	178	15.50	41.25	3.81	51.11
31.74	1-Phenylnaphthalene	204	—	—	—	1.40
31.97	o-Terphenyl	230	1.53	—	1.46	—
34.17	Fluoranthene	202	3.17	4.63	2.78	24.66
34.48	Pyrene	202	3.11	4.43	3.16	35.86
34.62	m-Terphenyl	230	2.64	2.82	2.49	29.99
41.98	1,3,5-triphenylbenzene	306	—	—	2.13	—
Tar Concentration (µg _{tar} /g _{RDF})			149.04	476.87	241.03	1716.52
Tar Concentration (mg _{tar} /g _{RDF})			0.15	0.48	0.24	1.72

From Table 5.2-4, it was observed that major contributions for all the tar samples came from phenol, cresols, naphthalene, fluorene and phenanthrene compounds. Some compounds such as styrene, phenol, naphthalene and phenanthrene have been previously identified in tar samples from the catalytic steam reforming of RDF [12, 13]. The highest tar concentration of 1.7 mg_{tar}/g_{RDF} was attained using the bed of sand; whereas significant improvement in tar decomposition was attained using the Ni/SiO₂ catalysts, reducing to 0.15

$\text{mg}_{\text{tar}}/\text{g}_{\text{RDF}}$. Considering the tar classification previously addressed in Section 5.1.3 (Table 5.1-5), the tar compounds reported in Table 5.2-4 were grouped accordingly from tar Class 2 to Class 5. Figure 5.2-2, shows the concentrations for each tar class.

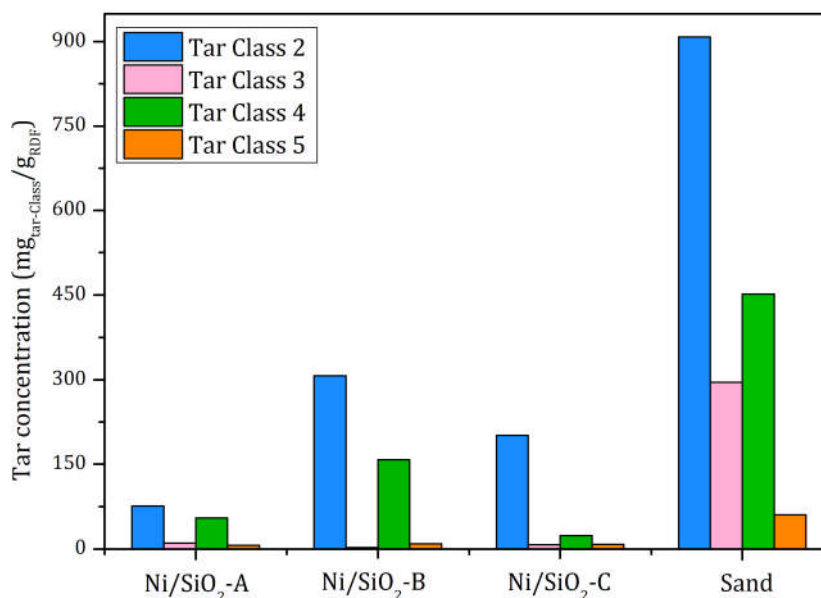


Figure 5.2-2. Classification of tar compounds

Figure 5.2-2, shows that the most abundant groups are tar Class 2 and Class 4 for all the samples, whereas lower concentrations of tar Class 3 and Class 5 were observed. Also a high catalytic activity for tar cracking is observed for the experiments carried out using the Ni/SiO₂ catalysts, when compared with the experiment carried out using the bed sand. Tar Class 2 includes heterocyclic aromatic compounds such as phenol which showed the highest concentration ranging from 62 up to 613 $\mu\text{g}_{\text{phenol}}/\text{g}_{\text{RDF}}$ (Table 5.2-4). Phenol is a relevant tar compound, as it has been referred to as tar model compound due to its major presence in tar samples [14, 15]. From Table 5.2-4, a significant catalytic activity for phenol conversion when using the Ni/SiO₂-A catalyst (Ni:CA, 1:1) was observed, the resulting phenol concentration was 62 $\mu\text{g}_{\text{phenol}}/\text{g}_{\text{RDF}}$. Whereas a concentration of ca. 613 $\mu\text{g}_{\text{phenol}}/\text{g}_{\text{RDF}}$, was obtained using the sand bed. The formation mechanism of aromatic hydrocarbons such as naphthalene and (methyl)indenes has been previously reported by Larsen and Egsgaard [16], and is shown in Figure 5.2-3. In general the cyclopentadienes resulting from the decarbonylation reaction undergoes a Diels-Alder reaction leading to dimer

formation. The system is then rearranged by further loss of hydrogen resulting in the formation of naphthalene and indene. This suggests that phenol is the precursor for the formation of naphthalene and (methyl)indene, during the pyrolysis process (Figure 5.2-3).

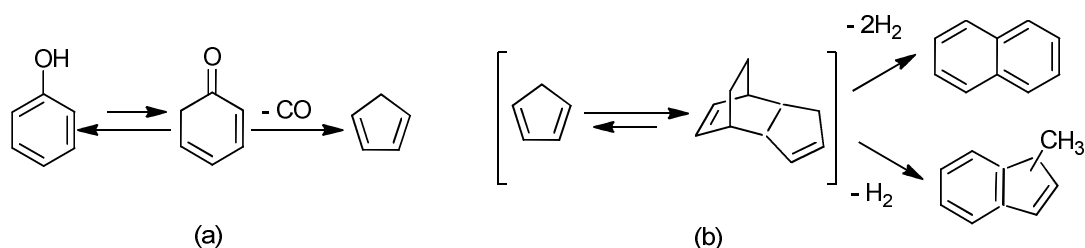


Figure 5.2-3. Pyrolysis of phenol (a); formation mechanism of naphthalene and (methyl)indene (b)

Figure 5.2-2, shows the reduction in the concentration of tar Class 3 when the Ni:CA ratio was increased from 1:1 to 1:2, however when the Ni:CA was further increased to 1:3 (Ni/SiO₂-C), the concentration of tar Class 3 was slightly increased. This effect might be related with the cracking properties of the catalyst, as the higher citric acid concentrations avoided the rupture of lighter compounds (1-Ring). Therefore more efficient catalytic activities might be present for higher aromatic compounds. In the tar Class 4 (Figure 5.2-2), grouped compounds including naphthalene and their methyl derivatives can be found along with phenanthrene, biphenyl and fluorene (Table 5.2-4). When the Ni:CA ratio was increased from 1:2 (Ni/SiO₂-B) up to 1:3 (Ni/SiO₂-C), a remarkable reduction in tar Class 4 was detected; the higher concentration of citric acid might have promoted the formation of higher pore volume and pore diameters in the catalyst structure (Table 5.2-1), which at the same time might have allowed larger molecules to be reformed by passing through the catalyst pore structure [1]. In general the concentration of the tar Class 5 was very low for all the experiments carried out, ranging from ca. 6 up to 9 $\mu\text{g}_{\text{tar-Class5}}/\text{g}_{\text{RDF}}$. From the analysed tar samples, major contributions to the tar Class 5, came from fluoranthene and pyrene. For the sand experiment, the lowest tar concentration was also related to tar Class 5, with a value of 9 $\mu\text{g}_{\text{tar-Class5}}/\text{g}_{\text{RDF}}$. Matas Güell et al [15], reported that the overall tar dew point seems to be governed by tar Class 5 despite its relatively low concentration. This feature is

highly relevant for the study of associated tar problems and with the use of the product gas downstream.

Major contribution to the concentrations of the tar samples analysed, came from phenol, cresols, naphthalene, fluorene and phenanthrene (Table 5.2-4). The catalytic activity for phenol and cresols was as follows: Ni/SiO₂-A > Ni/SiO₂-C > Ni/SiO₂-B; for naphthalene and fluorene: Ni/SiO₂-C > Ni/SiO₂-A > Ni/SiO₂-B; and for phenanthrene Ni/SiO₂-C > Ni/SiO₂-A > Ni/SiO₂-B. Therefore the Ni/SiO₂-C catalyst presented the best performance in terms of major tar compounds reduction, although final tar concentrations of 0.2 mg_{tar}/g_{RDF} was attained using both Ni/SiO₂-A and Ni/SiO₂-C catalysts.

5.2.4 Analysis of reacted catalysts

Thermogravimetric analysis (TGA), was used in order to study the carbon deposition over the reacted Ni/SiO₂ catalysts; the resulting temperature programmed oxidation curves (TGA-TPO), and their respective derivative curves (DTG-TPO) are shown in Figure 5.2-4.

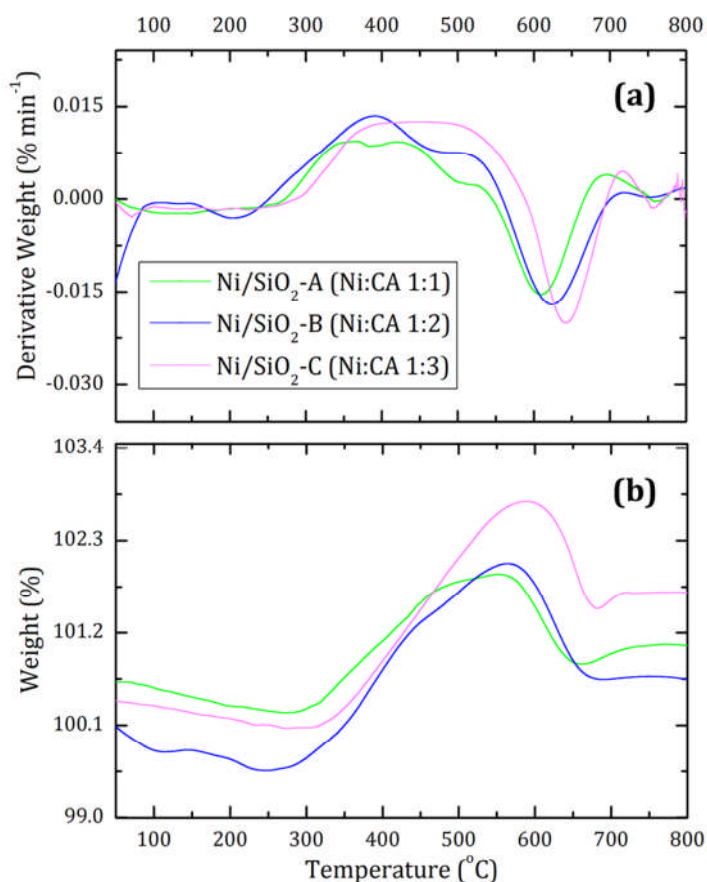


Figure 5.2-4. DTG-TPO (a) and TGA-TPO (b) of reacted Ni/SiO₂ catalysts

From Figure 5.2-4, different stages related to changes in the weight were observed for the thermogravimetric curves from the reacted Ni/SiO₂ catalysts. As mentioned in the TGA analysis in the previous Section 5.1, the initial weight lost (~100 °C) is normally associated with evaporation of water or moisture [1] (Figure 5.2-4(b)). After this initial weight loss, all the thermograms tend to increase from 350 °C up to 600 °C, and finally a weight decrease was noticed. Similar trends in the derivative thermograms (Figure 5.2-4(a)), indicated the nickel oxidation associated with the weight increase, followed by the presence of filamentous type carbon related with the major peak observed around 650 °C [17, 18]. In addition to the thermogravimetric analysis, the surface of the reacted catalysts was analysed by scanning electron microscopy, and the resulting images are shown in Figure 5.2-5.

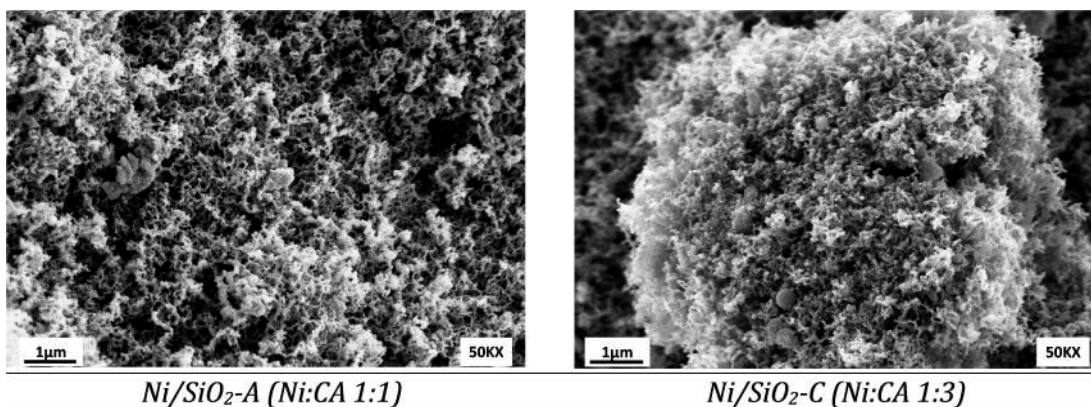


Figure 5.2-5. SEM images of reacted Ni/SiO₂ catalysts

From Figure 5.2-5, some filamentous type carbons were identified over the surface of reacted Ni/SiO₂-A and Ni/SiO₂-C catalysts; which is in accordance with the results from the thermogravimetric analysis. The analysis of the carbon deposition is a relevant parameter, as it is closely related to the catalyst deactivation, primarily due to masking of catalyst active sites. A common practice to assess the lifecycle of a catalyst includes the re-use of the catalyst; however this analysis has not been carried out in this work. However in general it might be expected that a decrease in the catalytic activity due to the amount and type of carbon deposits found on the catalyst surface is likely to occur.

5.2.5 Summary

The present Section 5.2, studied the effects of varying the nickel to citric acid ratios (Ni:CA) from 1:1, 1:2, and 1:3, over the catalysts characteristics. In addition the catalytic activity of the Ni/SiO₂ catalysts was tested in relation to hydrogen production and tar reduction, during the pyrolysis-gasification of RDF. Furthermore the catalytic activity was compared with a blank experiment, carried out using a bed of sand.

Regarding hydrogen production from the analysis of the produced gas, it was found that the major catalytic activity was given by the Ni/SiO₂-A catalyst; however very similar H₂ concentrations were attained when using the catalysts prepared at lower Ni:CA ratios of 1:1 and 1:2. Thus no positive effect of varying this property over the H₂ production was attained. The concentrations of CH₄ and C₂-C₄ were reduced in the produced gas as the Ni:CA ratio was increased.

Similar tar concentrations of about $0.2\text{mg}_{\text{tar}}/\text{g}_{\text{RDF}}$ were attained using the Ni/SiO₂-A and Ni/SiO₂-C catalysts, whereas a higher tar concentration of about $1.7\text{mg}_{\text{tar}}/\text{g}_{\text{RDF}}$ was found for the experiment carried out using the sand bed. The major identified tar compounds include phenol, cresols, naphthalene, fluorene, and phenanthrene; and the highest tar cracking activity for these compounds was observed when using the Ni/SiO₂-C catalyst (Ni:CA, 1:3).

It was found that filamentous carbons were formed over the catalysts surface, with very low influence of changing the Ni:CA ratio over the type of carbons deposited.

References

1. Wu, C.F. and P.T. Williams, *Hydrogen production from steam reforming of ethanol with nano-Ni/SiO₂ catalysts prepared at different Ni to citric acid ratios using a sol-gel method*. Applied Catalysis B-Environmental, 2011. 102(1-2): p. 251-259.
2. Takahashi, R., S. Sato, T. Sodesawa, M. Kawakita, and K. Ogura, *High surface-area silica with controlled pore size prepared from nanocomposite of silica and citric acid*. Journal of Physical Chemistry B, 2000. 104(51): p. 12184-12191.
3. Nguyen, C. and D.D. Do, *The Dubinin–Radushkevich equation and the underlying microscopic adsorption description*. Carbon, 2001. 39(9): p. 1327-1336.
4. Barrett, E.P., L.G. Joyner, and P.P. Halenda, *The Determination of Pore Volume and Area Distributions in Porous Substances. I. Computations from Nitrogen Isotherms*. Journal of the American Chemical Society, 1951. 73(1): p. 373-380.
5. Takahashi, R., S. Sato, T. Sodesawa, M. Suzuki, and N. Ichikuni, *Ni/SiO₂ prepared by sol-gel process using citric acid*. Microporous and Mesoporous Materials, 2003. 66(2-3): p. 197-208.
6. Sing, K.S.W., D.H. Everett, R.A.W. Haul, L. Moscou, R.A. Pierotti, J. Rouquerol, and T. Siemieniewska, *Reporting Physisorption Data for Gas Solid Systems with Special Reference to the Determination of Surface-Area and Porosity (Recommendations 1984)*. Pure and Applied Chemistry, 1985. 57(4): p. 603-619.
7. Rouquerol, F., J. Rouquerol, and K.S.W. Sing, *Adsorption by Powders and Porous Solids*. 1999, London: Academic Press.
8. Devi, L., K.J. Ptasinski, and F.J.J.G. Janssen, *Pretreated olivine as tar removal catalyst for biomass gasifiers: investigation using naphthalene as model biomass tar*. Fuel Processing Technology, 2005. 86(6): p. 707-730.
9. Abu El-Rub, Z., Bramer, E. A., Brem, G. , *Review of Catalysts for Tar Elimination in Biomass Gasification Processes*. Industrial and Engineering Chemistry Research, 2004. 43(22): p. 6911-6919.
10. Kim, J.-W., T.-Y. Mun, J.-O. Kim, and J.-S. Kim, *Air gasification of mixed plastic wastes using a two-stage gasifier for the production of producer gas with low tar and a high caloric value*. Fuel, 2011. 90(6): p. 2266-2272.
11. Pinto, F., R.N. André, C. Franco, H. Lopes, I. Gulyurtlu, and I. Cabrita, *Co-gasification of coal and wastes in a pilot-scale installation 1: Effect of catalysts in syngas treatment to achieve tar abatement*. Fuel, 2009. 88(12): p. 2392-2402.
12. Blanco, P.H., C. Wu, J.A. Onwudili, and P.T. Williams, *Characterization of Tar from the Pyrolysis/Gasification of Refuse Derived Fuel: Influence of Process Parameters and Catalysis*. Energy & Fuels, 2012. 26(4): p. 2107-2115.
13. Blanco, P.H., C. Wu, J.A. Onwudili, and P.T. Williams, *Characterization and evaluation of Ni/SiO₂ catalysts for hydrogen production and tar reduction*

- from catalytic steam pyrolysis-reforming of refuse derived fuel*. Applied Catalysis B: Environmental, 2013. 134–135(0): p. 238-250.
14. Abu El-Rub, Z., E.A. Bramer, and G. Brem, *Experimental comparison of biomass chars with other catalysts for tar reduction*. Fuel, 2008. 87(10-11): p. 2243-2252.
 15. Matas Güell, B., I.V. Babich, L. Lefferts, and K. Seshan, *Steam reforming of phenol over Ni-based catalysts – A comparative study*. Applied Catalysis B: Environmental, 2011. 106(3–4): p. 280-286.
 16. Larsen, E., Egsgaard, H., Pedersen, K., Zielke, U., Brandt, P. *Tar compounds in condensates from different types of gasifiers*. in *1st World Conference on Biomass for Energy and Industry*. 2000. Sevilla, Spain: James & James (Science Publishers) Ltd.
 17. Wu, C. and P.T. Williams, *Hydrogen production by steam gasification of polypropylene with various nickel catalysts*. Applied Catalysis B: Environmental, 2009. 87(3-4): p. 152-161.
 18. Wu, C. and P.T. Williams, *Investigation of coke formation on Ni-Mg-Al catalyst for hydrogen production from the catalytic steam pyrolysis-gasification of polypropylene*. Applied Catalysis B: Environmental, 2010. 96(1-2): p. 198-207.

5.3 Ni/SiO₂ catalysts prepared by homogeneous precipitation (HPG) and homogeneous precipitation with phase separation (B-HPG) methods

As shown in sections 5.1 and 5.2, the preparation method, the type and the amounts of raw materials used during the synthesis of nickel-based catalysts, has an effect on both catalysts properties and catalytic activity. The preparation methods reported in the literature such as impregnation, sol-gel, co-precipitation, etc., highlight the benefits and improvements of using a specific synthesis route. For example, it has been reported that the use of conventional impregnation or ion exchange during the preparation of Ni/SiO₂ catalysts can result in low surface area and poor nickel dispersion, and even more influence the catalyst deactivation. In addition the use of high nickel loadings can promote aggregation of nickel particles during calcination and reduction of the catalyst [1].

From sections 5.1 and 5.2, it was noted that Ni/SiO₂ catalysts prepared by sol-gel methods showed a better performance when compared with catalysts prepared by impregnation method, a similar performance has been reported in the literature when these type of catalysts have been tested during the CO₂ reforming of methane [2]. One of the main restrictions when preparing Ni/SiO₂ catalysts through the sol-gel method, has been to achieve a good dispersion of the metal particles, particularly when using nickel loadings higher than 15wt.% [3]. One of the alternatives proposed to promote a higher metal dispersion and to increase the surface area at the same time, has been to work in an acidic medium during the catalyst preparation; using tetraethyl orthosilicate (TEOS) as SiO₂ precursor and dispersed metal-hydroxide (or oxide) as metal precursor [3]. Moreover, the reaction between TEOS and nickel nitrate might result in an increase in the sintering resistance and a reduction in the catalysts deactivation [4, 5]. A sol-gel method known as homogeneous precipitation (HPG), has been used to promote the metal dispersion inside the porous silica matrix, thus the resulting catalyst possesses high thermal stability, and high sintering resistance as the Ni metal particles are entrapped within a silica network. Figure 5.3-1,

shows the silica oxide formation route towards the final Ni/SiO₂ catalyst, through the HPG preparation method [6-8].

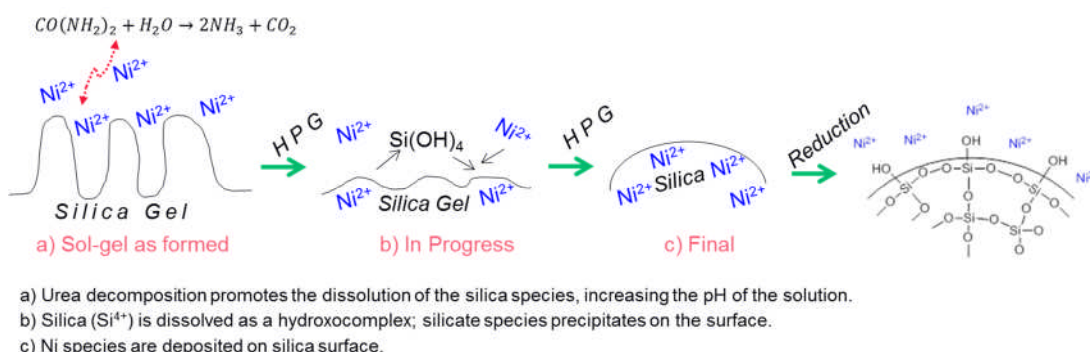


Figure 5.3-1. Homogeneous precipitation method (HPG), for Ni/SiO₂ catalyst preparation

From Figure 5.3-1, the sequential steps include; the urea decomposition that allows the dissolution of silica species also increasing the pH of the medium; the dissolution of silica species and further precipitation of silicates; to finally achieve the deposition of nickel over the silica surface and its interaction with the silica lattice. In order to further improve the properties of the final Ni/SiO₂ catalyst through the HPG method, Takahashi et al [9], suggested the addition of a phase separation step after the homogeneous precipitation, in order to allow the formation of a bimodal pores structure with macropores and mesopores. The formation pathway and the influence of the interaction between the phase separation and gelation process over the final pore structure, are shown in Figure 5.3-2.

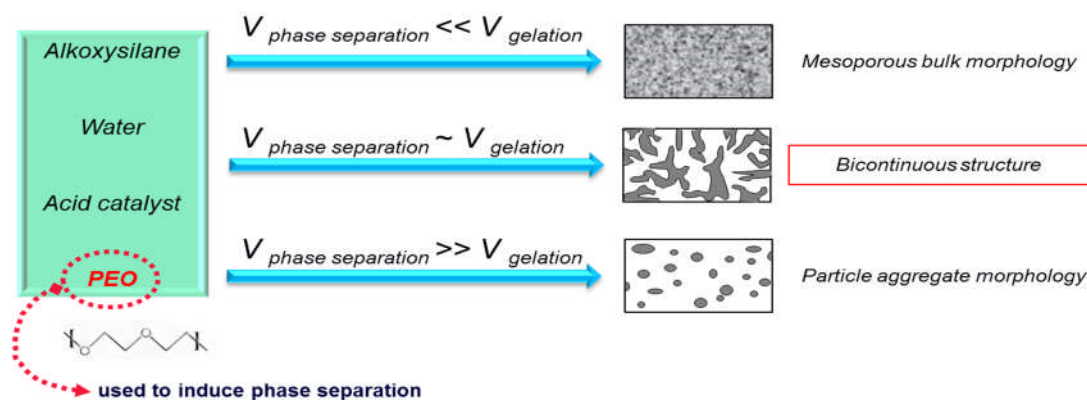


Figure 5.3-2. Phase separation followed by aging of the gel to promote wider pore distribution in the catalyst

In Figure 5.3-2, are shown the effects on the catalysts properties when increasing or reducing the velocity at which phase separation and gelation steps take place. The onset of phase separation and gelation processes, are major factors influencing the final structure of the catalysts. Thus for example if the gelation is much faster than the phase separation, a dense gelatinous mesoporous bulk morphology will be originated. Whereas if the phase separation takes place much faster than the gelation, a final particle aggregate morphology will be formed. Finally when both steps take place at similar velocities, a final bi-continuous catalyst can be obtained [10].

Considering the influence of the homogeneous precipitation (HPG), and the addition of the phase separation methods over the Ni/SiO₂ catalysts properties, in this section of the work a series of six different catalysts were synthesized through both routes. The final catalysts were characterised through different analytical techniques to identify their properties, in addition the six catalysts were tested in the two-stage pyrolysis-gasification reaction system (Chapter 3, Section 3.3), for their ability for hydrogen production during the thermal decomposition of RDF.

5.3.1 Characteristics of Ni/SiO₂ catalysts prepared by HPG and B-HPG methods

The preparation details of the Ni/SiO₂ catalysts used within this section can be found in Chapter 3, Section 3.2.2.4. The nickel loading was maintained constant at 10wt.% for all the catalysts, whereas three different calcination temperatures 500 °C, 700 °C and 900 °C were used during the preparation. The methodology followed for the preparation of the HPG catalysts was based on that reported by Tomiyama et al [6]. Whereas the methodology for the combined phase separation and HPG method was based on that reported by Takahashi et al [9]. The homogeneous precipitated catalysts were assigned as HPG500, HPG700 and HPG900, and those catalysts prepared through combined phase separation and HPG method were identified as to B-HPG500, B-HPG700 and B-HPG900.

The BET surface area and porous characteristics from the HPG and B-HPG catalysts are shown in the following Table 5.3-1.

Table 5.3-1. Surface area and porous properties of HPG and B-HPG catalysts

Catalyst	Ni content (wt%)	Surface area ¹ (m ² g ⁻¹)	Micropore volume ² (cm ³ g ⁻¹)	Mesoporous volume ² (cm ³ g ⁻¹)	Pore diameter ³ (nm)	Average Mesopore Size (nm) ⁴
HPG500	10	363.7	0.18	0.86	9.76	7.45
HPG700	10	347.3	0.18	0.91	12.50	8.92
HPG900	10	313.8	0.16	0.84	9.75	7.45
B-HPG500	10	387.3	0.22	0.80	12.58	8.92
B-HPG700	10	446.1	0.25	0.92	9.46	7.45
B-HPG900	10	318.2	0.16	0.82	12.63	11.17

¹ MultiPoint Brunauer, Emmett & Teller (BET) Method

² Dubinin-Radushkevich (DR) Method

³ Barrett, Joyner & Halenda (BJH) Method

⁴ Density Functional Theory (DFT)

From Table 5.3-1, it was noted a reduction in the surface area of the HPG series of catalysts, as the calcination temperature was increased. This trend might be related to the formation of interphase silica-like compounds during the calcination step [11]. Tomiyama et al [6], reported a decrease in the surface area as the calcination temperature was increased when working with Ni/SiO₂ catalysts prepared by the HPG method, which is in good agreement with the data reported in Table 5.3-1. On the other hand, surface area values from the series of B-HPG catalysts seemed to be increased with the increase of the calcination temperature from 500 to 700 °C. However when the calcination temperature was further increased up to 900 °C the surface area value was reduced. A similar effect in relation to the surface area was observed by Takahashi et al [9], when increasing the calcination temperature from 500 °C up to 700 °C during the preparation of Ni/SiO₂ catalysts by a similar method using a 20 wt.% Ni loading.

The nitrogen adsorption-desorption isotherms from the fresh Ni/SiO₂ catalysts, are shown in Figure 5.3-3.

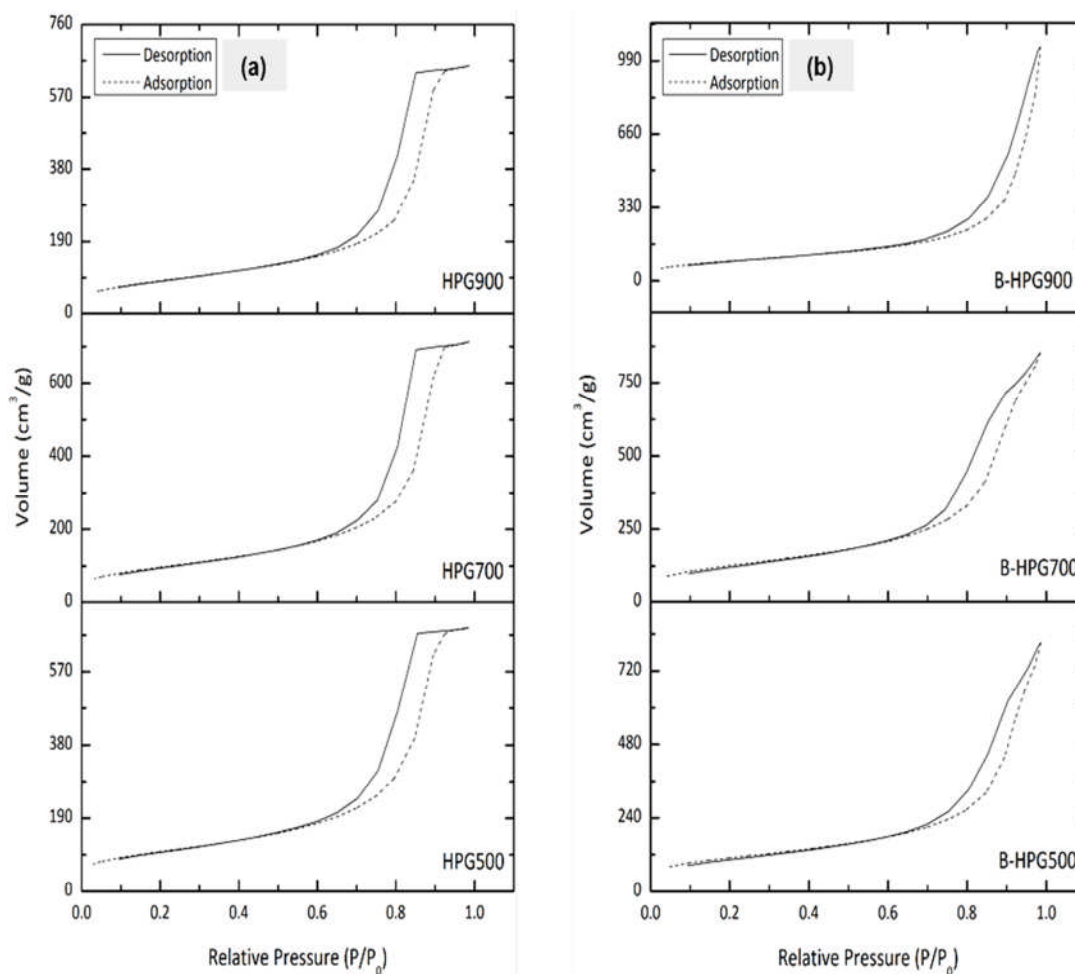


Figure 5.3-3. N₂ adsorption-desorption isotherms of fresh HPG (a), and B-HPG (b) Ni/SiO₂ catalysts

From Figure 5.3-3(a), it was noted that there was a similar trend for the isotherms of the Ni/SiO₂ catalysts prepared by conventional homogeneous precipitation method (HPG). All the isotherms belong from the uncommon IUPAC type V, normally related with porous adsorbents with weak adsorbent-adsorbate interactions [12]. From Figure 5.3-3(a), a sharp inflection was observed within the P/P₀ range from 0.70-0.90, normally associated with capillary condensation and evaporation processes in materials with uniform pores. This inflection is also related to the hysteresis H1 type, present in isotherms from porous materials consisting of agglomerates or compacts of uniform sphere arrays, also presenting a narrow distribution of pore size. This type of hysteresis has been detected in mesoporous silica with a regular array of cylindrical pores and predetermined diameters for example in commercial catalysts such as MCM-41 [13] and SBA-15 [14].

The pore size distribution was also obtained as it is useful to characterize materials according to their porous structure from the adsorption isotherms [15]. The pore distribution was calculated using the regularization method according to the Density Functional Theory (DFT), based on a molecular model of nitrogen adsorption in porous solids [16], described in Chapter 3, Section 3.4.2.4. The results from the DFT are shown in Figure 5.3-4.

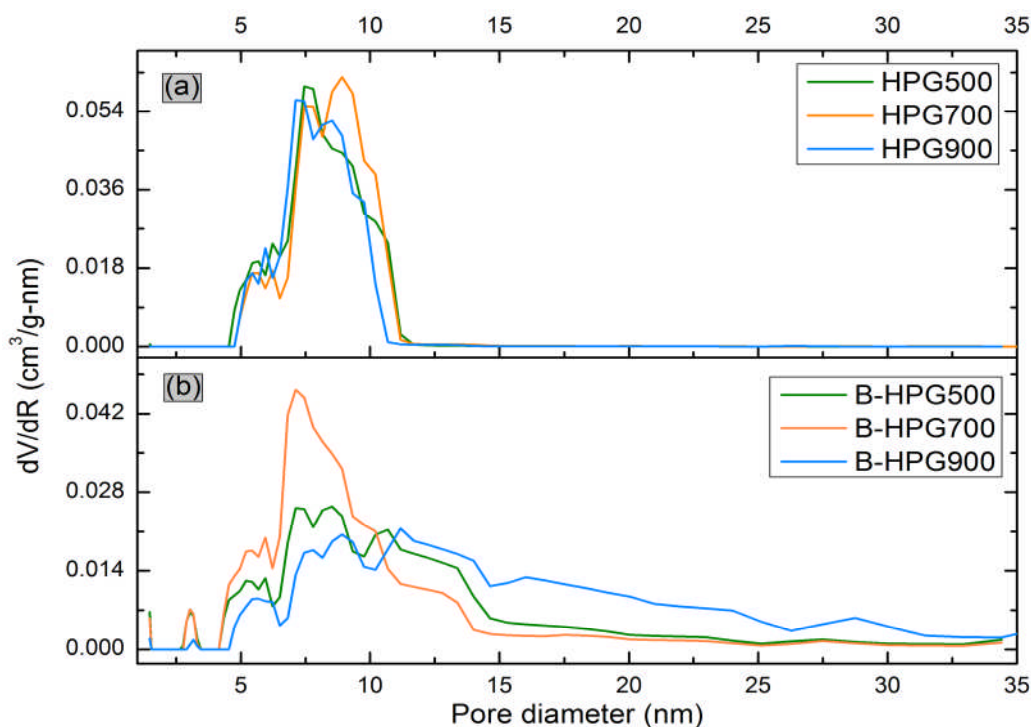


Figure 5.3-4. DFT pore size distribution for HPG (a) and B-HPG (b) Ni/SiO₂ catalysts

From Figure 5.3-4(a), it was noted a narrow pore size distribution for the HPG fresh catalysts, with an average pore size around 7.5nm for the HPG500 and HPG900 catalysts. The pore distribution curve for the HPG700 catalyst showed a shift, resulting in an increase of up to 9nm in the average pore diameter. From Table 5.3-1 higher mesoporous volume and pore diameter values were reported for the HGP700 catalyst, when compared with the HPG500 catalyst. However the further increase in the calcination temperature might have promoted a shrinkage of larger pores [6], as both mesoporous volume and pore diameter values were reduced when 900 °C was used as the calcination temperature.

The isotherms obtained for the B-HPG Ni/SiO₂ catalysts Figure 5.3-3(b), also belonged to the type V. Nevertheless in the isotherms from the B-HPG catalysts it was noted a hysteresis loop of the type H3, ending up very close to the saturation or equilibrium pressure (Figure 5.3-3(b)). Hysteresis of the H3 type are normally observed in solids with wide pore size distribution (Figure 5.3-4(b)), and are characteristic of adsorbents with slit-shaped pores. From Figure 5.3-4(b), it was observed that the catalysts had a polydisperse pore size distribution, attributed to the velocity at which the phase separation and gelation process took place followed by aging in a basic solution. This procedure might have resulted in the formation of a bi-continuous structure with larger pores within the silica skeleton. Macropores are known to be formed through spinodal decomposition process, whereas the mesopore formation was related with the thermal decomposition and changes in the pH in the wet silica gel [9].

XRD analyses were also carried out on the fresh Ni/SiO₂ catalysts in order to identify the different crystallites structures present in each catalyst. Nickel crystallite size was determined according to Scherrer's method from the broadening of the line [17]. In addition the samples were subjected to IR spectroscopy analysis in order to obtain information about the composition of the catalysts. The results obtained from both analyses are shown in Figure 5.3-5.

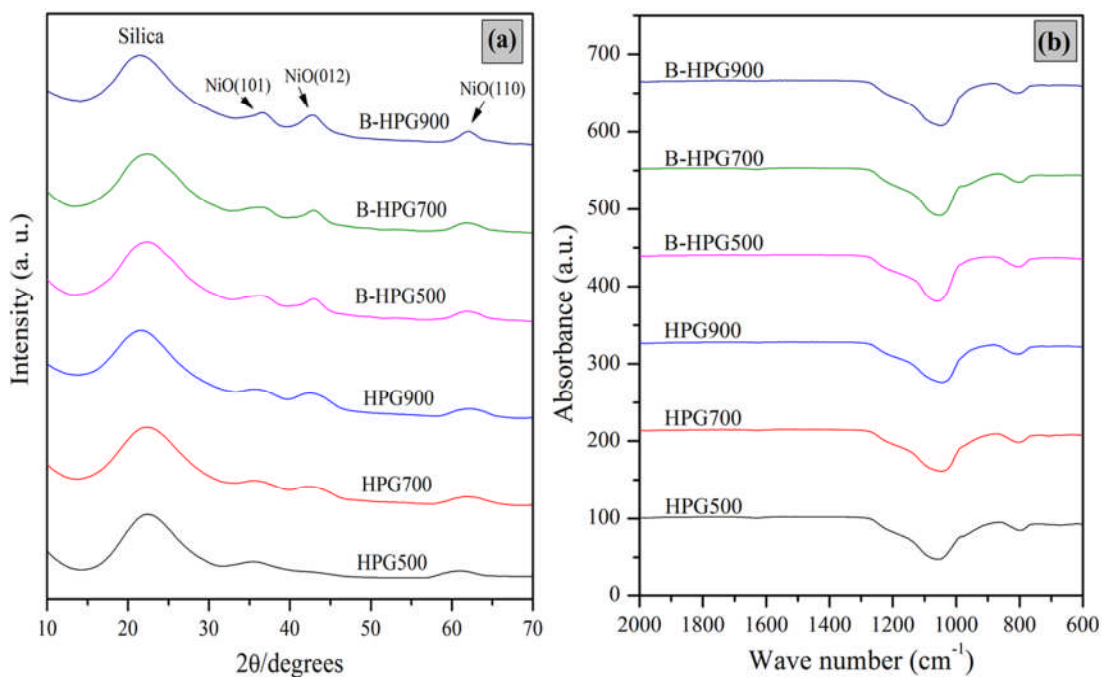


Figure 5.3-5. Analysis of Ni/ SiO₂ samples: (a) XRD analysis; and (b) IR spectra

From XRD analysis (Figure 5.3-5(a)), it was observed that all the samples exhibited similar XRD patterns, with a broad peak at around 22°, generally related with amorphous silica, and associated with a low degree of crystallization of the silica support [18]. The diffraction peaks around 36°, 43° and 62°, were related to the presence of the Ni oxide crystals assigned to NiO(101), NiO(012), and NiO(110), respectively [19]. It was expected that these NiO characteristic peaks became more defined as the calcination temperature was increased for the HPG catalysts [6, 20], however from Figure 5.3-5(a), no significant changes were observed. The three characteristic NiO peaks for the HPG samples were found to be smaller and broader, when compared with those from the B-HPG catalysts; this might indicate that the particle size of NiO was smaller for the HPG samples [9]. The crystallite size was determined using Scherrer's equation from the full width at half maximum of the diffraction peak, and for the HPG samples, crystallite sizes from 2-4nm were obtained, whereas for the B-HPG catalysts the size ranged between 3nm and 5nm.

Figure 5.3-5(b), shows that the IR spectra showed a similar trend for all the analysed catalysts. Two main adsorption bands were identified which have been previously attributed to asymmetrical (1060cm⁻¹) and symmetrical (790cm⁻¹)

stretching motions of the silica skeleton of the type Si-O. The absorption band identified around 1060cm^{-1} was related with the presence of Si-O bonds. The silica support characteristic band is normally identified at 1100cm^{-1} , and the shift to 1060cm^{-1} might be attributed to changes an increase in the temperature during the synthesis and also to the presence of phyllosilicate species such as nepouite ($\text{Si}_2\text{Ni}_3\text{O}_5(\text{OH})_4$) [11, 21].

Further details of the fresh Ni/SiO₂ catalysts surface were investigated by SEM and TEM analyses. The resulting micrographs of selected samples are shown in Figure 5.3-6.

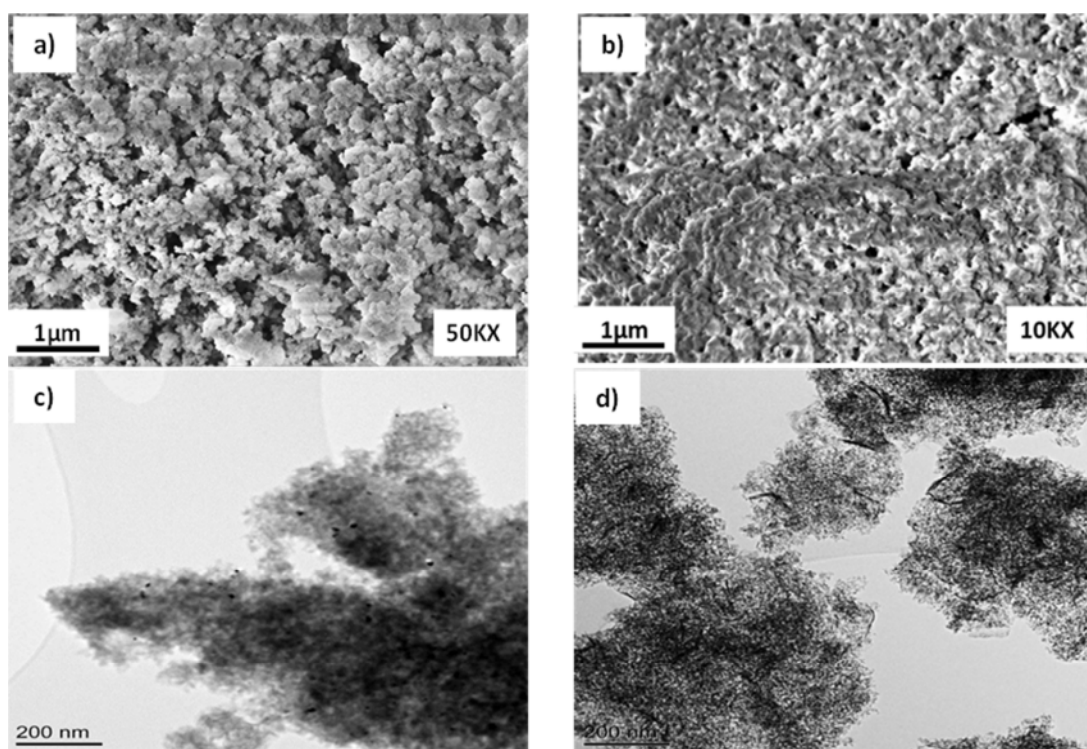


Figure 5.3-6. Analysis of fresh Ni/SiO₂ catalysts; SEM images: (a) HPG700; (b) B-HPG700; TEM images: (c) HPG700; (d) B-HPG700

Figure 5.3-6(a), and Figure 5.3-6(b), correspond to the micrographs of the HPG700 and B-HPG700 catalysts respectively. For both images it was observed the presence of a silica lattice with pores of different shapes and sizes. Further TEM analysis (Figure 5.3-6(c, d)) revealed larger differences, for example the presence and distribution of dark spheres corresponding to nickel particles throughout the silica matrix. Similar morphologies have been previously

reported for Ni/SiO₂ systems analysed by TEM [3, 6, 11, 22]. The HPG700 catalyst presented clear dark spheres distributed through the silica matrix, whereas the B-HPG700 catalyst showed the silica lattice together with some nickel oxide crystals. Similar structures with flake shapes have been reported for nickel oxide compounds [3]. The effect of the calcination temperature on the catalysts morphology is shown in Figure 5.3-7.

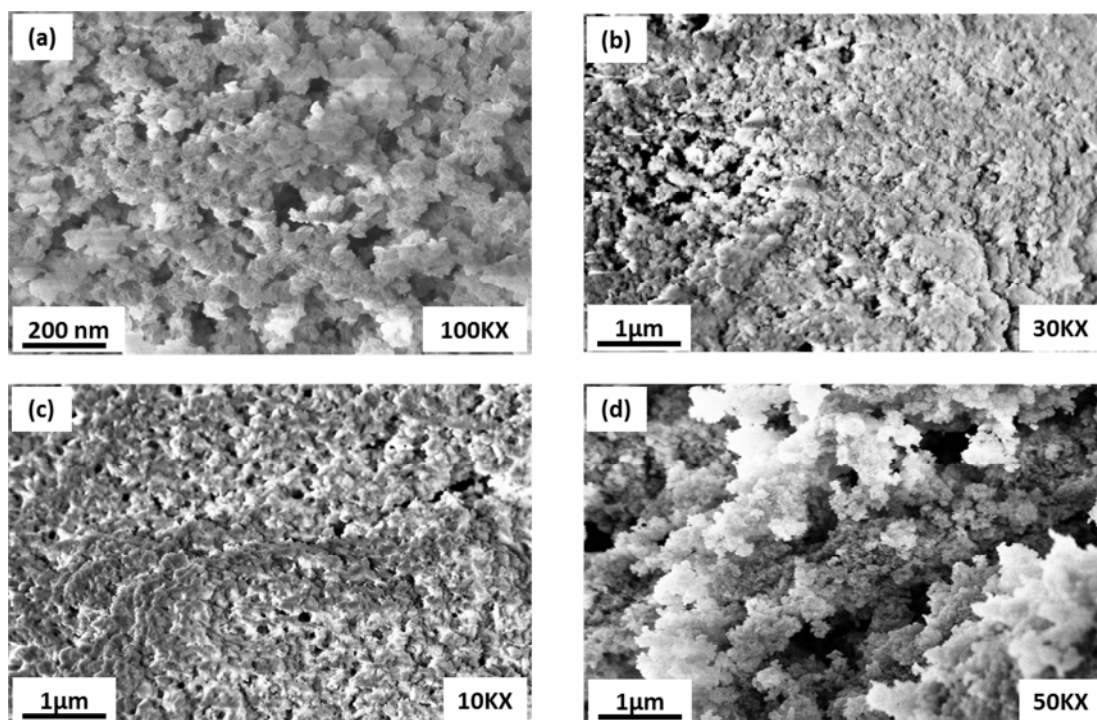


Figure 5.3-7. SEM images of fresh HPG700 (a), HPG900 (b), B-HPG700 (c), and B-HPG900 (d) catalysts

Similar morphologies were observed for the HPG700 (Figure 5.3-7(a)) and B-HPG900 (Figure 5.3-7(d)), whereas similar structures with pores of different shapes and sizes were observed for the HPG900 (Figure 5.3-7(b)) and B-HPG700 (Figure 5.3-7(c)) catalysts. The addition of nickel nitrate and urea in the TEOS-PEO system during the preparation of B-HPG catalysts was expected to increase the formation of bigger pores. This was observed in the Figure 5.3-4 for the pore size distribution and was also observed in the micrograph in Figure 5.3-7(d).

5.3.2 Analysis of catalytic activity of Ni/SiO₂ catalysts prepared by HPG and B-HPG methods

The catalytic activity was assessed during the pyrolysis-gasification of RDF using the two-stage pyrolysis-catalytic reactor described in Chapter 3. The product gases were analysed by gas chromatography and the concentration of permanent gases and light hydrocarbons was calculated. The products yields, gas composition, hydrogen production, RDF conversion, and mass balance are shown in Table 5.3-2.

Table 5.3-2. Gas composition, mass balance and gas yield from the pyrolysis-gasification products

Catalyst	Gas composition (Vol.%, N ₂ free)					H ₂ production (mmol H ₂ g ⁻¹ RDF)	Gas yield (wt.%)	Char/RDF (wt.%)	Mass Balance (wt.%)
	CO	H ₂	CO ₂	CH ₄	C ₂ -C ₄				
HPG500	22.4	55.3	17.2	3.8	1.3	18.5	53.2	29.4	96.2
HPG700	23.5	59.3	13.9	2.8	0.6	21.5	52.6	29.4	92.9
HPG900	23.3	52.0	17.3	5.3	2.1	14.4	46.2	28.9	90.8
B-HPG500	25.8	49.7	17.5	5.4	1.6	16.8	58.2	30.0	94.9
B-HPG700	28.0	53.4	14.7	3.1	0.7	19.4	58.6	29.2	95.7
B-HPG900	24.6	42.3	16.8	11.0	5.3	9.7	42.4	28.8	92.5

The hydrogen production reported in Table 5.3-2, was calculated from the mmol of hydrogen contained in the final gas mixture divided by the initial sample (RDF) weight. From Table 5.3-2, it was noted that the highest catalysts activity towards hydrogen production was attained using the HPG700 catalysts, producing about 60vol.% of H₂ or 22 mmol of H₂ per gram of RDF. The higher hydrogen yield might be due to further promotion of carbon-steam reactions, resulting in lower carbon deposition over the reacted catalyst, and more hydrogen released together with carbon monoxide. Li et al [23], reported a concentration of about 54vol.% of hydrogen in the syngas from the gasification of municipal solid waste (MSW), using a tri-metallic catalyst (Ni-La-Fe/Al₂O₃) in a fixed bed reaction system. When using the HPG700 catalyst, the lowest CH₄ and C₂-C₄ gas concentrations were achieved, this corresponds to less than 3vol.% and 0.6vol.% respectively. In addition, a low CO concentration was produced which might indicate a greater promotion of steam reforming

reactions and a reduced promotion of the water-gas shift reaction, when compared with the other two HPG catalysts.

From Table 5.3-2, for the series of B-HPG catalysts the highest activity in relation to hydrogen production was found when the B-HPG700 catalyst was used, attaining a hydrogen production of 19 mmol H₂ g⁻¹RDF, and a gas yield around 59wt.%. Also the lowest CH₄ and C₂-C₄ concentrations were achieved when compared with the other two B-HPG catalysts. Table 5.3-2, shows a reduction in the CO and an increase in the CO₂ concentrations when using the B-HPG900 catalyst, which might indicate a promotion of the water-gas shift reaction. In addition when the B-HPG900 catalyst was used, the highest concentrations of CH₄ and C₂-C₄ were produced.

In the following Figure 5.3-8, are shown the variations in the gas composition when using each catalyst.

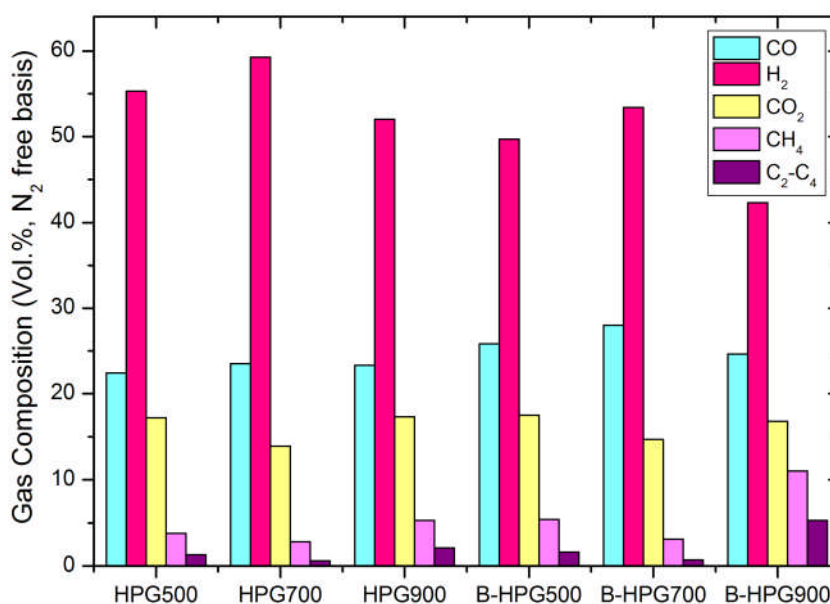


Figure 5.3-8. Variation in the gas composition for HPG and B-HPG catalysts.

From Figure 5.3-8 it was observed that for both series of catalysts, the lowest CH₄ and C₂-C₄ concentrations were achieved when using the catalysts calcined at 700 °C, whereas the lowest activity was attained using the catalysts calcined at 900 °C. This trend might indicate a lower promotion of hydrocarbons and tar

cracking reactions when using this type of catalyst calcined at temperatures higher than 700 °C, but also influenced by the catalysts properties. For example the surface area has been reported as a parameter that influences the catalytic activity as it is related with the accessibility of active sites in the catalyst [24]. From Table 5.3-1, it was observed that for both HPG and B-HPG catalysts, the surface area was reduced as the calcination temperature was increased from 700 °C to 900 °C. In addition, the HPG900 catalyst also exhibited the lowest surface area among the three HPG catalysts.

From the results obtained (Table 5.3-2) it was observed that for the B-HPG catalysts, the activity towards hydrogen production (Figure 5.3-8) followed the same order as the surface area (Table 5.3-1); the highest surface area of 440 m² g⁻¹ resulted in the highest hydrogen production of 19 mmol H₂ g⁻¹_{RDF}. In addition from the XRD analysis (Figure 5.3-5(a)) broader peaks for the NiO crystals were observed for the HPG700 catalyst which indicates a smaller crystal particle size when compared with those peaks for the B-HPG700 catalyst. The larger pore size and smaller crystal size, may have resulted in a better metal dispersion for the HPG700 catalyst, this was also verified by the TEM images of the fresh catalysts (Figure 5.3-6(c)). All the properties of the HPG700 catalysts might also have influenced the higher hydrogen yield attained when used this catalyst. The higher hydrogen production reported for the catalyst calcined at lower temperature (700 °C), when compared with the catalyst calcined at 900 °C, was also supported by results from temperature programmed reduction (TPR) analysis, shown in Figure 5.3-9.

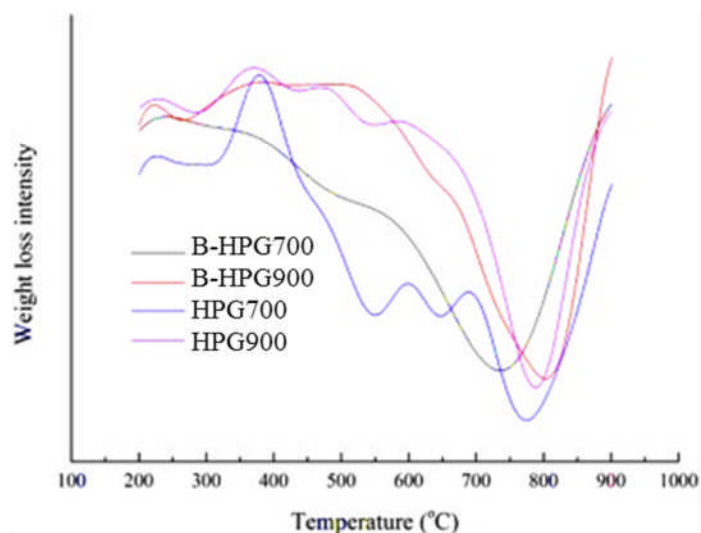


Figure 5.3-9. Temperature programme reduction (TPR) of fresh catalysts

From Figure 5.3-9, it was observed that the catalysts calcined at 900 °C showed a higher reduction temperature, which is normally associated with higher interactions between nickel and the silica support.

5.3.3 Analysis of reacted catalysts

The reacted catalysts were analysed in order to identify the carbon deposition over the catalysts surface, which normally is related with catalyst deactivation. The coke formation has been described as a complex phenomenon, for example Wauters et al [25], used a model based on elementary reactions to explain the coke formation mechanism. The five different reversible reactions reported include; hydrogen abstraction by gas phase radicals; substitution by radicals at the coke surface; addition of a radical surface species to a gas phase; addition of a gas phase radical to an olefinic bond; and cyclization of a radical surface species and decyclization. A proposed route showing the coke formation and further growth of the coke layer, through these radical elementary reactions is shown in Figure 5.3-10 [25].

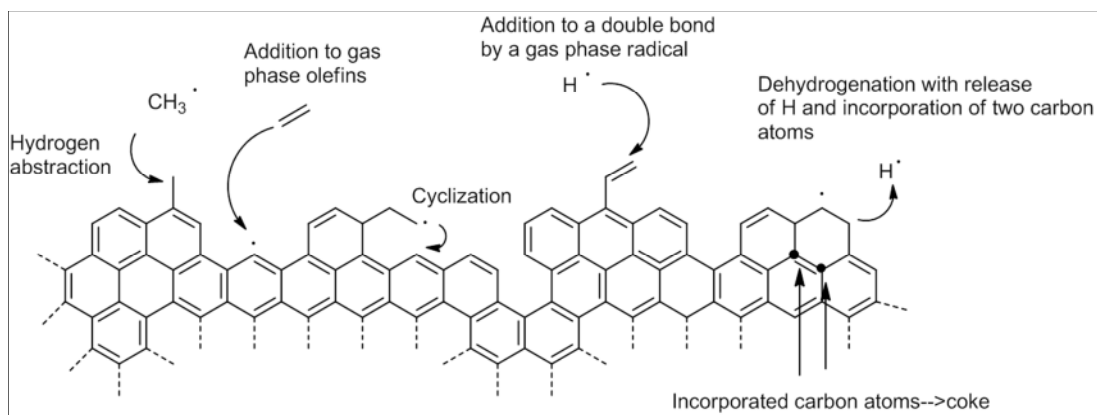


Figure 5.3-10. Elementary reactions taking place allowing growth of coke layer

The reacted catalysts were subjected to thermogravimetric analysis, also SEM-EDX and TEM analyses were undertaken. The thermogravimetric curves were obtained and their respective differential DTG-TPO thermograms are shown in Figure 5.3-11. The resulting SEM and TEM images of reacted catalysts are shown in Figure 5.3-12. Further SEM-EDX analysis was also carried out for selected fresh and reacted B-HPG700 catalyst; the results are shown in Figure 5.3-13.

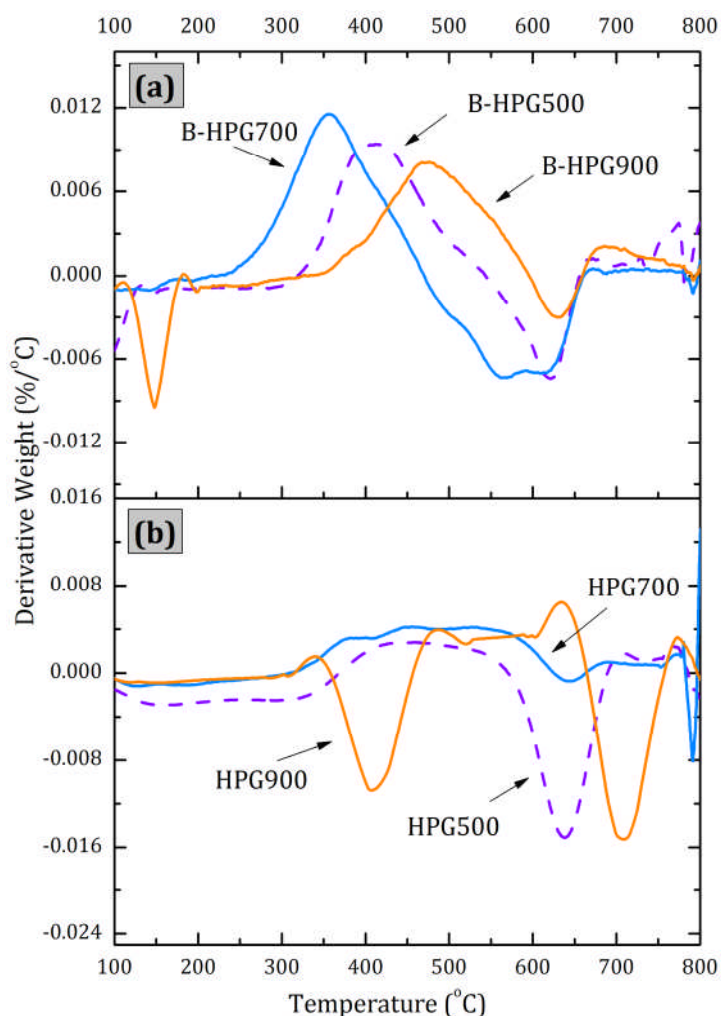


Figure 5.3-11. DTG-TPO thermograms from reacted Ni/SiO₂ catalysts: B-HPG (a), and HPG (b).

From Figure 5.3-11(a) the initial weight decrease at around 100 °C for the thermogram of the B-HPG900 reacted catalyst, was related to water vaporization followed by nickel oxidation peaks at around 400 °C and 500 °C [1, 19]. From Figure 5.3-11(a), it was also noted that the nickel oxidation peak was slightly shifted to lower temperatures for the B-HPG500 and B-HPG700 catalysts. This might be due to the increase in the calcination temperature from 700 °C to 900 °C which promoted a major metal oxidation. The double peak observed between 500-600 °C for the reacted B-HPG700 catalyst (Figure 5.3-11(a)), suggested the presence of two different types of carbon deposited over the catalyst surface. As mentioned in previous sections of this work, it has been reported that the oxidation of amorphous carbon starts at around 500 °C, where the first peak appears, whereas the oxidation of filamentous carbon

starts at around 600 °C, where the second peak was observed [26, 27]. From the SEM image of the B-HPG catalysts (Figure 5.3-12(c)), two different types of carbons might have been deposited over the reacted catalyst surface.

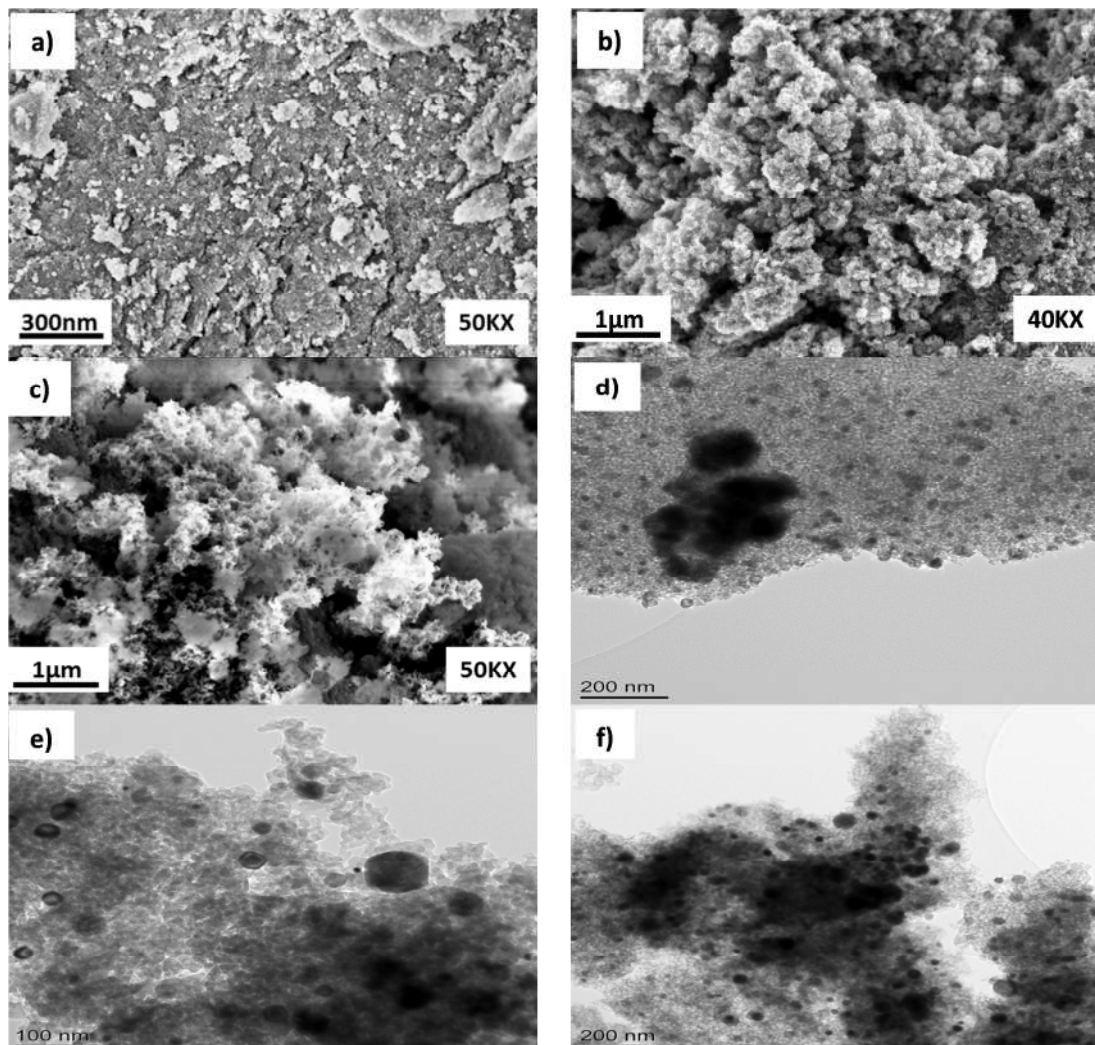


Figure 5.3-12. Morphologies of reacted Ni/SiO₂ catalysts; SEM: (a)HPG700; (b)HPG900; (c)B-HPG900. TEM: (d)HPG700; (e, f)B-HPG700

The amount of carbon deposited was calculated from the weight loss of the reacted catalyst after 400 °C and then this value was divided by the final weight of the catalyst after the TGA-TPO analysis [1]. It was found that for the series of B-HPG catalysts about 0.12, 0.13, and 0.11mg_{Carbon} g⁻¹_{RDF} were deposited over the reacted catalysts, prepared at calcination temperatures of 500 °C, 700 °C and 900 °C respectively. The similar amount of carbon deposited over the catalysts surface, suggests a low influence of the carbon over the catalysts activity, for this type of B-HPG catalysts.

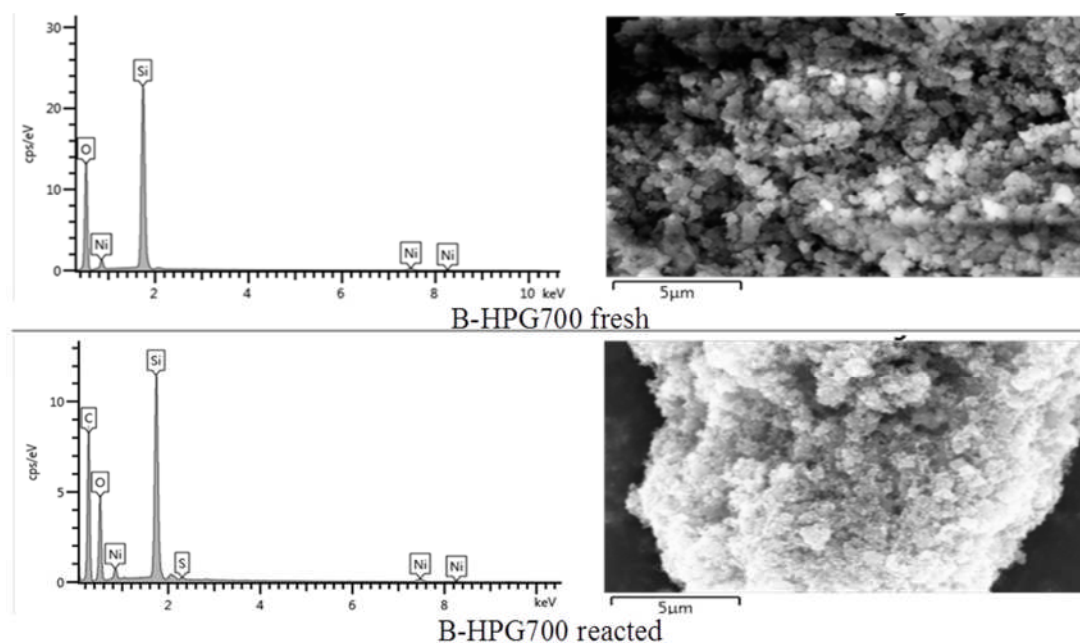


Figure 5.3-13. SEM-EDX from fresh and reacted B-HPG700 Ni/SiO₂ catalyst

From Figure 5.3-12(e, f), and Figure 5.3-13, some filamentous carbons were observed over the surface of the reacted B-HPG700 catalyst; the presence of carbon was verified through the SEM-EDX analysis (Figure 5.3-13). Additionally the presence of metal agglomerates was observed through TEM analysis for the reacted HPG700 (Figure 5.3-12(d)) and B-HPG700 (Figure 5.3-12(e, f)) catalysts; with a major presence of such agglomerates for the latter catalyst.

For the series of HPG reacted catalysts, different trends were observed from the differential thermogravimetric curves (Figure 5.3-11(b)). The oxidation peaks were observed at different temperatures, for example for the HPG900 catalyst the peak observed at around 700 °C might be more related with the presence of filamentous carbons, as the oxidation of this type of carbons starts around 600 °C [26, 27]. From the SEM images (Figure 5.3-12(b)), the presence of some filamentous carbons was observed over the surface of reacted HPG900 catalyst. HPG500 and HPG700 DTG-TPO thermograms (Figure 5.3-11(b)), showed the presence of oxidation peaks around 650 °C which might suggest the deposition of filamentous carbons over both catalysts. A comparison between the SEM images of reacted HPG700 (Figure 5.3-12(a)) and HPG900 (Figure 5.3-12(b)) catalysts, suggested the presence of different carbon types over the surface of

each reacted catalyst, which is in accordance with the results from the DTG-TPO thermograms.

5.3.4 Summary of HPG and B-HPG catalysts

In this section of the work two different Ni/SiO₂ catalysts were prepared by means of two different methods namely homogeneous precipitation (HPG), and HPG plus a separation phase step (B-HPG). The effects of varying the calcination temperature from 500, 700 and 900 °C were also studied in relation to the catalysts properties. The catalytic activity of the resulting catalysts was tested during the pyrolysis-gasification of refuse derived fuel (RDF). It was found that through the HPG preparation method, homogeneous nickel dispersion can be achieved for the resulting Ni/SiO₂ catalyst. The addition of the separation phase during the catalysts preparation resulted in the formation of larger pores and an increase in the surface area for the final Ni/SiO₂ catalyst. The addition of the separation phase involved longer preparation time, with no improvement in the catalytic activity towards hydrogen production.

The calcination temperature influenced both the catalysts properties and catalyst performance for both series of Ni/SiO₂ catalysts (HPG and B-HPG). For example the increase in the calcination temperature from 700 °C to 900 °C resulted in a reduction in both the surface area and hydrogen production. From the series of catalysts tested within this section, the catalytic activity in relation to hydrogen production followed the order: HPG700 > HPG500 > B-HPG700 > HPG900 > B-HPG500 > B-HPG900.

References

1. Wu, C.F. and P.T. Williams, *A Novel Nano-Ni/SiO₂ Catalyst for Hydrogen Production from Steam Reforming of Ethanol*. Environmental Science & Technology, 2010. 44(15): p. 5993-5998.
2. Goncalves, G., Lenzi, M. K., Santos, O. A. A., Jorge, L. M. M., *Preparation and characterization of nickel based catalysts on silica, alumina and titania obtained by sol-gel method*. Journal of Non-Crystalline Solids, 2006. 352: p. 3697-3704.
3. Ermakova, M.A. and D.Y. Ermakov, *High-loaded nickel-silica catalysts for hydrogenation, prepared by sol-gel Route: structure and catalytic behavior*. Applied Catalysis A: General, 2003. 245(2): p. 277-288.
4. Gil, A., A. Díaz, L.M. Gandía, and M. Montes, *Influence of the preparation method and the nature of the support on the stability of nickel catalysts*. Applied Catalysis A: General, 1994. 109(2): p. 167-179.
5. Udengaard, N.R., *Hydrogen production by steam reforming of hydrocarbons*. Preprints of Papers - American Chemical Society, Division of Fuel Chemistry, 2004. 49(2): p. 2.
6. Tomiyama, S., R. Takahashi, S. Sato, T. Sodesawa, and S. Yoshida, *Preparation of Ni/SiO₂ catalyst with high thermal stability for CO₂-reforming of CH₄*. Applied Catalysis A: General, 2003. 241(1-2): p. 349-361.
7. Nakanishi, K., R. Takahashi, T. Nagakane, K. Kitayama, N. Koheiya, H. Shikata, and N. Soga, *Formation of Hierarchical Pore Structure in Silica Gel*. Journal of Sol-Gel Science and Technology, 2000. 17(3): p. 191-210.
8. Takahashi, R., S. Sato, T. Sodesawa, N. Nakamura, S. Tomiyama, T. Kosugi, and S. Yoshidab, *Nanosized Ni/SiO₂ Catalyst Prepared by Homogeneous Precipitation in Wet Silica Gel*. Journal of Nanoscience and Nanotechnology, 2001. 1(2): p. 169-176.
9. Takahashi, R., S. Sato, S. Tomiyama, T. Ohashi, and N. Nakamura, *Pore structure control in Ni/SiO₂ catalysts with both macropores and mesopores*. Microporous and Mesoporous Materials, 2007. 98(1-3): p. 107-114.
10. Yang, H., Q. Liu, Z. Liu, H. Gao, and Z. Xie, *Controllable synthesis of aluminosilica monoliths with hierarchical pore structure and their catalytic performance*. Microporous and Mesoporous Materials, 2010. 127(3): p. 213-218.
11. Ermakova, M.A. and D.Y. Ermakov, *Ni/SiO₂ and Fe/SiO₂ catalysts for production of hydrogen and filamentous carbon via methane decomposition*. Catalysis Today, 2002. 77(3): p. 225-235.
12. Sing, K.S.W., D.H. Everett, R.A.W. Haul, L. Moscou, R.A. Pierotti, J. Rouquerol, and T. Siemieniewska, *Reporting Physisorption Data for Gas Solid Systems with Special Reference to the Determination of Surface-Area and Porosity (Recommendations 1984)*. Pure and Applied Chemistry, 1985. 57(4): p. 603-619.
13. Neimark, A.V., P.I. Ravikovitch, and A. Vishnyakov, *Adsorption hysteresis in nanopores*. Physical Review E, 2000. 62(2): p. R1493-R1496.

14. Ravikovitch, P.I. and A.V. Neimark, *Characterization of Micro- and Mesoporosity in SBA-15 Materials from Adsorption Data by the NLDFIT Method*. The Journal of Physical Chemistry B, 2001. 105(29): p. 6817-6823.
15. Olivier, J.P., *Improving the models used for calculating the size distribution of micropore volume of activated carbons from adsorption data*. Carbon, 1998. 36(10): p. 1469-1472.
16. Parr, R.G. and W. Yang, *Density-functional theory of atoms and molecules*. International Series of Monographs on Chemistry - 16, ed. O.S. Publications. 1989, Oxford: Oxford University Press.
17. Langford, J.I. and A.J.C. Wilson, *Scherrer after sixty years: A survey and some new results in the determination of crystallite size*. Journal of Applied Crystallography, 1978. 11(2): p. 102-113.
18. Cho, Y.S., J.C. Park, B. Lee, Y. Kim, and J.H. Yi, *Preparation of mesoporous catalyst supported on silica with finely dispersed Ni particles*. Catalysis Letters, 2002. 81(1-2): p. 89-96.
19. Wu, C.F., L.Z. Wang, P.T. Williams, J. Shi, and J. Huang, *Hydrogen production from biomass gasification with Ni/MCM-41 catalysts: Influence of Ni content*. Applied Catalysis B-Environmental, 2011. 108(1-2): p. 6-13.
20. Sookman, C., P. Kongkachuichay, and W. Tanakulrungsank, *The Effect of Calcined Temperature on the Property of Nickel Oxide Catalyst Synthesized by Sol-Gel Method*, in *Eco-Energy and Materials Science and Engineering International Conference*. 2005, EMSES: Chaing Mai, Thailand.
21. Kermarec, M., J.Y. Carriat, P. Burattin, M. Che, and A. Decarreau, *FTIR Identification of the Supported Phases Produced in the Preparation of Silica-Supported Nickel Catalysts*. The Journal of Physical Chemistry, 1994. 98(46): p. 12008-12017.
22. Takahashi, R., S. Sato, T. Sodesawa, M. Suzuki, and N. Ichikuni, *Ni/SiO₂ prepared by sol-gel process using citric acid*. Microporous and Mesoporous Materials, 2003. 66(2-3): p. 197-208.
23. Li, J., J. Liu, S. Liao, X. Zhou, and R. Yan, *Syn-Gas Production from Catalytic Steam Gasification of Municipal Solid Wastes in a Combined Fixed Bed Reactor*, in *International Conference on Intelligent System Design and Engineering Application (ISDEA)*. 2010: Changsha. p. 530-534.
24. Kim, P., Y. Kim, T. Kang, I. Song, and J. Yi, *Preparation of nickel-mesoporous materials and their application to the hydrodechlorination of chlorinated organic compounds*. Catalysis Surveys from Asia, 2007. 11(1): p. 49-58.
25. Wauters, S. and G.B. Marin, *Computer generation of a network of elementary steps for coke formation during the thermal cracking of hydrocarbons*. Chemical Engineering Journal, 2001. 82(1-3): p. 267-279.
26. Wu, C. and P.T. Williams, *Hydrogen production by steam gasification of polypropylene with various nickel catalysts*. Applied Catalysis B: Environmental, 2009. 87(3-4): p. 152-161.
27. Wu, C. and P.T. Williams, *Investigation of coke formation on Ni-Mg-Al catalyst for hydrogen production from the catalytic steam pyrolysis-gasification of polypropylene*. Applied Catalysis B: Environmental, 2010. 96(1-2): p. 198-207.

CHAPTER 6. COMPARISON BETWEEN NICKEL AND IRON BASED CATALYSTS

6.1 Fe/SiO₂ and Ni/SiO₂ catalysts

In previous Chapters of this work, nickel based catalysts have been synthesized, characterized and tested for their catalytic activity mainly for hydrogen production during the pyrolysis-gasification of refuse derived fuel (RDF). Iron-based catalysts have also been widely assessed during catalytic steam reforming processes as they are non-toxic and resistant to high temperatures [1, 2]. Ermakova et al [2], also reported that high carbon yields are attained when using iron catalysts, furthermore the carbon was found to contain thin wall nano-tubes which are of particular interest among carbon nano-fibres. Some authors have reported the incorporation of active iron species over different supports including silica [3], zeolites [4], and mesostructured materials (MCM-41, HMS-9 and SBA-15). For example Sivasangar et al [5], reported better performance towards hydrogen production during the methane reforming process of Ni/Al₂O₃ catalyst when Fe₂O₃ was used as dopant. According to the literature the use of iron-based catalysts promote an increase in the surface area, which allows the metal to interact with the support and also reduces the tendency to sintering [6].

In this Chapter 6, a series of five iron-silica catalysts were prepared using a nano-porous silica material and varying the metal loading, the resulting catalysts were characterised using diverse analytical techniques. The performance in relation to hydrogen production for the iron-silica catalysts was tested during the pyrolysis-gasification of RDF. The results are compared with a series of five nickel based catalysts synthesized under similar conditions. The characteristics and catalytic activity for hydrogen production for the series of nickel-silica catalysts were also assessed.

6.2 Characterization of fresh Fe/SiO₂ and Ni/SiO₂ catalysts

Fe/SiO₂ and Ni/SiO₂ catalysts were prepared by conventional impregnation method. Nano-porous silica was used as the oxide support and nickel and iron as metal precursors, according to the methodology described in Chapter 3, Section 3.2.2.5. The metal loadings were varied as 2.5wt.%, 5 wt.%, 7 wt.%, 10 wt.%, and 20 wt.%, for both series of catalysts. The resulting catalysts were assigned as follows: 2.5Ni/SiO₂, 5Ni/SiO₂, 7.5 Ni/SiO₂, 10 Ni/SiO₂, 15 Ni/SiO₂, 2.5Fe/SiO₂, 5Fe/SiO₂, 7.5Fe/SiO₂, 10Fe/SiO₂, 15Fe/SiO₂; where Ni and Fe correspond to the precursor used and the number to the oxide precursor loading. The surface area and porous properties of the prepared Fe/SiO₂ and Ni/SiO₂ catalysts, was obtained using the Brunauer, Emmet & Teller (BET) method, micropore and mesopore volumes were calculated using the Dubinin-Radushkevich (DR), and total pore volume and pore diameter were calculated by the Barret, Joyner & Halenda (BJH) method. The results are shown in Table 6.2-1.

Table 6.2-1. Surface area and porous properties of Ni/SiO₂ and Fe/SiO₂ catalysts

Catalyst	Metal content (wt%)	BET Surface area (m ² g ⁻¹)	Micropore volume (cm ³ g ⁻¹)	Mesopore volume (cm ³ g ⁻¹)	Total pore volume (cm ³ g ⁻¹)	Pore diameter (nm)
2.5Ni/SiO ₂	2.5	282.7	0.140	0.267	0.620	1.670
5.0Ni/SiO ₂	5.0	280.0	0.140	0.252	0.593	1.693
7.5Ni/SiO ₂	7.5	250.6	0.140	0.341	1.448	1.674
10Ni/SiO ₂	10.0	295.5	0.150	0.317	1.154	1.671
15Ni/SiO ₂	15.0	270.0	0.150	0.295	1.159	1.672
2.5Fe/SiO ₂	2.5	208.5	0.120	0.195	0.705	1.687
5.0Fe/SiO ₂	5.0	313.7	0.160	0.321	0.998	1.691
7.5Fe/SiO ₂	7.5	310.8	0.160	0.322	1.344	1.689
10Fe/SiO ₂	10.0	262.1	0.150	0.337	2.011	1.928
15Fe/SiO ₂	15.0	236.6	0.140	0.359	1.882	1.913

The N₂ adsorption-desorption curves from the Fe/SiO₂ and Ni/SiO₂ catalysts were also obtained, and the results are shown in Figure 6.2-1.

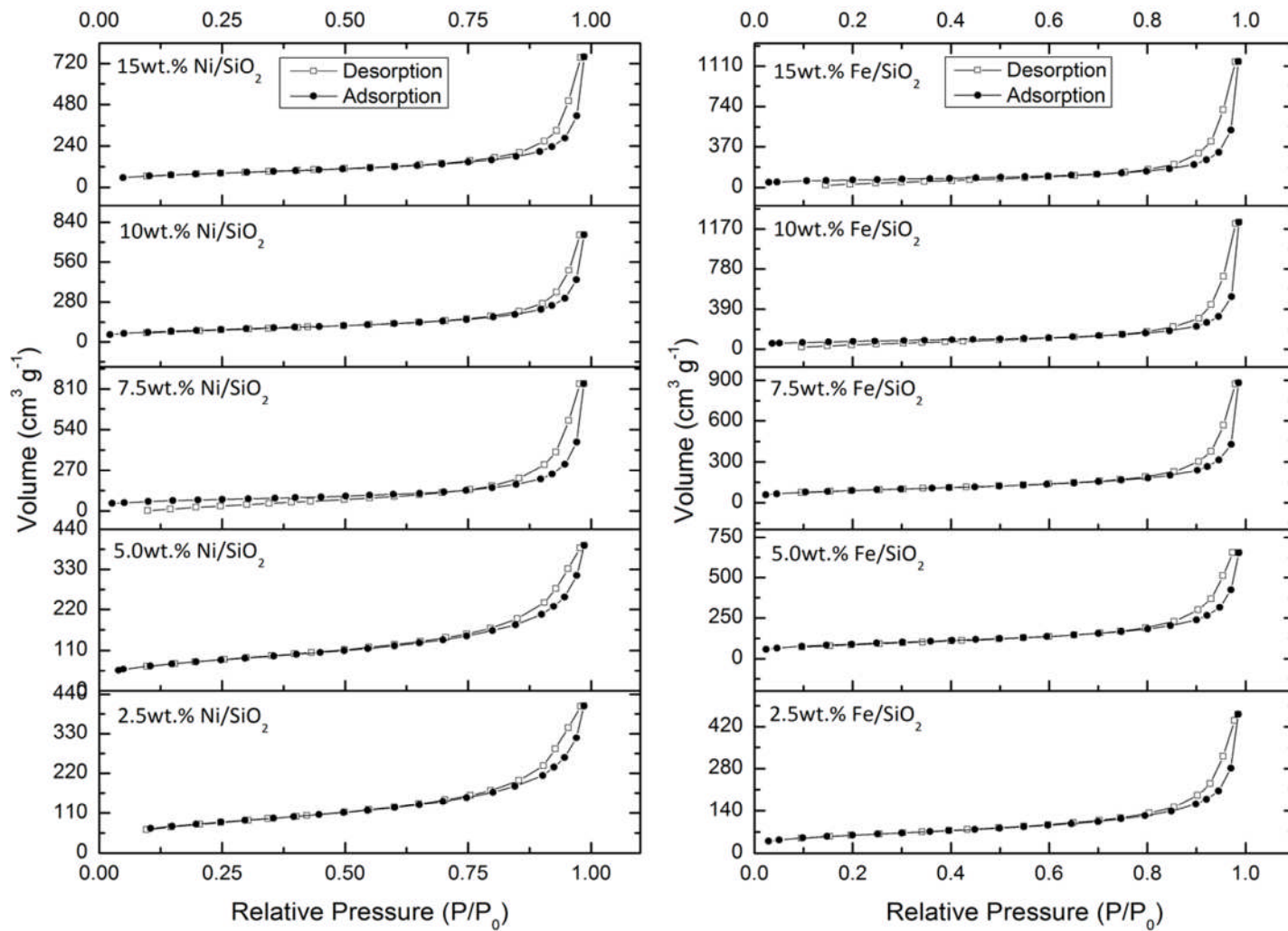


Figure 6.2-1. N₂ adsorption-desorption isotherms of fresh Fe/SiO₂ and Ni/SiO₂ catalysts

From Table 6.2-1, it was observed that for the series of Ni/SiO₂ catalysts the surface area was reduced as the nickel loading was increased from 2.5wt.% up to 10wt.%. However, when the nickel loading was further increased up to 15wt.% the surface area was reduced. Higher values of the surface area were observed for the series of Fe/SiO₂ catalysts, when compared with those reported for the Ni/SiO₂ catalysts. As a comparison, a surface area of about 290 m² g⁻¹ has been reported in the literature for mesoporous silica material obtained via a sol-gel catalyst preparation method [7], which might indicate no major influence in the surface area of the catalysts by using the nano-silica material as support. Also a reduction in the surface area when the metal loading was higher than 7.5wt.% was noted for this series of iron-based catalysts. Similar trends in relation to a reduction in the surface area at higher metal loadings have been observed for Ni/SiO₂ catalysts prepared by both sol-gel and impregnation methods, in Chapter 5, Section 5.1. All the resulting adsorption-desorption isotherms shown in Figure 6.2-1 indicate the same type III, which might indicate a high influence of the silica material used and weak interactions between the adsorbent and adsorbate, also the pronounced condensation steps might be related with the small pores of the silica support of less than 2nm (Table 6.2-1).

The pore size distribution of Ni/SiO₂ and Fe/SiO₂ catalysts was obtained according to the Density Functional Theory (DFT) described in Chapter 3, Section 3.4.2.4. The results for both series of catalysts with metal loadings of 2.5wt.%, 5.0wt.%, and 7.5wt.%, are shown in Figure 6.2-2.

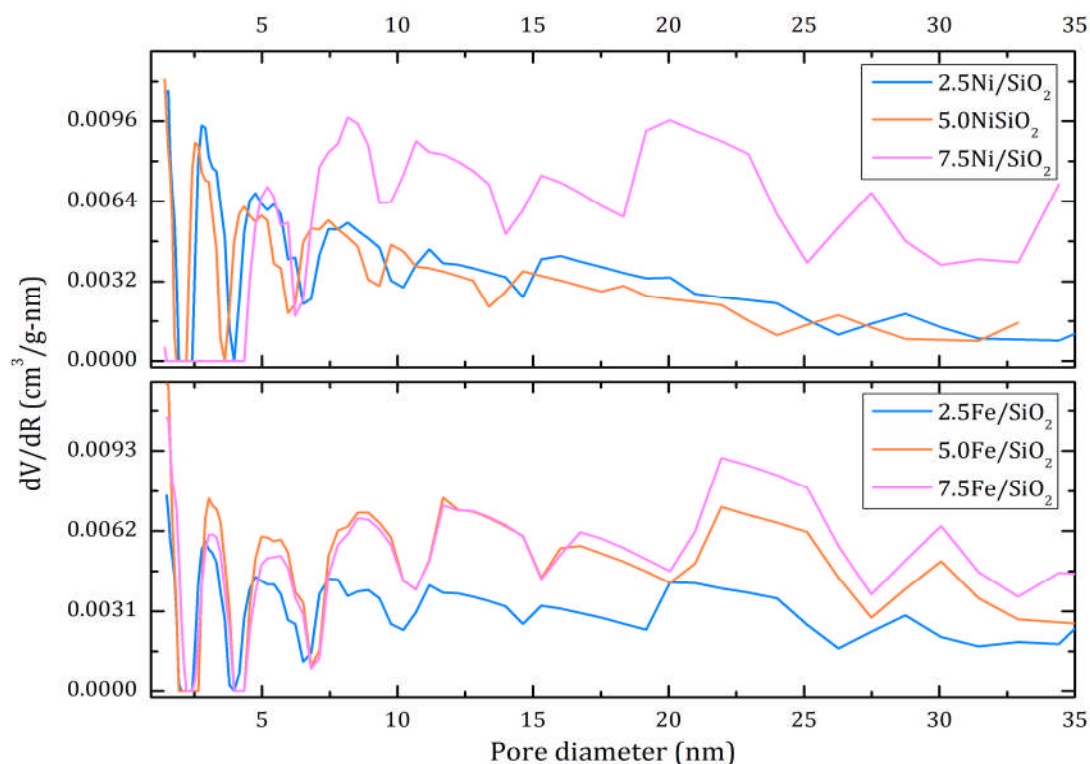


Figure 6.2-2. Pore size distribution of selected Ni/SiO₂ and Fe/SiO₂ catalysts

From Figure 6.2-2, it was noted that for pore diameters lower than 5nm the intensity of the signals was higher, which might be attributed to the use of the nano-porous silica, afterwards a wider distribution was observed for both series of catalysts. For the Ni/SiO₂ catalysts, a clear influence of increasing the nickel loading over the pore size distribution was observed, as major intensities were observed around 20nm for the 7.5wt.%Ni/SiO₂ catalysts, whereas 2.5wt.% and 5wt.%Ni/SiO₂ catalysts showed more similar pore size distributions. On the other hand Fe/SiO₂ catalysts presented more similar pore distributions, which might indicate stronger interactions between the metal and the silica support. In addition the pore distribution for the metal loading of 7.5wt.% for both Fe and Ni catalysts, was quite similar, which might suggest higher metal loadings promote a larger pore distribution and stronger interactions between the metal and the support for both series of catalysts. However additional analysis for higher metal loadings will be needed in order to verify these trends.

Similar trends in the pore size distribution for Ni/SiO₂ catalysts have been reported in the literature for catalysts prepared by conventional impregnation

method [8], resulting in problems related with the nickel dispersion related with the aggregation of Ni in the large mesopores.

In order to identify the different crystallite phases formed for both series of catalysts, XRD analyses were carried out, according to the description given in Chapter 3, Section 3.4.2.5. The resulting XRD spectra showing the different diffraction patterns for iron and nickel-based catalysts are shown in Figure 6.2-3.

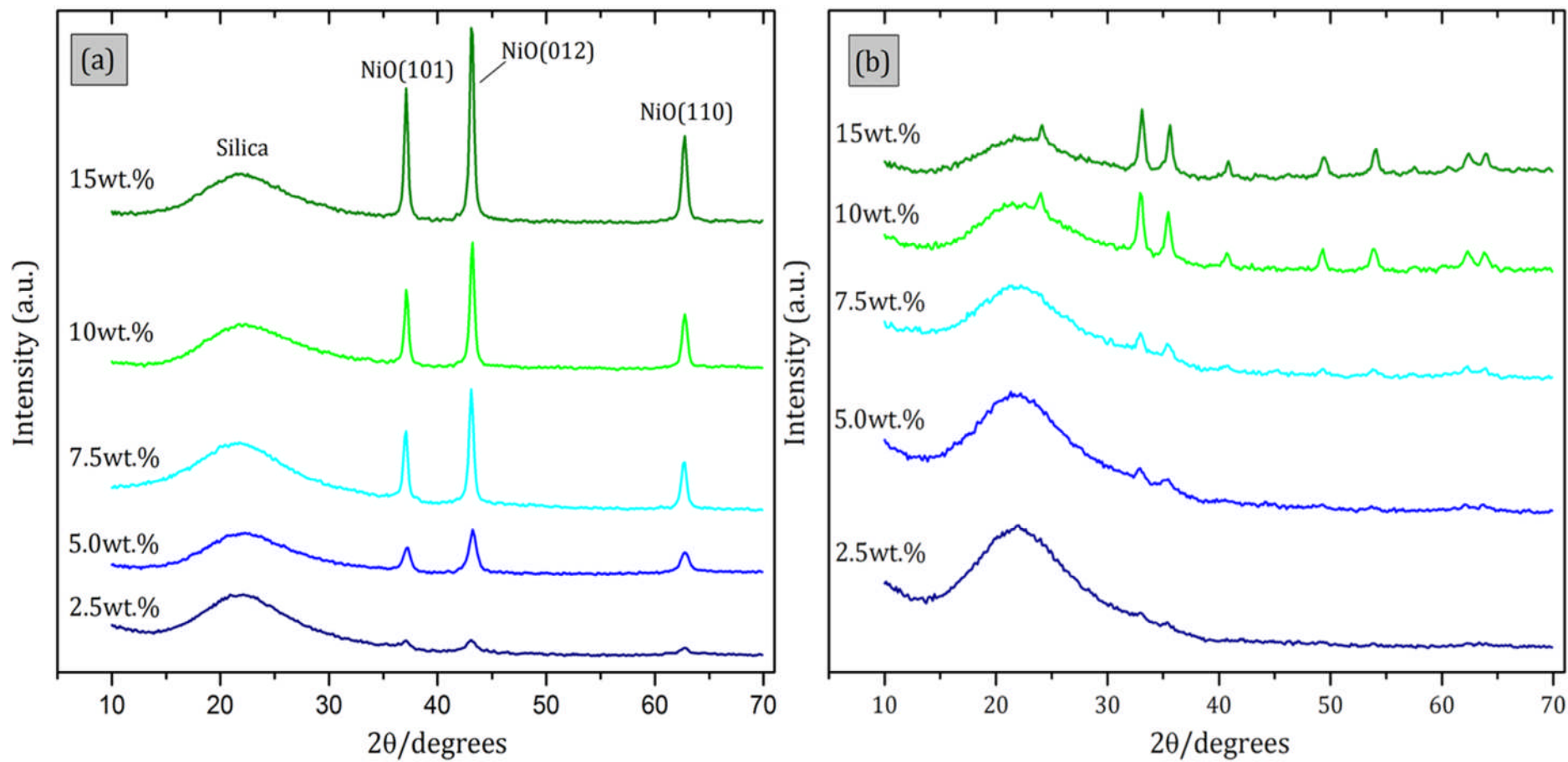


Figure 6.2-3. XRD patterns of (a) Ni/SiO₂ catalysts, and (b) Fe/SiO₂ catalysts

Figure 6.2-3(a) shows the XRD spectra for Ni/SiO₂ catalysts. The broad initial peak around 21° has been attributed to the presence of silica. The three sharp peaks at 37.5°, 43°, and 63° have been previously identified in XRD analysis from Ni/SiO₂ catalysts prepared by homogeneous precipitation method [9], and have been attributed to nickel oxide crystals of the types NiO(101), NiO(012), and NiO(110), respectively. Tomiyama et al [9], reported that the three characteristic nickel oxide crystal peaks become more intense and sharper as the calcination temperature was increased. However for this series of Ni/SiO₂ catalysts, it seems that this effect is related with the increase in the nickel loading rather than with the calcination temperature. Also this effect in the nickel oxide peaks might be influenced by the crystallite size, as for the 2.5Ni/SiO₂ catalyst a crystallite size of 9nm was calculated, and this value was noted to gradually increase up to 27nm for the 15Ni/SiO₂ catalyst.

For the series of Fe/SiO₂ catalysts, the XRD patterns shown in Figure 6.2-3(b), also show an influence as the metal loading was increased. From Figure 6.2-3(b), the broad and main peak at around 21° has been also attributed to the silica. As the iron loading was increased, the Fe/SiO₂ catalysts exhibited diffraction peaks around 33°, 36°, 42°, 62.5°, and 64°, which are characteristic of crystalline haematite particles (α -Fe₂O₃) [7, 10]. For the catalysts prepared using very low iron loadings (2.5wt%, and 5.0wt.%), the absence of these characteristic peaks might be associated with the small particle size of crystalline iron oxide, also related to the low iron loading used during the catalysts preparation [7]. Some morphological changes might occur to the fresh Fe/SiO₂ catalysts once they are exposed to activation and reduction. For example the haematite (α -Fe₂O₃) can be converted to magnetite (Fe₃O₄) and then to iron carbide (Fe_xC) after activation [11]. The interactions between the iron oxide and carbide result in a break-up of the iron oxide into iron carbide nanoparticles. These sequential steps proposed by Shroff et al [12], are shown in Figure 6.2-4.

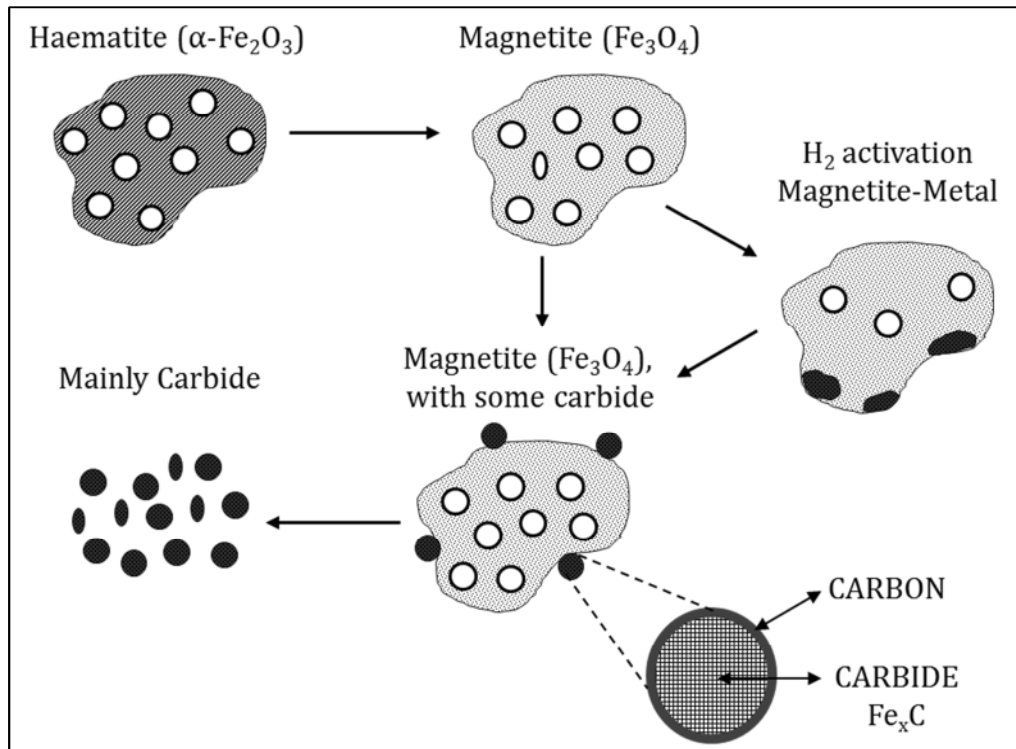


Figure 6.2-4. Fe/SiO₂ morphological changes occurring to crystalline haematite particles ($\alpha\text{-Fe}_2\text{O}_3$) during activation and reaction conditions

Finally electron microscopic images were obtained for both series of catalysts, in order to identify and compare the characteristic nickel oxide and iron oxide crystalline structures for Ni/SiO₂ and Fe/SiO₂ catalysts respectively. Such comparison is shown in Figure 6.2-5.

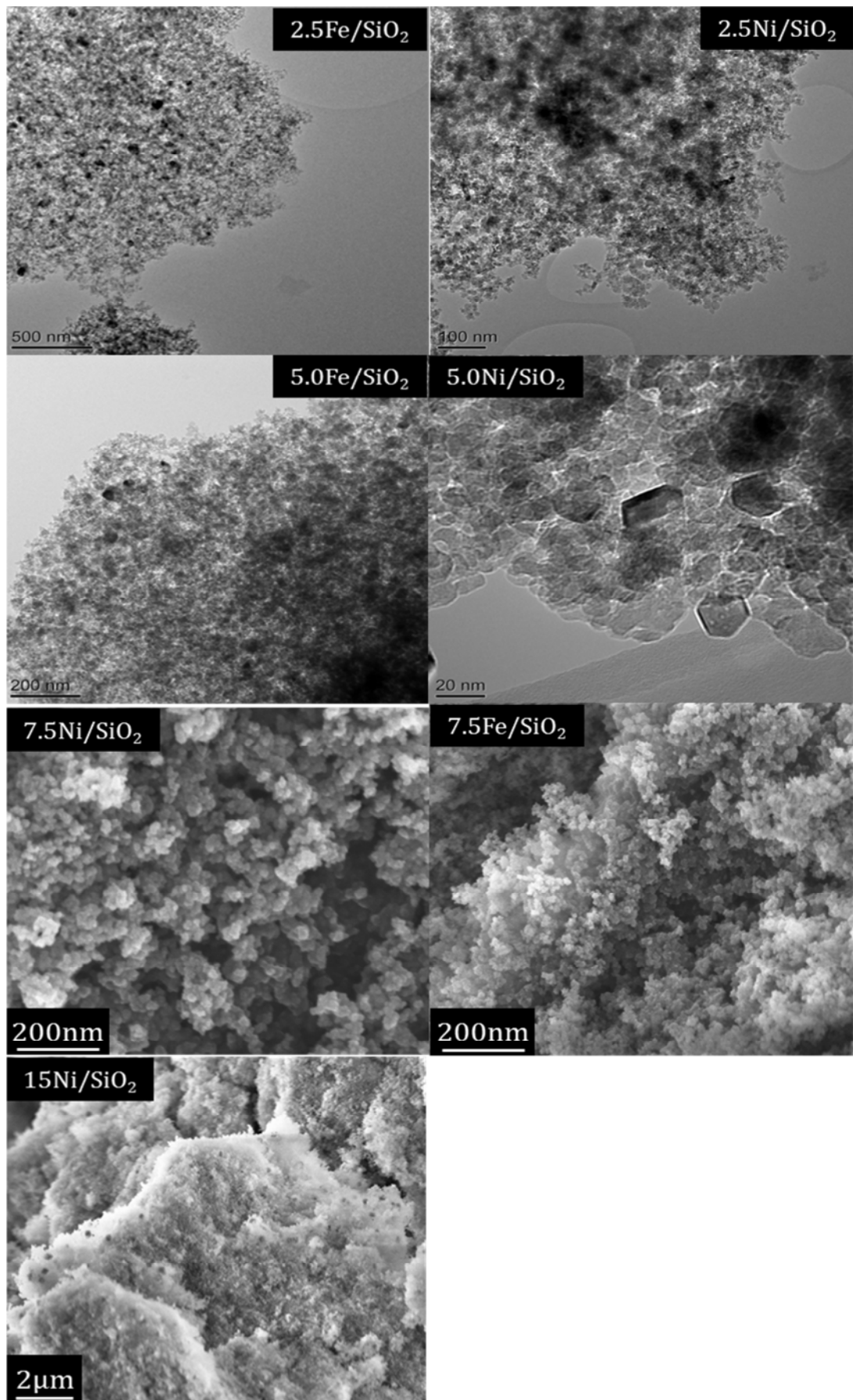


Figure 6.2-5. TEM and SEM images of fresh Ni/SiO₂ and Fe/SiO₂ catalysts

From the TEM images of both 2.5Fe/SiO₂ and 5Fe/SiO₂ catalysts, a good dispersion of the metal particles is indicated, that might correspond to single crystals of the hematite type (Figure 6.2-3). TEM images from the 2.5Ni/SiO₂ catalyst show the distribution of nickel particles over the silica lattices. It was also observed the similarity of the silica lattice for both types of catalysts for example for the 2.5Fe/SiO₂ and 2.5Ni/SiO₂ catalysts. The TEM image of the 5.0Ni/SiO₂ catalyst, showed specific shapes for the nickel metal, it has been reported in the literature that the particle size of the metal is strongly dependent on the synthesis method and on the type of silica support [7].

From the SEM images a similar morphology for both 7.5Ni/SiO₂ and 7.5Fe/SiO₂ catalysts can be observed. The SEM image obtained from the analysis of the 15Ni/SiO₂ catalyst shows some black points on the top of the silica lattice, these spheres might correspond to minute nickel particles that might have been identified due to the high nickel loading for this specific catalyst.

6.3 Hydrogen production using Fe/SiO₂ and Ni/SiO₂ in the pyrolysis-gasification process

The prepared catalysts were tested for their activity towards hydrogen production during the pyrolysis-gasification of RDF. The experimental details used are as described in the Chapter 3, Section 3.3. The gas composition was calculated on a nitrogen free basis, the hydrogen yield was expressed as mol_{H₂}/kg_{RDF}, and also gas and solid yields, as well as the mass balance were calculated. The obtained results are shown in Table 6.3-1.

Table 6.3-1. Gas composition, gas and solid yields and mass balance from the experiments carried out using Ni/SiO₂ and Fe/SiO₂ catalysts

Catalyst	2.5Ni/SiO ₂	5.0Ni/SiO ₂	7.5Ni/SiO ₂	10Ni/SiO ₂	15Ni/SiO ₂	2.5Fe/SiO ₂	7.5Fe/SiO ₂	10Fe/SiO ₂	15Fe/SiO ₂
<i>Gas composition (vol.%)</i>									
CO	22.74	22.69	24.51	27.10	26.84	28.96	23.57	25.63	25.27
H ₂	29.35	34.18	43.71	41.24	43.93	37.47	31.90	32.49	31.15
CO ₂	35.57	30.34	15.35	16.03	21.67	20.55	23.39	18.35	18.62
CH ₄	6.47	8.97	10.82	10.15	2.46	5.12	11.48	15.00	15.81
C _n H _m	5.87	3.81	5.61	5.47	5.10	7.90	9.65	8.52	9.16
H ₂ yield (mol _{H2} /kg _{RDF})	8.49	10.04	15.06	11.16	12.41	7.86	7.11	6.54	6.57
Gas yield (wt.%)	73.30	55.00	61.57	50.65	47.93	44.00	50.52	41.80	44.50
Solid yield (wt.%)	28.90	28.90	32.51	29.35	29.21	29.60	29.20	29.10	29.70
Mass Balance (wt.%)	98.20	90.10	103.59	94.78	94.11	92.00	95.80	99.50	99.30

Table 6.3-1, shows that higher hydrogen yields were attained when using Ni/SiO₂ catalysts, whereas lower yields were achieved using the series of Fe/SiO₂ catalysts. For all the experiments carried out, the gas composition calculated in a nitrogen free basis, showed a higher concentration of hydrogen when compared with other gases such as CO and CO₂. This is explained in general by the promotion of water gas and steam reforming reactions, due to the presence of catalysts and high process temperatures. For the series of Ni/SiO₂ catalysts, the highest catalytic activity of 15 mol_{H₂}/kg_{RDF}, was attained using the 7.5Ni/SiO₂ catalyst. This might suggest that using higher nickel loadings has an adverse effect over the catalysts properties, and also a negative effect towards the catalytic activity. When comparing the catalysts properties analysed in the previous Section 6.2, it was observed that the lowest surface area of about 250 m²g⁻¹ was reported for the 7.5Ni/SiO₂ catalyst, also the further increase in the nickel loading from 10wt.% up to 15wt.% resulted in a reduction from 295 to 270 m² g⁻¹, respectively. The reduction in the surface area for the 7.5Ni/SiO₂ catalyst can be related to the broad pore size distribution (Figure 6.2-2) and greater total pore volume (Table 6.2-1). Therefore despite the lower surface area, the high total pore volume might have promoted a better dispersion of the nickel for this catalyst, thus improving its catalytic activity. In addition it was expected that the higher hydrogen concentration also resulted in lower methane (CH₄) and light hydrocarbons (C_nH_m) concentrations. However from the results shown in Table 6.3-1, it was observed that the lowest methane concentration was attained using the 15Ni/SiO₂ catalyst, whereas the lowest C_nH_m concentration was achieved when using the 5Ni/SiO₂ catalyst. The low C_nH_m and H₂ concentrations attained using the 5Ni/SiO₂ catalyst, might indicate a promotion of reforming of low hydrocarbons but no further promotion of methane or carbon monoxide reforming (water gas-shift reaction), which resulted in no more formation of hydrogen, but consumed C_nH_m reactant.

For the series of Fe/SiO₂ catalysts higher activity towards hydrogen production would be expected, as for example higher surface areas were obtained during the catalysts characterisation (Table 6.2-1). However H₂ yields lower than 8mol_{H₂}/kg_{RDF}, were attained, which indicates lower activity for hydrogen

production than that attained using the Ni/SiO₂ catalysts. The highest catalytic activity toward hydrogen yield, for the series of Fe/SiO₂ catalysts, was attained using 7.5wt.% Fe loading, which was the same metal loading that reported the best performance for hydrogen yield in the Ni/SiO₂ catalysts series. Unfortunately experiments using the 5Fe/SiO₂ catalyst were not carried out, therefore this metal loading could not be analysed for this series of catalysts. However it was also observed that an increase in the iron loading higher than 7.5wt.%, also resulted in a reduction in the hydrogen yield, and in an increase in the methane concentration, which might indicate no further promotion of steam reforming reactions when metal loadings higher than 7.5wt.% are used for the preparation of this specific catalyst.

From Table 6.3-1, it was also noted that higher gas yields were attained when using the Ni/SiO₂ catalysts. In general a conversion of about 70wt.% of the initial RDF was attained for all the experiments as the solid fraction remained was maintained somewhat constant about 30wt.% for all the experiments reported in Table 6.3-1.

In general it was expected that a higher catalytic activity would be found when using iron instead of nickel as metal combined with silica, as stronger interactions between iron oxides and silica have been reported in the literature, and also iron possesses high specific saturation magnetization and low coercivity that improves when mixed with silica [2, 13]. From the results shown in Table 6.3-1, higher hydrogen yields were attained when using Ni/SiO₂ catalysts. One of the possible reasons associated with the lower efficiency of Fe-based catalysts, is that this type of catalysts require much higher activation temperatures than those required for Ni-based catalysts [14]. Therefore further work testing the influence of an increase in the gasification stage might be suggested for comparison.

6.4 Analysis of reacted Fe/SiO₂ and Ni/SiO₂ catalysts

SEM analysis was carried out on the 7.5Ni/SiO₂ catalyst, the resulting microscopic images are shown in Figure 6.4-1.

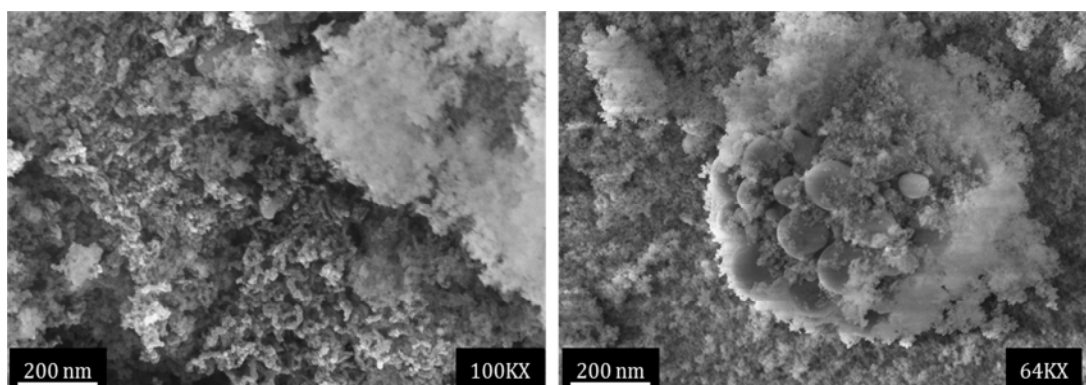


Figure 6.4-1. SEM images of reacted 7.5Ni/SiO₂ catalyst

The SEM images shown in Figure 6.4-1, revealed the possible deposition of filamentous carbons over the surface of the reacted catalyst. The carbon deposition in catalysts can be attributed to chemical reactions taking place in the catalysts surface and in its pores; these reactions include some of the following [15];



Also the circular spheres as agglomerates, observed in Figure 6.4-1, might correspond to nickel particles partly covered by filamentous carbon type. However, further characterisation of the reacted catalysts such as transmission electron microscopy (TEM), thermogravimetric analysis (TPO), and XRD is required to get a better understanding of the carbon deposition mechanism over reacted Ni/SiO₂ and Fe/SiO₂ catalysts.

In addition, lifetime tests for the best-performing catalyst, can give better information about the catalyst resistance. For example Wang et al [16], reported a longer lifetime for Ni-Fe-SiO₂ catalysts when compared with simple Ni-SiO₂ catalysts under similar process conditions during the methane decomposition process.

6.5 Summary

In this section it was expected that both the characteristics and the catalytic activity of the Fe/SiO₂ catalysts were better than those from the Ni/SiO₂ catalysts, as stronger interaction between the iron oxides and silica have been reported in the literature [2], and also due to the reported antioxidant capacity of iron nanoparticles [13]. However a higher activity in terms of hydrogen and gas yields, was demonstrated when using Ni/SiO₂ catalysts, even when using low metal loadings such as 2.5wt.% for hydrogen production during the pyrolysis-gasification of RDF.

However further characterisation of reacted catalysts, further tests at higher gasification temperatures, and lifetime tests are required in order to achieve a complete understanding of the performance of these catalysts.

References

1. Ermakova, M.A., D.Y. Ermakov, A.L. Chuvilin, and G.G. Kuvshinov, *Decomposition of methane over iron catalysts at the range of moderate temperatures: The influence of structure of the catalytic systems and the reaction conditions on the yield of carbon and morphology of carbon filaments*. Journal of Catalysis, 2001. 201(2): p. 183-197.
2. Ermakova, M.A. and D.Y. Ermakov, *Ni/SiO₂ and Fe/SiO₂ catalysts for production of hydrogen and filamentous carbon via methane decomposition*. Catalysis Today, 2002. 77(3): p. 225-235.
3. Melero, J.A., G. Calleja, F. Martínez, R. Molina, and K. Lázár, *Crystallization mechanism of Fe-MFI from wetness impregnated Fe₂O₃-SiO₂ amorphous xerogels: Role of iron species in Fenton-like processes*. Microporous and Mesoporous Materials, 2004. 74(1-3): p. 11-21.
4. Ovejero, G., J.L. Sotelo, F. Martínez, J.A. Melero, and L. Gordo, *Wet Peroxide Oxidation of Phenolic Solutions over Different Iron-Containing Zeolitic Materials*. Industrial & Engineering Chemistry Research, 2001. 40(18): p. 3921-3928.
5. Sivasangar, S. and Y.H. Taufiq-Yap, *The Effect of CeO₂ and Fe₂O₃ Dopants on Ni/Alumina Based Catalyst for Dry Reforming of Methane to Hydrogen*. Nanomaterials: Synthesis and Characterization, 2012. 364: p. 519-523.
6. Cagnoli, M.V., S.G. Marchetti, N.G. Gallegos, A.M. Alvarez, R.C. Mercader, and A.A. Yeramian, *Influence of the Support on the Activity and Selectivity of High dispersion Fe Catalysts in the Fischer-Tropsch Reaction*. Journal of Catalysis, 1990. 123(1): p. 21-30.
7. Botas, J.A., J.A. Melero, F. Martinez, and M.I. Pariente, *Assessment of Fe₂O₃/SiO₂ catalysts for the continuous treatment of phenol aqueous solutions in a fixed bed reactor*. Catalysis Today, 2010. 149(3-4): p. 334-340.
8. Takahashi, R., S. Sato, T. Sodesawa, M. Suzuki, and N. Ichikuni, *Ni/SiO₂ prepared by sol-gel process using citric acid*. Microporous and Mesoporous Materials, 2003. 66(2-3): p. 197-208.
9. Tomiyama, S., R. Takahashi, S. Sato, T. Sodesawa, and S. Yoshida, *Preparation of Ni/SiO₂ catalyst with high thermal stability for CO₂-reforming of CH₄*. Applied Catalysis A: General, 2003. 241(1-2): p. 349-361.
10. Ding, F.S., A.F. Zhang, M. Liu, X.W. Guo, and C.S. Song, *Effect of SiO₂-coating of FeK/Al₂O₃ catalysts on their activity and selectivity for CO₂ hydrogenation to hydrocarbons*. Rsc Advances, 2014. 4(17): p. 8930-8938.
11. Davis, B.H., *Fischer-Tropsch Synthesis: Reaction mechanisms for iron catalysts*. Catalysis Today, 2009. 141(1-2): p. 25-33.
12. Shroff, M.D., D.S. Kalakkad, K.E. Coulter, S.D. Kohler, M.S. Harrington, N.B. Jackson, A.G. Sault, and A.K. Datye, *Activation of Precipitated Iron Fischer-Tropsch Synthesis Catalysts*. Journal of Catalysis, 1995. 156(2): p. 185-207.

13. Tang, N.J., W. Chen, W. Zhong, H.Y. Jiang, S.L. Huang, and Y.W. Du, *Highly stable carbon-coated Fe/SiO₂ composites: Synthesis, structure and magnetic properties*. Carbon, 2006. 44(3): p. 423-427.
14. Takenaka, S., M. Serizawa, and K. Otsuka, *Formation of filamentous carbons over supported Fe catalysts through methane decomposition*. Journal of Catalysis, 2004. 222(2): p. 520-531.
15. Novosel, B., M. Marinsek, and J. Macek, *Deactivation of Ni-YSZ Material in Dry Methane and Oxidation of Various Forms of Deposited Carbon*. Journal of Fuel Cell Science and Technology, 2012. 9(6).
16. Wang, W.H., H.Y. Wang, Y. Yang, and S.B. Jiang, *Ni-SiO₂ and Ni-Fe-SiO₂ catalysts for methane decomposition to prepare hydrogen and carbon filaments*. International Journal of Hydrogen Energy, 2012. 37(11): p. 9058-9066.

CHAPTER 7. GASIFICATION AND COMBUSTION OF RDF: PILOT SCALE FLUIDISED BED

7.1 Introduction

This Chapter's aim is to briefly describe a series of experiments carried out in a bubbling fluidised bed gasification system, at the Energy Research Centre of the Netherlands (ECN) premises, located in Petten, the Netherlands. These experiments were undertaken thanks to the Biofuels Research Infrastructure for Sharing Knowledge (BRISK) programme, which is funded by the European Commission Seventh Framework Programme.

Seven different experiments were conducted in a multipurpose thermal converter also referred to as 'WOB'. This atmospheric bubbling fluidised bed gasifier has been widely used to carry out combustion, gasification and pyrolysis experiments using different feedstocks. Moreover it has a greater process capacity than the two-stage reaction system described and used in previous Chapters of this research work.

A selected tar/oil sample was collected using a solid phase adsorption (SPA) method, and was later analysed by gas chromatography coupled to mass spectrometry (GC/MS) at the ECN analytical laboratories. Selected ash samples from the cyclone equipment were collected and further characterised at University of Leeds laboratories using the SEM-EDX analytical technique.

7.2 Fluidised bed system

A description of a generalised fluidised bed gasification system can be found in Chapter 2 of this work. The bubbles of gas in fluidised bed gasifiers are originated at the base of the bed, carrying upwards some solid particles either

in groups or individually. The interaction between particles and bubbles is shown in Figure 7.2-1 [1].

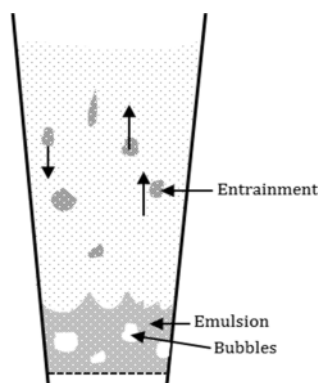


Figure 7.2-1. Interaction between bubbles of gas and particles in a fluidised bed gasifier

The WOB fluidised bed reaction system was electrically heated; seven different thermocouples were located along the reactor, allowing the measurement of temperatures during all the experiments. The feedstock capacity of the WOB gasifier was about 1kg/h, and the fuel feeding rate was fixed through a control system via computer. The fuel was moved by gravity into a screw to reach the bottom of the gasifier. Five main gas supply lines were used to introduce the carrier gases directly to the bottom of the reactor. The flow rate of the water steam supply line was manually set up before each experiment, and was also turned on or turned off manually. The temperature of the line (150 °C) allowed water steam to be introduced together with the other carrier gases used (air, nitrogen, oxygen, etc.). The mixture of solids inside the gasifier and the uniform temperature distribution were reached thanks to the continuous motion of the solid particles (bed material and RDF) originated by the fluidising gas, rising in the form of bubbles, through the overlying material [2]. Once the gases reached the main outlet of the gasifier, they were carried towards a small cyclone aimed to remove most of the unburned particles from the gas flow (commonly ash). Afterwards, the gases were passed through a high temperature gas filter (450 °C), where the last traces of dust and particulates were removed from the output gas [3, 4]. After the gas filter, a gas sample was taken using the solid phase adsorption method (SPA). The gas was further cooled down using a condenser equipped with a filter thimble which allows a further cleaning of the

gas by removing tars and moisture. A second backup cooler (5 °C) was placed before the gases reached the micro GC on-line gas analysis system. A simplified flow diagram of the WOB system is shown in Figure 7.2-2. In addition the appearance of the software used to manipulate variables such as flow rates and temperatures is shown in Figure 7.2-3.

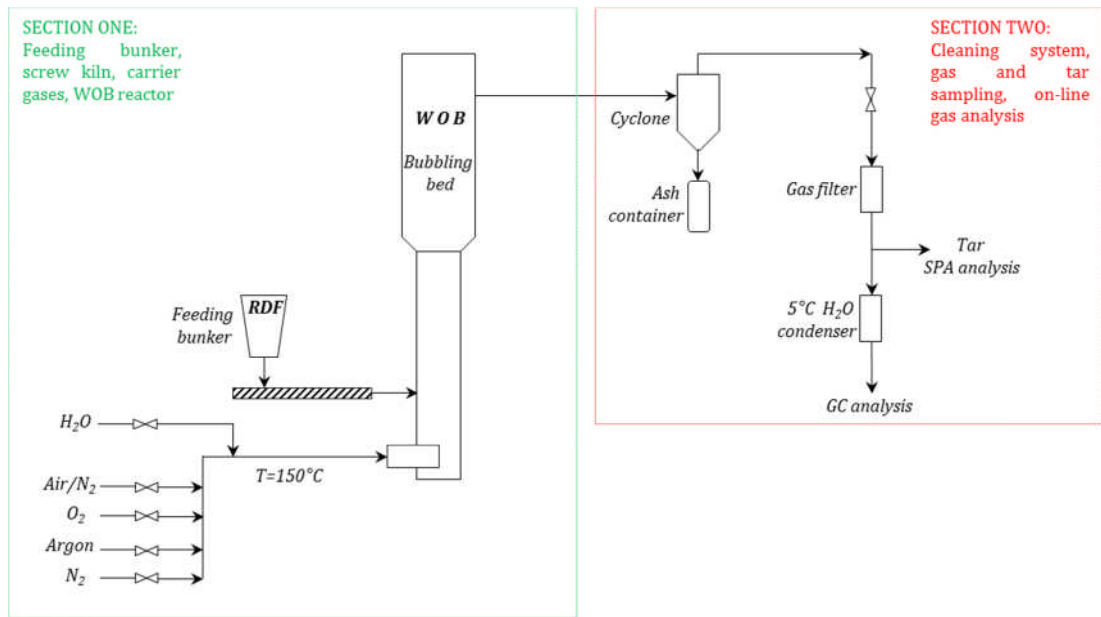


Figure 7.2-2. Flow diagram of the WOB fluidised bed gasification system

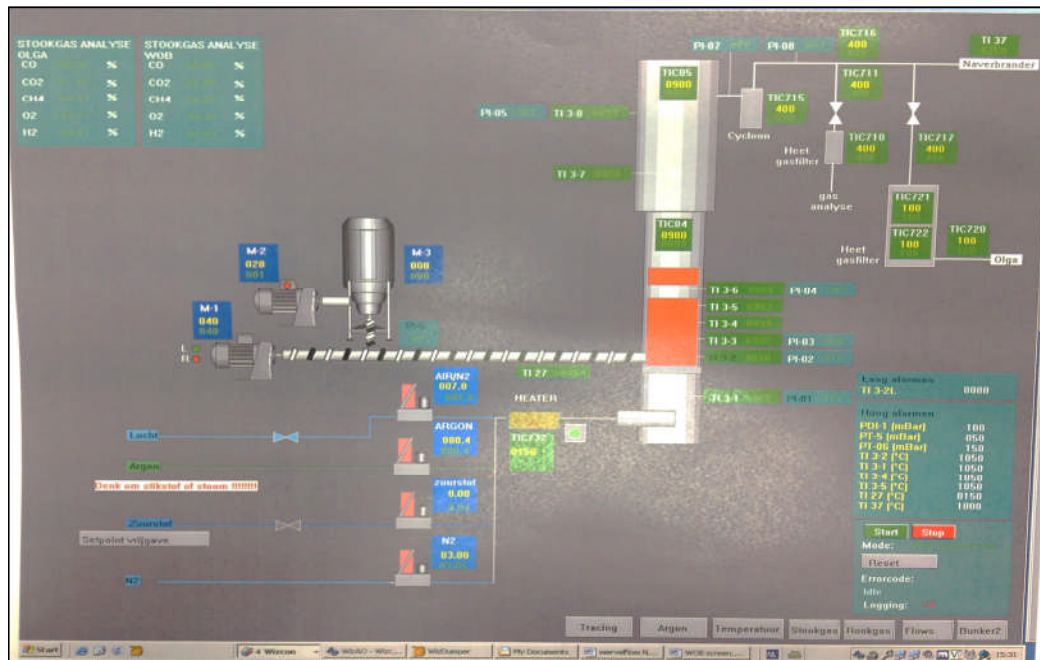


Figure 7.2-3. Appearance of the control system for the WOB gasifier

7.2.1 WOB reaction system considerations

The WOB gasification system has been widely tested using different types of solid waste including RDF, wood, straw and manure; and has been found that the solid waste is not fully converted when working at low pyrolysis or gasification temperatures (550-850 °C). Therefore some of the char that remained unconverted inside the reaction system was mixed up with the bed material (olivine), thus promoting some cracking reactions, which can influence the final gas composition. Furthermore when running more than one experiment per day, some char remained inside the reactor which might also influence the subsequent experiments.

7.3 Physical properties of the fuel and bed material

The fuel used for the gasification/combustion experiments in the WOB system was refuse derived fuel (RDF), the general properties of this raw material are given in Section 7.3.1. The selected bed material was olivine due to its availability and cheap cost compared with other types of catalysts.

7.3.1 Refuse derived fuel (RDF) characteristics

The same RDF used in the two-stage gasification system at the University of Leeds, was used as feedstock in the WOB reactor. However the pellets were pre-treated by staff at the ECN, according to the WOB gasifier requirements. The original RDF pellets had 4cm of length and about 1.5cm of diameter, and were ground to obtain smaller pellets with size about 4x3mm, as shown in Figure 7.3-1.

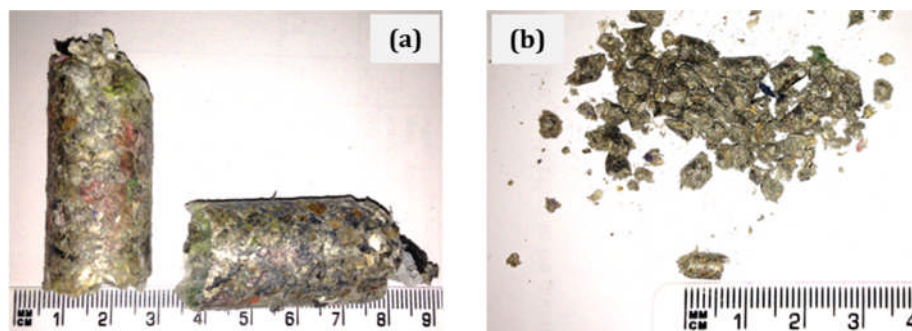


Figure 7.3-1. RDF pellets to be fed into the WOB reactor: (a) 4x1.5cm; (b) 4x3mm

The resulting RDF pellets were dried in air at 100 °C for a period of 24 hours, and the final pellets were found to contain 2.56wt.% of moisture.

7.3.2 Olivine as bed material

Olivine has been commonly used in fluidised bed gasifiers with positive results for tar reduction where cracking and reforming reactions take place, specifically for high molecular weight organic components [3, 5, 6]. Olivine is a common naturally occurring mineral, consisting mainly of a silicate material, with magnesium (e.g. Mg_2SiO_4), and iron cations (e.g. Fe_2SiO_4) fixed to a tetrahedral silica structure. Its silica content (SiO_2) is about 42wt.% compared to silica sand with normally 98wt.% SiO_2 . Tar reduction during gasification might be promoted due to the presence of active iron in the surface of the olivine, influencing CO-shift and methane reforming reactions. Olivine sand has a high mechanical strength even when exposed to elevated gasification temperatures, and there are no fouling or fines problems downstream when using olivine as bed material [6-8]. The olivine used for the experiments in the WOB system was a brownish material with some porosity, normally pre-treated between 1260-1600 °C during 2-4 hours, in order to improve its performance.

7.4 Sampling and analysis of gaseous and solid samples

Samples of the gaseous and solid products formed as a result of the RDF gasification were collected and examined using specific analytical techniques. The gaseous products were continuously monitored using an on-line gas chromatograph. Additional gas sample bags were collected to be analysed off-

line also through gas chromatography. Solid ash samples were collected after the cyclone; selected samples were analysed using scanning electron microscopy (SEM) with energy dispersive X-ray analysis (EDX).

7.4.1 Gas chromatography for on-line and off-line analyses

The micro GC on-line analyser allowed recording of the concentration of several gases using 4 different channels. Table 7.4-1 shows details about the column type of the micro GC and the gases analysed by each Channel.

Table 7.4-1. Column types and gases measured

Channel	Column Properties	Gases Analysed
Channel 1	CP7401148 Molsieve 10m, with back flush	H ₂ , O ₂ /Ar, N ₂ , CH ₄ , and CO
Channel 2	CP740152 PPU (Paraplot) 10m, with back flush	CO ₂ , C ₂ H ₄ , C ₂ H ₆ , and C ₂ H ₂
Channel 3		H ₂ S and carbonyl sulphide (COS)
Channel 4	CP914457 CP-Wax-52CB 10m	benzene and toluene

The micro-GC analyser was calibrated in a similar way as the calibration for the GC Varian analysers described in Section 3.4.1.3 of this work. The two gas sample bags taken during stable conditions were analysed off-line using a GC Shimadzu 14B equipped with a FPD sulphur selective detector to measure thiophenes and mercaptans, helium was used as carrier gas. The calibration of this device was carried out using a gas mixture containing H₂S, COS, methylmercaptane, dimethylsulfide, and thiophene. Images of the appearance of the on-line gas analyser and micro GC are shown in Figure 7.4-1.

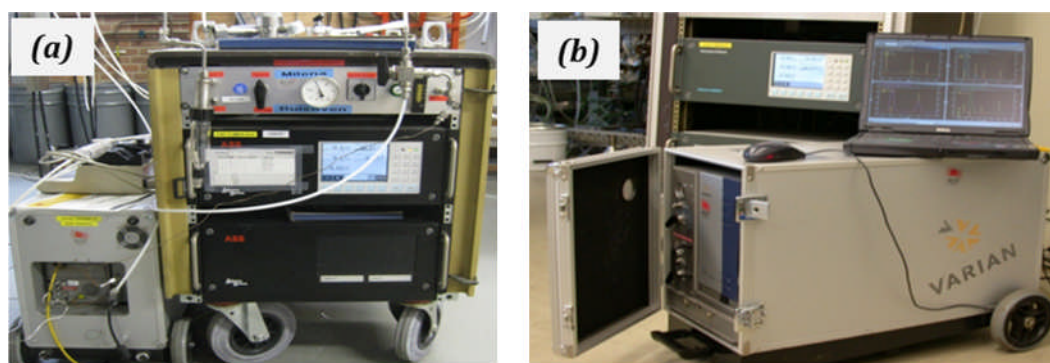


Figure 7.4-1. (a) Mobile GC online and micro GC; (b) GC four channel micro GC in flight case

7.4.1.1 Solid phase adsorption (SPA) tar sampling method

Once both the reaction system and the concentration of the gases reached stable conditions, a sample of the tar contained in the produced gas was extracted according to the Solid-Phase Adsorption (SPA) method previously described in Section 2.4.3 of this work. An injection needle was inserted into the sampling port, the other end of the syringe was connected to syringe pump equipped with a 100ml gastight syringe with 50 ml/min as flow rate, and also a manometer was used to measure the pressure drop. Once the pump reached 100ml of sample gas, the flow was stopped and both the column and the needle were removed as soon as the pressure dropped to zero. The syringe was sealed with a rubber cap, and the sample was stored for further GC/MS analysis.

7.4.2 Definition of operational variables and control system

The RDF was initially subjected to gasification, and then the system was switched into combustion conditions, aimed to burn most of the remaining char. The initial gasification conditions are shown in Table 7.4-2.

Table 7.4-2. Initial RDF gasification conditions

Parameter	Selected value/units
RDF feed rate	450g/h, 500g/h
Air/N ₂ flow rate	0.0 L/min
Ar Flow rate	0.40 L/min (5.5vol.%)
Oxygen Flow rate	2.00 L/min
N ₂ Flow rate	0.0 L/min
Steam Flow rate	750g/h; 825 g/h
Gasification temperature	700 °C, 800 °C, 900 °C

The gasification temperature was gradually increased until it reached the selected temperature, afterwards the RDF started to be fed. Parameters such as temperature and pressure were monitored at all times through the control system (Figure 7.2-3). During these stable conditions (pressure and temperature), gas bag and tar samples (SPA) were taken in duplicate. As some chars from the RDF gasification might have remained inside the gasifier itself; it was necessary to promote the combustion of the remaining char fraction. The main combustion parameter is the excess air ratio that relates the locally

available air and the stoichiometric amount of air to achieve complete combustion [9]. The experimental conditions used to promote char combustion are shown in Table 7.4-3.

Table 7.4-3. Operational conditions for RDF-char combustion

Parameter	Value and units
RDF feed rate	0.0 g/h
Air/N ₂ flow rate	7.0 L/min
Ar flow rate	0.40 L/min (5.5vol.%)
O ₂ flow rate	2.01 L/min
N ₂ flow rate	3.0 L/min
Steam flow rate	0.0 g/h
Gasification temperature	Maintained stable

The combustion was noted on the online gas composition screen by changes in the CO₂ and O₂ concentrations. Once the combustion ended, the temperature was turned off and the flow rates were gradually reduced. The general parameters selected for each experiment are shown in Table 7.4-4.

Table 7.4-4. Selected conditions for each experiment

Experiment	Gasification Temperature (°C)	Steam flow rate (g/h)	Total Steam supplied (g)	RDF flow rate (g/h)	Time feeding RDF (h)	Total RDF supplied (g)	Steam/RDF Ratio
1	800	750	1502	443	2.0	886.40	1.69
2	900	750	1503	443	2.0	886.77	1.69
3	700	750	2250	474	3.0	1420.67	1.58
4	800	700	1402	474	2.0	948.56	1.48
5	800	825	836	509	1.0	516.10	1.62
6	700	825	1652	567	2.0	1135.01	1.46
7	900	825	1651	567	2.0	1134.23	1.46

As shown in Table 7.4-4 the gasification temperature, steam flow rate and RDF feeding rate were the parameters varied between the experiments. The differences between the values of the RDF flow rate shown in Table 7.4-2 and those reported in Table 7.4-4, were attributed to variations in the feed rate and to the heterogeneous composition of RDF, initial values were set up through the control system at the beginning of the experiment, and final feed rates were calculated considering experimental values recorded during the experiments.

7.4.3 Gasification and combustion processes

Initially during the gasification process, all the moisture contained in the RDF sample was removed, then volatiles were released through pyrolysis and devolatilization reactions, then volatile species reacted in the oxygen-steam atmosphere to produce the final syngas. The main reaction occurring inside the gasification system can be described in terms of the RDF decomposition as follows:



7.5 Results from the analysis of gaseous and solid fractions

Gaseous and solid products were released as a result of the gasification and further combustion of RDF in the WOB system. The gaseous fraction was analysed to identify the different compounds and their respective concentration. In addition tar was analysed for polyaromatic and oxygenated tar compounds from a selected sample. The solid fractions produced were the char that was further combusted, the reacted olivine and ash were collected in the hot-gas filter. However the solid fraction that was further characterised was the ash collected in the filter after the cyclone (Figure 7.2-2). The general conditions as well as the results obtained for solid and gaseous fractions are shown in Table 7.5-1.

Table 7.5-1. Gas composition for experiments carried out in the WOB system

Units	EXPERIMENT 1	EXPERIMENT 2	EXPERIMENT 3	EXPERIMENT 4	EXPERIMENT 5	EXPERIMENT 6	EXPERIMENT 7	
1. General Process Conditions								
Gasification temperature	[°C]	800.00	900.00	700.00	800.00	800.00	700.00	900.00
Steam Flow rate	[g/h]	750.00	750.00	750.00	700.00	825.00	825.00	825.00
Time feeding RDF	[hh:mm:ss]	02:10:00	02:13:00	03:00:00	02:11:00	01:49:00	02:09:00	02:04:00
2. Feed								
RDF flow rate	[g/h]	442.59	442.59	473.56	473.56	509.17	566.80	566.80
RDF moisture	[wt%]	2.56	2.56	2.56	2.56	2.56	2.56	2.56
Ash content	[wt%,dry]	15.00	15.00	15.00	15.00	15.00	15.00	15.00
3. Steam/Fuel Ratio								
Steam/RDF	[-]	1.69	1.69	1.58	1.48	1.62	1.46	1.46
4. Ultimate Analysis Fuel								
%C	[wt%,dry]	44.30	44.30	44.30	44.30	44.30	44.30	44.30
%H	[wt%,dry]	5.90	5.90	5.90	5.90	5.90	5.90	5.90
%N	[wt%,dry]	1.10	1.10	1.10	1.10	1.10	1.10	1.10
%O	[wt%,dry]	48.80	48.80	48.80	48.80	48.80	48.80	48.80
%S	[wt%,dry]	0.00	0.00	0.00	0.00	0.00	0.00	0.00
5. Bed Material								
Amount olivine	[g]	1150.00	1150.00	1150.00	1150.00	1150.00	1150.00	1150.00
Particle size olivine	[mm]	~0.27	~0.27	~0.27	~0.27	~0.27	~0.27	~0.27
6. Gas analysis*								
H ₂	[vol%]	14.62	25.44	11.56	16.83	15.72	22.46	29.21
Ar/O ₂	[vol%]	5.43	3.84	4.84	4.12	4.16	5.74	3.37
N ₂	[vol%]	13.95	11.18	14.33	12.56	13.32	15.85	9.19
CH ₄	[vol%]	7.44	7.61	6.67	8.36	7.86	10.81	8.08
CO	[vol%]	15.78	17.28	16.33	17.54	16.80	18.99	18.02
CO ₂	[vol%]	31.83	28.78	32.89	29.77	30.66	14.52	25.90
C ₂ H ₂	[vol%]	0.17	0.22	0.10	0.19	0.17	0.24	0.22
C ₂ H ₄	[vol%]	5.09	2.26	4.36	5.55	5.42	6.74	2.77
C ₂ H ₆	[vol%]	0.23	0.04	0.62	0.30	0.25	0.75	0.08
Benzene	[ppmV]	6090.25	6824.04	4452.92	6419.21	5832.75	6676.96	7207.30
Toluene	[ppmV]	899.61	129.72	1421.14	968.62	684.00	1675.98	178.68
H ₂ S	[ppmV]	421.43	425.30	437.13	389.62	271.29	522.81	199.41
COS	[ppmV]	52.91	58.89	50.08	70.06	64.61	62.17	93.80
Control Total	[vol%]	102.01	104.09	98.07	103.07	101.23	105.03	104.52
7. After Test								
Cyclone ash	[g]	3.50	19.10	170.00	122.00	108.70	158.00	167.60

*Tar Contribution is not included (SPA)

7.5.1 Gas composition

The composition of the product gas was mainly obtained from the micro GC on-line analyser (4 Channels) which was connected directly into the main gas output line (Figure 7.2-2). The results from the off-line gas analyses were useful to compare the concentrations of some compounds given by the on-line gas chromatograph.

The concentrations shown in Table 7.5-1, correspond to average values calculated from the concentrations given from the on-line GC analyser, and recorded during stable conditions. From Table 7.5-1 it is observed that for the gasification temperature 800 °C (Experiments 1, 4 and 5), the gas composition was quite similar despite changes in the steam/RDF ratios (1.69, 1.48 and 1.62 for experiments 1, 4 and 5 respectively). The large decrease in the CO₂ concentration (Experiment 6), was attributed to a failure in the O₂ supply resulting in negative oxygen values from the GC-online analyser. Therefore the corresponding results might not be comparable with the results from the other experiments carried out. From Table 7.5-1, it was observed that the reduction in the steam/RDF slightly increased the H₂ and CO concentrations in the produced syngas, whereas the concentrations of C₂H₂, C₂H₄, and C₂H₆ remained somewhat constant. This might be due to the promotion of water-gas-shift reactions, whereas reactions such as tar cracking were not further promoted by modifying this parameter. It was also observed that increasing the gasification temperature from 800 °C up to 900 °C resulted in the increase of H₂ and CO concentrations. In addition C₂H₂ concentration remained quite similar, whereas reductions in the concentrations of C₂H₄ and C₂H₆ were noticed. This might indicate a further activity of the olivine at higher temperatures. The variation in the gas composition according to the temperatures in the gasifier (700 °C, 800 °C, and 900 °C), is shown in Figure 7.5-1.

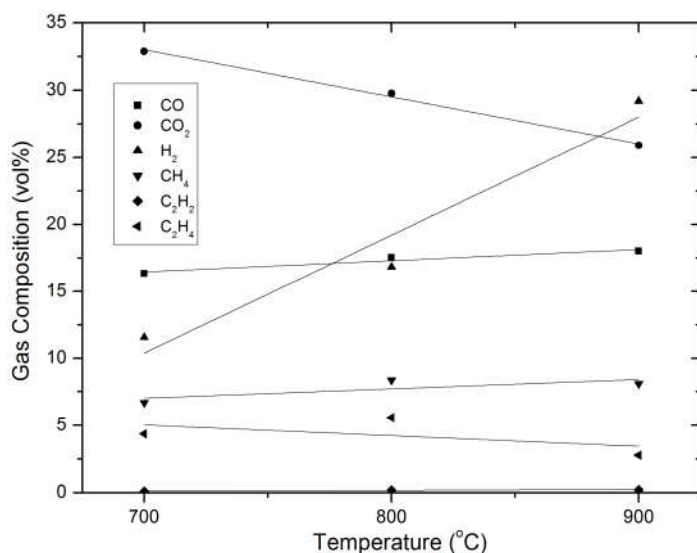


Figure 7.5-1. Gas composition of the produced syngas at different temperatures

From Figure 7.5-1, it is observed that the H₂, CO, and CH₄ concentrations tend to increase as the gasification temperature is increased, whereas the concentration of CO₂ is reduced and the concentration of C₂H₂ is maintained relatively constant, which is in agreement with previous results reported in the literature [10, 11]. From Table 7.5-1, it is also observed that for the same gasification temperature of 900 °C, reducing the steam/RDF ratio from 1.69 (Experiment 2) to 1.46 (Experiment 7) resulted in an increase in the H₂ concentration from 25vol.% up to 29vol.% (Figure 7.5-1). ; however a different trend was observed by changing the steam/fuel ratio at 800 °C, as shown in Figure 7.5-2.

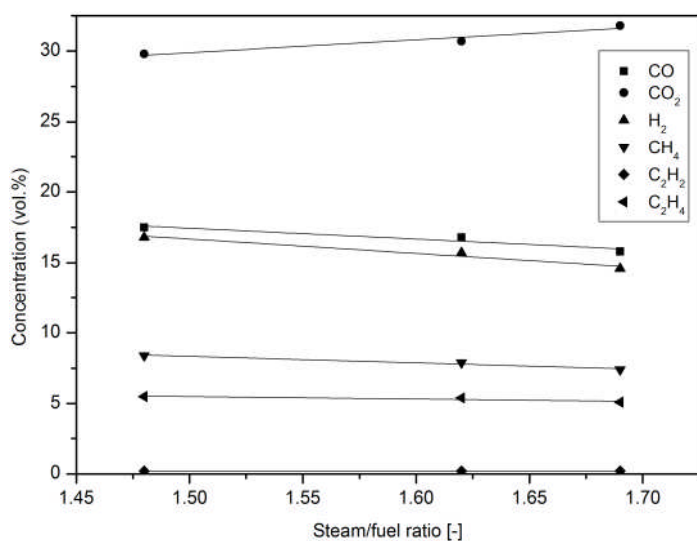


Figure 7.5-2. Effect of steam/fuel ratio on the gas composition at 800 °C

From Figure 7.5-2, the trends observed for all the gas compounds are in agreement with those previously reported in the literature [12]. However for the concentration of H_2 it was expected that the increase in the steam/fuel ratio resulted in an increase in the hydrogen concentration as has been previously reported by Seo et al [12], when working on the gasification of coal and biomass. This can be correlated with the lower ash yield collected after the experiment, attributed to a blockage in the system.

7.5.2 Tar analysis

From Table 7.5-1 it was observed that at 900 °C gasification temperature (Experiments 2 and 7), the concentrations of C_2H_4 , and C_2H_6 were reduced by increasing the steam/RDF ratio from 0.88 (Experiment 7) up to 1.13 (Experiment 2). The variations in the concentrations of C_2 compounds (C_2H_2 , C_2H_6), toluene (C_7H_8), hydrogen sulphide (H_2S), and carbonyl sulphide (COS), with the gasification temperature, are shown in Figure 7.5-3.

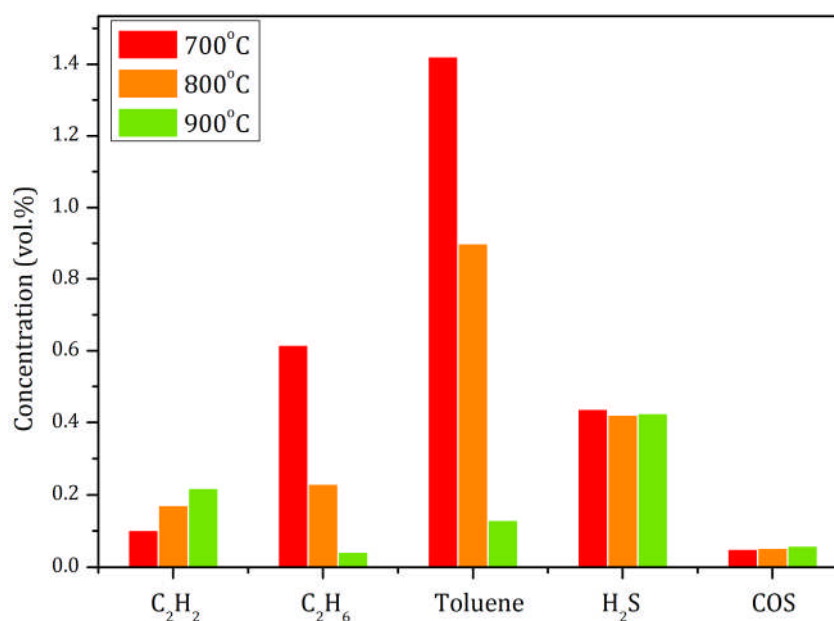


Figure 7.5-3. Variation of some compounds with the gasification temperature

The tar sample from the Experiment 4 (800 °C, steam/RDF=1.48), was analysed. The GC-MS results were reported as mg/m^3 dry gas, as shown in Figure 7.5-4.

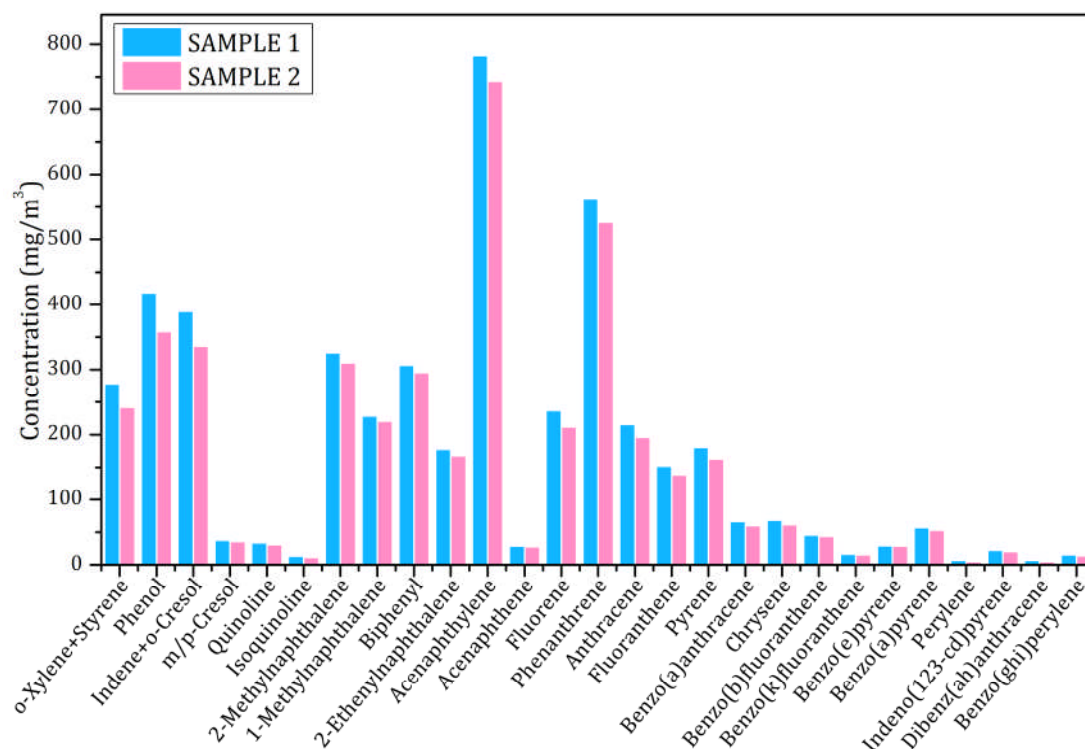


Figure 7.5-4. Identified compounds: SPA tar sample from Experiment 4

From Figure 7.5-4, Sample 1 and Sample 2 refers to the original SPA sample and a duplicate respectively. Naphthalene was not included in the compounds reported in Figure 7.5-4, as the concentrations obtained for this compound were 2888mg/m³ and 2377mg/m³ for Samples 1 and 2 respectively. Also the concentrations of benzene, toluene, ethyl benzene, and m/p-xylenes were calculated, however volatile compounds are known to present problems when collected using specific SPA sampling material, thus a large deviation in the concentrations of these compounds was noted when carrying out the GC-MS analysis, and the results are not reported here.

7.5.3 Ash characterisation using SEM-EDX

Selected samples of the ash collected from the cyclone after each experiment were analysed by scanning electron microscopy with energy dispersive X-ray analysis (SEM-EDX). The composition of the ash was expected to be mainly carbonaceous, however it was considered that some of the olivine used for the fluidised bed might be entrained together with the ash and particulates

contained in the produced gas. Some of the olivine particles might be very fine ($\sim 0.27\mu\text{m}$ particle size) and are transferred through to the main gas exit.

Selected ash samples from Experiments 1, 2, 5, and 6, were analysed at the University of Leeds using scanning electron microscopy (SEM). The resulting electron microscopy images are shown in Figure 7.5-5.

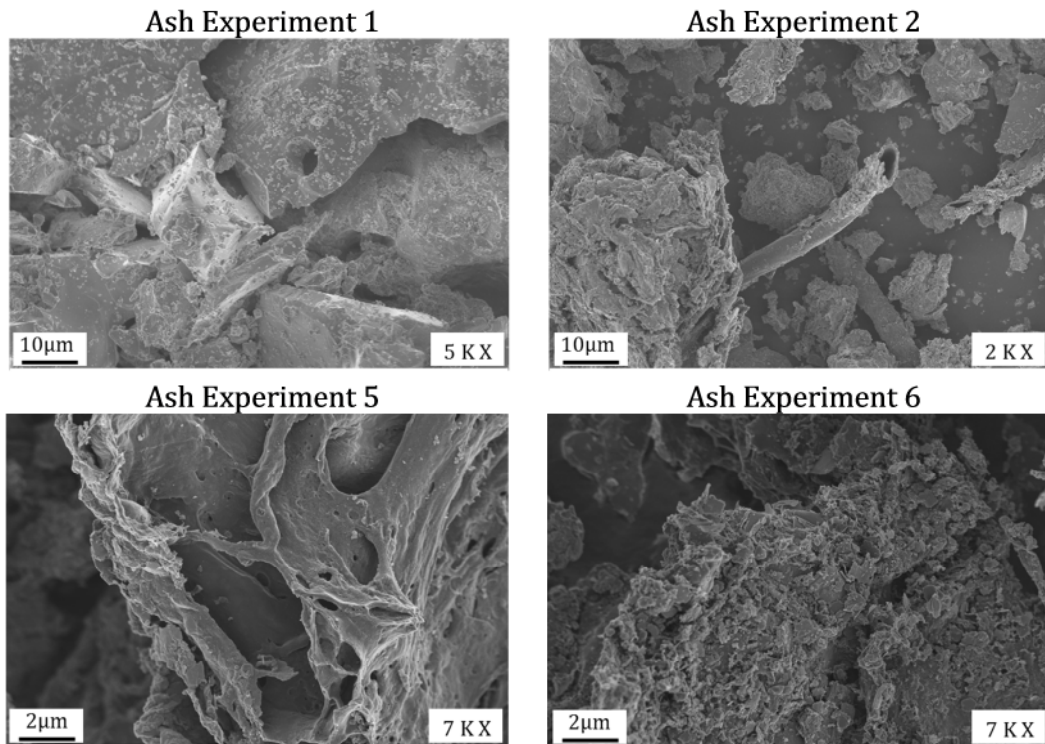


Figure 7.5-5. SEM images from selected ash samples collected from the cyclone

The SEM microphotographs (Figure 7.5-5) reveal that morphological changes took place in the ash surface since different structures are observed. Further SEM-EDX mapping analysis revealed the presence of Si, Mg and Fe, which was partly attributed to some olivine entrained from the gasifier itself towards the gases output and then into the cyclone. SEM-EDX analysis gave quantitative information in weight per cent of the elements present in the sample, these results are presented in Figure 7.5-6.

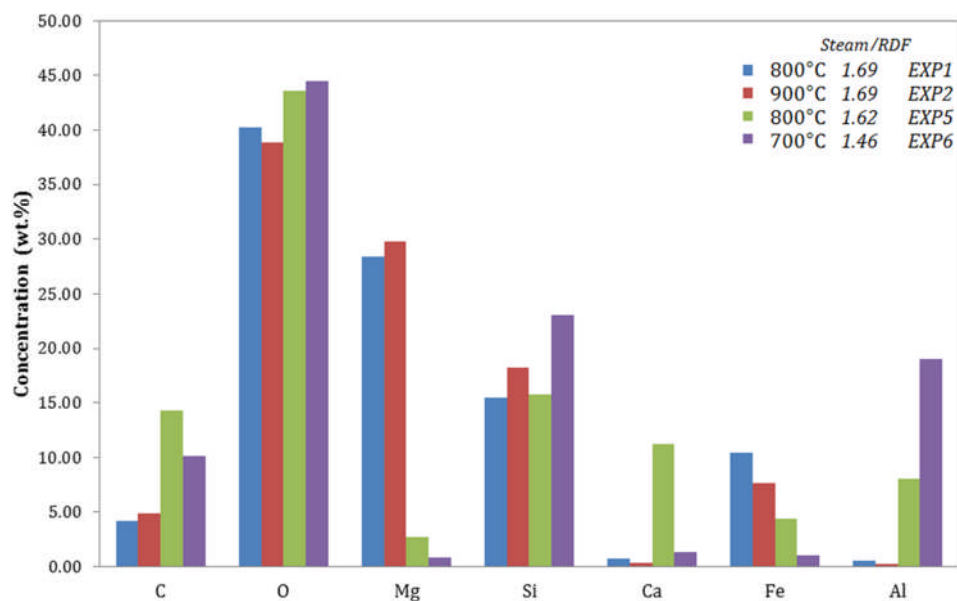


Figure 7.5-6. Variation in ash compositions of selected experiments

From Figure 7.5-6 it is observed that the steam/RDF ratio highly influenced the ash composition. The major identified compound was oxygen combined with other metals in the form of oxide-metal compounds, thus species such as SiO_2 , MgO , Mg_2O_3 , Al_2O_3 , etc., might be present in the ash samples.

7.6 Challenges of scaling up and additional results required

One of the challenges found while scaling up was to reach stable conditions. When RDF is subjected to thermal treatment, a series of parallel exothermic and endothermic reactions take place, resulting in a complex system. The previous experience of staff at ECN was useful to establish the parameters to carry out the gasification of RDF and subsequent combustion of the char formed.

During the operation of the WOB system there were many variables involved, and most of the parameters required to be monitored continuously, because any radical change could entail not only a failure in the experiment, but permanent damage to the equipment. Therefore monitoring the temperature and pressure at different points of the system was a fundamental guide to safe operation.

Additional analyses were required after the experiments. For example the analysis of all the SPA tar samples collected might give an idea of the tar

concentration for each experiment, and will be also useful to determine the influence of the temperature and steam/RDF ratios over tar concentration. Other parameters required might be the weight of the bed after each experiment, as some of the char might have remained even after combustion. Also additional XRD and elemental analysis might be also useful to understand the different compounds present in the collected ash.

It was observed that the increase in the gasification temperature from 700 °C up to 900 °C, resulted in an increase in the hydrogen concentration from 11.56 vol.% up to 25.44 vol.% in the produced gas. A similar trend was observed in the H₂ concentration in the syngas, when the gasification temperature was increased from 600 °C up to 800 °C in the small scale two-stage reaction system (Chapter 4, Section 4.1.2). Main tar compounds including naphthalene, acenaphthylene, phenanthrene, methylnaphthalenes, and biphenyl, were identified when analysing the tar sample from the RDF gasification in the WOB system. It is noteworthy that these compounds were also identified in tar samples obtained using the two-stage reactor (Chapter 4, and Chapter 5). These similarities in gas and tar compositions might indicate that despite the heterogeneity of the RDF, using small scale or bigger systems for gasification of this fuel might have similar results regarding these parameters. However, more experiments are required to obtain a more sensitive and accurate comparison among both systems.

7.7 Summary

The continuous fluidised bed system used for the gasification of RDF and further combustion of RDF char, allowed a good decomposition of the fuel into mainly into gaseous products. The highest H₂/CO ratio of 1.62 was attained at 900 °C, using a steam/RDF ratio of 1.46. In general it was found that increasing the gasification temperature resulted in an increase in the concentration of H₂, CO, and CH₄ and a reduction in the concentration of CO₂.

Some of the tar compounds reported from the SPA tar sample analysis such as phenanthrene, methylnaphthalenes, phenol, indene, cresols, naphthalene,

styrene, and fluorene, have been also found in the tar composition of samples from the pyrolysis/gasification of RDF in the two-stage reaction system used for this research. Additional analysis of tar samples would be helpful to understand the effects of varying the gasification temperature and steam/RDF ratio.

Major compounds found in ash samples were Mg, Si, Fe, C, Al, O, Ca, and Al; the high concentration of oxygen suggest that most of these compounds are present as metal-oxides. Similar compounds have been reported in the literature when analysing ash samples from the gasification of RDF.

References

1. Basu, P., *Combustion and Gasification in Fluidized Beds*, ed. T.F. Group. 2005, Florida, USA: CRC Press. 473.
2. Buekens, A.G. and J.G. Schoeters, *Mathematical Modelling in Gasification (Keynote paper)*, in *Thermochemical Processing of Biomass*, A.V. Bridgwater, Editor. 1984, Butterworths: Birmingham. p. 177-199.
3. Zwart, R., S. van der Heijden, R. Emmen, J. Dall Bentzen, J. Ahrenfeldt, P. Stoholm, and J. Krogh, *Tar removal from low-temperature gasifiers* E.-N. Bioenergy, Editor. 2010, ECN. p. 73.
4. Blackadder, W.H. and E. Resenfelt, *Synthesis Gas from Wood and Peat -The Mino Process*, in *Thermochemical Processing of Biomass*, A.V. Bridgwater, Editor. 1984, Butterworths & Co: Birmingham, UK. p. 137-149.
5. Devi, L., M. Craje, P. Thüne, K.J. Ptasinski, and F.J.J.G. Janssen, *Olivine as tar removal catalyst for biomass gasifiers: Catalyst characterization*. Applied Catalysis A: General, 2005. 294(1): p. 68-79.
6. Rapagnà, S., N. Jand, A. Kiennemann, and P.U. Foscolo, *Steam-gasification of biomass in a fluidised-bed of olivine particles*. Biomass and Bioenergy, 2000. 19(3): p. 187-197.
7. Pettersson, A., *Characterisation of Fuels and Fly Ashes from Co-Combustion of Biofuels and Waste Fuels in a Fluidised Bed Boiler -- A Phosphorus and Alkali Perspective*, in *Department of Energy and Environment*. 2008, Chalmers University of Technology/University College of Borås: Göteborg and Borås, Sweden.
8. Hrbek, J., *Bed materials*, in *Thermal gasification of biomass*, IEA Bioenergy, Editor. 2012, International Energy Agency (IEA): Istanbul, Turkey.
9. Nussbaumer, T., *Combustion and co-combustion of biomass: fundamentals, technologies, and primary measures for emission reduction*. Energy & Fuels, 2003. 17(6): p. 1510-1521.
10. Narváez, I., A. Orío, M.P. Aznar, and J. Corella, *Biomass Gasification with Air in an Atmospheric Bubbling Fluidized Bed. Effect of Six Operational Variables on the Quality of the Produced Raw Gas*. Industrial & Engineering Chemistry Research, 1996. 35(7): p. 2110-2120.
11. Nagaraja, M. and R. Sundaresan, *Gasification of Juliflora Chips in a Circulating Fluidized Bed Gasifier*. International Journal of Energy Science, 2013. 3(2): p. 91-98.
12. Seo, M.W., J.H. Goo, S.D. Kim, S.H. Lee, and Y.C. Choi, *Gasification Characteristics of Coal/Biomass Blend in a Dual Circulating Fluidized Bed Reactor*. Energy & Fuels, 2010. 24: p. 3108-3118.

CHAPTER 8. CONCLUSIONS AND SUGGESTIONS FOR FUTURE WORK

This research work was divided into several sections. Diverse nickel-based catalysts were tested during the pyrolysis and subsequent gasification of refuse derived fuel (RDF), in order to promote catalytic steam reforming reactions within the gasification stage. A two-stage pyrolysis-gasification reaction system was used to carry out most of the experiments described in this research work.

The improvement of the catalytic activity focused on hydrogen production and was one of the main objectives during all the experiments carried out. Also the catalyst performance was assessed through the reduction in the tar formation. A series of different nickel based catalysts were prepared through diverse synthesis methods, and varying the nickel loading and other parameters such as calcination temperature, in order to improve certain characteristics of the catalysts. The aim of investigating catalysts synthesis was to improve their activity, mainly towards hydrogen production and tar reduction.

8.1 General conclusions

The following conclusions were addressed considering the order of the Chapters and results presented in this research work.

8.1.1 Analysis of process conditions on gas and tar compositions

The effects of the gasification temperature were tested concerning the gas yield, and also regarding the gas and tar compositions. It was found that using nickel based catalysts, specifically Ni/Al₂O₃ catalysts, some cracking reactions were promoted in the presence of steam at a gasification temperature of 800°C. Also it was found that this temperature was suitable to promote the activation of the catalyst, which helped to improve their catalytic activity resulting in an increase in the hydrogen content in the produced gas up to 45 vol.% when compared with a H₂ concentration of 31 vol.% when using a bed of sand under similar

operational conditions. Furthermore the promotion of cracking reactions using a 10 wt.%Ni/Al₂O₃ catalyst, was verified by the reduction in the presence of 3 and 4-ring aromatic compounds such as anthracene, fluoranthene, pyrene, and triphenylene.

8.1.2 Characterisation and assessment of Ni/SiO₂ catalysts prepared by two methods and promoted with Mg, Ce and Al

A series of Ni/SiO₂ catalysts were prepared varying the nickel loading, preparation method, and adding Ce, Al, and Mg as metal promoters in order to improve certain characteristics such as surface area and sintering resistance. The resulting Ni/SiO₂ catalysts were tested for their efficiency towards hydrogen production and tar reduction during the pyrolysis/gasification of RDF. Sol-gel was found as the most suitable preparation method, as the resulting Ni/SiO₂ catalysts were effective to promote an increase in the hydrogen concentration, an increase in the gas yield and a reduction in the tar formation. Ni/SiO₂ catalyst prepared by sol-gel with a nickel loading of 20wt.% reported the better surface area, mesoporous volume, and particle size when compared with Ni/SiO₂ catalysts prepared by conventional impregnation method. Moreover the use of 20Ni/SiO₂ sol-gel catalyst during the pyrolysis-gasification process, resulted in the highest hydrogen concentration of about 58vol.%, and 0.24mg_{tar}/g_{RDF}. Whereas the same nickel loading in the catalyst prepared by impregnation method, resulted in 40.6vol.% and 0.60mg_{tar}/g_{RDF}, for H₂ and tar concentrations respectively. The addition of Ce, Mg, and Al as metal promoters did not result in the expected improvements for either catalyst's properties or performance.

8.1.3 Effects of varying the Ni:CA ratio over catalysts properties and performance towards hydrogen production and tar reduction

The variation in the ratio of nickel to citric acid (Ni:CA) was also assessed in regard to Ni/SiO₂ characteristics and performance. Similar catalytic properties such as surface area and pore diameter were reported for the Ni/SiO₂ catalysts prepared using Ni:CA ratios of 1:2 and 1:3. Concerning the hydrogen and tar

yields, it was found that using Ni:CA of 1:2 and 1:3 resulted in similar H₂ concentration of about 58 vol.%, whereas lower tar concentration of 0.15 mg_{tar}/g_{RDF} was attained using a Ni:CA ratio of 1:1.

8.1.4 Ni/SiO₂ catalysts prepared by homogeneous precipitation based methods; effects over catalysts properties and catalytic activity

The effects of using two different homogeneous precipitation, sol-gel based methods, and three different calcination temperatures (500 °C, 700 °C and 900 °C) over Ni/SiO₂ catalytic properties and activity were also analysed. Using a nickel loading of 10 wt.% for all the catalysts, it was found that the addition of a separation phase after the homogeneous precipitation allowed the formation of a bi-continuous macroporous structure, through the interaction of the phase separation and gelation processes. The addition of this step resulted in higher surface areas for the final Ni/SiO₂ catalysts; unfortunately there was no improvement in the catalytic activity. For example up to 60vol.% in the hydrogen concentration was attained in the produced gas, when using the Ni/SiO₂ catalysts, prepared with 10wt.% nickel loading, calcined at 700 °C and prepared by conventional homogeneous precipitation method. It was also found that there was a strong influence of the calcination temperature over both the catalysts properties and activity.

8.1.5 Comparison and assessment of Fe/SiO₂ and Ni/SiO₂ catalysts prepared using a nano-porous silica support

The use of two different metals (iron and nickel) and metal loadings were used during the synthesis of catalysts, using a nano-porous silica material as support. The catalysts were compared regarding their catalytic properties; in addition their catalytic activity was assessed for hydrogen production. At low metal loadings (2.5 and 5.0wt.%), a very high influence from the silica support was noted for both iron and nickel based catalysts, as not many specific crystal phases were detected. Higher surface areas and pore diameters were reported for the series of Fe/SiO₂ catalysts, however higher hydrogen yields of at least

$8\text{mol}_{\text{H}_2}/\text{kg}_{\text{RDF}}$ were obtained when using the Ni/SiO₂ catalyst prepared using the lowest nickel loading of 2.5wt.%.

8.1.6 Performance of olivine as bed material in a pilot scale fluidised bed gasifier, analysis of gas and tar composition

Olivine was used as catalyst within experiments carried in a fluidized bed gasifier for the thermal processing of RDF. A series of experiments were carried out at the Energy Research Centre of the Netherlands (ECN) facilities, located in Petten, Netherlands. Some operational parameters including steam to RDF ratios and gasification temperature were varied. It was found that the concentrations of H₂, CO and CH₄ tend to increase as the gasification temperature was increased from 700 °C to 900 °C. The highest hydrogen concentration of ~29vol.% was attained at 900 °C gasification temperature, and a steam/RDF ratio of 1.46. Major tar compounds identified in a selected tar sample included: naphthalene, acenaphthylene, phenanthrene, methylnaphthalenes, phenol, indene + *o*-cresol, *o*-xylene + styrene, fluorene, anthracene, 2-ethenylnaphthalene, pyrene, and fluoranthene. In addition the analysis of the residual ash revealed the presence of compounds such as Mg, Na, Si, K, Ca, C and Fe.

8.1.7 General remarks

In general it was found that the increase in the surface area of the catalysts prepared and assessed within this work, does not necessarily involve an improvement in the catalytic activity over hydrogen production or tar reduction, however it is still an important parameter that is commonly associated with the catalytic activity. Moreover other properties such as the pore size distribution, metal dispersion, and formation of specific crystal phases, can facilitate a better understanding of the catalytic activity. The highest hydrogen concentration attained was 60 vol.% using the Ni/SiO₂ catalyst with 10 wt.% metal loading, calcined at 700 °C and prepared by homogeneous precipitation (HPG) method. The most relevant tar compounds found from the analyses of several tar samples were naphthalene, fluorene and phenanthrene. In addition the lowest

tar concentration of $0.15 \text{ mg}_{\text{tar}}/\text{g}_{\text{RDF}}$, was attained using the 20 Ni/SiO₂ catalyst prepared by sol-gel method, and calcined at 500°C.

8.2 Future work

During the development of this research work, some of the original objectives were modified and also different aims were developed according to the experimental results obtained. Therefore it is suggested to perform certain additional tasks in order to attain some of these goals. A brief description of the future work suggested is given below.

8.2.1 Analysis of catalysts characteristics and activity

Ni/Al₂O₃ catalysts showed high catalytic selectivity to hydrogen production, attributed to the promotion of cracking and steam reforming reactions when compared with experiments carried out using a sand bed. Future work related to Ni/Al₂O₃ preparation methods and varying conditions such as calcination temperature, and nickel loadings, is suggested. The characterisation of these catalysts using some of the analytical techniques described in this work is also suggested to be assessed.

Further investigation to prepare novel nano-porous catalysts can be carried out in order to enhance the hydrogen concentration in the product gas and also to reduce the final tar concentration. Testing different preparation conditions high metal dispersion and surface areas greater than $900 \text{ m}^2 \text{ g}^{-1}$, might be achieved for nano-porous catalysts, which might result in the improvement of the catalytic activity for this type of catalysts.

8.2.2 Lifecycle tests of catalysts

For the Ni/SiO₂ catalyst prepared by homogeneous precipitation method, it is suggested to carry out lifecycle tests in order to identify the suitability for this catalyst to be used in continuous systems and also to obtain information about the resistance for catalyst deactivation. Regeneration of catalysts can also be studied when analysing the life cycle of the nickel-based catalysts.

8.2.3 Modifications in process conditions

For the Fe/SiO₂ catalysts, experiments increasing the gasification temperature can be carried out for comparison and to study the influence of the gasification temperature over the efficiency for the specific catalysts prepared using nano-silica material as support.

8.2.4 Efficiency of catalysts for tar reduction

Specific nickel-based catalysts can be assessed regarding their efficiency towards the promotion of tar cracking reactions during the catalytic steam reforming process, using tar model compounds. Most abundant identified tar compounds such as toluene, phenol, naphthalene, fluorene and phenanthrene, or specific mixtures can be studied under similar gasification conditions.

8.2.5 Applications of nickel-based catalysts for hydrogen production using RDF as feedstock

The use of this technology at large scale is promising; however certain improvements need to be approached. For example the effects of the RDF composition during the feeding in continuous systems such as the fluidized bed are required. In addition a sustainable and environmentally sustainable source of RDF needs to be identified, in order to ensure a continuous supply of this raw material. Regarding the catalysts properties and supply it is also suggested to undertake an integrated analysis including the advantages and disadvantages of the proposed nickel-catalysts, against those from the currently commercial available nickel catalysts. Further investigation of the subsequent use of the syngas is advised, especially for large scale facilities, where larger amounts of syngas will be generated.